

ERCOFTAC

Bulletin

March 2016

106

European Research Community on Flow, Turbulence and Combustion

ERCOFTAC is a leading European association of research, education and industry groups in the technology of flow, turbulence and combustion. The main objectives of ERCOFTAC are: To promote joint efforts of European research institutes and industries with the aim of **exchanging technical and scientific information**; to promote **Pilot Centres** for collaboration, stimulation and application of

research across Europe; to stimulate, through the creation of **Special Interest Groups**, wellcoordinated European-wide research efforts on specific topics; to stimulate the creation of advanced training activities; and to be influential on funding agencies, governments, the European Commission and the European Parliament.

www.ercoftac.org

Honorary Presidents

Mathieu, J. Spalding, D.B.

Executive Committee

Chairman

Tomboulides, A.
University of Western
Macedonia, Greece
Tel: +30 246 105 6630
atompoulidis@uowm.gr
ananiast@auth.gr

First Deputy Chairman

Von Terzi, D.

Second Deputy Chairman

Hirsch, C.

Treasurer

Hämäläinen, J.

Deputy Treasurer

Ooms, G.

SPC Chairman

Geurts, B.J.

SPC Deputy Chairman

Sagaut, P.

KNC Chairman

Hutton, A. G.

KNC Deputy Chairman

Geuzaine, P.

Industrial Eng. Officer

Seoud, R.E.

Knowledge Base Editor

Rodi, W.

Bulletin Editor

Elsner, W.

ERCOFTAC Seat of the Organisation

Director

Hirsch, C.
Chaussée de la Hulpe 189
Terhulpsessesteenweg
B-1170 Brussels, Belgium
Tel: +32 2 643 3572
Fax: +32 2 647 9398
ado@ercoftac.be

Scientific Programme Committee

Chairman

Geurts, B.J.
University of Twente
Mathematical Sciences
PO Box 217
NL-7500 AE Enschede
The Netherlands
Tel: +31 53 489 4125
b.j.geurts@utwente.nl

Deputy Chairman

Sagaut, P.

Knowledge Network Committee

Chairman

Hutton, A. G.
Airbus Operations Ltd.
Building 07S
Filton, Bristol, BS99 7AR
United Kingdom
Tel: +44 117 936 7 590
anthony.hutton@airbus.com

Deputy Chairman

Geuzaine, P.

Industrial Eng. Officer

Seoud, R.E.
richard.seoud-ieo@ercoftac.org

ERCOFTAC Central Administration and Development Office (CADO)

Admin. Manager

Jakubczak, M.
PO Box 53877
London, SE27 7BR
United Kingdom
Tel: +44 203 602 8984
admin@cado-ercoftac.org
Skype: Ercoftaccado

TABLE OF CONTENTS

Theme Issue on Transition Modelling <i>E. Dick and W. Elsner</i>	4
The Role of Linear Perturbation Methods in Transition Prediction <i>M. W. Johnson</i>	6
On Hypersonic Boundary Layer Transition: Role of Streaks <i>J. Ren and S. Fu</i>	11
Theory and Simulations of Bypass Transition in Two-Fluid Boundary Layers <i>T. A. Zaki and J. Page</i>	17
A Contribution to Investigations of the Leading Edge Shape Effect on the Flat Plate Boundary Layer Transition <i>P. Jonáš and P. P. Antoš</i>	25
Experimental Investigations on the Unsteady Transition Process of the Suction Side Boundary Layer of LPT Blades <i>D. Lengani, D. Simoni, M. Ubaldi, P. Zunino and F. Bertini</i>	31
Vortical Structures and Transition on Rotating Cones, Swept Cylinders and Turbomachinery Blades <i>J. P. Gostelow, S. J. Garrett, A. Rona and W. A. McMullan</i>	37
Advancements in the LCTM Approach to Modelling Laminar-Turbulent Transition <i>F.R. Menter and P. Smirnov</i>	42
On the Development of a Phenomenological Transition Model for Turbomachinery Flows <i>V. Marciniak</i>	49
An Intermittency Transport Model for Transitional Flows on Smooth and Rough Walls <i>L. Wei, X. Ge, J. George and P. Durbin</i>	54
An Algebraic Transition Model Combined with The $k\omega$ Rans Model for Turbomachinery Use <i>S. Kubacki and E. Dick</i>	60
Transition Modelling in Internal and External Aerodynamics Using Various Transition Models <i>J. Příhoda, J. Fürst, P. Straka, P. Louda and M. Kožíšek</i>	66
Adapting the $\gamma - \tilde{Re}_{\theta t}$ Transition Model to a $k - l$ Turbulence Modeling Framework <i>A. Minot, J. Marty, J. Perraud and G. Casalis</i>	72
Numerical Investigation of Surface Roughness Effect with Intermittency Transport Model <i>W. Elsner and P. Warzecha</i>	78
Comparison of RANS and Embedded LES Calculations with Measurements of Transitional Flow Along a Flat Plate <i>P. Bader, W. Sanz, C. Steinmayr and P. Leit</i>	84
Application Challenges for Transition Prediction Techniques in an Unstructured CFD Code <i>A. Krumbein, N. Krimmelbein, C. Grabe and N. Shengyang</i>	92
Integration of a DBD Plasma Actuator Model in Transitional Turbulence Modeling <i>P. Kaparos, Z. Vlahostergios and K. Yakinthos</i>	98

EDITOR	Marek, M.
TECHNICAL EDITOR	Kuban, Ł.
CHAIRMAN	Elsner, W.
EDITORIAL BOARD	Armenio, V. Dick, E. Geurts, B.J.
DESIGN & LAYOUT	Borhani, N. Nichita, B.A.
COVER DESIGN	Aniszewski, W.

SUBMISSIONS

ERCOFTAC Bulletin
Institute of Thermal Machinery
Częstochowa University of Technology
Al. Armii Krajowej 21
42-201 Częstochowa
Poland
Tel: +48 343 250 507
Fax: +48 343 250 507
Email: ercoftac@imc.pcz.czest.pl

HOSTED, PRINTED & DISTRIBUTED BY

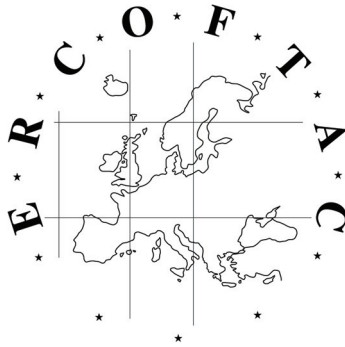


CZĘSTOCHOWA UNIVERSITY OF TECHNOLOGY

The reader should note that the Editorial Board cannot accept responsibility for the accuracy of statements made by any contributing authors

NEXT ERCOFTAC EVENTS

ERCOFTAC Spring Festival	ERCOFTAC Committee Meetings
April 21 st , 2016 Brno, Czech Republic	April 22 nd , 2016 Brno, Czech Republic



The ERCOFTAC Best Practice Guidelines for Industrial Computational Fluid Dynamics

The Best Practice Guidelines (BPG) were commissioned by ERCOFTAC following an extensive consultation with European industry which revealed an urgent demand for such a document. The first edition was completed in January 2000 and constitutes generic advice on how to carry out quality CFD calculations. The BPG therefore address mesh design; construction of numerical boundary conditions where problem data is uncertain; mesh and model sensitivity checks; distinction between numerical and turbulence model inadequacy; preliminary information regarding the limitations of turbulence models etc. The aim is to encourage a common best practice by virtue of which separate analyses of the same problem, using the same model physics, should produce consistent results. Input and advice was sought from a wide cross-section of CFD specialists, eminent academics, end-users and, (particularly important) the leading commercial code vendors established in Europe. Thus, the final document can be considered to represent the consensus view of the European CFD community.

Inevitably, the Guidelines cannot cover every aspect of CFD in detail. They are intended to offer roughly those 20% of the most important general rules of advice that cover roughly 80% of the problems likely to be encountered. As such, they constitute essential information for the novice user and provide a basis for quality management and regulation of safety submissions which rely on CFD. Experience has also shown that they can often provide useful advice for the more experienced user. The technical content is limited to single-phase, compressible and incompressible, steady and unsteady, turbulent and laminar flow with and without heat transfer. Versions which are customised to other aspects of CFD (the remaining 20% of problems) are planned for the future.

The seven principle chapters of the document address numerical, convergence and round-off errors; turbulence modelling; application uncertainties; user errors; code errors; validation and sensitivity tests for CFD models and finally examples of the BPG applied in practice. In the first six of these, each of the different sources of error and uncertainty are examined and discussed, including references to important books, articles and reviews. Following the discussion sections, short simple bullet-point statements of advice are listed which provide clear guidance and are easily understandable without elaborate mathematics. As an illustrative example, an extract dealing with the use of turbulent wall functions is given below:

- Check that the correct form of the wall function is being used to take into account the wall roughness. An equivalent roughness height and a modified multiplier in the law of the wall must be used.
- Check the upper limit on y^+ . In the case of moderate Reynolds number, where the boundary layer only extends to y^+ of 300 to 500, there is no chance of accurately resolving the boundary layer if the first integration point is placed at a location with the value of y^+ of 100.

- Check the lower limit of y^+ . In the commonly used applications of wall functions, the meshing should be arranged so that the values of y^+ at all the wall-adjacent integration points is only slightly above the recommended lower limit given by the code developers, typically between 20 and 30 (the form usually assumed for the wall functions is not valid much below these values). This procedure offers the best chances to resolve the turbulent portion of the boundary layer. It should be noted that this criterion is impossible to satisfy close to separation or reattachment zones unless y^+ is based upon y^* .
- Exercise care when calculating the flow using different schemes or different codes with wall functions on the same mesh. Cell centred schemes have their integration points at different locations in a mesh cell than cell vertex schemes. Thus the y^+ value associated with a wall-adjacent cell differs according to which scheme is being used on the mesh.
- Check the resolution of the boundary layer. If boundary layer effects are important, it is recommended that the resolution of the boundary layer is checked after the computation. This can be achieved by a plot of the ratio between the turbulent to the molecular viscosity, which is high inside the boundary layer. Adequate boundary layer resolution requires at least 8-10 points in the layer.

All such statements of advice are gathered together at the end of the document to provide a 'Best Practice Checklist'. The examples chapter provides detailed expositions of eight test cases each one calculated by a code vendor (viz FLUENT, AEA Technology, Computational Dynamics, NUMECA) or code developer (viz Electricité de France, CEA, British Energy) and each of which highlights one or more specific points of advice arising in the BPG. These test cases range from natural convection in a cavity through to flow in a low speed centrifugal compressor and in an internal combustion engine valve.

Copies of the Best Practice Guidelines can be acquired from:

ERCOFTAC (CADO)
PO Box 53877
London, SE27 7BR
United Kingdom
Tel: +44 203 602 8984
Email: magdalena.jakubczak@ercoftac.org

The price per copy (not including postage) is:

ERCOFTAC members		
First copy		<i>Free</i>
Subsequent copies		75 Euros
Students		75 Euros
Non-ERCOFTAC academics		
Non-ERCOFTAC industrial		140 Euros
EU/Non EU postage fee		230 Euros
		10/17 Euros

All in ERCOFTAC are deeply saddened to hear of the death of **Prof. Anthony G. Hutton**, our Knowledge Network Committee Chairman and a previous Chairman of our organisation. Tony was involved with ERCOFTAC for almost twenty years; for about ten years (1997- 2006) he was the Chairman of the Industrial Advisory Committee (with a short break at the end of 2003 when he was Deputy Chairman) and for 8 years (1997-2005) he was the Coordinator of the ERCOFTAC Quality and Trust Special Interest Group'. He was very active within the organization and contributed to its successful administration as member of its Executive Committee and Management Board. Most importantly, for six years - from 2006 to 2012 - he served as ERCOFTAC's Chairman and from 2013 was our KNC Chairman.



Under Tony's leadership, ERCOFTAC underwent a major transformation from a primarily academic organization to a professional organization with the capacity and means to respond and deliver effectively to the community's needs. Tony pioneered efforts to enhance industrial participation, to connect academic research with industry and to facilitate the collaboration between ERCOFTAC's scientific core and its industrial members. His strong interest in applied fluid dynamics research has resulted in an initiative on Quality and Trust in Industrial CFD, which evolved into the Best Practice Guidelines for industrial CFD, which is ERCOFTAC's most successful publication. Tony's vision has also led to a web-based fluids simulation data base, the QNET-CFD Knowledge Base, which has become the foremost repository of knowledge on flow simulation in the industrial environment.

Over the years, Tony's selfless voluntary contribution to ERCOFTAC and to the community at large was sustained and substantial in terms of scientific knowledge and leadership as well as skillful and committed administration. More importantly, Tony was a great guy, a true leader and a visionary. We are truly grateful and proud for all of his accomplishments and contributions to ERCOFTAC during all these years. In the near future we plan to honour and commemorate his passing in several ways, such as an honorary lecture and an award in his name and possibly also a special journal volume in his honour.

He will be greatly missed.

A. Tomboulides
On behalf of ERCOFTAC's Executive Committee

THEME ISSUE ON TRANSITION MODELLING

E. Dick¹ and W. Elsner²

¹ *Department of Flow, Heat and Combustion mechanics, Ghent University,
St.-Pietersnieuwstraat 41, 9000 Gent, Belgium; erik.dick@ugent.be*

² *Institute of Thermal Machinery, Czestochowa University of Technology,
Al. Armii Krajowej 21, 42-200 Czestochowa, Poland; welsner@imc.pcz.czyst.pl*

The ERCOFTAC Bulletin Theme Issue on Transition Modelling aims to overview recent activities of SIG10. It contains 16 contributions covering a wide variety of topics over theoretical analysis by perturbation methods and experimental analysis of pre-transitional boundary layer behaviour, instability and breakdown, as well as validation, testing and adaptation of new or established transition models with some applications. The characteristics of each paper are summarised below.

M.W. Johnson applies a linear perturbation method for prediction of pre-transitional boundary layer distortions by Tollmien-Schlichting waves and by streaks. He demonstrates that a favourable pressure gradient inhibits fluctuation growth and an adverse pressure gradient promotes it. He shows that transition onset can be predicted by a criterion of 23 % near-wall local turbulence level.

J. Ren and S. Fu analyse by non-linear parabolised stability equations the role of Klebanoff-type and Görtler-type streaks in hypersonic boundary layers. They demonstrate that Klebanoff-type streaks of appropriate amplitude, i.e. large enough to modulate a laminar boundary layer, but not so large to trigger the associated secondary instability, can damp the growth of fundamental instability modes.

T.A. Zaki and J. Page analyse two-fluid boundary layers by a linear perturbation method. They show that a thin near-wall film with a fluid of lower viscosity than the fluid farther away from the wall stabilises a pre-transitional boundary layer perturbed by streaks. The theory explains the weakening of the lift-up mechanism responsible for the secondary instability of a streaky laminar boundary layer.

P. Jonáš and P.P. Antoš investigate experimentally transition in zero pressure gradient boundary layer flow on smooth flat plates with three different leading edge profiles, two levels of free-stream turbulence and several values of free-stream velocity. They demonstrate that transition is the earliest and the shortest with the most rounded leading edge and the latest and the longest with the sharpest leading edge, both for the low and high free-stream turbulence level.

D. Lengani, D. Simoni, M. Ubaldi, P. Zunino and F. Bertini apply proper orthogonal decomposition (POD) to particle image velocimetry images of flow over the suction side of a low-pressure turbine profile, for visual-

isation of the effects of free-stream turbulence intensity (FSTI) and wake passing. They demonstrate that for steady low FSTI, the two most energetic POD modes correspond to Kelvin-Helmholtz rolls in the separated boundary layer, while for high FSTI to low- and high speed longitudinal streaks in the attached boundary layer. For wake-induced transition, the two most energetic modes correspond to the velocity perturbation by the negative jet and a high-speed streak near the wall.

J.P. Gostelow, S.J. Garrett, A. Roma and W.A. McMullan present experimental results on pre-transitional vortex structures in boundary layers on rotating cones and swept cylinders. For rotating cones, they demonstrate pairs of counter-rotating Görtler-type vortices for small half-angles and co-rotating vortices for high half-angles (cross-flow instability). For swept cylinders, they demonstrate stream-wise streaks corresponding to contour-rotating vortices for normal cylinders and low sweep angles and co-rotating vortices for high sweep angles (cross-flow instability).

F.R. Menter and P. Smirnov discuss a recently developed local correlation-based transition model (LCTM) by Menter et al., with a single transport equation for intermittency coupled to the $k - \omega$ SST turbulence model. The intermittency is a multiplier of the production term of the k -equation. Transition is modelled by control of the production and destruction terms of the intermittency equation, involving empirical transition correlations, but formulated as functions of local characteristic Reynolds numbers and local estimates of turbulence level and pressure gradient. The good functioning of the model is demonstrated for an aerofoil and a low-pressure turbine cascade.

V. Marciniak discusses his recently developed physics-based transition model with a single transport equation for pre-transitional laminar fluctuation kinetic energy coupled to the standard $k - \omega$ turbulence model ($k - k_L - \omega$). Transition is modelled by control of the production term in the equation of laminar fluctuation

kinetic energy, with similar form as the equation of turbulent fluctuation kinetic energy, and by a transfer term in these two equations. The crucial terms are made dependent on local Reynolds numbers characterising the physics of bypass transition. The model was calibrated for the low-pressure T107 turbine cascade for several Reynolds numbers involving bypass transition in attached boundary layer and transition in separated boundary layer.

L. Wei, X. Ge, J. George and P. Durbin discuss their new local intermittency-based transition model for smooth and rough surfaces. It consists of a single transport equation for intermittency coupled to the standard $k - \omega$ turbulence model. Transition is modelled, for one part, by the destruction and production terms in the intermittency equation, which depend on several local Reynolds numbers, characterising the physics of bypass transition. The second ingredient is a multiplication factor of the production term in the equation for turbulent kinetic energy, which is the intermittency by the transport equation, but modified by sensors of pressure gradient and boundary layer separation. The model is intermittency-equation-based, but it does not use empirical correlations, but local sensor Reynolds numbers.

S. Kubacki and E. Dick discuss their recently developed physics-based algebraic transition model, coupled to the newest $k - \omega$ turbulence model by Wilcox. Bypass transition is modelled by two multiplication factors of the production of turbulent kinetic energy, expressing damping of short-wavelength disturbances induced by the free-stream in a laminar boundary layer and instability of a pre-transitional boundary layer perturbed by streaks. The good performance for bypass transition in attached boundary layer state is demonstrated on two turbine cascades for high free-stream turbulence. Transition in separated boundary layer state with the same turbine cascades for low free-stream turbulence is not modelled, but resolved by 3D Unsteady RANS.

J. Přihoda, J. Fürst, P. Straka, P. Louda and M. Kožíšek test three transition models of very different nature on a series of cases. The models are the local correlation-based algebraic intermittency model of Straka and Přihoda, the $k - k_L - \omega$ laminar fluctuation kinetic energy model by Walters and Cokljat and the $\gamma - \zeta$ two-equation non-local correlation-based intermittency transport model of Lodefier and Dick. The transition models are combined with the $k - \omega$ explicit algebraic Reynolds stress turbulence model of Hellsten. The test cases are Ercoftac T3 flat plate flows, a subsonic gas turbine vane cascade, an aerofoil in the wake of another aerofoil, a transonic steam turbine blade cascade and a 3D transonic gas turbine blade cascade.

A. Minot, J. Marty, J. Perraud and G. Casalis discuss the adaptation of the $\gamma - Re_\theta$ two-equation local correlation-based intermittency transport model of Menter et al. for combination with a two-equation

$k - l$ turbulence model, replacing the two-equation $k - \omega$ turbulence model. The adaptation for bypass transition in attached boundary layer state involves expressing some parameters as functions of k and l instead of k and ω . Recalibration for bypass transition is done with a high-pressure turbine cascade and for transition in separated boundary layer state with a high-lift low-pressure turbine cascade.

W. Elsner and P. Warzecha illustrate the performance of their model for surface roughness, added to the $\gamma - Re_\theta$ two-equation local correlation-based intermittency transport model of Menter et al. The roughness extensions consist of a wall boundary condition for ω depending on surface roughness, an additional limiter function in the eddy viscosity expression and modification of the Re_θ produced by the transport equation for this parameter. They verify the performance for rough flat plates with turbulent boundary layers with and without pressure gradient and a high-pressure gas turbine blade cascade for three values of surface roughness with transition in attached boundary layer state and a flat plate flow with transition in boundary layer separation state.

P. Bader, W. Sanz, C. Steinmayr and P. Leitel test four transition models against own Constant Temperature Anemometry and Laser Doppler Anemometry data of a transitional flow over a flat plate under a slightly favourable pressure gradient. The models are the recently developed one-equation γ -model of Menter et al., the two-equation $\gamma - Re_\theta$ model of Menter et al., the $k - k_L - \omega$ model of Walters and Cokljat and Large Eddy Simulation embedded in a RANS zone (eLES). They observe that the γ - and $\gamma - Re_\theta$ models produce nearly identical results, very close to the experimental data, while the two other produce a somewhat delayed transition zone.

A. Krumbein, N. Krimmelbein, C. Grabe and N. Shengyang discuss challenges for transition models applied to external aeronautical flows. First, they threat streamline-based approaches combining e^N -methods for natural transition by Tollmien-Schlichting waves and cross-flow waves and for separation-induced transition and empirical criteria for bypass transition. They illustrate the necessity to extend the $\gamma - Re_\theta$ method for cross-flow instability and the necessity to combine it with Reynolds stress models for strongly three-dimensional flows. Finally, they illustrate the still remaining deficiencies for the strongly unsteady flow over an aerofoil in pitching oscillation.

P. Kaparos, Z. Vlahostergios and K. Yakinthos investigate numerically the effect of a dielectric barrier discharge (DBD) plasma actuator for boundary layer control with the $k - k_L - \omega$ transition model of Walters and Cokljat and the model by Suzen and Huang for the effect of the ionic wind produced by the actuator. They demonstrate that bypass transition can be delayed by the exerted stream-wise force.

THE ROLE OF LINEAR PERTURBATION METHODS IN TRANSITION PREDICTION

M. W. Johnson

University of Liverpool, UK

Abstract

A linear perturbation method for predicting the fluctuating flow within the pre-transitional boundary layer is presented. The method captures the full flow physics including the formation of low speed streaks and Tollmien Schlichting waves. Results for zero, adverse and favourable streamwise pressure gradients show how adverse pressure gradient promotes fluctuation growth whereas favourable pressure gradient inhibits it. A fluctuation level threshold is introduced in order to predict a transition onset position which correlates closely with published empirical transition correlations.

Nomenclature

k	$= \frac{\nu}{U^2} \frac{dU}{dx}$	acceleration parameter
p		static pressure
p'		fluctuation pressure
R		receptivity (equation 30)
Re_x, Re_y, Re_z	$= \frac{U_0 x}{\nu}, \frac{U_0 y}{\nu}, \frac{U_0 z}{\nu}$	
Re_{x0}	$= \frac{U_0 x_0}{\nu}$	leading edge Reynolds number
t		time
u, v, w		mean velocity components in x, y and z directions
u', v', w'		perturbation velocities in x, y and z directions
u_f, v_f, w_f		perturbation velocity amplitudes (equation 6)
U		mean freestream velocity
U'	$= (U_f^2 + V_f^2 + W_f^2)^{0.5}$	freestream velocity fluctuation amplitude
U_f, V_f, W_f		perturbation velocity amplitude components in freestream
x, y, z		streamwise, normal and spanwise coordinates
x_0		distance from turbulence generating grid to plate leading edge
β		turbulence decay constant (equation 24)
δ		boundary layer thickness
ω		temporal frequency
$\Omega_x, \Omega_y, \Omega_z$		spatial frequencies
$\Omega_x, \Omega_y, \Omega_z$	$= \frac{\nu \omega_x}{U_0}, \frac{\nu \omega_y}{U_0}, \frac{\nu \omega_z}{U_0}$	
ν		fluid dynamic viscosity
ρ		fluid density
Subscripts		
0		value at turbulence generating grid
nw		near wall value ($y/\delta = 0.1$)
	$k = \frac{\nu}{U^2} \frac{d}{dx}$	

1 Introduction

The accurate prediction of transition onset remains challenging particularly for flows in complex geometries. Current transition models (e.g. Abu-Ghannam and Shaw [1]) rely heavily on empirical data largely taken from simple geometries, (commonly flat plates) and hence most models fail to account for the many effects present in real engineering geometries. It also seems improbable that an empirical transition model can be formulated which accounts for all these factors (e.g. sweep, concave curvature, pressure gradient, turbulence intensity and scale). Direct Numerical Simulation (e.g. Wu

and Moin [2]) can capture the full physics, however it is currently impractical for the high Reynolds numbers and complex geometries typical of most engineering problems. Large Eddy Simulations (LES) offer more economical solutions but require modelling for the sub grid scale eddies and hence can fail to capture the full physics. Theoretical approaches are therefore needed which capture the full physics without the fine spatial resolution of DNS.

2 Theory

The transition process commences with the emergence of Reynolds stresses which enhance the transport of momentum in regions of shear. Mathematically, the Reynolds stresses originate from the convection terms in the Navier Stokes equations when the velocity is split into its time mean and fluctuating components. E.g.

$$uv = (\bar{u} + u')(\bar{v} + v') = \bar{u}\bar{v} + (\bar{u}v' + u'\bar{v}) + u'v' \quad (1)$$

The 3 terms resulting from the splitting are of 0^{th} , 1^{st} and 2^{nd} order in the fluctuating components. In the pre-transitional boundary layer, the Reynolds stress or 2^{nd} order terms remain negligible and hence can be ignored in predicting the fluctuating flow up to transition onset. The governing equations therefore only contain the 1^{st} order (or linear) perturbation terms once the time mean equations (0^{th} order terms) are subtracted.

These linear perturbation equations can be derived for any flow, but here the analysis is limited to 2-d boundary layers in incompressible flow. The governing equations are then, the continuity equation

$$\frac{\partial u'}{\partial x} + \frac{\partial v'}{\partial y} + \frac{\partial w'}{\partial z} = 0 \quad (2)$$

and the momentum equations in the streamwise x, normal y and spanwise z, directions

$$\begin{aligned} \frac{\partial u'}{\partial t} + \frac{\partial}{\partial x} \left(\frac{p'}{\rho} + 2uu' \right) + \frac{\partial}{\partial y} (vu' + uw') \\ + \frac{\partial}{\partial z} (uw') - \nu \nabla^2 u' = 0 \end{aligned} \quad (3)$$

$$\begin{aligned} \frac{\partial v'}{\partial t} + \frac{\partial}{\partial x} (vu' + uw') + \frac{\partial}{\partial y} \left(\frac{p'}{\rho} + 2vv' \right) \\ + \frac{\partial}{\partial z} (vw') - \nu \nabla^2 v' = 0 \end{aligned} \quad (4)$$

$$\frac{\partial w'}{\partial t} + \frac{\partial}{\partial x} (uw') + \frac{\partial}{\partial y} (vw') + \frac{\partial}{\partial z} \left(\frac{p'}{\rho} \right) - \nu \nabla^2 w' = 0 \quad (5)$$

noting that, as the mean flow is two dimensional w and the z derivatives of u , v and p are zero. These equations are therefore the same as the linearised Navier Stokes equations used by Leib et al. [3] and others but retain the streamwise derivatives in the mean velocity.

The variation in the flow perturbations can be considered as periodic in time and also in the spanwise direction as the mean flow is invariant in this direction and so

$$u' = u_f(x, y)e^{i(\omega_z z + \omega t)} \quad (6)$$

with similar expressions for v' , w' and p' . The equations can then be written as

$$\frac{\partial u_f}{\partial x} + \frac{\partial v_f}{\partial y} + \omega_z w_f = 0 \quad (7)$$

$$i\omega u_f + \frac{\partial}{\partial x} \left(\frac{p_f}{\rho} + 2u u_f \right) + \frac{\partial}{\partial y} (v u_f + u v_f) + \omega_z u w_f - \nu \nabla^2 u_f + \nu \omega_z^2 u_f = 0 \quad (8)$$

$$i\omega v_f + \frac{\partial}{\partial x} (v u_f + u v_f) + \frac{\partial}{\partial y} \left(\frac{p_f}{\rho} + 2v v_f \right) + \omega_z v w_f - \nu \nabla^2 v_f + \nu \omega_z^2 v_f = 0 \quad (9)$$

$$i\omega w_f + \frac{\partial}{\partial x} (u w_f) + \frac{\partial}{\partial y} (v w_f) + \frac{\partial}{\partial z} \left(\frac{p_f}{\rho} \right) - \nu \nabla^2 w_f + \nu \omega_z^2 w_f = 0 \quad (10)$$

3 Boundary Conditions

At the inlet, a boundary condition must be specified which represents the perturbed flow in the freestream. This boundary condition must be a solution of the set of equations just derived, simplified for the uniform freestream inlet flow $u = U$ and $v = 0$. These simplified momentum equations are

$$i\omega u_f + \frac{\partial}{\partial x} \left(\frac{p_f}{\rho} + U u_f \right) - \nu \nabla^2 u_f + \nu \omega_z^2 u_f = 0 \quad (11)$$

$$i\omega v_f + \frac{\partial}{\partial x} (U v_f) + \frac{\partial}{\partial y} \left(\frac{p_f}{\rho} \right) - \nu \nabla^2 v_f + \nu \omega_z^2 v_f = 0 \quad (12)$$

$$i\omega w_f + \frac{\partial}{\partial x} (U v_f) + \frac{\partial}{\partial z} \left(\frac{p_f}{\rho} \right) - \nu \nabla^2 w_f + \nu \omega_z^2 w_f = 0 \quad (13)$$

Equations 10, 11 and 12 can be combined to eliminate the velocity components u_f , v_f and w_f resulting in

$$\nabla^2 p_f = 0 \quad (14)$$

Freestream turbulence consists of spatially and temporally periodic waveforms which decay in the streamwise direction and satisfy the flow equations. The freestream solution of the current equations at the inlet must therefore be of the form

$$u' = u_1 e^{i(\omega_x x + \omega_y y + \omega_z z + \omega t) - \beta x} \quad (15)$$

$$v' = v_1 e^{i(\omega_x x + \omega_y y + \omega_z z + \omega t) - \beta x} \quad (16)$$

$$w' = w_1 e^{i(\omega_x x + \omega_y y + \omega_z z + \omega t) - \beta x} \quad (17)$$

Substituting for p' in equation 14

$$p' = u_1 e^{i(\omega_x x + \omega_y y + \omega_z z + \omega t) - \beta x} \quad (18)$$

$$\beta^2 + \omega_x^2 - \omega_y^2 - \omega_z^2 - 2i\beta\omega_x = 0$$

It therefore follows from equation 18 that if w_x and b are non zero, $p_1 = 0$.

The freestream solution of these equations is therefore

$$u_f = u_1 e^{i(\omega_x x + \omega_y y) - \beta x} \quad (19)$$

$$v_f = v_1 e^{i(\omega_x x + \omega_y y) - \beta x} \quad (20)$$

$$w_f = w_1 e^{i(\omega_x x + \omega_y y) - \beta x} \quad (21)$$

$$p_f = 0 \quad (22)$$

This freestream solution is therefore a travelling wave with spatial frequencies ω_x , ω_y and ω_z which decays in the streamwise direction at a rate β . It should be noted that although there are no pressure fluctuations present in the freestream, pressure fluctuations are induced in the boundary layer by the freestream velocity fluctuations. Substituting these expressions into any one of the momentum equations and equating the real and imaginary parts also provides a relationship between the streamwise spatial and temporal frequencies

$$\omega = -(U + 2\beta\nu)\omega_x \quad (23)$$

and an expression for the streamwise decay rate

$$\beta = -\frac{U}{2\nu} + \left(\left(\frac{U}{2\nu} \right)^2 + \omega_x^2 + \omega_y^2 + \omega_z^2 \right)^{0.5} \quad (24)$$

or

$$\beta x = -\frac{Re_x}{2} + \frac{Re_x}{2} (1 + 4(\Omega_x^2 + \Omega_y^2 + \Omega_z^2))^{0.5} \quad (25)$$

where $\Omega_x = \frac{\nu\omega_x}{U_0}$, $\Omega_y = \frac{\nu\omega_y}{U_0}$ and $\Omega_z = \frac{\nu\omega_z}{U_0}$
Typically in engineering problems

$$\Omega_x^2 + \Omega_y^2 + \Omega_z^2 \ll 1 \quad (26)$$

and so

$$\beta x \approx Re_x (\Omega_x^2 + \Omega_y^2 + \Omega_z^2) \quad (27)$$

These relationships indicate that, for a uniform mean flow, the freestream perturbation is convected at a velocity slightly greater than the freestream velocity and decays in proportion to n and approximately in proportion to the square of the overall spatial frequency

$$\Omega_x^2 + \Omega_y^2 + \Omega_z^2 \quad (28)$$

The amplitudes of the velocity fluctuations, u_1 , v_1 and w_1 must also satisfy the continuity equation and so

$$(i\omega_x - \beta)u_1 + i\omega_y v_1 + i\omega_z w_1 = 0 \quad (29)$$

The velocity vector must therefore lie in a plane which is perpendicular to the frequency vector $(i\omega_x - \beta, i\omega_y, i\omega_z)$.

In the current work, this velocity vector is divided into two mutually perpendicular components. The first component is in the x-y plane and hence has a zero component in the z direction ($w_f = 0$) and lies in the same plane as the mean flow velocity. The second component is then

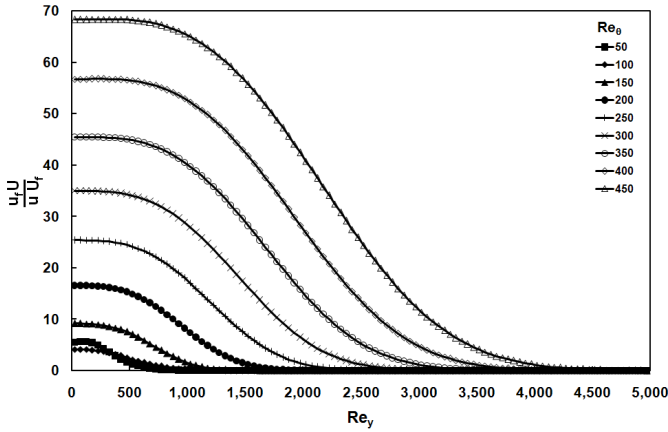


Figure 1: Streamwise fluctuations induced by freestream second component with $\Omega_x = 10^{-6}$ and $\Omega_y = \Omega_z = 5.3 \times 10^{-4}$

perpendicular to this first component and the frequency vector and hence is in the direction with the maximum w_f component. Any general velocity vector can then be formed as a weighted average of these two components. It should be noted that although the freestream fluctuation velocity vector for a single component or a combination of components lies within a plane, the fluctuation velocities induced within the boundary layer do not lie in a plane and are fully 3-d in nature. An appropriately weighted combination of the two components over a complete range of $\Omega_x, \Omega_y, \Omega_z$ spatial frequencies will result in the receptivity solution for isotropic turbulence in the freestream. It should also be noted that the combination of a solution with its 'mirror', where one of the spatial frequencies reverses sign, will result in an array of vortices in the freestream which are frequently used in receptivity studies. Equations 19, 20 and 21 are used to determine the velocities on the inlet boundary for each individual frequency solution where the values of u_1, v_1 and w_1 satisfy equation 29.

The remaining boundary conditions are more straightforward. On the plate the usual no slip boundary condition is used. The fluctuating pressure is set to zero on the boundaries parallel to and downstream of the plate, which is consistent with the freestream fluctuating velocity condition used at the inlet and the freestream solution. This pressure boundary condition differs from the velocity fluctuation condition used in other work (e.g. Leib et al. [3]), however the resulting velocity fluctuations in the freestream will be the same. This is because the velocity fluctuations prescribed at the inlet are convected through the boundaries where the zero pressure fluctuation boundary condition is used.

4 Results

Solutions to the governing equations were obtained for both the first and second components of the freestream perturbation for the frequency ranges Ω_x from 10^{-6} to 10^{-3} and Ω_y and Ω_z from 3×10^{-5} to 3×10^{-3} . Details can be found in Johnson and Pinarbasi [4]. It was found that the boundary layer receptivity is dominated by the second component at low Ω_x , i.e. vortices aligned in approximately the streamwise direction. A typical result is shown in figure 1 which also shows how the fluctuations grow with distance downstream. The near wall receptivity compares the near wall fluctuation amplitude with a

reference value at a point in the freestream upstream of the boundary layer surface and is defined by

$$R = \left(\frac{u_f}{w} \right)_{nw} \frac{U}{U_{f0}} \quad (30)$$

The reference position is at a distance x_0 upstream of the leading edge where $Re_{x0} = 500,000$. The ranges of fluctuation frequency which dominate the receptivity (> 20) are identified in figure 2. For ZPG (Zero pressure gradient), the receptivity is greatest for low Ω_x and a band of Ω_z frequencies centred at 5.3×10^{-4} . This frequency has a spanwise wavelength (approximately 1.5δ) which is similar to that observed for the streaky structures observed in experiments. Results are also shown in figure 2 for a FPG (favourable pressure gradient) and an APG (adverse pressure gradient). The corresponding acceleration parameters k vary from 6.9×10^{-7} to 4.4×10^{-7} for the FPG and from -2.8×10^{-7} to -3.4×10^{-7} for the APG. The iso-surface for FPG encloses a smaller region than that for ZPG and hence indicates a lower overall receptivity. In contrast the iso-surface for APG encloses a larger region and also a second iso-surface is present at higher Ω_x . The fluctuations depicted by this second iso-surface are due to Tollmien Schlichting waves, which are also more prevalent in APG experiments (Hughes and Walker [5]).

4.1 Spot Inception

Johnson and Fasihfar [6] observed that transition occurs when the near wall local turbulence level reaches approximately 23%. They suggested that this was due to transient local separation of the boundary layer. The nearwall instantaneous velocity is normally distributed and hence the proportion of the time that the flow is reversed can be determined as a function of the rms fluctuation level as shown in figure 4. The reversed flow occurrence rate and hence the probability of spot formation increases by 4 orders of magnitude for an increase in rms level from 17% to 27%, which suggests that spot formation does result from instantaneous flow reversal.

The 23% near wall turbulence level threshold is used to determine the start of transition Re_θ as a function of the freestream turbulence level as shown in figure 5. The current ZPG results are seen to lie close to the empirical transition correlation due to Mayle [7] with transition predicted at lower Re_θ for APG and higher Re_θ for FPG. It should be noted that the pressure gradient is zero in all cases up to $Re_\theta = 170$.

5 Conclusions

1. Flow perturbations in the pre-transitional boundary layer due to Tollmien Schlichting waves or receptivity of freestream turbulence are predicted by linear perturbation methods.
2. The boundary layer is most receptive to freestream vortices which are orientated in or close to the streamwise direction.
3. Receptivity is decreased by favourable and increased by adverse pressure gradient.
4. Tollmien Schlichting activity occurs at lower Reynolds number for adverse pressure gradients.
5. Transition onset can be predicted using linear perturbation methods and a 23% near wall turbulence (instantaneous separation) criterion.

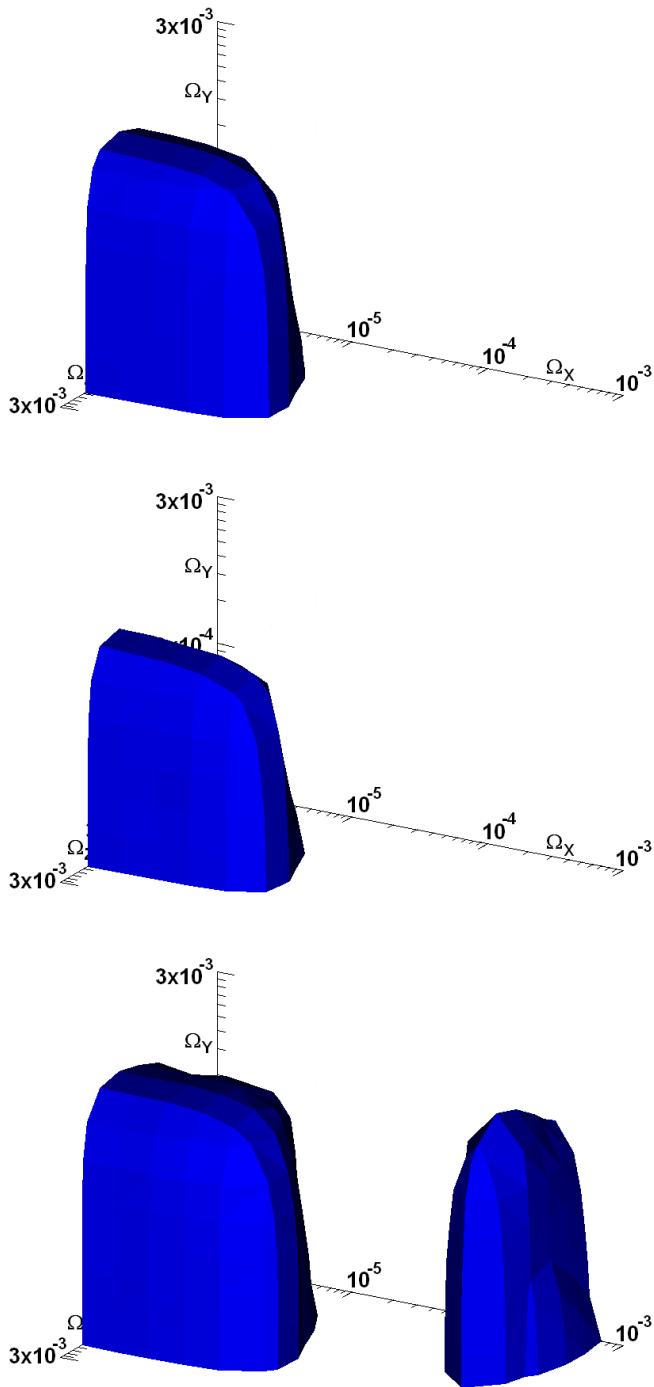


Figure 2: Near wall receptivity iso-surfaces ($= 20$) for second component freestream disturbances, $Re_\theta = 350$. ZPG (top), FPG (middle) and APG (bottom)

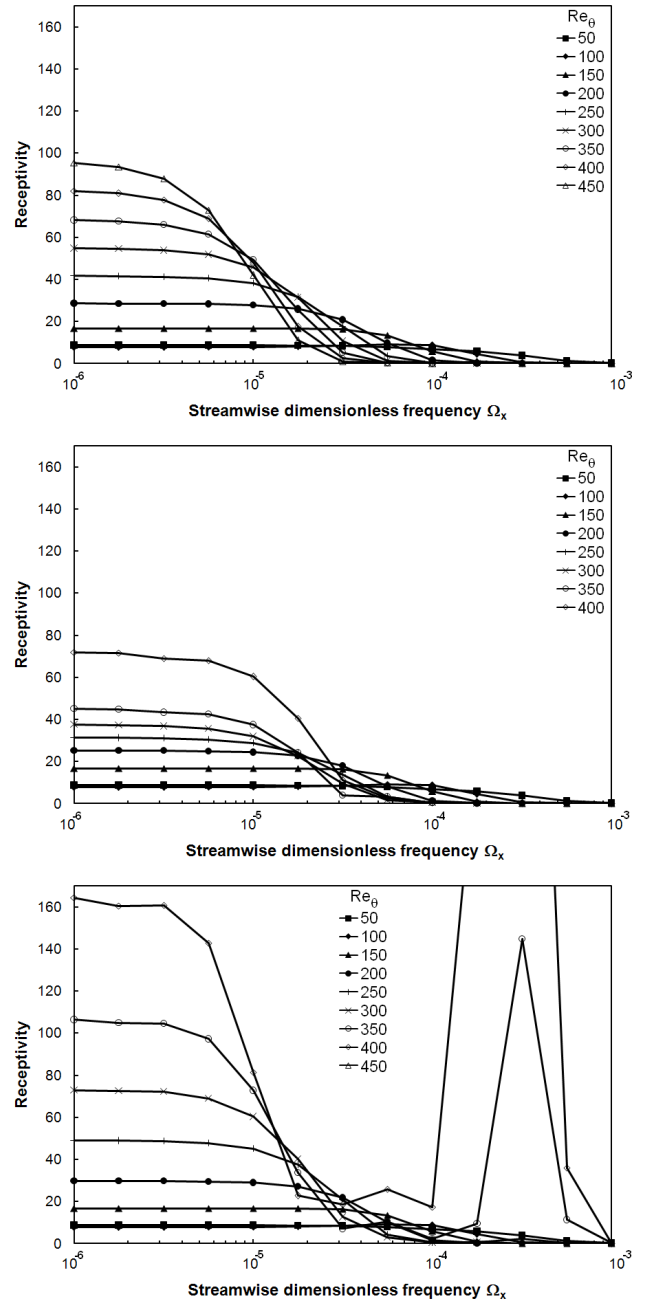


Figure 3: Spanwise and wall normal averaged second component receptivities. ZPG (top), FPG (middle) and APG (bottom)

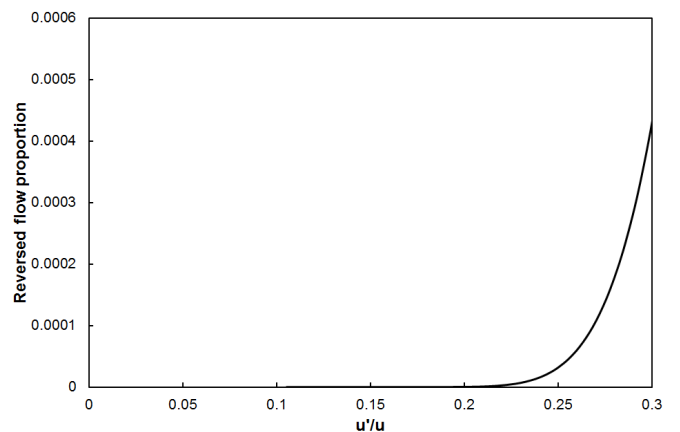


Figure 4: Reversed flow occurrence for normally distributed fluctuation

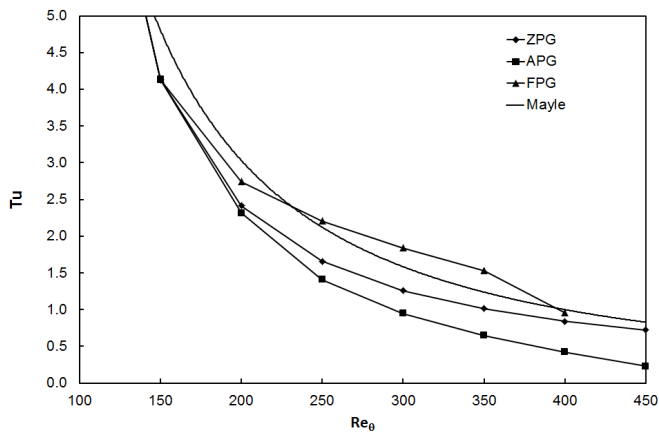


Figure 5: Start of transition prediction

References

- [1] Abu-Ghannam, B.J., Shaw, R., Natural transition of boundary layers-the effects of turbulence, pressure gradient and flow history. *J. Mech. Eng. Sci.* 22, 213- 228, 1980.
- [2] Wu, X., Moin, P., Direct numerical simulation of turbulence in a nominally zero-pressure-gradient flatplate boundary layer. *J. Fluid Mech.* 630, 5-41, 2009.
- [3] Leib, S.J., Wundrow, D.W., Goldstein, M.E., Effect of free-stream turbulence and other vertical disturbances on a laminar boundary layer. *J. Fluid Mech.* 380, 169- 203, 1999.
- [4] Johnson, M.W., Pinarbasi, A., The Effect of Pressure Gradient on Boundary Layer Receptivity, Flow turbulence and combustion, Vol. 93, 1-24, 2014.
- [5] Hughes, J.D., Walker, G.J., Natural transition phenomena on an axial compressor blade. *J. Turbomach.* 123, 392-401, 2001.
- [6] Fasihfar, A., Johnson, M.W., An Improved Boundary Layer Transition Correlation, Proc. ASME Intl. Gas Turbine Congress, Cologne, Paper No. 92-GT-245, June 1992.
- [7] Mayle, R.E., The role of laminar-turbulent transition in gas turbine engines. *ASME J. Turbomach.* 113, 509-537, 1991.

ON HYPERSONIC BOUNDARY LAYER TRANSITION: ROLE OF STREAKS

J. Ren and S. Fu

School of Aerospace Engineering, Tsinghua University, Beijing, 100084, China

Abstract

The role of streaks in hypersonic boundary layer transition is discussed. Boundary-layer flows at Mach numbers 4.5 and 6.0 are studied in which both the first- and second modes are supported. The streaks considered here are driven either by the so-called optimal perturbations (Klebanoff-type or K-type) or the centrifugal instability (Görtler-type or G-type). When the streak amplitude is in an appropriate range, i.e., large enough to modulate the laminar boundary layer but low enough to not trigger secondary instability, both the first- and second modes can effectively be suppressed by K-type streaks. G-type streaks ultimately lead to flow transition as long as the Görtler modes keep growing exponentially.

1 Introduction

Streaks substantially affect the boundary layer transition. The outcome can be either promotion [1] or suppression [2] of transition. Both shall be regarded as marketable controls in aerodynamic applications. Regardless of the Mach number, streamwise vortices are common generators of streaks (through *lift-up* mechanism [3]) in laminar boundary layers. The optimal perturbations and Görtler vortices are considered. The streaks they generated are termed Klebanoff-type (K-type) and Görtler-type (G-type) respectively hereafter.

Laminar-turbulent transition in flows dominated by streamwise-elongated streaks is often caused by their sinuous/varicose secondary instabilities [1]. Prior to the onset of secondary instabilities, T-S waves can, to a remarkable extent, be stabilized. The direct numerical simulations (DNS) by Cossu and Brandt [4, 5] showed that the T-S waves can be effectively stabilized by K-type streaks. Increase in the amplitude of the streaks shows a stronger effect of stabilization. This is due to the modification to the mean flow caused by the nonlinear development of streaks.

The experiments performed by Fransson and co-workers successfully materialized the idea of passive control with circular roughness elements [6] and miniature vortex generators (MVGs) [7]. The threshold streak amplitude is substantially increased from 12% to 32% with the latter. The elaborated streaky flow excited in the boundary layer (e.g., with aforementioned MVGs) suffers from considerable viscous dissipation. To prevent the rapid decay of streaks, multiple MVGs in the streamwise direction could be necessary [7]; The control was also shown to be robust when subjected to random noise. Recently, free-stream vortices are proved to be able to generate effective streaks [8].

Apart from the two-dimensional (2-D) disturbances in a flat-plate boundary layer, streaks can stabilize the oblique waves [9] as well. Similar approach for transition control in three-dimensional boundary-layer flow

over swept-wings has been studied intensively by Saric *et al.* [10, 11]. Here, the sub-critical crossflow modes are excited by the micron-sized roughness elements, which through their nonlinear interactions with the mean flow weakened the critical crossflow mode as well as its secondary instabilities. [12]

Görtler instability, known as the centrifugal instability of boundary layer over a concave wall, arises due to the imbalance between the centrifugal force and the wall-normal pressure gradient. The streamwise-oriented, counter-rotating vortices (Görtler vortices) are consequently generated, maintained and can be significantly intensified downstream promoting flow transition (See reviews by Saric [13]).

Again, the low- and high- speed streaks are produced and enhanced by the long-persisting streamwise counter-rotating vortices. The difference (between K-type) is that transient growth is replaced with exponential growth. Identifying the most dangerous secondary mode is of fundamental importance as it determines both the scenario and location of transition. For incompressible Görtler flow, the sinuous and varicose modes are found [14, 15] and analyzed with energy balancing mechanisms [16, 17, 18]. It had been found that the sinuous mode appeared first and required a lower amplitude of the streak [19, 1] while varicose modes were stronger for large wavelengths of Görtler vortices [20].

Up to today, the most of existing studies performed on this topic are confined in incompressible flows. The present study thus aims at understanding the mechanism in high-speed boundary layer flows as well as exploiting this potential control methodology. The first mode and second mode are both considered. The formulation and methodology are described in §2. Results on the stabilization of first- & second modes are presented and discussed in §3. The present study is concluded in §4.

2 Methodology

In the framework of the stability analysis, the instantaneous flow field $q = (\rho, u, v, w, T)$ is considered as a superposition of the perturbation \tilde{q} on the laminar base flow Q . For a 2-D boundary layer,

$$q(x, y, z, t) = Q(x, y) + \tilde{q}(x, y, z, t). \quad (1)$$

The base flow investigated is given by the self-similar solution to the compressible boundary layer. To derive the perturbation equations, we substitute (Eq. (1)) into the compressible Navier-Stokes (N-S) equations and subtract the equations for the mean flow. The resulted equations can be written in a well-identified and compact form:

$$\begin{aligned}
\mathbf{F} \frac{\partial \tilde{q}}{\partial t} + \mathbf{A} \frac{\partial \tilde{q}}{\partial x} + \mathbf{B} \frac{\partial \tilde{q}}{\partial y} + \mathbf{C} \frac{\partial \tilde{q}}{\partial z} + \mathbf{D} \tilde{q} = \\
\mathbf{V}_{xx} \frac{\partial^2 \tilde{q}}{\partial x^2} + \mathbf{V}_{yy} \frac{\partial^2 \tilde{q}}{\partial y^2} + \mathbf{V}_{zz} \frac{\partial^2 \tilde{q}}{\partial z^2} \\
+ \mathbf{V}_{xy} \frac{\partial^2 \tilde{q}}{\partial x \partial y} + \mathbf{V}_{yz} \frac{\partial^2 \tilde{q}}{\partial y \partial z} + \mathbf{V}_{zx} \frac{\partial^2 \tilde{q}}{\partial z \partial x} + \tilde{\mathbf{N}}.
\end{aligned} \quad (2)$$

The matrices \mathbf{F} , \mathbf{A} , \mathbf{B} , ... in (Eq. (2)) are functions of the mean flow quantities (detailed expressions can be found in the authors' previous papers [21]). Formulation of the nonlinear parabolized stability equations (NPSE) is standard and thus omitted here. Readers may refer to Herbert [22] for overview of the method, and Li & Malik [23] and Andersson *et al.* [24] for numerical issues related to the residue ellipticity of the equations.

In the present study, the space coordinates are scaled with the boundary layer length scale $\delta_0^* = \sqrt{\nu_\infty^* x_0^*/U_\infty^*}$ where asterisk stands for dimensional quantities. x_0 is the streamwise coordinate of a specified position. All the flow quantities are scaled with their free-stream values except the pressure by $\rho_\infty^* (U_\infty^*)^2$. The flow is thus characterized with the following dimensionless numbers:

$$Re_0 = \frac{\rho_\infty^* U_\infty^* \delta_0^*}{\mu_\infty^*}, \quad Ma = \frac{U_\infty^*}{\sqrt{\gamma R_{air}^* T_\infty^*}}, \quad Pr = \frac{\mu_\infty^* C_p^*}{\kappa_\infty^*}. \quad (3)$$

2.1 K-type Streaks

The optimal disturbances can be computed using an eigenfunction expansion or a marching approach (with adjoint equations). In compressible boundary layers, they are described in work by Hanifi *et al.* [25] and Tumin & Reshotko [26, 27]. The readers may refer to these papers for the formulation and relevant computational methods. Here, we utilize the local approach to compute the optimal perturbations. The optimal disturbance is given by a linear combination of the eigenvectors.

2.2 G-type Streaks

When a large enough concave curvature is present, Görtler instability becomes the leading mechanism for the amplification of streaks. We define the global curvature K as $K = k/Re = -\nu_\infty^*/(U_\infty^* R^*)$ where R^* is the local radius of curvature and k is local curvature. It should be noted that, a continuous transformation from Klebanoff modes to Görtler modes can be achieved by gradually increasing the curvature. To investigate these two type of modes, in the present paper we study streaks in cases with $K = 0$ and $K = -10^{-6}$. These are termed here Klebanoff-type (K-type) and Görtler-type (G-type) streaks, respectively.

2.3 Interactions Between Streaks and First/Second Mode

In 2-D hypersonic boundary layers, Mack's second mode [28] usually has the largest growth rate thus becoming the dominant instability. Employing the terminology suggested by Fedorov and Tumin [29], this mode becomes unstable when the fast mode (mode F) and slow mode (mode S) synchronize with each other. The second mode can be mode F or mode S depending on the branching of the discrete spectrum [30]. In fact, the amplification of the second mode is related to both mode F and mode S, i.e., a *double-mode* activity.

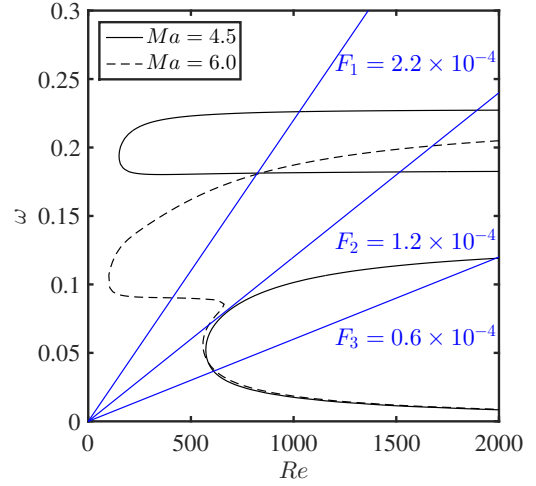


Figure 1: Neutral curves of two-dimensional disturbances in hypersonic boundary layers with $Ma = 4.5$ and 6.0

Flow case	Flow parameters	Perturbations)
Case 1	$Ma = 4.5, F = F_1$	second mode
Case 2	$Ma = 4.5, F = F_3$	first mode
Case 3	$Ma = 6.0, F = F_2$	first & second mode
Case 4	$Ma = 6.0, F = F_3$	first & second mode

Table 1: The flow and disturbance parameters for 2-D perturbations studied in the current work

The neutral curves of the 2-D disturbance in $Re - \omega$ plane at $Ma = 4.5$ and 6.0 are shown in Figure (1). $Re = \sqrt{\rho_\infty^* U_\infty^* x^*/\mu_\infty^*}$ is used as a measure of the streamwise coordinate. In the range of the parameters considered here, the unstable regions of the first- and second modes are well separated for $Ma = 4.5$ while they overlap at $Ma = 6.0$. The current study employs the perturbations with frequencies $F_1 = 2.2 \times 10^{-4}$, $F_2 = 1.2 \times 10^{-4}$ and $F_3 = 0.6 \times 10^{-4}$ where $F = \omega/Re$. The parameters of the four cases studied are listed in Tab. Table (1). Perturbations considered in Case 1 and 2 are the second- and first modes, respectively. Note that in the $Ma = 6.0$ flow (Case 3 and 4), perturbations with F_2 and F_3 manifest both the first- and second modes successively.

The steady Görtler or Klebanoff mode with spanwise wavenumber $\beta = 0.1$ is introduced into the laminar boundary layer either near the leading edge $Re < 100$ (for Klebanoff mode) or at $Re = Re_0 = 300$ (for Görtler mode). The 2-D disturbances are obtained from the local eigenmode and they are added to the flow at $Re = 500$ (ahead of branch-I of the neutral curve). The Klebanoff mode has been optimized for $Re = 1200$ with the inlet corresponding to $Re = Re_0 = 300$. All the cases share the following parameters: stagnation temperature $T_s^* = 333K$, Prandtl number $Pr = 0.7$, Reynolds number $Re_0 = 300$. Adiabatic wall boundary condition is specified for the mean flow.

3 Results and Discussions

3.1 Interaction with K-type Streaks

The stabilizing effects on the first- and second modes are investigated first at $Ma = 4.5$. The modal perturbations of frequencies F_1 and F_3 become unstable as the second- and first mode respectively as shown in Figure (1). The interaction between the streak and first/second mode is computed through the following procedure. The Kle-

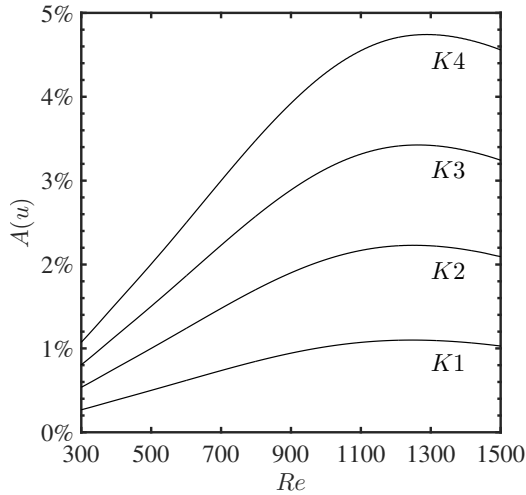


Figure 2: Spatial development of the streak amplitude. The maximum amplitudes are $A(u; K1) = 1.1\%$, $A(u; K2) = 2.2\%$, $A(u; K3) = 3.4\%$ and $A(u; K4) = 4.7\%$ respectively

banoff mode (mode(0, ± 1)) is introduced into the boundary layer near the leading edge. Initially this perturbation is integrated linearly up to a given position eliminating the influence of initial transient behavior. The amplitude of the Klebanoff mode is then prescribed and nonlinear development of the streak is followed downstream. The 2-D disturbance (mode(1,0)) is later initialized at $Re = 500$ with a sufficient low amplitude thus ensuring linearity. The number of Fourier components kept in the calculation is -12 to 12 in the spanwise wavenumber and 0 to 3 in the frequency which has been tested to be sufficient to characterize the nonlinear interactions.

Four sets of streaks of different amplitudes are denoted as $K1$, $K2$, $K3$ and $K4$. The spatial development of the streaks as a function of the local Reynolds number Re is presented in Figure (2). The maximum amplitudes are $A(u) = 1.1\%$, 2.2% , 3.4% and 4.7% respectively. The amplitude is defined as:

$$A(u) = 0.5 \left(\max_{y,z}(\tilde{u}) - \min_{y,z}(\tilde{u}) \right) \quad (4)$$

The amplitude of the T-S waves measured in terms of temperature and streamwise velocity perturbations are given in Figure (3). The temperature perturbation T' has the largest amplitude in hypersonic flows considered here and can be regarded as a measure of $|q'|_{max}$. The dashed lines indicate the amplitude of the 2-D perturbations in the absence of streaks. It is therefore obvious that the streaks can stabilize both the first- and second modes. An increase of the streak amplitude resulted in a stronger stabilization. This is demonstrated as decreased amplitude of the 2-D perturbations in Figure (3)(a,b). It is worth noting that the effect of streaks on the component of u' is not always stabilizing, e.g., the first mode shown in Figure (3)(b ii). Since $|u'|$ is one order of magnitude smaller than $|T'|$, the general stabilizing effect should not be influenced.

In hypersonic boundary layers, perturbations can be co-modulated by the first- and second modes, e.g., the $Ma = 6.0$ boundary layer (Case 3 and 4). Here, we consider perturbations with frequency $F = F2$ and $F = F3$. With the increase of Re , they behave as the first- and second mode successively. The second mode exerts relatively more influence on Case

3 ($F = F2$). The streaks included here are of Klebanoff-type. The maximum amplitudes are $A(u) = 0.75\%$ ($K1$), 1.2% ($K2$), 1.6% ($K3$) and 2.1% ($K4$) in Case 3. In Case 4, they are 0.71% , 1.1% , 1.5% and 1.9% . The stabilization is revealed in Figure (3)(c,d) indicating that the combined first/second mode can be effectively stabilized with finite amplitude streaks as well.

3.2 Interaction with G-type Streaks

On concave walls, the first/second modes become more unstable as well (see also [31]). The streamwise curvature ($K = -10^{-6}$) included here stands for the most commonly investigated case and represents typical Görtler instability (see Sec. 2). Figure (4) shows the interactions between Görtler instability and the first/second mode. The dash-dotted lines (without curvature) and dashed lines (with curvature) in Figure (4)(a,b) indicate the flow without streaks. Both the first- and second modes are enhanced by concave curvature. Görtler vortices with different amplitudes are considered ($G1$, $G2$, ..., $G7$). The initial amplitudes are prescribed as $A(u; G1) = 2 \times 10^{-11}$, $A(u; G2) = 2 \times 10^{-10}$, ..., $A(u; G7) = 2 \times 10^{-5}$. In the current Görtler flow, the threshold amplitude [32] for the sinuous secondary instability is close to $A(u) = 9\%$ and is shown with a dashed line in Figure (4)(c). The streak amplitude increases rather fast and exceeds this critical value regardless of the initial amplitude. Figure (4)(a,b) shows the evolution of the second/first mode in the presence of Görtler-type streaks. The perturbations though, can be stabilized by a certain extent, they finally become more unstable due to the secondary instability of the streaks. This is shown with a sudden uplift of the amplitude. The circle and square symbols indicate the uplift point of $|T'|_{max}$. It is the secondary instability of streaks that causes the failure of stabilization. Calculations are stopped before the amplitude becomes extremely large and computations blow up.

4 Conclusions

From the above analysis, it can be concluded that the mechanism behind the stabilization in hypersonic boundary-layer flows is similar to that in incompressible flows — a favorable modification to the mean flow. Although the two modes are different in nature, this study shows that both the first- and second modes can be effectively stabilized with finite amplitude streaks. Klebanoff-type streaks are more interesting as they have a mild spatial growth and their amplitude is more controllable. With regard to the Görtler-type streaks, where curvature is large enough, the secondary instability becomes more inevitable due to exponential growth. The concave curvature, *per se*, destabilizes the perturbations. On the other hand, curvature can be regarded as an effective controller on streak amplitude offering further potential improvement and optimization of the control methodology.

Acknowledgment

The authors acknowledge the financial support by the National Key Basic Research Program of China (Grant No.2014CB744801) and National Natural Science Foundation of China (Grant No.11272183, 11572176 and 11572178).

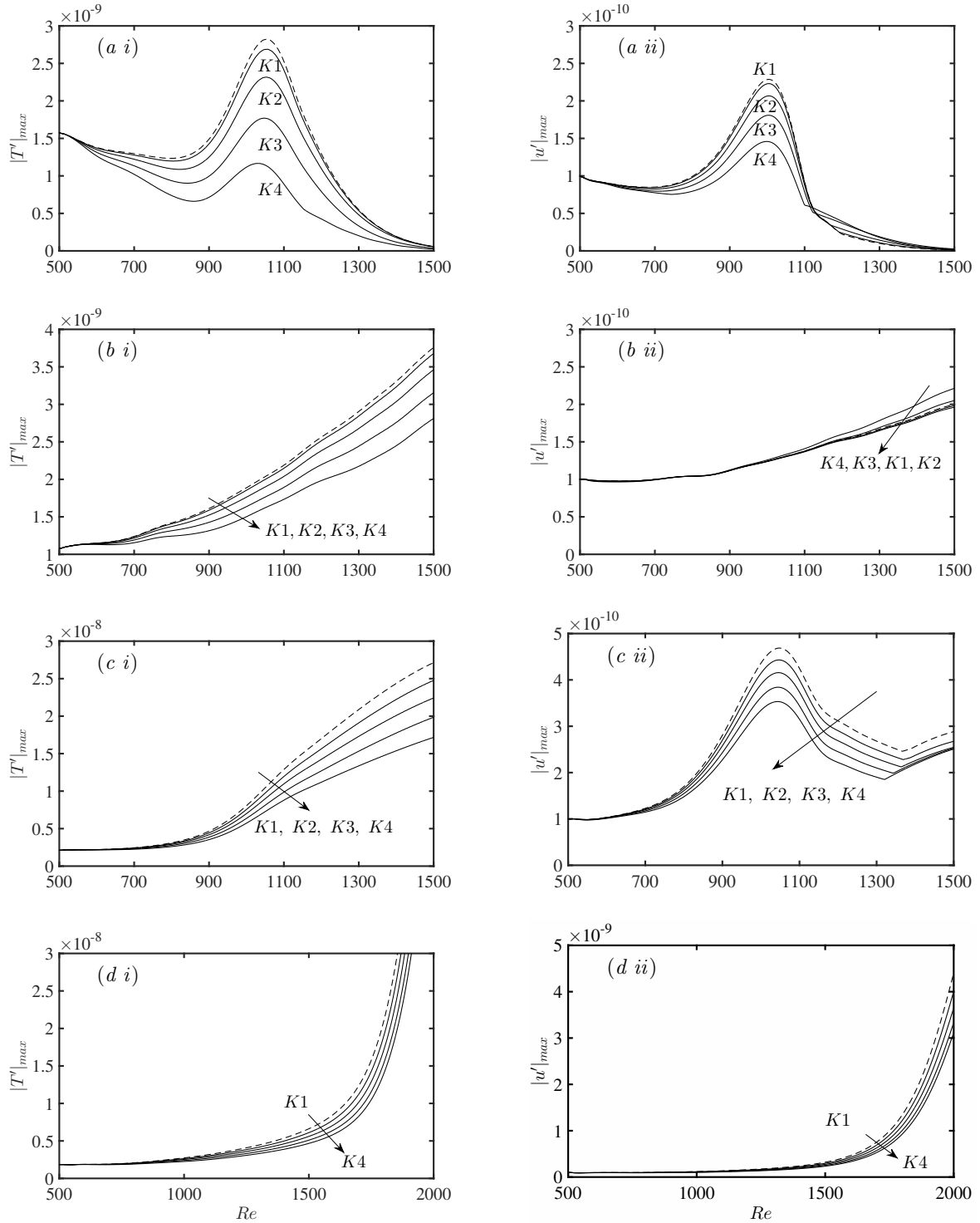


Figure 3: Evolution of the 2-D perturbations in a streaky (Klebanoff-type) flow with $Ma = 4.5$ and $Ma = 6.0$. The initial amplitude of the 2-D perturbation is $|u'|_{max} = 10^{-10}$. The amplitude of the temperature and streamwise velocity perturbations $|T'|_{max}$ and $|u'|_{max}$ are shown here. $K1, K2, K3$ and $K4$ indicate the streaks of different amplitudes. Development of the 2-D perturbations without streaks are shown with dashed lines. (a) The second mode (Case 1, $F = F1$). (b) The first mode (Case 2, $F = F3$). (c) The first/second mode (Case 3, $F = F2$). (d) The first/second mode (Case 4, $F = F2$)

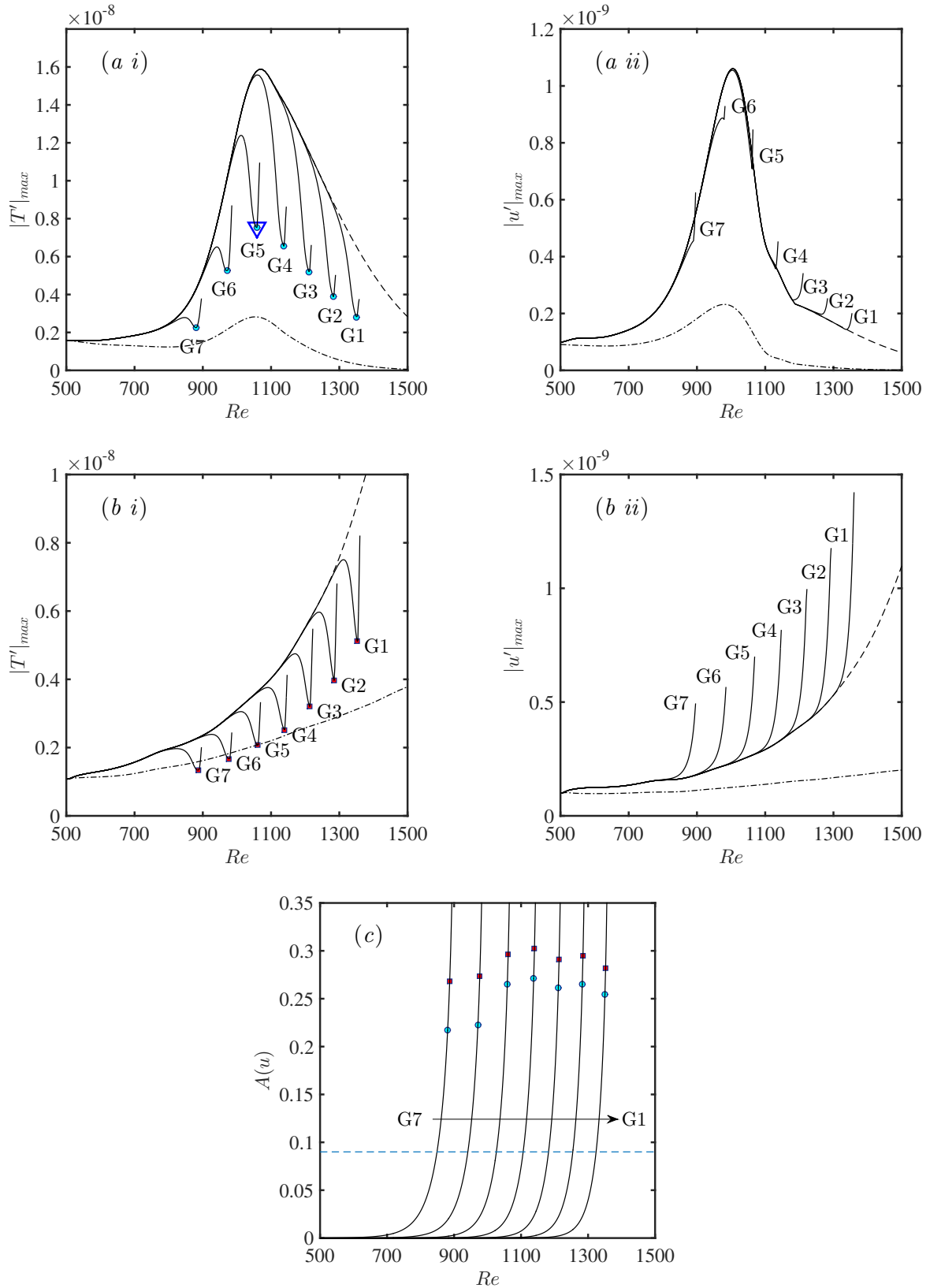


Figure 4: Evolution of the 2-D perturbations in a streaky (Görtler-type) flow with $Ma = 4.5$. The initial amplitude of the 2-D perturbation is $|u'|_{max} = 10^{-10}$. The amplitude of the temperature and streamwise velocity perturbation $|T'|_{max}$ and $|u'|_{max}$ are shown here. $G1, G2, \dots, G7$ indicate the streaks of different initial amplitudes. Development of the 2-D perturbations without streaks are shown with dashed lines. Dash-dotted lines correspond to the result without curvature (same as the dashed lines in Figure (3)(a,b)). The circle and square symbols indicate the onset of secondary instability. (a) The second mode (Case 1, $F = F1$). (b) The first mode (Case 2, $F = F3$). (c) Spatial development of the streaks

References

- [1] P. Andersson, L. Brandt, A. Bottaro, and D. S. Henningson, "On the breakdown of boundary layer streaks," *Journal of Fluid Mechanics*, vol. 428, pp. 29–60, 2001.
- [2] K.-S. Choi, "Fluid dynamics: The rough with the smooth," *Nature*, vol. 440, no. 8, p. 754, 2006.
- [3] M. T. Landahl, "Wave breakdown and turbulence," *SIAM Journal on Applied Mathematics*, vol. 28, no. 4, pp. 735–756, 1975.
- [4] C. Cossu and L. Brandt, "Stabilization of tollmien-schlichting waves by finite amplitude optimal streaks in the blasius boundary layer," *Physics of Fluids*, vol. 14, no. 8, pp. L57–L60, 2002.
- [5] C. Cossu and L. Brandt, "On tollmien-schlichting-like waves in streaky boundary layers," *European Journal of Mechanics - B/Fluids*, vol. 23, no. 6, pp. 815 – 833, 2004.
- [6] J. H. M. Fransson, A. Talamelli, L. Brandt, and C. Cossu, "Delaying transition to turbulence by a passive mechanism," *Phys. Rev. Lett.*, vol. 96, p. 064501, 2006.
- [7] J. H. M. Fransson and A. Talamelli, "On the generation of steady streamwise streaks in flat-plate boundary layers," *Journal of Fluid Mechanics*, vol. 698, pp. 211–234, 2012.
- [8] L. Siconolfi, S. Camarri, and J. H. M. Fransson, "Boundary layer stabilization using free-stream vortices," *Journal of Fluid Mechanics*, vol. 764, p. R2, 2015.
- [9] S. Shahinfar, S. S. Sattarzadeh, and J. H. M. Fransson, "Passive boundary layer control of oblique disturbances by finite-amplitude streaks," *Journal of Fluid Mechanics*, vol. 749, pp. 1–36, 2014.
- [10] W. S. Saric, R. B. Carillo, and M. S. Reibert, "Leading-edge roughness as a transition control mechanism," *AIAA Paper 98-0781*, 1998.
- [11] W. S. Saric and H. L. Reed, "Supersonic laminar flow control on swept wings using distributed roughness," *AIAA paper 2002-0147*, 2002.
- [12] S. M. Hosseini, D. Tempelmann, A. Hanifi, and D. S. Henningson, "Stabilization of a swept-wing boundary layer by distributed roughness elements," *Journal of Fluid Mechanics*, vol. 718, p. R1, 2013.
- [13] W. S. Saric, "Görtler vortices," *Annual Review of Fluid Mechanics*, vol. 26, no. 1, pp. 379–409, 1994.
- [14] P. Hall and N. J. Horseman, "The linear inviscid secondary instability of longitudinal vortex structures in boundary layers," *Journal of Fluid Mechanics*, vol. 232, pp. 357–375, 1991.
- [15] X. Yu and J. T. C. Liu, "The secondary instability in Goertler flow," *Physics of Fluids A: Fluid Dynamics*, vol. 3, no. 8, pp. 1845–1847, 1991.
- [16] W. Liu and J. A. Domaradzki, "Direct numerical simulation of transition to turbulence in Görtler flow," *Journal of Fluid Mechanics*, vol. 246, pp. 267–299, 1993.
- [17] X. Yu and J. T. C. Liu, "On the mechanism of sinuous and varicose modes in three-dimensional viscous secondary instability of nonlinear Görtler rolls," *Physics of Fluids*, vol. 6, no. 2, pp. 736–750, 1994.
- [18] D. S. Park and P. Huerre, "Primary and secondary instabilities of the asymptotic suction boundary layer on a curved plate," *Journal of Fluid Mechanics*, vol. 283, pp. 249–272, 1995.
- [19] A. Bottaro and B. Klingmann, "On the linear breakdown of Görtler vortices," *European journal of mechanics. B, Fluids*, vol. 15, no. 3, pp. 301–330, 1996.
- [20] F. Li and M. R. Malik, "Fundamental and subharmonic secondary instabilities of Görtler vortices," *Journal of Fluid Mechanics*, vol. 297, pp. 77–100, 1995.
- [21] J. Ren and S. Fu, "Competition of the multiple Görtler modes in hypersonic boundary layer flows," *SCIENCE CHINA Physics, Mechanics & Astronomy*, vol. 57, no. 6, pp. 1178–1193, 2014.
- [22] T. Herbert, "Parabolized stability equations," *Annual Review of Fluid Mechanics*, vol. 29, pp. 245–283, 1997.
- [23] F. Li and M. R. Malik, "On the nature of pse approximation," *Theoretical and Computational Fluid Dynamics*, vol. 8, no. 4, pp. 253–273, 1996.
- [24] P. Andersson, D. Henningson, and A. Hanifi, "On a stabilization procedure for the parabolic stability equations," *Journal of Engineering Mathematics*, vol. 33, no. 3, pp. 311–332, 1998.
- [25] A. Hanifi, P. J. Schmid, and D. S. Henningson, "Transient growth in compressible boundary layer flow," *Physics of Fluids*, vol. 8, no. 3, pp. 826–837, 1996.
- [26] A. Tumin and E. Reshotko, "Spatial theory of optimal disturbances in boundary layers," *Physics of Fluids*, vol. 13, no. 7, pp. 2097–2104.
- [27] A. Tumin and E. Reshotko, "Optimal disturbances in compressible boundary layers," *AIAA Journal*, vol. 41, no. 12, pp. 2357–2363, 2003.
- [28] L. M. Mack, "Boundary-layer linear stability theory," AGARD Report 709, 1984. Special Course on Stability and Transition of Laminar Flows.
- [29] A. Federov and A. Tumin, "High-speed boundary-layer instability: Old terminology and a new framework," *AIAA Journal*, vol. 49, no. 8, pp. 1647–1657, 2011.
- [30] V. Gushchin and A. Fedorov, "Excitation and development of unstable disturbances in a supersonic boundary layer," *Fluid Dynamics*, vol. 25, no. 3, pp. 344–352, 1990.
- [31] J. Ren and S. Fu, "Study of the discrete spectrum in a Mach 4.5 Görtler flow," *Flow, Turbulence and Combustion*, vol. 94, no. 2, pp. 339–357, 2015.
- [32] J. Ren and S. Fu, "Secondary instabilities of Görtler vortices in high-speed boundary layer flows," *Journal of Fluid Mechanics*, vol. 781, pp. 388–421, 2015.

THEORY AND SIMULATIONS OF BYPASS TRANSITION IN TWO-FLUID BOUNDARY LAYERS

T. A. Zaki¹ and J. Page²

¹*Department of Mechanical Engineering, Johns Hopkins University, Baltimore, MD 21218, USA*

²*Department of Mechanical Engineering, Imperial College London, SW7 2AZ, UK*

Abstract

Bypass transition in boundary layers is sensitive to the flow configuration, and small changes in the mean-flow profile near the wall can have a dramatic impact on transition location. This change can be effected by introducing a thin wall film of different viscosity, which alters the mean-velocity profile and the boundary-layer response to free-stream vortical forcing. A judicious choice of the film properties can therefore stabilize the pre-transitional region and delay the onset of turbulence far downstream of its location in the single-fluid case. Linear theory provides a framework for making this choice and avoiding conditions that can be detrimental to stability. The theory explains how the film can weaken the lift-up mechanism that causes the amplification of streaks. Direct numerical simulations confirm this trend which is ultimately responsible for delaying the onset of secondary instability and reducing the frequency of formation of turbulence spots. As a result, the entire transition process is delayed relative to the single-fluid boundary layer.

1 Introduction

The sensitivity of boundary layers to environmental disturbances leads to a wealth of possible routes to boundary-layer turbulence [1]. The same sensitivity can, however, be exploited to our advantage in order to control the onset of turbulence to either delay it or promote it. The latter objective being less challenging at moderate Reynolds number, we place our focus on the former, namely delaying bypass transition to turbulence by manipulating the fluid properties near the wall. Our strategy builds on our understanding of the various stages of bypass transition in single-fluid boundary layers, and the choice of the thin wall-film aims to disrupt these stages. Here we will focus on the case where the film has the same density but different viscosity as the outer flow. This configuration is examined as a strategy to delay transition, but it is also relevant to many other practical problems, for example in heated liquid flows where the high-Prandtl number of the fluid leads to a thin thermal boundary layer that can mimic the effect of the film.

Bypass transition takes place when the boundary layer is exposed to moderate levels of free-stream disturbances, with intensity $Tu_\infty \approx O(1 - 3\%)$ (for a recent review, see Zaki (2013) [2]). The transition process proceeds in three main stages. In the first, the low-frequency free-stream perturbations permeate the mean shear. The higher frequency disturbances appear irrelevant at this stage; they are simply advected in the free stream and decay relatively quickly due to viscosity. The boundary-

layer response to the low-frequency component is energetic, elongated structures known as Klebanoff streaks. The final stage of transition is a secondary instability of the streaky base state, which ultimately leads to the appearance of localized turbulence spots. The onset of spots corresponds to the initial departure of the intermittency from zero, and it continues to increase as the spots spread. The spots ultimately merge together and with the edge of the downstream turbulent boundary layer. A balance between streamwise advection and spot merging maintains a laminar-turbulent boundary beyond which the flow is always turbulent, and therefore the intermittency is unity.

1.1 Single-fluid Boundary Layers

The first stage of transition concerns the signature of the free-stream disturbances inside the laminar boundary layer. Based on experiments and simulations, only the low frequencies maintain their amplitude within the mean shear, while higher frequencies have a very weak signature. An intuitive understanding can be formed by examining the ratio of two timescales, $k_x d_y U \delta / \nu k_y^2$ [3]. Here $d_y U$ is shear rate; ν is the kinematic viscosity; k_x and k_y are the streamwise and wall-normal disturbance wavenumbers. This quantity can be interpreted as the number of waves of length $1/k_x$ that traverse an observer inside the boundary layer within a diffusion timescale $1/\nu k_y^2$. For elongated free-stream disturbances, $k_x \rightarrow 0$, this ratio tends to zero and the observer experiences a persistent, or long-lived, effect of the free-stream perturbation. In the reciprocal limit of short disturbances or strong shear, the observer can not “resolve” the disturbance within the diffusion timescale. These perturbations are said to be sheltered by the strong shear [4, 5, 6, 3].

The above line of reasoning explains the role of k_x , and the prominence of elongated disturbances within the pre-transitional boundary layers. But the wall-normal wavenumber also appears in the same expression which predicts that high- k_y perturbations are most effective at penetrating the shear by virtue of their very short diffusion time. Experiments and simulations, however, show that the perturbations within the pre-transitional boundary layer are not fine-scale, but rather have a wall-normal size commensurate with the boundary-layer thickness [7, 8, 9]. This scale is “selected”, or preferred due to a compromise between penetration and decay. Larger wall-normal scales are expelled from the boundary layer as predicted by the quantity $k_x d_y U \delta / \nu k_y^2$. Finer scales penetrate the shear, but are more prone to viscous decay.

The low-frequency disturbances trigger a strong response within the boundary layer. The physical mechanism is wall-normal displacement of mean streamwise momentum [10]: A weak, positive v -perturbation can displace the near-wall low-momentum fluid upward and cause a strong low-speed streak. Conversely, a small, negative v -perturbation displaces the high-speed fluid towards the wall and leads to the amplification of a high-amplitude, high-speed streak. This lift-up mechanism is most effective for low-frequency disturbances for two reasons: their forcing v -perturbation has a slow viscous decay and the response is not tempered by a restoring pressure [11]. It is therefore not surprising that the pre-transitional boundary layer is dominated by elongated streaks [7, 9, 8, 12, 13]. High-frequency background disturbances are sheltered by the shear, and have an appreciable pressure disturbance and high viscous decay rate.

When the streaks reach high amplitude, with root-mean-square perturbation levels $\sim O(10\%)$ of the mean-flow speed, secondary instabilities are observed in the boundary layer. As a result, streaks have been assumed to be complicit although their exact contribution to secondary instability was not clear in the early studies. Empirical evidence suggested that the low-speed streaks become unstable when they are lifted to the edge of the boundary layer and are exposed to the high-frequency content of the free-stream turbulence [8, 14, 15]. It was even possible to demonstrate that one low- and one high-frequency perturbations are sufficient to replicate the entire bypass transition scenario [16, 17]; The former leads to the amplification of streaks and the second provides the seed for secondary instability and breakdown. That neither alone can cause transition demonstrates definitively that the streaks are a pre-requisite for breakdown.

Linear analysis provided a theoretical basis for the earlier empirical observations [18, 19]. The streaky base flow is susceptible to secondary instabilities that are absent for a simple Blasius profile, and which can be classified into outer and inner instabilities depending on the height of their critical layers [19]. The outer modes are the most dominant in zero-pressure-gradient boundary layers, while the inner modes become more frequent with increasingly adverse pressure gradient. The theory also demonstrates a dependence of the growth rate of the secondary instability on the streak amplitude, shape and configuration (e.g. low- and high-speed streaks overlapping). The most recent success of the theory has been its ability to accurately identify the most unstable streak among the entire population in realistic flow fields [20].

Once the secondary instability takes hold, it leads to the inception of turbulence spots that spread as they are advected downstream. This nonlinear stage of transition has not been as amenable to analysis, and therefore progress in understanding this stage of bypass transition has relied on experiments and numerical simulations.

1.2 The Wall Film

The introduction of a thin wall-film with different properties has the capacity to significantly alter the stability of the boundary layer [21, 22, 23, 24]. The Tollmien-Schlichting wave of the outer flow is still present, but its growth rate is modified. In addition, new instability modes are introduced when the film has a different viscosity. A ‘soft’ mode due to the viscosity mismatch was first reported by Yih [21], and can be stabilized if the wall film is thinner and less viscous than the outer fluid [22]. Another instability is possible at high-Reynolds-numbers when the wall film is less viscous [23]. The choice of the

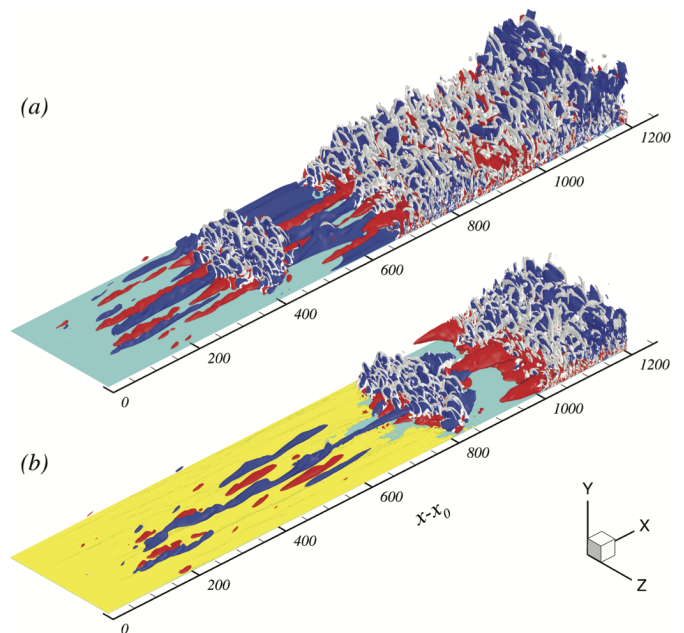


Figure 1: Comparison of bypass transition in (a) single- and (b) two-fluid boundary layers. The two-fluid interface in (b) is marked by the yellow surface. Red and blue isosurfaces are positive and negative boundary-layer streaks. White isosurfaces are vortical structures, identified using the Q-criterion

film properties can target either promoting these instabilities and as a result transition to turbulence, or stabilizing these modes. The latter option does not guarantee that bypass transition to turbulence will be delayed since it is not dependent on the growth rate of exponential modes but rather the response to free-stream perturbations.

In order to effectively leverage the sensitivity of the boundary layer to the wall film, it is important to evaluate the impact of the viscosity stratification on the amplification of streaks. Linear theory offers an avenue to explore this effect. However, transition being ultimately a nonlinear process where finite-amplitude disturbances play an important role, the theory must be complemented with either experiments or nonlinear simulations.

In this work, the influence of a thin wall-film of different viscosity on bypass transition is examined. Figure (1) shows snapshots from direct numerical simulations (DNS), and compares the single- and two-fluid configurations with a lower viscosity film. Transition to turbulence is clearly delayed in the two-fluid case. An important observation can be made towards explaining the shift in transition location, and will guide the analysis: In the presence of the film, the low-frequency streaks inside the boundary layer are much less abundant at the selected isosurface level. Assuming the nature of the streak instability is not changed, their weaker amplitude is sufficient to delay transition. We therefore focus on the streaks and whether the presence of the film reduces the effectiveness of the lift-up mechanism.

We will start with results from linear analysis (§2). We then report the results from the direct numerical simulations (§3), and interpret them in light of the linear analysis. Concluding remarks are made in the final section (§4).

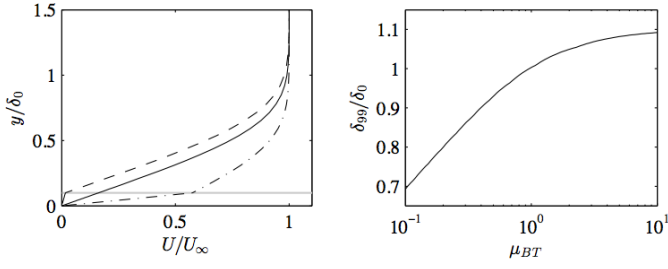


Figure 2: Two fluid base flow. (Left) Streamwise velocity (Eq. (1)) for $\mu_{BT} \equiv \mu_B/\mu_T = 1$ (—), $\mu_{BT} = 10$ (---), $\mu_{BT} = 0.2$ (- · -). (Right) Boundary layer thickness relative to the single-fluid value, δ_0

2 Linear theory

In this section linear theory is invoked to examine the early stages of bypass transition in two-fluid boundary layers, namely the effect of the film on the formation and amplification of streamwise streaks.

In linear theory, the total flow is written as $\mathbf{u}(\mathbf{x}, t) = U(y)\mathbf{e}_x + \mathbf{u}'(\mathbf{x}, t)$, where $U(y)$ is a parallel base state and \mathbf{u}' is a small perturbation. The base state is given by the large- x similarity solution for two-fluid boundary layers presented by Nelson et. al. [25],

$$\nu_\alpha^* \frac{d^3 F}{d\xi^3} + \frac{F}{2} \frac{d^2 F}{d\xi^2} = 0, \quad (1)$$

where $\alpha = \{T, B\}$ in the top fluid and wall film respectively, and $\nu_T^* = 1$, $\nu_B^* = \nu_B/\nu_T$. The streamwise velocity profile is $U = U_\infty d_\xi F$, and the similarity variable is based on outer-fluid properties, $\xi = y\sqrt{U_\infty x/\nu_T}$. The similarity solution must approach the free-stream value as $\xi \rightarrow \infty$ and satisfy no penetration/slip at the wall, $d_\xi F(\infty) = 1$, $F(0) = 0$, $d_\xi F(0) = 0$. In addition, the velocities and stresses are continuous at the interface, $[[F]] = 0$, $[[d_\xi F]] = 0$, $[[\mu_\alpha^* d_\xi^2 F]] = 0$, where $[[\bullet]] = (\bullet)_+ - (\bullet)_-$ is the jump in a quantity across the interface $y = \delta_f$. Throughout this work the densities of the two fluids are assumed equal. Variables are normalized by reference quantities in the top fluid, and length-scales are normalized by the boundary layer thickness in the single-fluid case, δ_0 , which yields a definition of the Reynolds number $Re_{\delta_0} \equiv \rho U_\infty \delta_0/\mu_T$.

Example base flows are reported in Figure (2) for a range of viscosity ratios. Reducing the film viscosity weakens the shear in the outer fluid, and enhances it in the film. This effect is accompanied by a reduction in the boundary layer thickness relative to the single-fluid value.

The continuity and momentum equations for the linear perturbations evolving over the parallel base flow are

$$\frac{\partial u'}{\partial x} + \frac{\partial v'}{\partial y} + \frac{\partial w'}{\partial z} = 0, \quad (2a)$$

$$\rho \left(\frac{\partial u'}{\partial t} + U \frac{\partial u'}{\partial x} + v' \frac{dU}{dy} \right) = -\frac{\partial p'}{\partial x} + \mu_\alpha \nabla^2 u', \quad (2b)$$

$$\rho \left(\frac{\partial v'}{\partial t} + U \frac{\partial v'}{\partial x} \right) = -\frac{\partial p'}{\partial y} + \mu_\alpha \nabla^2 v', \quad (2c)$$

$$\rho \left(\frac{\partial w'}{\partial t} + U \frac{\partial w'}{\partial x} \right) = -\frac{\partial p'}{\partial z} + \mu_\alpha \nabla^2 w'. \quad (2d)$$

Perturbations to the interface location satisfy the kinematic condition,

$$\left(\frac{\partial f'}{\partial t} + U \frac{\partial f'}{\partial x} \right) \delta(y - \delta_f) = v' \delta(y - \delta_f). \quad (3)$$

Furthermore, the total velocity and stress must remain continuous across the interface,

$$[[u']] = -[[d_y U]] f', \quad [[v']] = 0, \quad [[w']] = 0; \quad (4a)$$

$$\begin{aligned} [[\mu(\partial_y u' + \partial_x v')]] &= -[[\mu d_y^2 U]] f', & [[\mu(\partial_z v' + \partial_y w')]] &= 0, \\ [[-p' + 2\mu \partial_y v']] &= \sigma k^2 f', \end{aligned} \quad (4b)$$

where σ is the surface tension. The base flow is homogeneous in the streamwise and spanwise directions, and a normal-modes assumption is adopted, for example $v'(\mathbf{x}, t) = \hat{v}(y, t) \exp[i(k_x x + k_z z)]$.

Optimal growth analyses are used to examine streak amplification. An additional growth mechanism that emerges due to the presence of the two-fluid interface is also reported.

In order to compute the influence of the wall-film on transient amplification mechanisms, the linear equations (Eq. (2)) are considered as an initial value problem, and an initial disturbance is sought which maximizes the kinetic energy at a target time, $t = T$. Previous analyses of optimal growth in two-fluid configurations have included an unphysical contribution from the interface displacement, \hat{f} , in the measure for disturbance “energy” [26, 27], which is necessary to form a well-posed optimization problem. However, our interest in streak amplification means that the kinetic energy is the appropriate disturbance measure. In order to optimize for this quantity we adopt the formalism of seminorms [28, 29] and constrain the interface to be flat at $t = 0$.

The seminorm constraints appear in the Lagrangian defining the optimization problem,

$$\begin{aligned} L[\phi, \phi^\dagger, \phi_o, \phi_o^\dagger, \{\lambda_j\}] &= \underbrace{J[\phi(T)]}_{(i)} - \underbrace{\langle \phi^\dagger, \mathcal{A}\phi \rangle}_{(ii)} \\ &- \underbrace{(\phi_o^\dagger, \phi(t=0) - \phi_o)}_{(iii)} - \underbrace{\lambda_u (\|\phi_o\|_u^2 - 1)}_{(iv)} - \underbrace{\lambda_f \|\phi_o\|_f^2}_{(v)}, \end{aligned} \quad (5)$$

where $\phi = [\hat{u}, \hat{v}, \hat{w}, \hat{p}, \hat{f}]$ is the state vector and ϕ^\dagger is its adjoint, which plays the role of a Lagrange multiplier. The local and global inner products appearing in Eq. (5) are,

$$\langle \varsigma, \vartheta \rangle = \int_0^\infty \bar{\varsigma} \vartheta dy \quad \text{and} \quad \langle \varsigma, \vartheta \rangle = \int_0^T \int_0^\infty \bar{\varsigma} \vartheta dy dt, \quad (6)$$

where the overbar indicates Hermitian transpose. The objective functional labelled (i) in Eq. (5) is the disturbance kinetic energy and can be written in the form of a local inner product,

$$J[\phi] = \|\phi\|_u^2 = (\phi, \mathbf{E}\phi), \quad (7)$$

where $\mathbf{E} = \text{diag}(\rho, \rho, \rho, 0, 0)$. The remaining terms in Eq. (5) define the system of constraints. Constraint (ii) ensures that the disturbance evolution satisfies the governing equations, $\mathcal{A}\phi = 0$, while constraint (iii) sets the initial disturbance to be the optimal. The final two terms, (iv) and (v), are the *seminorm* constraints. They fix the initial kinetic energy to be unity and the initial

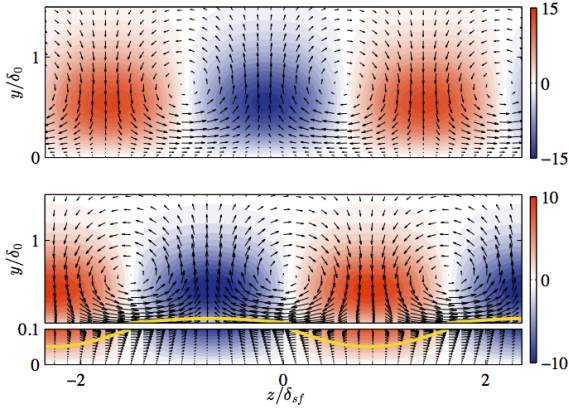


Figure 3: Optimal disturbance field, (v'_o, w'_o) (vectors), and response at the time of maximum amplification, $u'(T)$ (colours) at $Re_{\delta_0} = 800$. (Top) Single fluid boundary layer. (Bottom) Two-fluid boundary layer with $\mu_{BT} = 0.4$, $\delta_f = 0.1\delta_0$; the interface deformation is identified in yellow, and has been normalized such that $|f'(T)|_{\max} = 0.05$

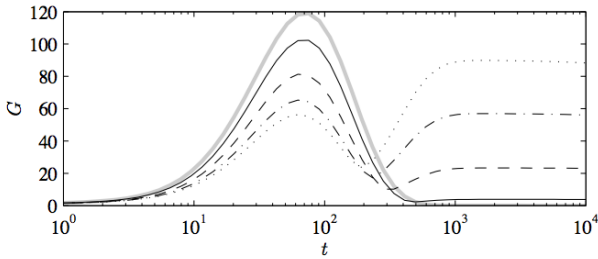


Figure 4: Growth envelopes for a two-fluid boundary layer with $Re_{\delta_0} = 800$, $\delta_f = 0.1\delta_0$. The disturbance wavenumber is $(k_x, k_z) = (0.001, 2)$. (—) $\mu_{BT} = 0.6$, (---) $\mu_{BT} = 0.4$, (— · —) $\mu_{BT} = 0.3$, (····) $\mu_{BT} = 0.25$. The grey line is the single fluid result at the same Reynolds number

interface deformation to be zero. Note that $\|\phi_o\|_f^2 \equiv (\phi_o, \mathbf{F}\phi_o) = |\hat{f}_o|^2$, where $\mathbf{F} = \text{diag}(0, 0, 0, 0, \delta(y - \delta_f))$.

Optimal disturbances are found by setting the variation of Eq. (5) to zero, $\delta L = 0$. This procedure results in a system of equations satisfied by the optimal disturbance, which are solved using an iterative adjoint-looping procedure similar to that described by Luchini [28] and Schmid [30].

The optimal initial disturbance and response at the time of maximum amplification for a particular wavenumber pair, $(k_x, k_z) = (0.001, 2)$, and subcritical Reynolds number, $Re_{\delta_0} = 800$, are reported in Figure (3) for both a single-fluid boundary layer and a two-fluid case with $\mu_{BT} \equiv \mu_B/\mu_T = 0.4$. In both flows the optimal takes the form of a row of counter-rotating streamwise vortices, while the response consists of streaks in the streamwise velocity. The streak amplitude in the two-fluid configuration is damped relative to the single-fluid value. In addition, the interface in the two-fluid flow is significantly deformed at the time of maximum amplification, and this deformation has an associated jump in the streamwise velocity perturbation.

Optimal growth envelopes are provided in Figure (4) for a range of viscosity ratios. Interestingly, there are two clear peaks in the two-fluid curves. The peak at early times, $t \sim O(100)$, corresponds to the growth of the streamwise streaks. There is a monotonic decrease

in the streak amplification with decreasing film viscosity, consistent with the perturbation field shown in Figure (3). This trend is due to the film absorbing more of the shear as its viscosity decreases, as remarked in connection with Figure (2). The mean shear reduction in the outer fluid decreases the efficacy of the lift-up term, $v'd_y U$, in the momentum equation (Eq. (2b)). The increasing shear in the film cannot compensate for this effect due to the vanishing normal velocity at the wall [31].

The perturbation field reported in Figure (3) shows that the interface becomes significantly deformed in the process of streak formation through lift-up. The interface deformation, which can be associated with a stable, almost-neutral eigenmode of Eq. (2), is the source of the long-time amplification reported in the growth envelopes in Figure (4). While the streaks ultimately decay due to viscosity, the slowly decaying interface deformation has an associated jump in streamwise velocity, which may be written as (cf. Eq. (4a)) $[\hat{u}] = [(1 - \mu_{BT})/\mu_{BT}]d_y U_T(y = \delta_f)\hat{f}$, and indicates that the long-time energy growth scales with $1/\mu_{BT}^2$ as $\mu_{BT} \rightarrow 0$. Accordingly, the growth envelopes in Figure (4) indicate that this mechanism becomes dominant below a critical film viscosity, and can lead to significant kinetic energy growth at long times.

In summary, linear theory predicts that a lower viscosity wall-film can effectively reduce the amplitude of boundary layer streaks. However, if the viscosity is reduced below a critical value, a new mode of disturbance amplification becomes dominant and can be destabilizing. The critical value of μ_{BT} depends on the ratio of the film to the boundary-layer thickness. In spatially developing flows, this value varies downstream since the spreading rate of the film and of the outer boundary layer differ. Nonetheless, the results from extensive linear analyses similar to those presented herein [31] have informed our choice of flow parameters in the direct numerical simulations (§3).

3 Direct Numerical Simulations

The entire transition process through the nonlinear amplification of streaks, their secondary instability and the onset of turbulence is simulated by solving the full Navier-Stokes equations for two incompressible and immiscible fluids,

$$\frac{\partial u_j}{\partial x_j} = 0, \quad (8)$$

$$\frac{\partial u_i}{\partial t} + \frac{\partial u_i u_j}{\partial x_j} = -\frac{\partial p}{\partial x_i} + \frac{1}{Re_{\delta_0}} \frac{\partial}{\partial x_j} \left[\mu \left(\frac{\partial u_i}{\partial x_j} + \frac{\partial u_j}{\partial x_i} \right) \right]. \quad (9)$$

In keeping with the normalization in §2, the reference scales are the free-stream velocity, U_∞ , and the inlet boundary-layer thickness from the single-fluid simulation, δ_0 . The viscosity, μ , is normalized by the free-stream reference value and the quantity μ_{BT} denotes the ratio of the film, or bottom, to top-fluid viscosities. The Reynolds number for the simulations is $Re_{\delta_0} (\equiv \rho U_\infty \delta_0 / \mu_T) = 800$.

The computational domain is rectangular with dimensions $(L_x, L_y, L_z) = (1200, 40, 30)$ in the streamwise, wall-normal and spanwise directions. The streamwise extent spans $2.6 \times 10^4 < Re_x (\equiv \rho U_\infty x / \mu_T) < 9.9 \times 10^5$. In order to fully resolve the flow, the number of grid points required were $(n_x, n_y, n_z) = (4097, 193, 193)$. While a uniform grid was adopted in the streamwise and spanwise directions, a hyperbolic stretching function was used to cluster the grid points near the wall in the vertical direction.

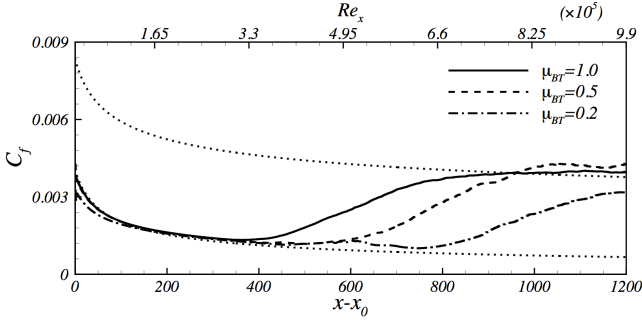


Figure 5: Skin-friction coefficient versus distance from the inlet of the computational domain. The three curves correspond to (—) the single-fluid configuration, (---) $\mu_{BT} = 0.5$ and (- · -) $\mu_{BT} = 0.2$

Periodicity is enforced in the spanwise direction. The inflow condition comprises a mean-velocity profile, which is similar to the base state used in the linear analysis, and free-stream turbulence. The turbulence is synthesized as a superposition of vortical disturbance with a specified von Kármán spectrum. The free-stream turbulence lengthscale was on the order of the boundary-layer thickness, and the intensity at the inlet is $Tu = 2.5\%$. At the downstream boundary, a convective boundary condition is used to advect disturbances out of the domain. The bottom wall is a no-slip surface, and a suction velocity is applied at the top boundary in order to ensure zero-pressure-gradient.

The numerical approach adopts a standard fractional step algorithm for the Navier-Stokes equations. A level-set equation is solved to capture the two-fluid interface (see [32] for details). The level set algorithm is based on the work by Desjardins *et al.* [33], and was validated against the nonlinear stability results by Cheung & Zaki [34, 35]. We compute the evolution of a hyperbolic-tangent function, $\psi \equiv 0.5 (\tanh(\phi/2\epsilon) + 1)$, where ϵ is a small parameter that controls the thickness of the interface and ϕ is the unit-distance function,

$$\frac{\partial \psi}{\partial t} + \frac{\partial u_j \psi}{\partial x_j} = 0. \quad (10)$$

This algorithm has superior mass conservation properties to the traditional level-set method [36]. The local viscosity can then be reconstructed,

$$\mu = \mu_{BT} + (1 - \mu_{BT})\psi. \quad (11)$$

Three different viscosity ratios were compared, $\mu_{BT} = \{1.0, 0.5, 0.2\}$, the first being a single-fluid reference case, and the two subsequent conditions representing a lowering of the film viscosity. The film thickness at the inflow was assumed to be $\delta_f = 0.1\delta_0$, or 10% of the inlet single-fluid boundary-layer thickness.

The skin-friction coefficients from the three simulations are compared in Figure (5). The figure also includes the laminar and turbulent levels based on the parameters of the single-fluid configuration. The skin friction shows that transition is progressively delayed as the viscosity of the film is reduced. For the lowest viscosity ratio, $\mu_{BT} = 0.2$, transition starts at twice the distance from the inlet of the domain as the single-fluid flow.

The skin-friction results in Figure (5) should be interpreted as the mean signature at the wall of the transition process shown in Figure (1). The pre-transitional C_f level corresponds to the region in Figure (1) where

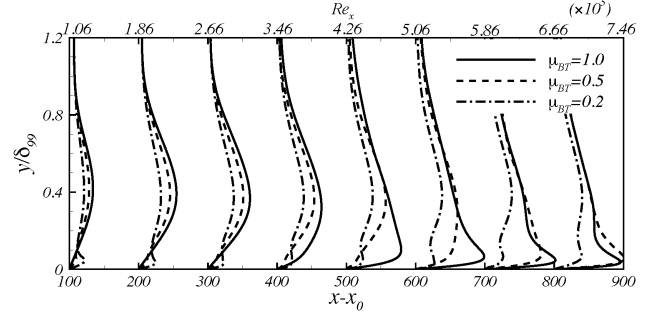


Figure 6: Wall-normal profiles of the root-mean-square perturbation, u'_{rms} , at various downstream locations

the boundary layer is laminar and the only visible disturbances are the streaks. The rise of the skin friction curve corresponds to the mean spot-inception location. Farther downstream, the sustained high level of C_f corresponds to the fully turbulent region in Figure (1).

The analysis in §2 predicted that the propensity of boundary-layer to amplify streaks is reduced in the presence of the lower-viscosity film, which can explain the cause for transition delay. A preliminary assessment of this hypothesis is given in Figure (6), where profiles of u'_{rms} are plotted at various downstream locations. The results show that the less-viscous wall-film weakens the perturbation field in the outer part of the boundary layer. Near the two-fluid interface, however, the value of u'_{rms} is enhanced in the stratified flow. This near-wall peak in the u'_{rms} profile is due to the jump condition across the interface, which in the linear problem is given by $[[u']] = -[[d_y U]]f'$ (see Eq. (4a)).

The outer and inner maxima in the u'_{rms} profiles were extracted and are plotted versus the streamwise coordinate in Figure (7)a and Figure (7)b, respectively. The single-fluid curve is repeated in both panels since it only has one peak. For the two-fluid configuration, the outer peak is appreciably decreased as the viscosity ratio is reduced, while the inner peak becomes more pronounced. For the lowest ratio, $\mu_{BT} = 0.2$, the two curves coalesce, or become indistinguishable, at the onset of transition.

In linear theory, the amplification of streaks is attributed to the lift-up mechanism whereby vertical velocity perturbations displace the mean momentum. In the nonlinear computation, the production term in the u'^2 equation is $\overline{u'v'}(\partial U/\partial y)$. The Reynolds shear stress is examined in Figure (8), where it is divided into four contributions based on the signs of u' and v' . Only the single-fluid and $\mu_{BT} = 0.2$ cases are reported, and the sampling location is $x - x_0 = 400$ which is near the onset of transition in the single-fluid flow. Quadrants 1 and 3 show some activity in the single-fluid flow due to the proximity of the sampling plane to transition onset, and are nearly void of any stresses in the two-fluid case. We therefore focus on quadrants 2 and 4, which correspond to ejection and sweep events (or upward and downward displacement of mean momentum), respectively. The conditionally sampled shear stress is weakened in both quadrants in the presence of the wall film, which is another indication that the streaks in the two-fluid configuration are more feeble.

The above results all provide indirect statistical evidence of the streaks being weaker in the two-fluid configuration. In order to provide a direct measure, we have formed a database of three-dimensional flow fields extracted from the simulations, and performed a detailed analysis of the streaks [37]. Figure (9) shows top views

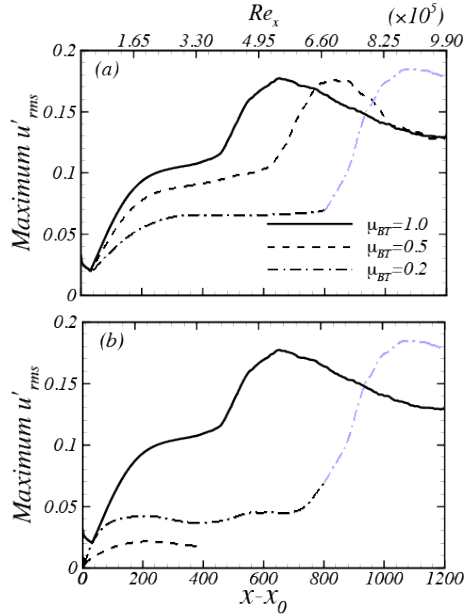


Figure 7: The wall-normal maximum of u'_{rms} plotted versus downstream distance. (a) The outer and (b) inner interface maxima. The single-fluid configuration has only one peak, which is shown in both panels

of the perturbation fields within the boundary layer from the simulations with $\mu_{BT} = \{1, 0.2\}$. The first step in the analysis is laminar-turbulent discrimination, and the result is marked by the black line in the figure. Once the non-turbulent region of the flow is isolated, the streaks were identified by computing the local extrema in successive cross-flow planes and establishing their connectivity. We can then define the amplitude of the streaks, $\mathcal{A}_u^s(\mathbf{x}^s, t) \equiv u'(\mathbf{x} = \mathbf{x}^s, t)$. By cross-correlating the amplitude in successive time-steps, we can track the streaks through space-time as Lagrangian entities. In addition, since secondary instability is most sensitive to the streak amplitude, we record at each x -position the maximum A_u^s that every streak achieves during its evolution,

$$A_u^s(x) = \begin{cases} \max_{t,y,z} (\mathcal{A}_u^s(\mathbf{x}^s, t)), & \text{for } \mathcal{A}_u^s > 0 \\ \min_{t,y,z} (\mathcal{A}_u^s(\mathbf{x}^s, t)), & \text{for } \mathcal{A}_u^s < 0. \end{cases} \quad (12)$$

The probability density function (PDF) of A_u^s is plotted in Figure (10) versus downstream distance. The streamwise extent spans the entire pre-transitional region from the single-fluid flow. By that location, the

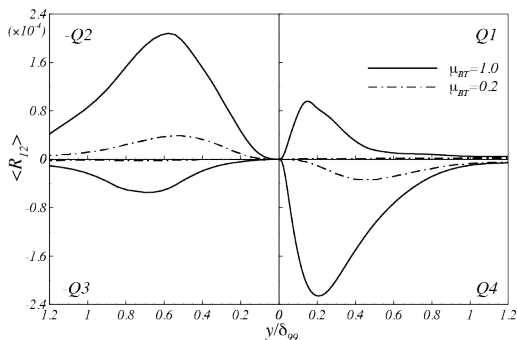


Figure 8: Quadrant contributions to the Reynolds shear stress at $x - x_0 = 400$

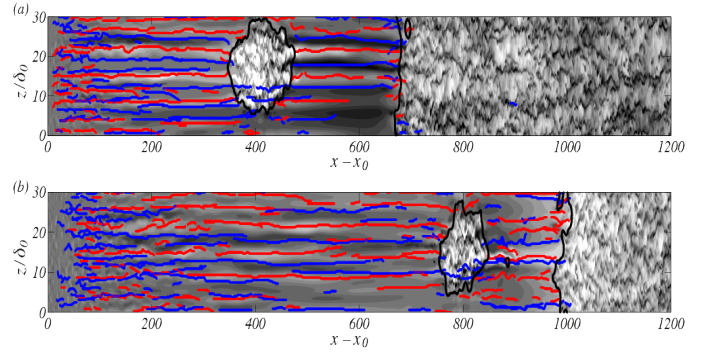


Figure 9: Top views of the (a) single-fluid and (b) $\mu_{BT} = 0.2$ flows. The black line marks the laminar-turbulent interface. Red and blue lines are the cores of the high- and low-speed streaks

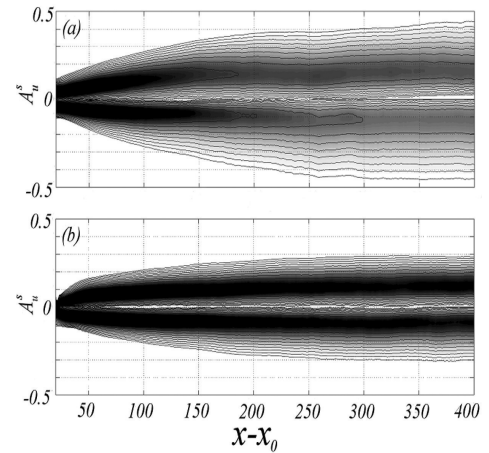


Figure 10: The probability density function of maximum streak amplitude, A_u^s , versus downstream distance for (a) the single-fluid and (b) $\mu_{BT} = 0.2$ flows

distribution shows values of $A_u^s \approx 0.4$, which is a substantial streak perturbation. At such high amplitudes, the streaks are likely sites for inception of turbulence spots. The spread of the PDF of the two-fluid flow is much slower with downstream distance, and the amplitude remains within the range $|A_u^s| < 0.3$. These streaks are therefore much weaker and less likely to breakdown to turbulence than their counterparts in the single-fluid configuration.

The simulation results demonstrate the effectiveness of a thin, lower viscosity film to delay bypass transition in boundary layers. This strategy is most effective when the streaks are near the threshold for instability, and the wall film reduces their amplitudes to benign levels. The present flow configuration with free-stream turbulence intensity $Tu = 2.5\%$ falls into this regime. At higher free-stream turbulence intensities the streaks will be more energetic and, as a result, the wall film becomes less effective at delaying transition.

4 Conclusion

The influence of a different-viscosity wall-film on bypass transition was examined using both linear theory and direct numerical simulations. The film viscosity was selected such that the two-fluid interface does not in-

roduce any new exponential instabilities, and that the boundary layer is stabilized in comparison to the single-fluid configuration.

The linear analysis was used to evaluate the maximum possible amplification of an initial disturbance with unit energy. A seminorm constraint was adopted in order to ensure that the initial disturbance is without any interface deformation, otherwise energy can be hidden in the initial displacement of the interface and later released in the flow. The results of the linear analysis demonstrated that the lower-viscosity film has a dual effect. On the one hand, it reduces the maximum achievable amplification of streaky disturbances, and on the other hand it introduces a new mechanism for disturbance growth due to the interface mode.

Direct numerical simulations of the full nonlinear transition process showed that the lower viscosity wall-film can indeed delay bypass breakdown. In the pre-transitional region, the profile of the streamwise velocity perturbation has two peaks, one in the outer flow and a second peak at the two-fluid interface. While the outer peak weakens with decreasing film viscosity, the peak at the interface intensifies. The focus was placed on the outer peak which is related to the streaks, since their weaker amplification can explain the delay in transition onset. A more detailed view of the streak amplitudes was sought using structure identification and tracking techniques. The results showed that the probability density function of streak amplitudes becomes narrower in the two-fluid flow. The appreciable reduction in the probability of high-amplitude streaks is the principal factor in delaying the onset of secondary instability and delaying breakdown to turbulence.

Acknowledgment

The authors would like to acknowledge support from the UK Engineering and Physical Sciences Research Council (EPSRC), the National Science Foundation (NSF) and the US Air Force Office of Scientific Research (AFOSR).

References

- [1] M. V. Morkovin, *Viscous Drag Reduction*, ch. On the many faces of transition. Plenum, 1969.
- [2] T. A. Zaki, "From streaks to spots and on to turbulence: Exploring the dynamics of boundary layer transition," *Flow, Turbulence and Combustion*, vol. 91, no. 3, pp. 451–473, 2013.
- [3] T. A. Zaki and S. Saha, "On shear sheltering and the structure of vortical modes in single and two-fluid boundary layers," *Journal of Fluid Mechanics*, vol. 626, pp. 113 – 148, 2009.
- [4] J. C. R. Hunt and P. A. Durbin, "Perturbed vortical layers and shear sheltering," *Fluid Dynamics Research*, vol. 24, no. 6, pp. 375–404, 1999.
- [5] R. G. Jacobs and P. A. Durbin, "Shear sheltering and the continuous spectrum of the Orr-Sommerfeld equation," *Physics of Fluids*, vol. 10, no. 8, 1998.
- [6] D. Hernon, E. J. Walsh, and D. M. McEligot, "Experimental investigation into the routes to bypass transition and the shear-sheltering phenomenon," *Journal of Fluid Mechanics*, vol. 591, pp. 461–479, 2007.
- [7] K. J. A. Westin, A. V. Boiko, B. G. B. Klingmann, V. V. Kozlov, and P. H. Alfredsson, "Experiments in a boundary layer subjected to free stream turbulence. Part 1. Boundary layer structure and receptivity," *Journal of Fluid Mechanics*, vol. 281, no. -1, pp. 193–218, 1994.
- [8] R. G. Jacobs and P. A. Durbin, "Simulations of bypass transition," *Journal of Fluid Mechanics*, vol. 428, pp. 185–212, 2001.
- [9] M. Matsubara and P. H. Alfredsson, "Disturbance growth in boundary layers subjected to free-stream turbulence," *Journal of Fluid Mechanics*, vol. 430, pp. 149–168, 2001.
- [10] M. T. Landahl, "A note on an algebraic instability of inviscid parallel shear flows," *Journal of Fluid Mechanics*, vol. 98, pp. 243–251, 1980.
- [11] O. M. Phillips, "Shear-Flow Turbulence," *Annual Review of Fluid Mechanics*, vol. 1, no. 1, pp. 245–264, 1969.
- [12] L. Brandt, P. Schlatter, and D. S. Henningson, "Transition in boundary layers subject to free-stream turbulence," *Journal of Fluid Mechanics*, vol. 517, pp. 167–198, 2004.
- [13] A. C. Mandal, L. Venkatakrishnan, and J. Dey, "A study on boundary-layer transition induced by free-stream turbulence," *Journal of Fluid Mechanics*, vol. 660, pp. 114–146, 2010.
- [14] M. Asai, Y. Konishi, Y. Oizumi, and M. Nishioka, "Growth and breakdown of low-speed streaks leading to wall turbulence," *Journal of Fluid Mechanics*, vol. 586, pp. 371–396, 2007.
- [15] P. Schlatter, L. Brandt, H. C. de Lange, and D. S. Henningson, "On streak breakdown in bypass transition," *Physics of Fluids*, vol. 20, 2008.
- [16] T. A. Zaki and P. A. Durbin, "Mode interaction and the bypass route to transition," *Journal of Fluid Mechanics*, vol. 531, pp. 85–111, 2005.
- [17] T. A. Zaki and P. A. Durbin, "Continuous mode transition and the effects of pressure gradient," *Journal of Fluid Mechanics*, vol. 563, pp. 357–388, 2006.
- [18] P. Andersson, L. Brandt, A. Bottaro, and D. S. Henningson, "On the breakdown of boundary layer streaks," *Journal of Fluid Mechanics*, vol. 428, pp. 29–60, 2001.
- [19] N. J. Vaughan and T. A. Zaki, "Stability of zero-pressure-gradient boundary layer distorted by unsteady Klebanoff streaks," *Journal of Fluid Mechanics*, vol. 681, pp. 116–153, 2011.
- [20] M. J. P. Hack and T. A. Zaki, "Streak instabilities in boundary layers beneath free-stream turbulence," *Journal of Fluid Mechanics*, vol. 741, pp. 280–315, 2014.
- [21] C. S. Yih, "Instability due to viscosity stratification," *Journal of Fluid Mechanics*, vol. 27, pp. 337–352, 1967.
- [22] Y. Renardy, "The thin-layer effect and interfacial stability in a two-layer Couette flow with similar liquids," *Physics of Fluids*, vol. 30, no. 6, pp. 1627–1637, 1987.

- [23] A. P. Hooper and W. G. C. Boyd, “Shear-flow instability due to a wall and a viscosity discontinuity at the interface,” *Journal of Fluid Mechanics*, vol. 179, pp. 201–225, 1987.
- [24] L. Ó Náraigh, P. Spelt, O. Matar, and T. A. Zaki, “Interfacial instability in turbulent flow over a liquid film in a channel,” *Int. J. Multiphase Flow*, vol. 37, pp. 812–830, 2011.
- [25] J. J. Nelson, A. E. Alving, and D. D. Joseph, “Boundary layer flow of air over water on a flat plate,” *Journal of Fluid Mechanics*, vol. 284, pp. 159–169, 1995.
- [26] M. J. South and A. P. Hooper, “Linear growth in two-fluid plane Poiseuille flow,” *Journal of Fluid Mechanics*, vol. 381, pp. 121–139, 1999.
- [27] S. V. Malik and A. P. Hooper, “Three-dimensional disturbances in channel flows,” *Physics of Fluids*, vol. 19, p. 052102, 2007.
- [28] P. Luchini, “Reynolds-number-independent instability of the boundary layer over a flat surface: optimal perturbations,” *Journal of Fluid Mechanics*, vol. 404, pp. 289–309, 2000.
- [29] D. Foures, C. Caulfield, and P. Schmid, “Variational framework for flow optimization using seminorm constraints,” *Physical Review E*, vol. 86, no. 2, p. 026306, 2012.
- [30] P. J. Schmid, “Nonmodal stability theory,” *Annual Review of Fluid Mechanics*, vol. 39, pp. 129–162, 2007.
- [31] S. Saha, J. Page, and T. A. Zaki, “Disturbance amplification in boundary layers over thin wall films,” *Physics of Fluids*, 2016. In press.
- [32] S. Y. Jung and T. A. Zaki, “The effect of a low-viscosity near-wall film on bypass transition in boundary layers,” *Journal of Fluid Mechanics*, vol. 747, pp. 330–360, 2015.
- [33] O. Desjardins, V. Moureau, and H. Pitsch, “An accurate conservative level set/ghost fluid method for simulating turbulent atomization,” *Journal of Computational Physics*, vol. 227, pp. 8395–8416, 2000.
- [34] L. C. Cheung and T. A. Zaki, “Linear and nonlinear instability waves in spatially developing two-phase mixing layers,” *Physics of Fluids*, vol. 22, p. 052103, 2010.
- [35] L. C. Cheung and T. A. Zaki, “A nonlinear PSE method for two-fluid shear flows with complex interfacial topology,” *Journal of Computational Physics*, vol. 230, pp. 6756–6777, 2011.
- [36] S. Osher and J. A. Sethian, “Fronts propagating with curvature-dependent speed: Algorithms based on hamilton-jacobi formulations,” *Journal of Computational Physics*, vol. 79, pp. 12–49, 1988.
- [37] K. P. Nolan and T. A. Zaki, “Conditional sampling of transitional boundary layers in pressure gradients,” *Journal of Fluid Mechanics*, vol. 728, pp. 306–339, 2013.

A CONTRIBUTION TO INVESTIGATIONS OF THE LEADING EDGE SHAPE EFFECT ON THE FLAT PLATE BOUNDARY LAYER TRANSITION

P. Jonáš and P. P. Antoš

Institute of Thermomechanics AS CR, Prague, Czech Republic,
jonas@it.cas.cz, antos@it.cas.cz

Abstract

Boundary layer laminar-turbulent transition was experimentally investigated on smooth flat plates with three different profiles of leading edges (L.E.): circle (diameter 2 mm), ellipse ($a \times b = 30 \text{ mm} \times 20 \text{ mm}$) and modified super ellipse after Schrader et al, 2010, ($a/b = 6$, $a = 36 \text{ mm}$). Outer stream Reynolds number (at $L = 1 \text{ m}$) was in the range from 3.3×10^5 to 1.1×10^6 ; turbulence intensity was either natural, RMS velocity fluctuations about 0.3 per cent of external flow velocity, U_e , or with increased RMS fluctuations up to 3.0 per cent of U_e by means of a plane woven grid. Only start and initial phase of transition process were possible to study at natural turbulence level as the termination of the process did not come on in the measurement space (up to $x = 1.6 \text{ m}$ from the L.E.). It was ascertained that transition starts first on the plate with elliptical L.E., later in boundary layer with the super ellipse shape of the L.E. and finally, in the layer with cylindrical L.E., developed for boundary layer stability investigations by Kosorygin et al 1982. The differences are quite distinct. Investigations are still in progress.

1 Introduction

The effect of free stream turbulence (FST) on boundary layer development, namely on laminar turbulent transition, is investigated systematically since the forties of the twentieth century. Plenty contributions dealing with this problem are published every year e.g. surveys Saric et al. [1] and Lee and Wu [2]. Regardless of this, it is still an open problem of fluid mechanics. The reasons for this state of the art are "many faces of transition" Morkovin [3], i.e. the boundary layer receptivity for a number of environmental unsteady disturbances.

Effects of individual categories of disturbances e.g. turbulence are systematically investigated but at simultaneous action of the remaining ones if these are not sufficiently suppressed. The structure of the "minor" impacts may differ from case to case. So it is very desirable give the full description of the "minor disturbances" when presenting results of experiments. The "minor disturbances" can cause differences between individually published results on laminar turbulent transition. Unfortunately, this description is often incomplete, sometimes missing. On example, the by-pass transition studies often focussed only on the external flow turbulence intensity regardless that the subsequent research also clearly proved the effect of the turbulence length scale e.g. Jonáš et al. [4], Roach and Brierley [5] and Brandt et al. [6].

Another example of a "minor impact" is the effect of the L.E. shape. It is of particular importance as the ex-

ternal disturbances first enter the boundary layer in the leading edge region. Numerous published studies dealing with this effect confirm this opinion; recently e.g. Hanson and Buckley [7], Schlatter and Örlü [8], Schröder et al. [9], Ustinov and Uspensky [10] and Walsch et al. [11].

The experimental research of laminar turbulent transition started at the Institute of Thermomechanics, Academy of Sciences, Czech Republic (IT) in 1988, Jonáš [12]. Having in mind some results published at ITPM AS USSR, Novosibirsk on the sensitivity of the boundary layer stability studies to the leading edge shape (Kosorygin et al. [13] and [14]), the preliminary experiments in the boundary layer were accomplished on the smooth wall with the sucked hydraulically smooth porous band embedded crosswise the flow direction in the smooth side wall of the working section ($0.1 \times 0.1 \text{ m}^2$, in length 2 m) of the IT small wind-tunnel of vacuum storage drive. Thus it was approved that the local state of boundary layer can be shifted to the former state due to the proper suction through a sufficiently large porous part of wall. Then the development of laminar-turbulent boundary layer transition can be investigated directly on the wind tunnel working section wall without the influence of the leading edge effect.

Afterwards the IT investigations concerned on study of the role of external flow turbulence length scale in by-pass transition e.g. Jonáš [4 and 15]. The working section (cross section $0.5 \times 0.9 \text{ m}^2$, length 2.69 m) of the closed circuit wind tunnel of the IT has been rebuilt to make possible comparative investigations of the flat plate boundary transition with grid turbulence. The investigated boundary layers are developing on aerodynamically smooth plate made from a laminated wood-chip board 25 mm thick, 2.75 m long and 0.9 m wide. The cylindrical shape of the L.E. (diameter 2 mm) has been designed and examined by Kosorygin et al. [13]. This leading edge has been precisely made from duralumin in the IT-workshop. For more details on the experimental facility see e.g. [4 and 16]. The effect of turbulence length scale on beginning and extent transitional region has been clearly established on the investigated class of boundary layers. In few words: the onset and the termination of by-pass transition move upstream with increasing length scale of turbulent disturbances at a fixed intensity of the external flow turbulent fluctuations in the leading edge plane.

Preliminary validation of the previous conclusion on the class of boundary layers on rough surfaces has been done in the same experimental facility but with boundary layers developing on plate covered by sand paper. Three plates made from thin plywood (7 mm) with glued sand paper (different roughnesses) equipped with the simple wooden elliptical leading edge ($a = 20 \text{ mm}$, $b = 10 \text{ mm}$) were made. This rough plates are individually pushed

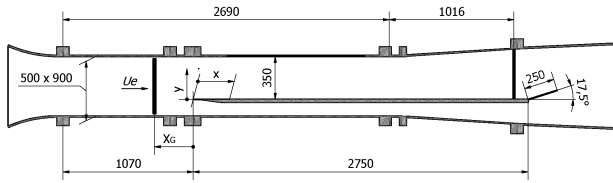


Figure 1: Flat plate in the wind tunnel

to the primary smooth plate so that they cover, with their simple elliptical leading edge the thin cylindrical leading edge of the smooth main plate. This leading edge has been available on free market at low cost and it is not difficult to paste smooth sand paper on it. This configuration, described in detail e.g. Jonáš et al. [16 and 17] and Antoš et al. [18], is meeting requirements of preliminary experiments but the results can be applied only for qualitative comparison with the results received on the smooth layer due to different shapes of leading edges.

This fact moves the authors to equip the experimental facility with smooth/rough flat plates each with the same leading edge in shape and dimensions for the subsequent investigations of by-pass transition in non-zero gradient flows. The importance of the L.E. effect is discussed in several papers above mentioned. At least the super-ellipse shape of the leading edge has been chosen with the regard to the limitations of home-made realisation. The chosen shape has been examined experimentally and by numerical simulations (Hansom and Buckley [7], Schrader et al. [13]). The shape is defined by

$$\left(\frac{y}{b}\right)^2 = 1 - \left(\frac{a-x}{a}\right)^p; \quad p = 2 + \left(\frac{x}{a}\right)^2 \quad (1)$$

where x is the coordinate in streamwise direction, y is perpendicular to the surface ($a/b = 6$, $a = 36 \text{ mm}$). These leading edges were carefully custom made from hardwood.

The aim of this contribution is answer the question: how the shape of the leading edge affects the location of the by-pass turbulent transition start and the length of transitional region at identical external flow turbulence intensity, T_u and length scale, Le .

Compared are results of investigations on aerodynamically smooth flat plates with the leading edge shapes: cylindrical L.E. ($d = 2 \text{ mm}$), elliptical L.E. ($a \times b = 20 \text{ mm} \times 10 \text{ mm}$) and the super-elliptical (1). External flow turbulence was either natural ($T_u = 0.003$, $Le \cong 100 \text{ mm}$) or grid turbulence ($T_u = 0.03$, $Le = 3.9 \text{ mm}$).

2 Experimental Facility

The experimental set up employed at the IT investigations of by-pass boundary layer transition is briefly described in Introduction. Some details are obvious from the Figure 1 which also helps to better notion of the facility. More detailed descriptions are given in [4, 16 and 19]. The orthogonal clockwise co-ordinate system (x, y, z) is introduced with (x, y) plane in the vertical plane of the working section (W.S.) symmetry, centre in the projection of the L.E. zero point into (x, z) plane, x-axis has the same direction as the external mean flow.

The representative pressure $q_r [Pa]$ and the external flow static pressure $P_e [Pa]$ are measured by means of the Pitot-static probe (dia = 6 mm) positioned 0.23 m upstream from the plate nose and sufficient far away from

side wall W.S. and investigated boundary layer. The above mentioned pressures together with temperature $T_e [K]$ serve for determination of physical features of air and for the compensation of small and slow variations of external flow.

Basic source of further analysis the L.E. effect are the mean flow velocity profiles, $U(x, y)$, measured in boundary layers at prescribed boundary conditions.

The CTA measuring technique was employed during first period of investigation executed in the framework of COST/ERCOTAC Test Case T3A+. As to reach top measuring accuracy this procedure is time consuming e.g. the calibration of each probe is repeated after 2 - 3 hours of its exposure in flow; successive shifts of the probe are measured by means of cathetometer ($\pm 0.01 \text{ mm}$) etc. This procedure, together with extra developed evaluation procedures (e.g. correction of the wall proximity effect on HW reading), improves the accuracy of results. Uncertainties of the mean velocity $U [m/s]$ and the intensity of turbulent velocity fluctuations T_u are 0.3 percent and 3 percent of the velocity U_e respectively. Error estimates of the zero velocity level and of the velocity derivative $(dU/dy)_w$ are $\pm 0.02 \text{ mm}$ and ± 2 percent. This refined measuring and evaluation procedures are described minutely in [4].

Another method of the velocity measurement utilizes the couple of the flattened Pitot probe (outer dimensions $0.18 \text{ mm} \times 2.95 \text{ mm}$) and round nosed static pressure probe (dia = 1.8 mm). The reasons to employ pressure probe instead of the CTA method are following: the spikes of roughness grains on rough surface can easily broken a hot wire probe operating near the rough wall and economy in time necessary for experiment. Axes of both probes are in the plane $z = 0$ and the distance between them is 55 mm. Dynamic pressure $q(x, y, 0) [Pa]$ is measured by means of the accurate pressure transducer (max 1 kPa , $\pm 0.02 \%$ of reading above 20 Pa). The effect of the wall proximity on the flattened Pitot probe readings is corrected after the procedure proposed by Mac Millan, see Tropea et al. [20]. Details to this brief description of the method are given in Antoš et al. [17 and 21].

The third measuring method applied is based on the use of a rake consisted from thirty Pitot tubes (dia = 0.3 mm) and simultaneous readings of pressure differences by means of an intelligent pressure scanner (max 2.5 kPa , $\pm 0.15\%$ F.S.). Corrections of measured data are made after recommendations in [20]. This measuring method speeded up the preliminary experiments significantly.

Accuracy of the employed instrumentation, the spread of repeated readings and calculated root mean square errors of interpolations support following uncertainties estimates: mean velocity U less than $\pm 0.1 \text{ m/s}$, thicknesses of boundary layer $\delta, \delta_1, \delta_2$ about $\pm 2 \%$, the wall friction $\tau_w = \mu(dU/dy)_w$ from 3 % up to 10 %, in dependence on the thickness of the layer, δ defined by $U(y = \delta) = 0.99U_e$.

3 Outline of the Evaluation Procedure

At first a series of $U[y'_i] \equiv U_i, i = 1, 2, \dots, n = 30$ is calculated in each section x using canonical formulas inclusive all required corrections. Here y'_i are recorded probe positions.

The correct space of the probe from the surface must be approved i.e. it is necessary determine the velocity zero level. Positions of probe during the profile mea-

surement are measured by means of the cathetometer, so spaces between the individual coordinates $y'_i - y'_{i+1}$, $i \neq j$ are determined with high accuracy, with the error less than $\pm 0.02 \text{ mm}$. But the true spaces of the measured points little differ from the recorded ones. The true value is $y = y' + y'_0$. The correction y'_0 is derived by linear extrapolation for both the HW-probe measurement and the flattened Pitot tube ones. Usually at the same time the velocity derivative at the wall is determined $(dU/dy)_w$ and thus the local wall friction can be calculated using generally known formulas e.g. [22].

The correction y'_0 is neglected when the Pitot rake is employed at measurement in a smooth wall boundary layer. Then the external flow velocity U_e is calculated as the average of readings $U(y_i) = U_i$ outside the layer

$$U_e = \frac{1}{b-a} \sum_{i=a}^{i=b \leq n} U_i \quad (2)$$

The range $(a; b); b - a \geq 2\delta$ is chosen so, as to reach the relevant standard deviation less than about $0.005 U_e$.

Within the next step the non-dimensional profiles U/U_e vs. y are computed and the points $0.8 \leq U/U_e \leq 1$ are interpolated by 4th order polynomial in y . Boundary layer thickness δ is then determined as the intersection of polynomial with the level 0.99.

The trapesoidal rule is used for approximating definite integrals representing integral thicknesses δ_1 and δ_2 . Sometimes, the space from the wall of the first valid reading $U_1(x, y_1)$ is too large. Then a small correction is necessary in the first step of integration i.e. numerical integration is exchanged by analytical integration of the polynomial interpolation through few valid readings nearest to the wall [23].

The direct evaluation of the derivative $(dU/dy)_w$ or of the skin friction coefficient C_f from velocity profile measured by the Pitot tubes rake is almost impossible even though the zero pressure gradient boundary layers are investigated. Satisfactory good estimates of the mentioned characteristics are possible in the quasilaminar state of the layer i.e. from comparison between the measured profiles U/U_e against the Blasius solution $F'(\eta)$. The relevant value of Blasius variable is calculated after the formulae $\eta = 0.664y/\delta_2$. If the slope of the trend line possesses value near one, at least (1 ± 0.01) the layer is assumed as quasi laminar one and the coefficient C_f is refined according to Blasius solution.

Likewise, if H_{12} is near the value adequate to turbulent boundary layer the Logarithmic overlap law and Law of the wake in fully turbulent layer can be used for determination of the skin friction, e.g. Schlichting and Gersten [21].

The skin friction estimates in transitional region of boundary layer can be gained either from additional Pitot tube measurement near the surface or using the correlation between the shape parameter $H_{12} = \delta_1/\delta_2$ and the skin friction coefficient designed in Jonáš [22].

4 Results

4.1 Boundary Conditions

Boundary conditions are set up as to maintain the external flow mean velocity U_e steady in the main part of the plate, from L.E., $x = 0$ up $x = 1.62 \text{ m}$. Farther downstream started diffuser and the velocity is decreasing to $0.96 U_e$. Throughout the whole experimental program U_e were set on values 5 m/s , 10 m/s and 14 m/s in

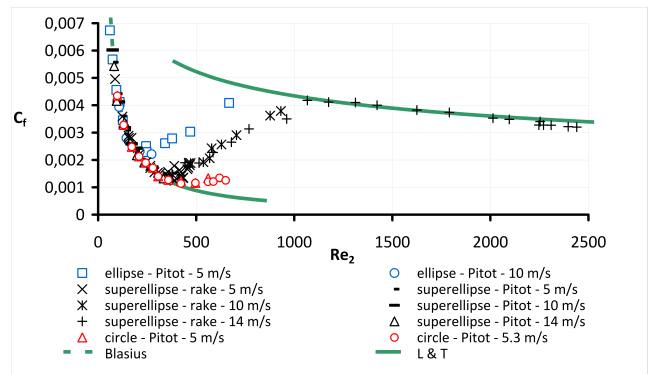


Figure 2: Skin friction coefficient $C_f = f(Re_2)$, $T_u = 0.003$

the limits ± 7 percent. These limits reduce to about one third for individual boundary layer.

The effect of the free stream Reynolds number on dimensionless boundary layer characteristics was not observed within the current experimental set up and velocity range from 5 m/s to 14 m/s . The distribution of the pressure gradient parameter was calculated after the formulae

$$F = \frac{\delta_2}{U_e} \frac{dU_e}{dx} \sim 3.6 \times 10^4; \quad 0 < x \leq 1.62 \text{ m} \quad (3)$$

The free stream sound - the wavy disturbances - were not measured yet though the receptivity to them might exceed the boundary layer receptivity to turbulent disturbances [1] and thus it affects observed laminar-turbulent transition.

The free stream turbulence level T_u , ratio of the velocity fluctuations RMS value to the mean velocity, was either natural (intensity $T_{u_e} \cong 0.003$) or raised downstream turbulence generator (GT8; intensity $T_{u_e} = 0.03$ in the plane $x = 0$). The label generator GT8 denotes the square mesh ($M = 5.75 \text{ mm}$) plane grid made from cylindrical rods ($d = 1.65 \text{ mm}$) placed in plane $x_G = 0.194 \text{ m}$ upstream from L.E. It produces homogeneous (in planes $x = \text{const.}$) close to isotropy turbulence. This grid turbulence decreases according to the decay law downstream from the L.E. The principal characteristics of GT8 are described in [4].

4.2 External Flow with Natural Turbulence

The wall friction is one of the most important boundary layer characteristics being the base for determination of the inner scales in a boundary layer and for the friction losses predictions. The distributions of skin friction coefficient versus momentum thickness Reynolds number, C_f vs. Re_2 are plotted in Figure 2 together with the Blasius solution for laminar boundary layer and the empirical relation derived by Ludwieg H. and Tillman W. (L&T, see [21], p. 590). Measurements were executed in boundary layers on plates with tested leading edges in external flow with natural turbulence level $T_u = 0.003$ and at mean velocities 5 m/s , 10 m/s and 14 m/s respectively.

Apparently regions with pseudo-laminar flow structure occur near each tested L.E. They follow the Blasius solution till some distance downstream the L.E. depending on the shape of L.E. and on the state of layer characterized by e.g. Re_2 .

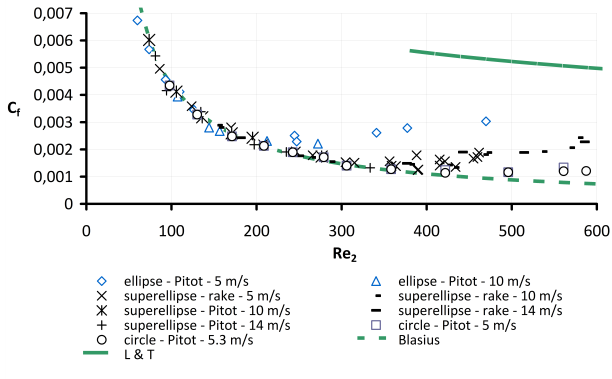


Figure 3: Transition onset -skin friction coefficient $C_f = f(Re_2)$

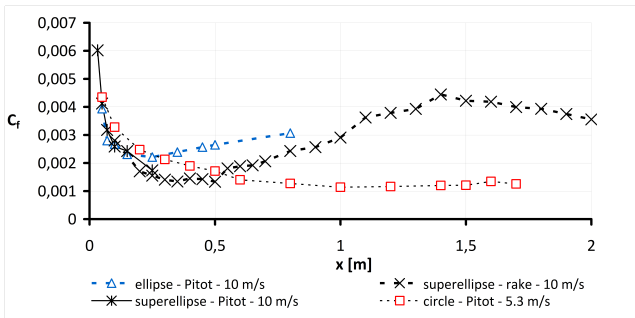


Figure 4: The skin friction coefficient $C_f = f(x)$

Detail of the Figure 2 shown in the Figure 3 demonstrates more distinctly that the start of the departure of the skin friction distribution from the Blasius function, depends on the leading edge shape, regardless of the free stream velocity. Apparently estimates of the momentum thickness Reynolds number Re_2 at this start are found in natural turbulence flow as follows:

- downstream the elliptic L.E. at $(Re_2)_0 \approx 200$;
- downstream the super-elliptic L.E. at $(Re_2)_0 \approx 350$;
- downstream the thin cylindrical L.E. at $(Re_2)_0 \approx 400$.

It should be mentioned that Figure 2 and Figure 3 serve also as an illustration of the effect of the mean flow velocity and the applied measuring method on results of experiment. These figures together with the furthermore presented figures confirm that the effect of outer stream velocity U_e , differences on boundary layer dimensionless characteristics can be validated as negligible in the frame of the measuring accuracy like in [19]. As well the observed differences between results received by means of flattened Pitot tube or by the less accurate rake of Pitot tubes appear acceptable.

The courses of skin friction coefficient with the distance x downstream from the leading edge ($x = 0$) are shown in the Figure 4. Apparently the minimum of the skin friction coefficient distribution indicates the onset of transitional region. So, the plot of results in the Figure 4 demonstrates the dramatic effect of the L.E. shape on laminar - turbulent transition origin in space.

Identical information follows from the distributions of the shape factor H_{12} shown in the Figure 5.

The scatter of points evaluated from measurement by the Pitot tubes rake demonstrates some imperfection of

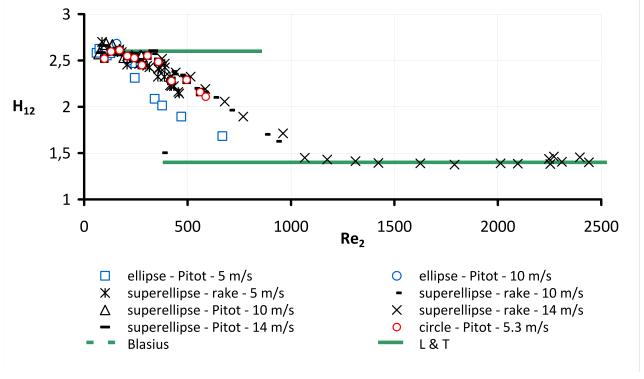


Figure 5: The shape factor $H_{12} = f(Re_2)$

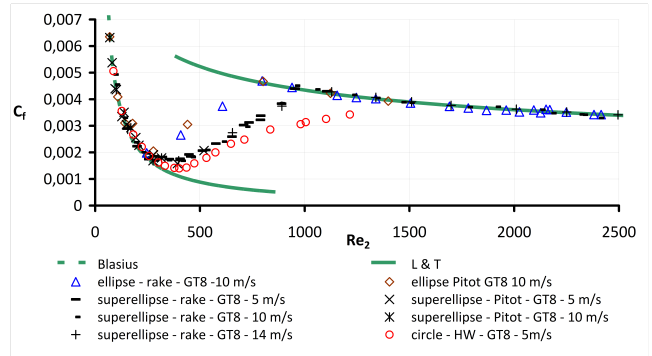


Figure 6: Amplified turbulence level - the skin friction coefficient $C_f = f(Re_2)$

originally performed numerical integrations. This was motive for the study [22].

4.3 External flow with Grid Turbulence

The effect of the L.E. shape on transition in boundary layer under flow with amplified turbulence, $T_u = 0.03$, is shown in the Figure 6. The outsets of transitional region move upstream of about

$$\Delta Re_2 \approx (Re_2)_0/4 \quad (4)$$

from the location, $(Re_2)_0$, determined in low turbulence free stream.

Similar comparison cannot be done about termination of transitional region as it was found only in case with super-elliptic L.E. (Figure 2). However it is quite clear that the width of transitional region is smallest at ellipse L.E., longer at super-ellipse L.E. and longest in boundary layer on plate with the circle L.E.

The plots of the shape factor distributions, determined boundary layers under grid turbulence flow, are shown in the Figure 7. They correspond with the foregoing discussion. The effect of outer stream velocity U_e , differences on boundary layer dimensionless characteristics was validated as negligible in the frame of the measuring accuracy like in the paper [19].

5 Conclusions

The executed investigations clearly document dramatic differences in the development and behaviour of boundary layer on flat plate under as much as possible same boundary conditions except of the shape of their leading edges. Results of experiments with transitional

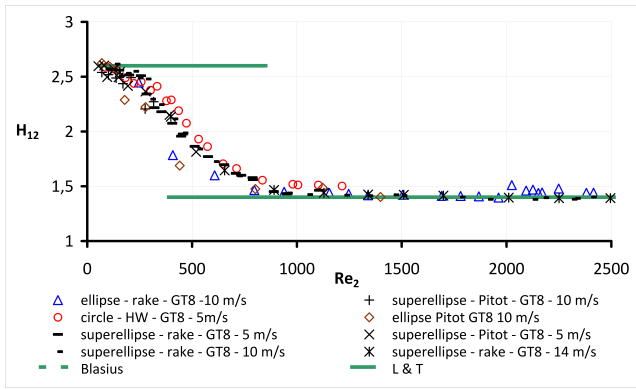


Figure 7: Amplified turbulence level - the shape factor $H_{12} = f(Re_2)$

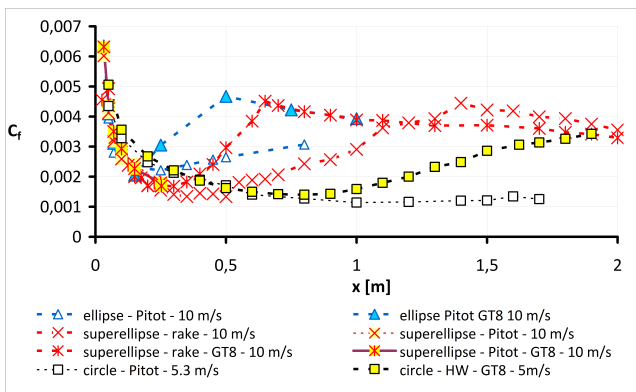


Figure 8: The skin friction coefficient $C_f = f(x)$

boundary layers confirm this conclusion in the case of external flow with natural turbulence, turbulence level $T_u = 0.003$, and in the external flow downstream the grid turbulence generator GT8, turbulence level $T_u = 0.03$ in the leading edge plane, $x = 0$. This conclusion is clearly confirmed by skin friction distributions shown in the Figure 8. As it was already mentioned, the receptivity of boundary layers on plates with different leading edges rises stepwise from the circle shape L.E. to the superellipse shape L.E. and to the ellipse shape of the leading edge. The development to self-preserving turbulent boundary layer accelerates in the same sequence of leading edges shapes. So the results of by-pass investigations received from experiments on plates with different leading edges can be mutually compared only qualitatively now.

Validations of presented conclusions, related to boundary layers developing on smooth surface, on rough wall layers are in progress.

Acknowledgement

This work has been supported by the Grant Agency of the Czech Republic GACR GAP101/12/127. This support is acknowledged.

References

[1] Saric W.S., Lee H.L. and Kerschen E.J., "Boundary layer receptivity to free stream turbulence", *Annu.Rev. Fluid Mech.* 34, 2002

[2] Lee C.B. and Wu J.Z., "Transition in Wall-Bounded Flows", *ASME Appl. Mech. Rev.* Vol. 61/030802, 2008

[3] Morkovin M.V., "On the many faces of transition", In: *Viscous Drag Reduction*, (ed. C.S. Wells), Plenum, New York, 1-31, 1969

[4] Jonas P., Mazur O. and Uruba V., "On the receptivity of the by-pass transition to the length scale of the outer stream turbulence", *Eur.J.Mech. B* 19, 707-722, 2000

[5] Roach P.E. and Brierley D.H., "Bypass transition modeling: a new method which accounts for free-stream turbulence intensity and length scale", *ASME Paper* 2000-GT-0278, 2000

[6] Brandt L., Schlatter P. and Henningson D.S., "Transition in boundary layers subject to free-stream turbulence", *J. Fluid Mech.* 517, 167-198, 2004

[7] Hanson R.E. and Buckley H.P., "Aerodynamic optimization of the flat-plate leading edge for experimental studies of laminar and transitional boundary layers", *Exp. Fluids* 53, 863-871, 2012

[8] Schlatter P. and Örlü R., "Assessment of direct simulation data of turbulent boundary layers", *J. Fluid Mech.* 659, 116 - 126, 2010

[9] Schröder L.U., Brandt L., Mavriplis C. and Henningson D.S., "Receptivity to free stream vorticity of flow past a flat plate with elliptic leading edge", *J. Fluid Mech.* 653, 245 - 271, 2010

[10] Ustinov M.V. and Uspensky A.A., "Influence of turbulence scale and shape of leading edge on FST-induced laminar-turbulent transition", *Proc. 28th Int. Congress Aeronautical Sci.*, 1 - 10, 2012

[11] Walsh E.J., Herson D., Davies M.R.D. and McEligot D.M., "Preliminary measurements from a new flat plate facility for aerodynamic research", *6th Eur. Conf. Turbo Machinery*, INEEL/CON-04-02301 Preprint, 1 - 10, 2005

[12] Jonáš P., "Study of boundary layer transition in flows with various turbulence." *Rep. Z - 1126/90*, IT CAV, Praha, 1990, (In Czech)

[13] Kosorygin V.S., Levchenko V.Ya. and Polyakov N.F., "On problem of the origin of waves in a laminar boundary layer. Preprint 12-82, ITPM SO AN USSR, Novosibirsk, 1982 (In Russian)

[14] Kosorygin V.S., Levchenko V.Ya. and Polyakov N.F., "The laminar boundary layer in the presence of moderately turbulent freestream", *Preprint 16-88*, ITPM SO AN USSR, Novosibirsk, 1988 (In Russian)

[15] Jonas P., "On the role of the length scale in the by-pass transition", *ZAMM - Z. angew. Math. Mech.* 77, S1 S145-S146, 1997

[16] Jonáš P., Mazur O. and Uruba V., "Comparison between the wall roughness effect and the free stream turbulence impact and their joint action on a boundary layer development", *ERCOFTAC Bulletin* 80, 82-86, 2009

[17] Jonáš P., Hladik O., Mazur O., Uruba V., "By-pass transition of flat plate boundary layers on the surfaces near the limit of admissible roughness", *J. Physics: Conf. Series* 318, 032030, 1-19, 2011

- [18] Antoř P., Jonáš P. and Procházka P., "A comment on the flat plate leading edge shape on laminar-turbulent transition", Proc. of the International conference Experimental Fluid Mechanics , Liberec, s. 32-37, 2015.
- [19] Antoř P. and Jonáš P., "Reynolds number effect on the transition on a flat plate", HEFAT2014 Conf. Proc., 903-906, 2014
- [20] Tropea C., Yarin A.L. and Foss J.F., "Handbook of Experimental Fluid Mechanics", Springer Berlin, 2007
- [21] Schlichting H. and Gersten K., "Boundary Layer Theory", Springer Berlin, 2000
- [22] Jonáš P., "Preliminary study on correlation between the shape parameter and the skin friction coefficient in transitional zero pressure gradient boundary layer", Proc. Conf. Topical Problems of Fluid Mechanics, IT AVCR, Praha, 2016 (to be published)
- [23] Antoř P., Jonáš P., Procházka P. and Uruba V., "Examples of the Re-number effect on the transitional flat plate boundary layers", PAMM, Proc. Appl. Math. Mech., Vol. 14-1, pp. 605-606, 2014

EXPERIMENTAL INVESTIGATIONS ON THE UNSTEADY TRANSITION PROCESS OF THE SUCTION SIDE BOUNDARY LAYER OF LPT BLADES

D. Lengani¹, D. Simoni¹, M. Ubaldi¹, P. Zunino¹ and F. Bertini²

¹ *DIME - Università di Genova, Genova, Italy*

² *GE AvioAero, Torino, Italy*

Abstract

In the present paper recent advancements in the understanding of the transition process of the suction side boundary layer of Low Pressure Turbine (LPT) blades are discussed. Particle Image Velocimetry (PIV) measurements are considered in order to highlight the influence of free-stream turbulence intensity (FSTI) level and passing wake effects on the transition process. Proper Orthogonal Decomposition (POD) has been applied to the data set measured for the different conditions in order to identify and characterize the occurrence of large scale coherent structures into the flow. At low FSTI level the most energetic POD modes make evident the occurrence of Kelvin-Helmholtz (KH) rolls driving the transition through a separated like type process, while elevated FSTI levels and turbulence carried by wakes induce elongated low and high speed streaky structures, responsible for a by-pass transition process. Turbulent Kinetic Energy (TKE) and Reynolds shear stress distributions of the dominant modes for the different cases exhibit a strong influence of both FSTI and passing wake effects. POD applied to large amount of snapshots gives a fast and clear visualization of the main dynamics involved into the process, thus contributing to the understanding and modeling of the transition of the suction side boundary layer of LPT blades for the different conditions.

1 Introduction

For a Low Pressure Turbine blade the aerodynamic loading, flow Reynolds numbers, FSTI levels and unsteady wakes coming from upstream are the main flow parameters affecting the flow evolution, thus the boundary layer transition. In LPT blades the attached (by-pass) or the separated like transition processes are the commonly detected mechanisms, depending on the combination of the aforementioned parameters [1]. By-pass and separation induced transition mechanisms are governed by completely different dynamics that, however, share the generation and propagation of large scale coherent structures. Recently, Large Eddy Simulations (LES), Direct Numerical Simulations (DNS) and PIV indubitably gave new light and renewed interest into the understanding of the dynamics leading to generation, propagation and breakdown of such structures, that could be useful for modeling purposes.

At high loading level and low flow Reynolds numbers the boundary layer likely separates from the blade

surface. In this case the Kelvin-Helmholtz instability process developing inside the separated shear layer induces the exponential amplification of disturbances, definitively leading to the shear layer rollup behind the bubble maximum displacement position, and thus transition of the separated shear layer [2, 3, 4, 5]. Conversely, high Reynolds numbers, mild adverse pressure gradients and elevated FSTI levels move the transition process toward the by-pass type. In this condition streaky structures dominate the pre-transitional part of the boundary layer [6, 7, 8, 9]. They amplify through a transient (algebraic) behavior until sinuous or varicose instability drives their breakdown, leading to the formation of vortical structures inducing the fully turbulent condition of the flow [10, 11]. Turbulence carried by upstream wakes, characterizing the real operation of the turbine stage, excites the formation of streaky structures in the former part of the blade surface [12], and eventually interacts with the inflectional instability of the laminar separation bubble (if any) that may grow between two adjacent wakes [13, 14]. These diversified and complex scenarios make the understanding of the dynamics driving transition in LPT blades very complicated. Reduced order model techniques can be invoked to quickly identify the main dynamics driving the transition process for the different cases. POD is today a well-established technique adopted in fluid dynamics applications. It provides a modal decomposition of instantaneous observation (snapshots), ranking the dynamisms of the flow through their energy contribution to the whole Turbulent Kinetic Energy (TKE) [15]. Even though POD modes are not exactly “structures”, they isolate the main (most energetic) dynamics involved into the production of TKE, and can be also used to compute the corresponding Reynolds shear stress.

In the present paper, PIV data obtained in a highly loaded LPT blade at two different FSTI levels, operating under steady and unsteady inflows, are reported with the aim of empathize the capability of POD to clearly distinguish between the different transition modes, as well as in the identification and characterization of the largest scale structures contributing to the transition process. TKE and Reynolds shear stress distributions for the dominant modes are reported and discussed. The energy distribution of the whole set of modes complements the analysis. Results reported in the paper highlight the capability of this technique in providing a direct view of the main dynamics leading to transition for real LPT geometry and operative conditions, useful to identify modeling terms when large data sets obtained for sensibly different flows and geometrical parameters are available.

2 Experimental Apparatus and Data Reduction

2.1 Test Facility and Instrumentation

The experimental investigations have been performed in the blow-down wind tunnel installed at the Aerodynamics and Turbomachinery Laboratory of the University of Genova. The test section is constituted of a 7 blade large scale planar cascade (Figure (1)), representative of highly loaded LPT blade profiles. Blades are characterized by a chord of 120 mm and an aspect ratio $AR = 2.5$ to ensure two-dimensional flow at midspan. Measurements have been carried out at a low Reynolds number condition $Re = 70000$ (defined with the blade chord and isentropic exit velocity). Two different conditions of free-stream turbulence intensity have been tested. The low FSTI case has been generated by means of the spontaneous turbulence level of the facility ($Tu=0.19\%$), while for the high FSTI case a turbulence generation grid has been adopted to rise the turbulence level to values more representative of the real engine ones ($Tu=5.2\%$).

Upstream wakes have been simulated by means of a tangential wheel of radial rods. The wheel rotates in a plane parallel to the cascade leading edges plane. It is located at a distance of 33% of the blade chord upstream of the blade leading edges. The flow coefficient and the reduced frequency were chosen to be representative of real engine operative conditions ($\varphi = 0.675$ and $f^+ = 0.69$, respectively). The bar diameter ($d = 3$ mm) was chosen so that the wakes shed from the bars produce the same losses as those generated by a typical upstream LPT row. The total pressure loss coefficient for the bars was evaluated to be 3.3%.

The blade aerodynamic loading distributions are reported in Figure (2) for the different conditions. The peak velocity on the suction side occurs close to $s/s_{max} = 0.45$. With low FSTI the suction side boundary layer separates, as shown by the evident deviation of the corresponding loading distribution as compared with the other conditions, where the boundary layer grows attached to the blade surface.

PIV measurements have been performed in order to characterize the unsteady transition process of the suction side boundary layer. The PIV field of view covers the flow region between $0.74 < s/s_{max} < 1.1$ and 0.0

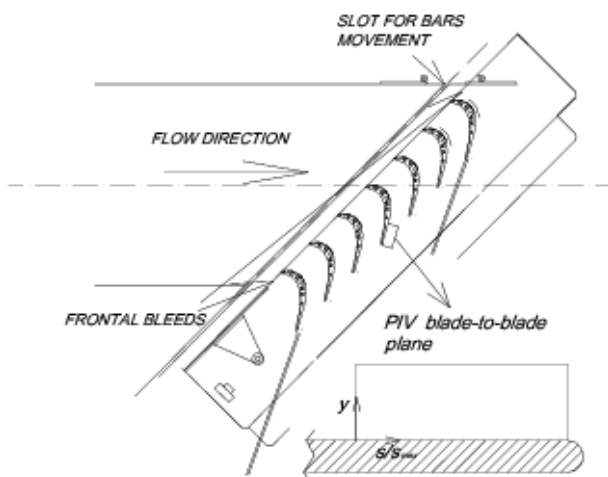


Figure 1: Sketch of the test section and PIV interrogation area

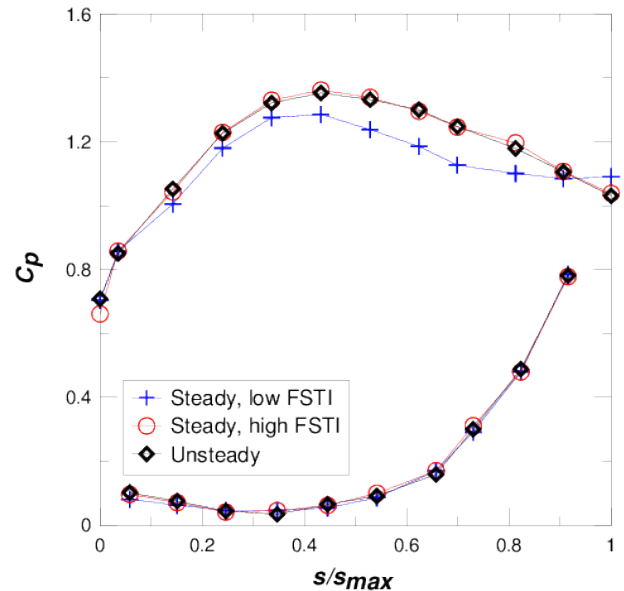


Figure 2: Loading distributions

$< y/g < 0.1$ (Figure (1)). 2000 couples of images have been acquired in order to obtain high statistical accuracy in the evaluation of time-mean quantities as well as convergence of the Proper Orthogonal Decomposition (POD) procedure.

The PIV instrumentation is constituted by a double-cavity Nd: Yag pulsed laser BLUESKY-QUANTEL CFR200 (energy 2×100 mJ per pulse at 532 nm, pulse duration 8 ns, repetition rate 10 Hz). The optical system forms a light sheet of 1 mm thickness. The light scattered by the seeding particles (mineral oil droplets with a mean diameter of $1.5 \mu\text{m}$) is recorded on a high sensitive digital camera with a cooled CCD matrix of 1280×1024 pixels (with single pixel dimension of $6.7 \times 6.7 \mu\text{m}^2$). The camera maximum frame rate in the double frame mode is 4.5 Hz, and the minimum frame interval is 200 ns. The magnification factor for the present experiments was set to $M = 0.165$. The cross-correlation function has been calculated on a 16×16 pixels interrogation area with a 50% overlap. This corresponds to a spatial resolution of $0.325 \times 0.325 \text{ mm}^2$. The instantaneous velocities have been estimated with an accuracy of $\pm 3.0\%$.

2.2 POD

Nowadays the POD is a well established technique for the identification of coherent structures into the flow [15, 16], allowing the reduction of the degree of freedom of systems highlighting the dominant modes involved into the dynamics of the process. The POD provides a triplet of information: the eigenvalues, the eigenvectors, and the POD modes. The eigenvalue of the i^{th} mode ($\lambda^{(i)}$) represents the energy contribution of the mode to the total kinetic energy of velocity fluctuations. The eigenvector of the i^{th} mode ($\chi^{(i)}$) retains the temporal information related to each mode. The POD modes ($\phi_u^{(i)}, \phi_v^{(i)}$) constitute an orthogonal basis that provides the spatial information identifying coherent structures in the flow. Hence, the method extracts and separates spatial from temporal information determining the most energetic structures and ordering them by their energy contribution to the overall TKE of the flow. Moreover, combination of the spatial distributions of the POD modes of two velocity components provides information on the contribution to the overall time-mean Reynolds shear

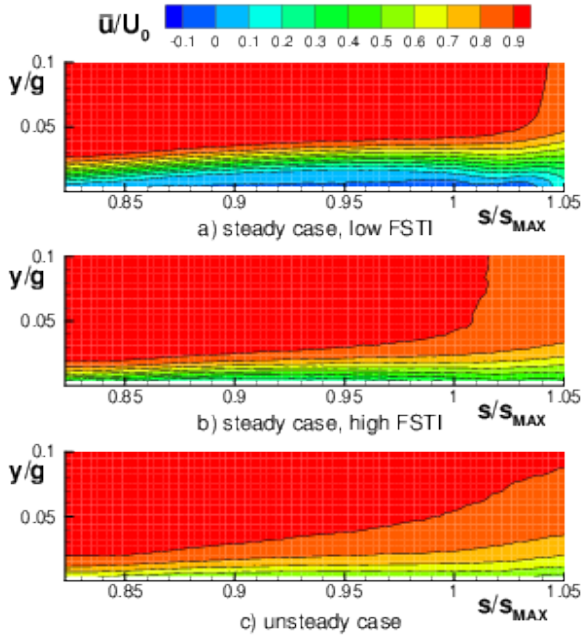


Figure 3: Time-mean streamwise velocity component.

stress due to that mode ($\overline{u'v'^{(i)}}$) which is computed as the product $\lambda^{(i)}\phi_u^{(i)}\phi_v^{(i)}$. These properties of POD are here considered to provide a clear overview of the dominant modes involved in the distribution of the TKE as well as of the Reynolds shear stress for the different cases.

3 Results and discussion

3.1 Time-mean results

The time-mean boundary layer evolutions of the three different conditions in analysis are shown in Figure (3) that reports the time-mean streamwise velocity normalized by the free-stream velocity at the measuring domain inlet (U_0). The time-mean boundary layer of the steady state condition with low FSTI shows a large separation bubble that does not reattach before the blade trailing edge (top of Figure (3)). In this case a separation induced transition process grows in the separated shear layer, as it may be observed looking to the root mean square of velocity fluctuations in Figure (4)a. The fluctuations are represented as the square root of the RMS of the two velocity components and made non-dimensional by the free-stream velocity at the measuring domain inlet (U_0). The separation induced transition mechanism acting in this case induces the amplification of velocity fluctuations along the separated shear layer. They reach the maximum values just behind the blade surface, in the wake region. Vortices shed behind the maximum displacement position are responsible for this elevated turbulent activity, and will be characterized in the following looking to the POD mode spatial distributions.

The time-mean boundary layer evolution is sensibly altered by the FSTI level. In Figure (3)b, describing the case at high FSTI level, the time-mean values of \bar{u}/U_0 do not show reverse flow region or a state approaching to separation up to the blade trailing edge. In this case elevated values of flow oscillations can be observed just at the measuring domain inlet. Peak rms grows moderately moving toward the trailing edge, with maxima localized in the close to the wall region. A by-pass type

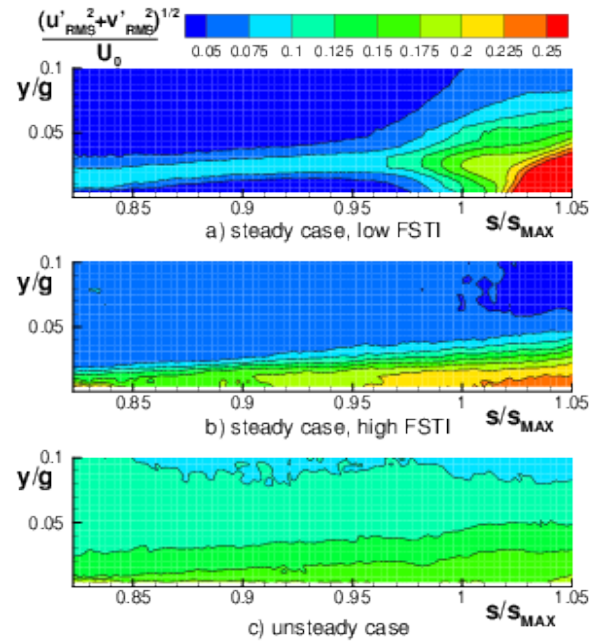


Figure 4: Root mean square of velocity fluctuations.

transition mechanism drives the flow evolution keeping the boundary layer attached to the blade surface.

In the unsteady cases, irrespective of the FSTI level (results for the two different FSTI levels are practically coincident), the boundary layer is kept well attached to the wall, due to the prompter transition process induced by the passing wake effects. The periodic wake passage is responsible for the large time-mean values of velocity fluctuations outside of the boundary layer. It is worth noting that within the boundary layer the values of the velocity fluctuations are lower than in the steady case with high FSTI. The anticipation of the transition process makes the boundary layer fully turbulent in the whole measuring domain, avoiding the intermittent switching between the laminar and the turbulent state characterizing the former part of the by-pass process [17, 18].

3.2 POD Analysis

In order to provide a statistical representation of the dominant dynamics involved into the generation of TKE as well as Reynolds shear stress for the different cases,

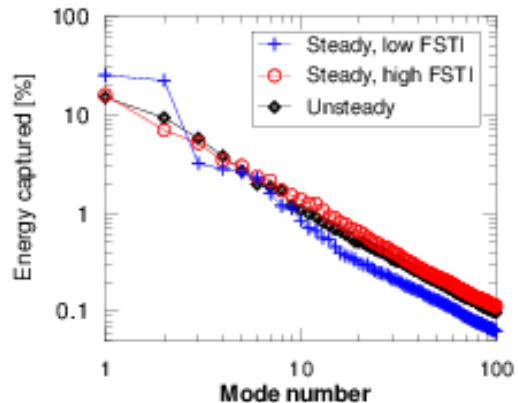


Figure 5: Relative energy of POD eigenvalues: percentage of the total kinetic energy.

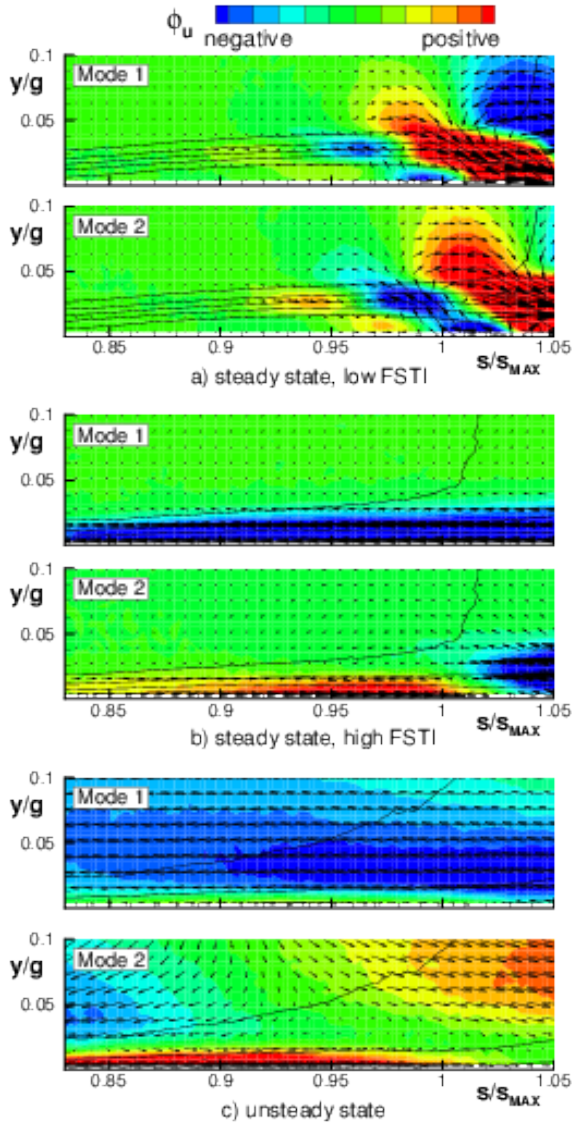


Figure 6: Vectorial representation of the POD modes and their streamwise velocity component. Iso-contour lines of \bar{u}/U_0 are superimposed on the plots.

POD data are reported. Figure (5) shows the distribution of the POD eigenvalues. Logarithmic scales are used for both axes of the plot to visualize large variations. For the three different cases the energy captured by the modes above the 10^{th} becomes rapidly low. This is more evident for the steady case at low FSTI, for which between the first two modes and the following there is a difference of about one order of magnitude. The modes after the 10^{th} are about two order of magnitude lower than the first two. Moreover, the first two modes appear energetically coupled. This indicates the presence of deterministic structures that capture a very large amount of the total kinetic energy, as further described in a previous authors' work [19]. On the contrary, the energy captured for the other two cases has different distributions: the decrease of the energy captured by each mode is approximately linear in the log-log scale. This is representative of less organized (deterministic) structures developing into the flow, coherently with the evolution of a by-pass like transition process at high FSTI and in the unsteady case.

The spatial distributions of the first two POD modes for the different cases are shown in Figure (6) as contour plot of the POD mode of the streamwise velocity compo-

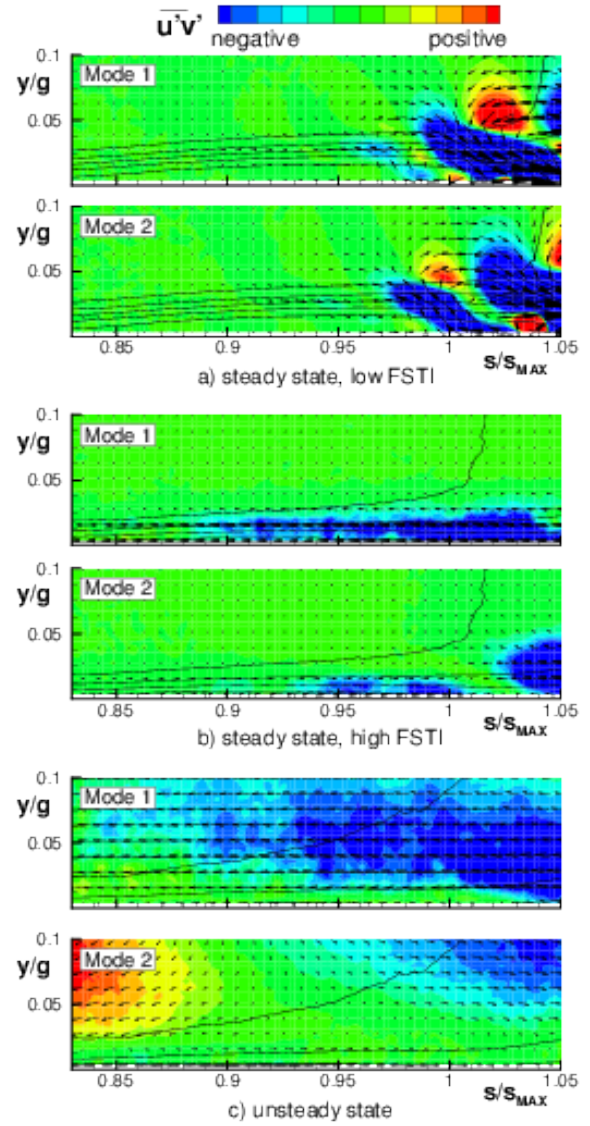


Figure 7: Vectorial representation of the POD modes and $u'v'$ contributions of each mode. Iso-contour lines of \bar{u}/U_0 are superimposed on the plots.

nent ϕ_u and the vectorial representation which is constituted by the components ϕ_u, ϕ_v of each POD mode. It is worth noting that the POD modes shown in these figures have been normalized (the POD modes are orthonormal), thus the vector length of the different modes does not provide a direct comparison between their contribution to the time-mean Reynolds shear stress. The contribution of each POD mode to the whole time-mean $u'v'$ is provided by the color maps of Figure (7), where blue and red contours represent negative and positive contributions, respectively. Differently to the vector length, these distributions preserve the energy information contained within the eigenvalue. The iso-lines of the time-mean streamwise velocity as depicted in Figure (3) are superimposed to both figures. Data in Figures (6) and (7) can be considered as the main contributions to the whole TKE and Reynolds shear stress driving the transition process for the different cases.

The distributions of the 1^{st} and 2^{nd} POD mode of the steady case with low FSTI (Figure (6)a) appear very similar. The first mode starts to assume values slightly larger than zero within the separated shear layer only behind $s/s_{MAX} = 0.89$. Similarly, the second one shows value larger than zero at $s/s_{MAX} = 0.92$. The intensity of

the POD modes reported in the picture increases downstream, showing their maximum values downstream of the blade trailing. This indicates a vortex train which is growing in intensity in the flow direction also behind the blade surface. The vectorial representation of the first POD mode shows a small clockwise rotating vortex at $0.98 < s/s_{MAX} < 1.0$ and a larger one, counter-clockwise rotating, downstream of the trailing edge. The second mode depicts a clockwise rotating vortex between the previous ones for mode 1. Hence, the spatial shift of the two modes correspond to a shift of $1/4$ of the wavelength, which is typical of a vortex shedding phenomenon (e.g., [20, 21, 19]). Furthermore, the POD modes clearly indicate where the shedding begins. The first POD mode shows a local maximum in the shear layer for $0.89 < s/s_{MAX} < 0.92$. The second POD mode shows a local maximum for $0.92 < s/s_{MAX} < 0.95$. These positions are located just upstream of the bubble maximum displacement position, where the growth rate of the oscillations in the Kelvin-Helmholtz frequency range is expected to reach saturation, as shown in [5] and in [22].

Results concerning the steady case with high FSTI show a completely different behaviour. The first mode identifies a region of velocity vectors pointing upstream (negative streamwise velocity) within the boundary layer. As discussed in Lengani and Simoni [11], this distribution can be attributed to unsteady phenomena characterized by streamwise wavelength longer than the extension of the investigated area. This result gives the evidence for the occurrence of elongated structures in the streamwise direction, as it can be also observed by the second POD mode that clearly highlights an high speed streak attached to the wall. These elongated structures drive the by-pass like transition process at high FSTI level. Furthermore, the first two modes do not identify the presence of vortical structures embedded within the flow. In Lengani and Simoni [11], it has been shown that vortical structures, associated with the stochastic breakdown of streaks, are captured just by higher order POD modes behind $s/s_{MAX} = 0.87$.

The POD modes of the unsteady case (Figure (6)c) depict a different scenario. In this case, the two POD modes isolate velocity fluctuations outside of the boundary layer. Particularly, the first POD mode shows vectors pointing upstream in a large portion of the investigated area, but in the close to the wall region. The second POD mode shows vectors pointing towards the wall. According to previous publications, these two modes identify the perturbation to the flow field due to the negative jet induced by the passing wakes [23]. In fact, the wakes convected through the blade passage induce a counter-clockwise rotating vortex at its leading boundaries and a clockwise rotating one at the trailing boundary. Clearly, in the unsteady case, these perturbations represent the largest deterministic structures, that are well captured and isolated by the most energetic POD mode. However, an high speed streak can be again observed close to the wall. It is due to the turbulence carried by wakes that excites an unsteady by-pass like transition process, as traced by higher order POD modes (refer to [23] for further details).

For completeness, Figure (7) shows the contribution of the POD modes to the time-mean Reynolds shear stress. The steady case with low FSTI (on top of the figure) shows flow regions with negative values of the term $\overline{u'v'}^{(i)}$, clearly related to the vortical structures shed by the separation bubble previously observed. Indeed, Reynolds shear stress appears only behind the maximum displacement position where the vectorial representation

of POD modes highlights the occurrence of large scale vortical structures. It has to be mentioned that the sum of the shear stress captured by the first two modes approximate almost entirely the whole time-mean shear stress. This makes further evident that, in this particular case with low FSTI, the vortical structures shed by the laminar separation bubble are the main responsible for the turbulent activity into the flow.

On the contrary, for the two other cases, the shear stress related to the first two modes is a rough approximation of the overall shear stress. For the steady case at high FSTI, the contribution of the first two modes to the Reynolds shear stress is confined in the boundary layer region behind $s/s_{max} > 0.87$, where transition starts as a consequence of breakdown of streaks, as well described in [11]. In this case the maximum values of Reynolds shear stress can be observed very close to the wall. In the unsteady case, the contribution to the Reynolds shear stress of the first POD mode is observed in the outer region of the boundary layer. This contributes to the generation and production of turbulent activity in the potential flow region during migration of the unsteady wake across the channel, as observed in [24]. The second POD mode does not sensibly affect the boundary layer, and consequently does not contribute to the Reynolds shear stress in the close to the wall region. In this case the contribution to the whole Reynolds shear stress due to the first and second modes mainly describes the dynamics due to the wake advection across the blade passage, instead of the effects of wake on the periodic transition process of the suction side boundary layer that is captured by higher order modes (not shown in the paper, see [23] for further details).

4 Conclusions

PIV has been employed to investigate the different transition processes that occur on the suction side boundary layer of a LPT blade under different levels of inlet turbulence intensity with and without passing wake. Time mean results, root mean square of the velocity fluctuations and the proper orthogonal decomposition of the PIV data have been analyzed to describe the different dynamics developing for the different cases.

The boundary layer in the steady case with low FSTI separates. The velocity fluctuations suggest that the turbulent activity is caused by the vortices shed behind the bubble maximum displacement. This is made clear by the first two POD modes that show vortical structures downstream of that position. In the steady case with high FSTI the transition process is different and can be associated to the by-pass type. Velocity fluctuations and Reynolds shear stress grow within the boundary layer and are caused, according to the POD results, by structures elongated in the streamwise direction, also known as boundary layer streaks. The transition of the boundary layer in the unsteady case is instead ruled by the passing wakes. Unsteady velocity fluctuations occur even outside of the boundary layer. These are caused by the perturbation to the flow field induced by the passing wakes as captured by the first, most energetic POD modes.

Results reported in the present overview paper clearly highlight the capability of POD in capturing the main dynamics responsible for both TKE and Reynolds shear stress into the flow during the transition process, thus providing new light in the applicability of this technique for transition modeling once systematically applied in

the future to a large amount of data obtained (both with FR-PIV or LES and DNS) for different flow and geometrical parameters characterizing the real operation of LPT blades.

References

- [1] R. E. Mayle, "The role of laminar-turbulent transition in gas turbine engines," *ASME J. of Turbomach.*, vol. 113, pp. 509–537, 1991.
- [2] R. Hain, C. J. Kähler, and R. Radespiel, "Dynamics of laminar separation bubbles at low-Reynolds-number aerofoils," *J. Fluid Mech.*, vol. 630, pp. 129–153, 2009.
- [3] Z. Yang and P. R. Voke, "Large-eddy simulation of boundary-layer separation and transition at a change of surface curvature," *J. Fluid Mech.*, vol. 439, pp. 305–333, 2001.
- [4] O. Marxen, M. Lang, U. Rist, and S. Wagner, "A combined experimental/numerical study of unsteady phenomena in a laminar separation bubble," *Flow Turbul. and Combust.*, vol. 71, pp. 133–146, 2003.
- [5] D. Simoni, M. Ubaldi, P. Zunino, D. Lengani, and F. Bertini, "An experimental investigation of the separated-flow transition under high-lift turbine blade pressure gradients," *Flow Turbul. and Combust.*, vol. 88, pp. 45–62, 2012.
- [6] R. G. Jacobs and P. A. Durbin, "Simulations of bypass transition," *J. Fluid Mech.*, vol. 428, pp. 185–212, 2001.
- [7] L. Brandt, F. Schlatter, and D. S. Henningson, "Transition in boundary layers subject to free-stream turbulence," *J. Fluid Mech.*, vol. 517, pp. 167–198, 2004.
- [8] M. Matsubara and P. H. Alfredsson, "Disturbance growth in boundary layers subjected to free-stream turbulence," *J. Fluid Mech.*, vol. 430, pp. 149–168, 2001.
- [9] S. Lardeau, M. Leschziner, and T. Zaki, "Large eddy simulation of transitional separated flow over a flat plate and a compressor blade," *Flow Turbul. and Combust.*, vol. 88, pp. 919–944, 2012.
- [10] R. J. Adrian, "Hairpin vortex organization in wall turbulence," *Phys. Fluids*, vol. 19, pp. 041301–1–16, 2007.
- [11] D. Lengani and D. Simoni, "Recognition of coherent structures in the boundary layer of a low-pressure-turbine blade for different free-stream turbulence intensity levels," *Int. J. Heat Fluid Flow*, vol. 54, pp. 1–13, 2015.
- [12] V. Nagabhushana Rao, P. G. Tucker, R. J. Jefferson-Loveday, and J. D. Coull, "Large eddy simulations in low-pressure turbines: Effect of wakes at elevated free-stream turbulence," *Int. J. Heat and Fluid Flow*, vol. 43, pp. 85–95, 2013.
- [13] S. Sarkar and P. Voke, "Large-eddy simulation of unsteady surface pressure over a low-pressure turbine blade due to interactions of passing wakes and inflexional boundary layer," *ASME J. of Turbomach.*, vol. 128, pp. 221–231, 2006.
- [14] D. Simoni, M. Ubaldi, and P. Zunino, "Experimental investigation of the interaction between incoming wakes and instability mechanisms in a laminar separation bubble," *Exp. Therm. Fluid Sci.*, vol. 50, pp. 54–60, 2013.
- [15] J. L. Lumley, "The structure of inhomogeneous turbulent flows," *A.M. Yaglom, V.I. Tatarski (Eds.), Atmospheric Turbulence and Wave Propagation*, pp. 166–178, 1967.
- [16] L. Sirovich, "Turbulence and the dynamics of coherent structures. part I-III," *Q Appl Math*, vol. 45, pp. 561–590, 1987.
- [17] R. P. E. and B. D. H., "The influence of a turbulent free-stream on zero-pressure gradient transitional boundary layer development," *Numerical simulation of unsteady flows and Transition to Turbulence*, vol. CUP, pp. 319–347, 1991.
- [18] S. Kubacki, K. Lodefier, R. Zarzycki, W. Elsner, and E. Dick, "Further development of a dynamic intermittency model for wake-induced transition," *Flow Turbul. and Combust.*, vol. 83, pp. 539–568, 2009.
- [19] D. Lengani, D. Simoni, M. Ubaldi, and P. Zunino, "POD analysis of the unsteady behavior of a laminar separation bubble," *Exp. Therm. Fluid Sci.*, vol. 58, pp. 70–79, 2014.
- [20] D. Wee, T. Yi, A. Annaswamy, and A. F. Ghoniem, "Self-sustained oscillations and vortex shedding in backward-facing step flows: Simulation and linear instability analysis," *Phys. Fluids*, vol. 16, pp. 3361–3373, 2004.
- [21] M. Ben Chiekh, M. Michard, M. S. Guellouz, and J. C. Béra, "POD analysis of momentumless trailing edge wake using synthetic jet actuation," *Exp. Therm. Fluid Sci.*, vol. 46, pp. 89–102, 2013.
- [22] S. Burgmann and W. Schröder, "Investigation of the vortex induced unsteadiness of a separation bubble via time-resolved and scanning PIV measurements," *Exp. Fluids*, vol. 45, pp. 675–691, 2008.
- [23] M. Berrino, D. Lengani, D. Simoni, M. Ubaldi, P. Zunino, and F. Bertini, "Dynamics and turbulence characteristic of wake-boundary layer interaction in a low pressure turbine blade," in *Proceedings of ASME Turbo Expo 2015, June 15-1917, Montreal, Canada, ASME Paper No. GT-2015-42626*, 2015.
- [24] R. D. Stieger and H. P. Hodson, "The unsteady development of a turbulent wake through a downstream low-pressure turbine blade passage," *ASME J. of Turbomach.*, vol. 127, pp. 388–394, 2005.

VORTICAL STRUCTURES AND TRANSITION ON ROTATING CONES, SWEEPED CYLINDERS AND TURBOMACHINERY BLADES

J. P. Gostelow, S. J. Garrett, A. Rona and W. A. McMullan

*Department of Engineering
University of Leicester*

Abstract

Nose cones and the blades of turbomachines have rotating components and represent very practical geometries for which the modal behaviour of vortex structures is not completely understood. These rather different physical cases are being studied. A common theme of competition between modes and vortex types, whether counter-rotating or co-rotating, emerges. The objective of ongoing work is to obtain physical confirmation, enhanced understanding and predictive capability for the vortex structures encountered in rotating machines.

1 Introduction

Stable vortex structures have been observed in a range of flows of industrial relevance, such as flows over conical aerodynamic fairings, compressor blades and turbine blades with cylindrical leading edges. The persistence of the vortical structures, over a defined duty or flight envelope represents a common theme among these applications.

Investigations of experimental results over the envelope of geometrical and flow parameters have guided the development of predictive methods for these structures, based on asymptotic perturbation methods of inviscid baseline flow models. Examples of flows generating vortical structures indicate a possible common driver, involving stationary streamwise vorticity. This encourages the development of the current models to give a generalised representation for this class of flows.

2 Surface Flows over Rotating Cones

Evidence for the existence of a hitherto unidentified instability mode in boundary-layer flows over rotating cones exists in the literature. This new mode is in addition to the crossflow (type I) and streamline curvature (type II) modes that are already known to exist [1] on rotating cones, disks and spheres.

Evidence set 1: experimental observations.

The visualisation studies by Kobayashi and co-workers [2, 3] of rotating cones with slender half-angles show the existence of pairs of counter-rotating Görtler-type vortices prior to the first appearance of turbulence. However, as the half-angle ψ is increased beyond 40° , the visualizations clearly show that these vortices change to co-rotating vortices as are usually reported on rotating disks and spheres. One might suppose that the counter-rotating vortices are expected

to arise from a dynamic instability induced by the centrifugal force of the flow field, and are in contrast to the co-rotating vortices, attributed to an underlying crossflow instability.

Evidence set 2: experimental measurements of the onset of turbulence.

Further evidence is obtained by considering experimental measurements for the onset of turbulence by [3] and Nickels & Bertényi, University of Cambridge (personal communication, 2007) compared to the onset of local absolute instability predicted by Garrett & Peake [4]. Although the exact role of local absolute instability in transition over the rotating disk is less clear than originally proposed by Lingwood [5,6], see [7] for example, the theoretical onset of local absolute instability is extremely close to numerous consistent measurements of the onset of turbulence over the rotating disk and this provides a useful basis for comparison. Garrett & Peake demonstrate that the critical local Reynolds number for local absolute instability over rotating cones is independent of half-angle, with $R_X \approx 2.5 \times 10^5$.

Figure 1 shows the comparison with experimental measurements for the onset of turbulence reported by [3]. For cones with $\psi > 60^\circ$, we see that transition occurs at a local Reynolds number independent of the half-angle and reasonably close to the predicted onset of local absolute instability. This close agreement suggests that local absolute instability may well be involved in the transition over broad rotating cones, consistent with the rotating-disk flow. For more slender cones, the measured critical Reynolds and occur in advance of the predicted onset of local absolute instability. It should be noted that the precise definition of turbulent flow is somewhat subjective in experimental terms and Kobayashi & Izumi's measurements are subject to some flexibility. This is clearly demonstrated by comparing their measurements for half-angles close to 90° with Lingwood's measurement on a rotating disk [6] (the horizontal dashed line at 90°). Figure 2 shows Nickels & Bertényi's measurements for the onset of turbulence over three cones, each with distinct half-angle, at different rotation rates. We see that the measured critical Reynolds number over the broadest cone ($\psi = 60^\circ$) is in good agreement with the predicted onset of local absolute instability and is independent of rotation rate (which suggests that the dashed line in Fig. 1 can be extended to at least this half-angle). However, the onset of turbulence over the slender cones with $\psi = 30^\circ$ and $\psi = 15^\circ$ is again well in advance of the predicted onset of local absolute instability and dependent on the rotation rate. Furthermore, they reported different behaviour in the turbulent intensity through transition in the case of the most slender cone.

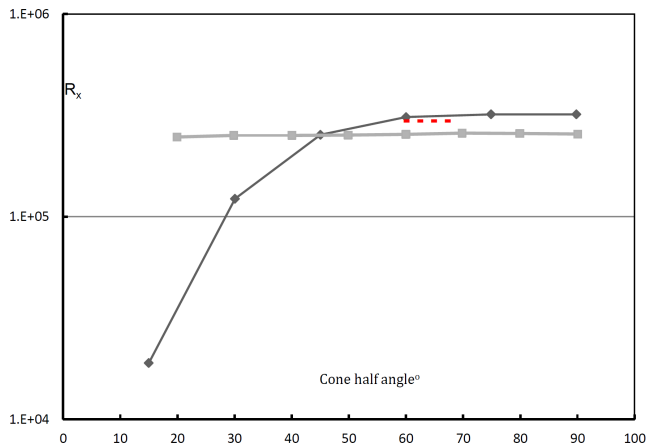


Figure 1: Critical R_X for the Onset of Local Absolute Instability [4] and Measured Transitional Values [3]

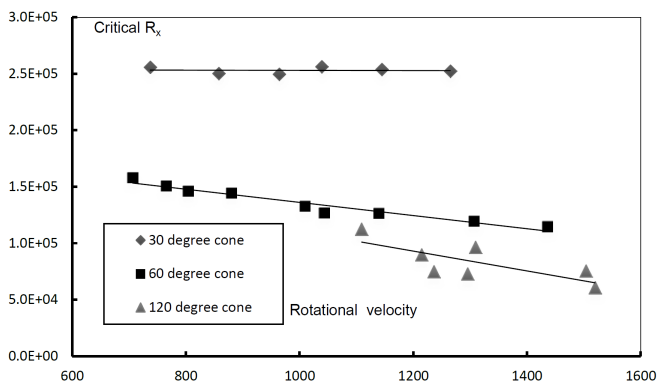


Figure 2: Experimental Data Due to Nickels & Bertényi for the Onset of Turbulence

Evidence set 3: analytical predictions of convective instability.

Garrett et al. [1] present mathematical studies of the rotating-cone boundary layers using a formulation consistent with other rotating-disk studies ([6], for example) and demonstrate that convective modes of type I and II exist for all ψ . The onset of convective instability is then associated with the onset of the spiral vortices and the critical Reynolds numbers and other measurable quantities of the spiral vortices (number, angle of orientation) compare well with experimental observations of [3] for $\psi \geq 40^\circ$. However, an increasing discrepancy is found for $\psi < 40^\circ$. This is clearly seen in Fig. 3, where the theoretical predictions of the orientation angle for vortices arising from the type I mode are compared with the experimental observations at each half-angle. Such comparisons suggest that the vortices found on slender cones cannot be attributed to the type I and II modes. (Note that the type II predictions are of much higher wave angles.)

The behaviour of the type I and II modes was further elaborated by Garrett [8] who extended the numerical results of [1] to consider the amplification rates of the modes through the convectively-unstable region as a function of half-angle. He found that the amplification rates of both mode types reduce with decreased half-angle. This finding is consistent with the hypothesis of a centrifugal mode that dominates at slender half-angles.

These three distinct sets of evidence clearly suggest an instability mode arising from centrifugal effects that exists in addition to the three existing modes. It exists in

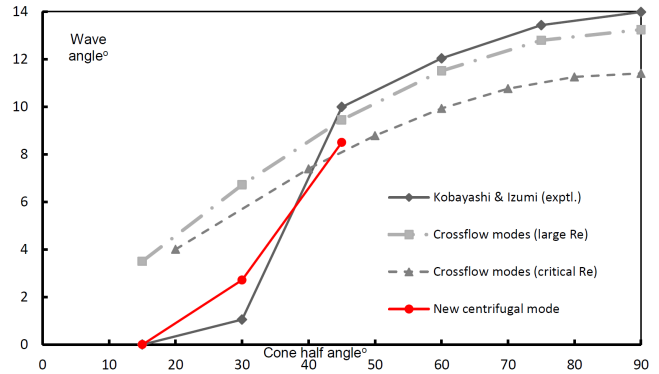


Figure 3: Comparison between Experimental Observations of Vortex Orientation Angle [3] against Type I Predictions [1] and Centrifugal Predictions

the flow over rotating cones of any half-angle, but with a relative in the well-known type I and II modes. We envisage all dominance that depends on the particular half-angle. It is therefore likely that a critical half-angle exists for the switch from a predominantly centrifugal instability (manifesting as counter-rotating vortices) to the cross-flow instability (manifesting as co-rotating vortices) as the half-angle is increased. Although experiments have only been conducted at a small number of distinct half-angles, the evidence suggests this critical half-angle to be around 40° . From an engineering perspective, this means that the transition mechanisms at work over rotating propeller and fan nose cones are distinct from the mechanisms over sharp spinning missiles, for example, and warrants further study.

An analytical study into the hypothesized centrifugal mode is ongoing and we have found that a fundamentally different approach is required to existing broad-cone studies in order to make progress. In particular, the centrifugal analysis requires greater attention to small-scale effects (at a scale comparable to the boundary-layer thickness) in all directions. A preliminary asymptotic analysis was completed, based on the assumptions of short wavelength and high spin rates, that clearly shows the existence of the centrifugal mode. The analysis is complicated and the reader is referred to [9-11] for full details. The preliminary results of a complementary numerical analysis of the same governing equations can be seen in Fig 3. For slender cones the numerical predictions of the centrifugal mode clearly show better alignment with experiments.

3 Swept Cylinders and Turbomachinery Blading

Suction surface flow visualization on turbine blades at subsonic and transonic speeds showed robust streamwise streaks on a lengthy time-average basis [12] (Fig. 4). The flow on the suction surface, under the influence of a strong favourable pressure gradient, was initially laminar but further downstream, laminar separation and transition to turbulence were encountered. The turbulent layer then persisted to the trailing edge and the streaks were unaffected by the boundary layer state. Similar behavior was observed by Halstead [13], who had surface film confirmation of the boundary layer state throughout. The streamwise vortex structures, whilst not particularly strong, are persistent and would seem to exert a stabilizing influence on the flow. Observations of streaks on

turbine blades and unswept cylinders were to provide a firm basis for referencing the influence of sweep.

The lateral spacing between streaks on convex surfaces was predicted by Kestin and Wood [14]. That work used an inviscid flow model to predict the spanwise wavelength (λ) of the streamwise vortices, normalised by the cylinder diameter (D) for different Reynolds number and free stream turbulence levels (Tu) at zero sweep. The resulting prediction is given by Eq. (1):

$$\lambda = 1.79\pi D/Re^{0.5} \quad (1)$$

A broad agreement is found between the predicted and measured λ/D from differing test facilities. Streaks on turbine blades and unswept cylinders provided a firm basis for referencing the influence of sweep. Low and high speed experiments gave excellent agreement with theory [15].

The normal flow past a circular cylinder is a canonical case [16] and testing was undertaken at high speeds on a $37.3mm$ diameter cylinder and at low speeds on a $152mm$ diameter cylinder. The lateral spacing between streaks on cylinders had been predicted by Kestin and Wood [14] and the present tests gave excellent agreement with their theory. Their work on unswept circular cylinders provides a good benchmark for understanding and predicting sweep effects on cylinders and turbomachinery blading. In earlier work on a normal cylinder, Kestin and Wood [17] published two-point hot wire measurements at a 60° azimuth from the leading edge stagnation line on the circular cylinder. The observed periodicity demonstrated that flow structures were present away from the surface and were compatible with the observed surface streaks.

Most of the available information on fine structures has come from surface flow visualization. Work is now in progress on hot wire measurements away from the surface. The aim is to demonstrate the relationship between the structures and the surface traces. Insight into the streamwise structures that print the surface traces is sought by hot-wire measurements at a Reynolds number of 150,000 on an unswept circular cylinder.

The wind tunnel centreline velocity is measured by a combined head Pitot tube placed below the cylinder and three diameters upstream of its leading edge.

Two constant temperature TSI anemometers power the hot-wire probes with a 1.8 over-heat on their balanced resistance. The output is sampled at $2kHz$ by LabView through a National Instruments acquisition card. Averages and standard deviations from 800 samples per position, repeated 30 times, are recorded. Each hot wire is calibrated using a DISA Type 55D41 with a TT320S digital pressure transducer. Two Dantec P15 single hot wires are located $1mm$ above the windward cylinder surface, at 60° azimuth from the leading edge stagnation line. The probe wires are parallel to the unswept cylinder axis. The ratio of the velocity from the moving hot wire to the fixed hot wire velocity shows significant scatter with high velocity ratio clusters at $2mm$ intervals. This ratio compensates for wind tunnel velocity drift effects. Figure 5 shows as a continuous line with circles the velocity trace from the traversing hot wire normalized by the velocity synchronously recorded by the fixed hot wire.

The dotted lines show the t-distribution 95% confidence interval band of this ratio from the hot wire standard deviation records. These hot wire measurements indicate that, within the limits of the instrumentation, a spanwise velocity distribution pattern with a spanwise wavelength of $2mm$ is present. This compares with



Figure 4: Suction Surface Flow Visualisation between 80% and 95% Axial Chord of NRC Turbine Blade at a Discharge Mach Number of 1.16

a flow visualization deduced wavelength in the range $2.14mm < \lambda < 2.31mm$ and with $\lambda = 2.2mm$ from Eq. (1). These results appear to support the presence of near-surface streamwise vorticity over the surface.

One outcome of these investigations is to establish that organized streamwise vorticity may occur more frequently on convex surfaces, such as turbine blade suction surfaces, than was previously appreciated. Investigations and predictions of flow behaviour should be extended to encompass this possibility. These applications often also have an appreciable degree of sweep and it is appropriate to enquire how sweep affects the instabilities. Information will be provided on the changing behaviour of the spanwise velocity field as the sweep angle is increased. The streamline curvature disturbance has been found to be stationary in nature and to be resilient. The crossflow instability becomes more significant as sweep is increased. It grows aggressively and rapidly, being predominantly of a traveling nature, and has a major role to play in the transition process.

Experimental work on a circular cylinder has been undertaken over a range of sweep angles from zero to 61° , giving surface visualization results for lateral spacing and angular orientation of the vortical streaks [17]. Figure 6 demonstrates that at high-sweep angles the results are consistent with those of Poll [18] and of Takagi et al. [19]. The experiments, confirming the zero-sweep results, gave a reference for subsequent work over a wide range of sweep angles. No data had been published on streamwise and crossflow vortices in the useful sweep range of up to 50° . Testing has been undertaken over a range of sweep angles from zero to 61° , giving results for the lateral spacing and angular orientation of the streaks. At high-sweep angles, the results are consistent with those of Poll [18]. At low Reynolds numbers first order-theories for circular cylinders predict the effects of sweep quite well. The approach of Takagi et al. [19] using hot wire techniques, offers an opportunity to identify both stationary and traveling instability modes.

The introduction of sweep brings consideration of a wide range of instabilities. Crossflow instability results from the inflectional behaviour of a three-dimensional boundary layer. Streamwise and crossflow structures are present on the suction surface of swept and unswept turbine blades. Crossflow instability becomes more signif-

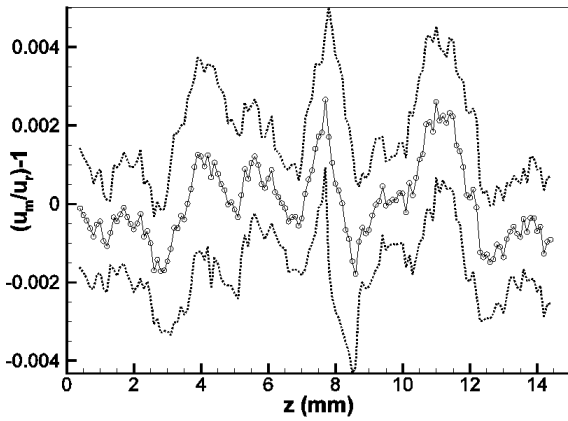


Figure 5: Measurements of Velocity Variation on a Circular Cylinder from Present Investigation

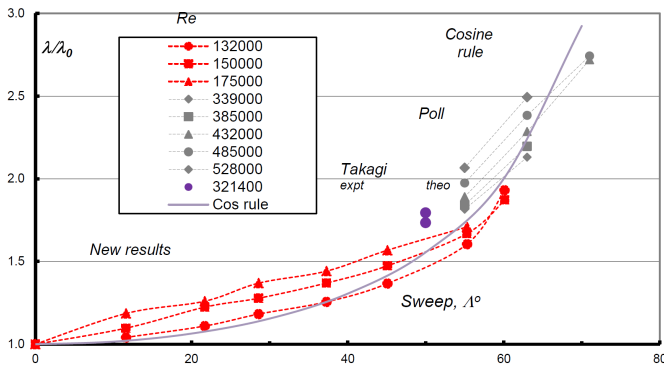


Figure 6: Normalised Lateral Streak Spacing

icant at high sweep angles. It grows aggressively and rapidly, being mainly of a travelling nature. The observed streaks could be of concern for the thermal design of turbine blades.

Care was taken to check that the wind tunnel results and the results of Poll were quoted and normalised in the same way, using the unswept results as a reference. Kestin and Wood's theoretical result is accessible and agrees closely with a regression line fit through the experimental results for unswept cylinders. Different first order theoretical approaches to generalising the Kestin and Wood's prediction of vortex spacing to non-zero sweep angle resulted in the same simple modification:

$$\lambda = 1.79\pi D / Re^{0.5} \cos(A) \quad (2)$$

This is the traditional Cosine Rule used to predict sweep effects on aerofoils. This approach had been found to be valid only for subcritical flows with a critical Reynolds number that decreased with increasing sweep [20].

It was found [17] that $\lambda/\lambda_0 = 1/\cos(A)$ is a reasonable descriptor of the measurements over the sweep angle range 0° to 60.1° . Equation (2) is used to plot the lateral vortex spacing, normalised by the unswept case, in Fig. 6. These results are self-consistent and also compatible with Poll's results, which were obtained at higher Reynolds numbers. The $\lambda/\lambda_0 = 1/\cos(A)$ theoretical curve is plotted and demonstrates reasonable agreement with both the Poll data and the new data. At 50° sweep, the theoretical and experimental points of Takagi et al. [19] involved ingenious use of theory and hot wire data to discriminate between stability modes.

Takagi discovered that, at 50° sweep, the crossflow mode dominated; this is the same mode identified by Poll and it is the lateral spacing from the crossflow mode that is plotted in Fig. 6. Takagi also examined the mode caused by streamline curvature from the upstream free stream. This appears to be mostly a result of the local concave streamline curvature in the flow region delimited by the mean stagnation streamline to the cylinder front stagnation point and the windward surface of the cylinder. This local concave streamline curvature moderates the stabilising effect of the cylinder's convex surface. At these low Reynolds numbers, Takagi found that the streamline curvature mode persisted much longer than the crossflow mode. Takagi's results are broadly consistent with our results and those of Poll.

A good summary of the difference between the two modes is given by Tokugawa et al. [21]: "Detailed observations, however, show that the crossflow mode decays with the distance from the source much faster than the streamline curvature mode and allows the latter to be dominant in a region further downstream." Essentially, the crossflow instability may have a major role to play in the transition process but it is the streamline curvature mode that is still present, and seemingly unchanged, when the boundary layer becomes turbulent.

Compressor and turbine blades may exhibit extremes of surface curvature, both convex and concave, and of pressure gradient, both favourable and adverse. Leading edge bluntness, temperature, Reynolds number and Mach number are all quite challenging. As a consequence, turbine blades are susceptible to the different modes and it should not have come as such a surprise that these instability modes exist. Given their potential role in boundary layer transition and its modeling, in heat transfer and in blade sweep, it seems important to be fully aware of the modes and their incorporation into the blade design process. The observed streaks of the various modes, both stationary and traveling, could be of particular relevance for the thermal design of turbine blades. It is hoped to give designers confidence about the flow regimes they might anticipate for a given sweep angle and particularly of when and how the vigorous crossflow instability mode is likely to be encountered.

4 Conclusions

A review of existing literature concerning boundary-layer transition over rotating cones presents clear evidence of an alternative instability mode. Observations report that this mode leads to counter-rotating vortex pairs, consistent with occurrences of centrifugal instabilities, and is in contrast to co-rotating vortices present over rotating disks that arise from crossflow effects. It is suggested that this mode competes with the crossflow mode but is dominant only over slender cones, where $\psi < 40^\circ$. Analytical progress has been made that confirms theoretically the existence of the centrifugal mode and preliminary predictions are aligned with experimental measurements over slender cones.

Low-speed and high-speed tests were performed on $152mm$ and $37.3mm$ diameter normal cylinders respectively. Experimental work confirmed the suitability of the zero-sweep Kestin and Wood theory as a basis for predicting streamwise streaks and vortical structures on normal cylinders. Although the Kestin and Wood work is related to unswept circular cylinders, it also provides an excellent starting point from which to obtain a predictive model that includes sweep effects.

This work has shown that organized and systemic fine-scale streamwise vorticity may occur more frequently on convex surfaces than hitherto appreciated. The conventional view of purely two-dimensional laminar boundary layers following blunt leading edges is not realistic. Such boundary layers need to be treated three-dimensionally, particularly when sweep is present. The vortical structures are counter-rotating for normal cylinders and co-rotating under high sweep conditions. Crossflow instabilities may have a major role to play in the transition process but the streamline curvature mode is still present, and seemingly unchanged, when the boundary layer becomes turbulent. On the suction surface of turbine blades the lateral spacing between vortical structures remains virtually constant and does not scale with boundary layer parameters.

A common theme of competition between modes and vortex types, whether counter-rotating or co-rotating, emerges. The objective of ongoing work is to obtain physical confirmation, enhanced understanding and predictive capability for the vortex structures encountered in rotating machines.

Prediction of these modes requires a sufficiently fine spanwise spacing for the streamwise structures to be resolved. Application of computational methods to these problems is likely to be expensive. A combined approach of analysis, computation and experiment is indicated. Streaks observed by surface flow visualization do have aerodynamic significance; they are not mere artefacts of the visualization medium.

Acknowledgment

Flow visualization by Dr. Ali Mahallati at the National Research Council of Canada (NRC) was appreciated as was the use of the NRC Trisonic Wind Tunnel by Dr. Jon Ackerman. Excellent experimental work by Dr. Myriam De Saint-Jean was supported by an Erasmus internship.

References

- [1] Garrett, S. J., Hussain, Z., & Stephen, S. O., 2009 "The crossflow instability of the boundary layer on a rotating cone," *Journal of Fluid Mechanics*, 622:209-232.
- [2] Kobayashi, R., Kohama, Y. & Kurosawa, M. 1983 "Boundary-layer transition on a rotating cone in axial flow," *Journal of Fluid Mechanics*, 127:341-352.
- [3] Kobayashi, R. & Izumi, H. 1983 "Boundary-layer transition on a rotating cone in still fluid," *Journal of Fluid Mechanics*, 127:353-364.
- [4] Garrett, S. J. & Peake, N. 2007 "The absolute instability of the boundary layer on a rotating cone", *European. J. Mech. B.*, 26:344-353
- [5] Lingwood, R. J. 1995 "Absolute instability of the boundary layer on a rotating disk," *Journal of Fluid Mechanics*, 299:17-33.
- [6] Lingwood, R. J. 1996 "An experimental study of absolute instability of the rotating-disk boundary-layer flow," *Journal of Fluid Mechanics*, 214:373-405.
- [7] Imayama, S., Alfredsson, P. H. & Lingwood, R. J. 2013 "An experimental study of edge effects on rotating-disk transition," *Journal of Fluid Mechanics*, 716:638-657.
- [8] Garrett, S. J. 2010 "Linear growth rates of type I & II convective modes within the rotating-cone boundary layer," *Fluid Dyn. Res.* 42 025504
- [9] Hussain, Z., Stephen, S. O. & Garrett, S. J. 2010 "The centrifugal instability of a slender rotating cone," *Journal of Algorithms and Computational Technology*, 6(1).
- [10] Hussain, Z., Garrett, S.J. & Stephen, S.O. 2014, "The centrifugal instability of the boundary-layer flow over slender rotating cones," *J. Fluid Mech.* 775, 274-293.
- [11] Hussain, Z., Garrett, S.J., Stephen, S.O. & Griffiths, P.T. 2016 "The centrifugal instability of the boundary-layer flow over a slender rotating cone in an enforced axial free-stream," *J. Fluid. Mech.*, 788,70-94.
- [12] Gostelow, J. P., Mahallati, A., Carscallen, W. E. and Rona, A., 2010, "Organized Streamwise Vorticity on Convex Surfaces with Particular Reference to Turbine Blades," 48th AIAA Aerospace Sciences Meeting, Orlando, AIAA 2010-904.
- [13] Halstead, D. E., 1989, "The Use of Surface-Mounted Hot-Film Sensors to Detect Turbine-Blade Boundary-Layer Transition and Separation", Master of Science Thesis, Iowa State University.
- [14] Kestin, J., and Wood, R. T., 1970, "On the Stability of Two-Dimensional Stagnation Flow," *Journal of Fluid Mechanics*, 44:461-479.
- [15] Gostelow, J. P., Rona, A, De Saint Jean, M., Garrett, S. J. and McMullan, W. A., 2012, "Investigation of Streamwise and Transverse Instabilities on Swept Cylinders and Implications for Turbine Blading," *ASME J. Turbomach.* 135 p. 051018
- [16] Kestin, J., and Wood, R. T., 1969, "Enhancement of Stagnation-Line Heat Transfer by Turbulence," *Progress in Heat Transfer*, 2:249.
- [17] Gostelow, J. P., Garrett, S. J., Rona, A, and McMullan, W. A., 2014, "Some Canonical Examples of Streamwise Vortex Structure for Rotating Components," *ASME FEDSM2014-21790*, Chicago.
- [18] Poll, D. I. A., 1985, "Some Observations of the Transition Process on the Windward Face of a Long Yawed Cylinder," *Journal of Fluid Mechanics*, 150:329-356.
- [19] Takagi, S., Tokugawa, N. and Itoh, N., "Characteristics of Unsteady Disturbances due to Streamline Curvature Instability in a Three-Dimensional Boundary Layer," 2006, *Proc. 6th IUTAM Symposium. on Laminar-Turbulent Transition*, R. Govindarajam, ed. Springer, 369-374.
- [20] Bursnall, W. J. and Loftin, L. K., 1951, "Experimental Investigation of the Pressure Distribution about a Yawed Circular Cylinder in the Critical Reynolds Number Range," *NACA TN-2463*.
- [21] Tokugawa, N., Takagi, S., and Itoh, N., 2005, "Experiments on Streamline-Curvature Instability in Boundary Layers on a Yawed Cylinder," *AIAA Journal*, 43, 6:115.

ADVANCEMENTS IN THE LCTM APPROACH TO MODELLING LAMINAR-TURBULENT TRANSITION

F.R. Menter and P. Smirnov

ANSYS Germany GmbH

1 Introduction

Modelling of laminar-turbulent transition in boundary layers has proven one of the most challenging tasks in CFD for many decades. While many industrial flows are in the range where significant portions of the boundary layers can be laminar, there was simply no reliable way of including these effects even to first order in general-purpose CFD codes. Laminar-turbulent transition affects many aspects of industrial flows. The main aerodynamic effect of laminar zones in the simulation of airfoils and wings is that they reduce the thickness of the downstream turbulent boundary layer relative to a fully turbulent simulation. As a result, the turbulent boundary layer is more energetic and can overcome stronger adverse pressure gradients before separating. This leads to increased performance numbers at high angles of attack. For lower angles of attack, the impact of the reduced skin friction in the laminar section of the wing reduces friction and thereby reduces overall drag. Transition also affects heat transfer predictions strongly with much reduced heat transfer in the laminar zone.

The current group has proposed a modelling concept for inclusion of transitional effects within the RANS modelling framework termed Local Correlation based Transition Modelling (LCTM) some years ago (Menter et al. 2002, Menter et al., 2006a/2006b, Langtry et al., 2009). LCTM allows the inclusion of experimental correlations with local transport equations for triggering the transition process. All physics is thereby included in the experimental correlations. This has the advantage that different transition mechanisms can be covered by a single model, as long as suitable correlations can be found and translated into the LCTM framework.

The first industrial-strength realization of the LCTM concept was the model given in Menter et al. (2006a/2006b) and Langtry and Menter (2009). Two additional transport equations have been formulated - one for the turbulence intermittency and another one for the transition onset correlation. As the turbulence intensity, Tu , entered into the experimental correlations, the $\gamma - Re_\theta$ model was not Galilean invariant. This means that the model is only applicable to simulations where the transitional walls are stationary relative to the coordinate system (or additional logic is required in the code in case of multiple moving walls in a single domain). In most practical applications, this poses no severe limitation, however, in general-purpose CFD codes, Galilean invariance is desirable. In addition, the equation for Re_θ was always considered by the current authors as fairly artificial, causing a potentially unnecessary increase in complexity of the model formulation. Attempts to avoid this equation were proposed e.g. by Coder and Maughmer (2012) who introduced a shape function-like parameter, which allowed them to include the effect of the pres-

sure gradient locally inside the boundary layer. This is an attractive simplification, which significantly reduces the model complexity. The downside is that, like the original $\gamma - Re_\theta$ model, the shape-parameter uses the local velocity relative to the wall and is therefore also not Galilean invariant. In addition, the effect of the turbulence intensity is not captured automatically by this approach, restricting the models applicability to external aerodynamic flows with known and essentially constant freestream turbulence levels. Extensions for crossflow instability for the $\gamma - Re_\theta$ model were proposed by Seyfert and Krumbein (2012), Grabe and Krumbein (2014) and Medida and Baeder (2013). A further extension for the $\gamma - Re_\theta$ model is the inclusion of wall roughness effects by Dassler et al. [16]. These extensions show the versatility of the model for inclusion of essentially any transitional effect for which correlations can be formulated.

An alternative to LCTM are 'physics-based' RANS model formulations. The most prominent of these models being the Laminar Kinetic Energy model ($k - kl$ model) by Walters and Leylek (2004) and Walters and Cokljat (2008). These approaches use a model equation for the laminar fluctuation energy which is then linked to the underlying turbulence model through source and sink terms. By this mechanism, the laminar kinetic energy can be transferred into the turbulent kinetic energy equation and initiate the transitional process. Considering that the pre-transitional phase is very different for different transition scenarios, it is at first surprising that such a formulation would be able to handle in one formulation e.g. natural and bypass transition. However, the $k - kl$ model uses numerous 'threshold functions' to trigger the transition onset which are similar in nature to the triggering functions in the $\gamma - Re_\theta$ model. For example, for the natural transition mechanism the $k - kl$ threshold function reads: $\phi_{NAT} = \max(Re_\Omega - C_{NAT}/f_{NAT} - 1, 0)$, where Re_Ω is the vorticity Reynolds number, C_{NAT} is a constant and f_{NAT} a calibration function. The triggering function in the $\gamma - Re_\theta$ model essentially reads $F_{Onset} = \max(Re_\Omega/(2.2Re_{\theta crit}) - 1, 0)$ where $Re_{\theta crit}$ is an experimental correlation. Therefore, C_{NAT}/f_{NAT} can be interpreted as an equivalent to the natural transition correlation part in the $\gamma - Re_\theta$ model. In other words, similar triggering concepts have been employed independently in different modelling frameworks, making both model families close cousins. The advantage of the $k - kl$ model over the $\gamma - Re_\theta$ model so far has been that it requires only one additional transport equation and that the formulation is Galilean invariant. On the downside, the transition $k - kl$ model is currently combined with the standard Wilcox model (1993) and inherits that models freestream dependency in the fully turbulent regime. Due to the relatively high model complexity, it is also not easily fine-tuned and adjusted to other underlying turbulence models (like e.g. one-equation models), or additional physics.

Another interesting transition model based on a single intermittency transport equation using only local variables was recently proposed by Durbin (2012) and Ge et al. (2014). The basic framework of this model is similar to the one introduced by Menter et al. (2002), but more general and with a significantly wider range of calibration. The model of Durbin (2012) and Ge et al. (2014) is geared towards bypass transition for which the authors observed that it could be modelled by relying essentially on the diffusion processes of the equations for turbulence quantities and intermittency, the mechanism being that lower freestream turbulence levels require longer running lengths than high freestream values to penetrate into the boundary layer. This mechanism seems to work surprisingly well for numerous bypass cases. The model does not involve external data correlations but empirical calibration input in the source and sink terms in the intermittency equation, where the sink term ensures a laminar boundary layer upstream of transition. Reliance on the diffusion process is likely not to be suitable for natural transition and transition through cross-flow instabilities, but a modification was introduced to predict transition in separated boundary layers.

The current group is convinced that the LCTM concept is still the most flexible method for including transitional effects into industrial CFD simulations. Due to its generic character, it allows the inclusion of essentially any transitional effect for which sufficient experimental information is available. In addition, the intermittency concept is generic with respect to the underlying turbulence model and can easily be combined with existing and new model formulations. Finally, the concept can be fine-tuned by improved and optimized transition correlations, without a need for understanding all details of the underlying model formulation.

A new member of the LCTM model family has recently been proposed (Menter et al., 2015). The goal was to avoid the transport equation for Re_θ by evaluating the correlations inside the boundary layer and not outside. This also eliminated a current deficiency of the Re_θ model, which is not Galilean invariant due to the use of the freestream turbulence intensity. The $\gamma - Re_\theta$ model is therefore only valid for walls which are stationary with respect to the coordinate system of the simulation (or would require additional software infrastructure for moving walls). Furthermore, the Re_θ model features fairly complex formulations for the experimental correlations, which were simplified in the new formulation.

The new model (Menter et al., 2015) is based on a transport equation for the turbulence intermittency, γ , and maintains the LCTM concept of explicit correlations for triggering the transition onset. The resulting model was termed γ -model. Like the $\gamma - Re_\theta$ model, it uses transition onset criteria in terms of Re_θ , but computes the latter algebraically using local variables. At that, it does not require the velocity U and maintains Galilean invariance. The γ -model has currently been combined with the SST model (Menter, 1994). It can also be used in combination with other models. The main requirement for any underlying turbulence model is however, that such models require a suitable viscous sublayer formulation, which will not interfere with the laminar and transitional flow behavior (models need to predict an earlier transition location than the transition model).

It needs to be stressed that the current calibration of the new model is covering a wide range of flows and that the model constants should be of sufficient generality for most applications. Only if consistent deviations of results for a given type of applications are observed, should

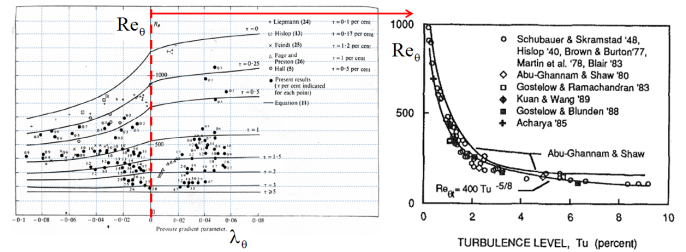


Figure 1: Correlations for transition momentum thickness Reynolds number: (left) the correlation of Abu-Ghannam and Shaw (AGS), (right) Mayle correlation

the constant and or correlations be fine-tuned. All test cases in the current work were computed with a fixed set of constants.

During the model formulation and calibration, a large number of test cases have been computed. It was not the goal to capture all cases in perfect agreement with the experimental data, as this would have lead again to a highly complex set of correlations, similar to those of the $\gamma - Re_\theta$ model. The strategy was therefore to calibrate the model carefully for self-similar flows (Falkner-Skan family) and to extend this calibration with limited complexity into non-equilibrium flows, especially flows with separation. Some differences to experimental data were accepted as being part of the modelling approach. This seems sensible, as experimental data are not fully consistent and at times in contradiction with expected behavior (correlations). The current overview discusses the basic calibration and some of the validation test cases.

The γ -model was implemented in both ANSYS CFD solvers, ANSYS CFX and ANSYS Fluent. The simulations in this work have been computed mostly with ANSYS CFX, but several cross-comparisons with an in-house boundary layer code and with ANSYS Fluent have been performed to ensure implementation consistency.

2 Model Formulation

The details of the γ -model formulation are given in Menter et al. (2015) and are not repeated here. The main challenge in correlation based models lies in the need to provide the freestream turbulence intensity Tu and a nondimensional pressure gradient to the experimental correlation. Since the model is triggered inside the boundary layer, these variables need to be supplied there. In the new model, local formulations of these quantities have been developed, thereby avoiding the need for the Re_θ transport equation. Again, details are given in Menter et al. (2015). The γ -model can be combined with any ω -equation based turbulence model, where slight re-calibration might be required when moving from one turbulence model formulation to another.

Model Calibration Empirical correlations like the ones shown in Figure 1 served as a basis for the initial model calibration. The idea is to tune the new model such that for each pair of Tu and λ_θ it transitions at a momentum thickness Reynolds number Re_θ close to that from the correlations. In particular, in case of zero steamwise pressure gradients the model should be able to match the Re_θ dependency versus Tu shown on the right chart of Figure 1. For calibration, a very large number of cases have been run with different Tu and λ_θ parameters using an in-house boundary layer code.

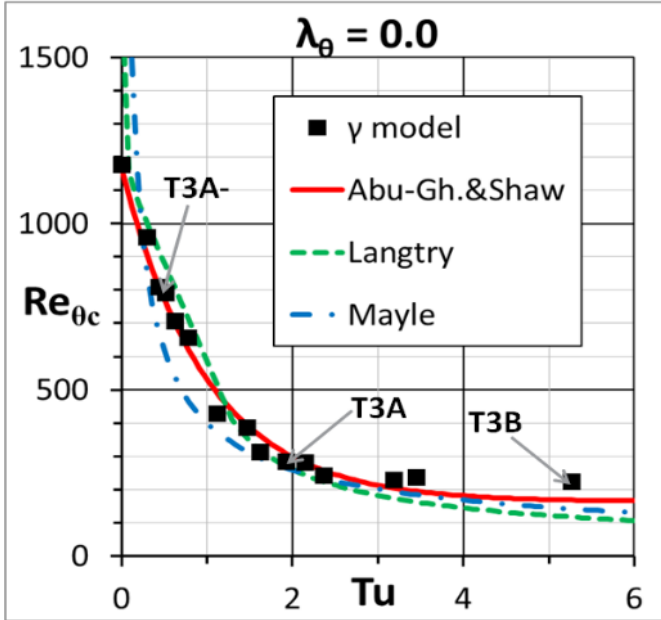


Figure 2: Results of model calibration on boundary layer flow developing on flat plate and under zero streamwise pressure gradient

Due to the low cost of the boundary layer simulations, all cases were run on excessively fine meshes ensuring grid independence. In addition, consistency checks were performed between the boundary layer and the full Navier-Stokes codes.

Results for Zero Pressure Gradient

To calibrate the model for cases with zero streamwise pressure gradient ($\lambda_\theta = 0$), eighteen combinations of inlet turbulence intensity and eddy-to-molecular viscosity ratio were selected for the test matrix. Note that the inlet values specified for eddy-to-molecular viscosity ratio mainly determine the rate at which the turbulence kinetic energy decays, whereas the values for Tu determine the transition location. For the final set of the model constants, results are shown in Figure 2. In this figure, data of the γ -transition model for each parameter combination (black symbols) are compared with three different versions of empirical correlation, namely, Abu-Ghannam and Shaw (ABS 1980), Mayle (1991) and the correlation from Langtry and Menter (2009). Transition for the γ -model location was defined based on minimal wall shear stress.

One can see that the model fits the correlations quite well. Three of the selected combinations of inlet parameters correspond to T3 cases with zero pressure gradient, namely to T3A-, T3A and T3B. Results for these three cases have corresponding labels in Figure 2.

Results for Non-Zero Pressure Gradient

When the distribution of the external boundary layer edge velocity $U_e(x)$ obeys a certain power law of x , solutions of the laminar boundary layer equations become self-similar with a parameter corresponding to a constant λ_θ . The solution of these self-similar equations is known as Falkner-Skan series of profiles. A profile from this series is defined by the parameter β which enters the formula for $U_e(x)$ in the following way:

$$U_e(x) = U_0(x - x_0)^{\frac{\beta}{2-\beta}} \quad (1)$$

Positive β correspond to favorable pressure gradients

characterized by positive while negative β stand for adverse pressure gradients with negative λ_θ . The value of $\lambda_\theta = -0.0681$ corresponds to separation onset.

Figure 3 shows the results of the γ -transition model for a series of β values which corresponds to λ_θ values as indicated on each plot. These simulations have been used as a basis for the calibration of the coefficients. In general, the selected set of constants provides a good agreement with the empirical correlations. For strong favorable pressure gradients ($\lambda_\theta = 0.0614$), the model follows the lower correlation bound given by the Mayle criteria, but this was calibrated deliberately for the sake of a compromise for the T3C5 test case. Matching the experimental data of this test case requires somewhat earlier triggering of transition in areas with favorable pressure gradient.

Re-laminarization under strong favorable pressure gradient

The last test case in this chapter is designed to investigate the ability of the transition model to predict re-laminarization. Re-laminarization should occur in a strong favorable pressure gradient when the acceleration parameters

$$K = \frac{\nu}{U^2} \frac{dU}{dx} \quad (2)$$

exceeds 3×10^{-6} . Conversely, transition should never occur until the acceleration parameter drops below 3×10^{-6} . A hypothetical test case has been proposed in order to test the ability of the new transition model to predict re-laminarization. The test case is identical to T3A up to the streamwise coordinate $x = 0.7[m]$, at which point a strong favorable pressure gradient is imposed in the boundary layer code. Figure 4 shows the distribution of the parameter K using $U(x) = \tanh(7x - 9) + 2$ as boundary layer edge velocity.

The skin friction calculated by the boundary layer code for the laminar, transitional and turbulent cases are shown also in Figure 4. It is seen that the model does in fact predict re-laminarization once the acceleration parameter exceeds 3×10^{-6} . It also predicts re-transition downstream once the strong favorable pressure gradient has subsided.

3 Model Validation

Figure 5 presents a comparison of the measured and computed skin friction coefficients for all T3 cases and the Schubauer-Klebanoff case. The results of all test cases

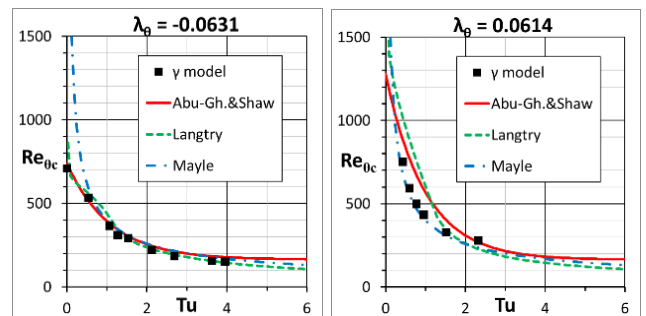


Figure 3: Critical momentum thickness Reynolds number predicted by the current model for equilibrium boundary layer flows developing on a flat plate under adverse and favorable streamwise pressure gradient conditions Comparison with established correlations

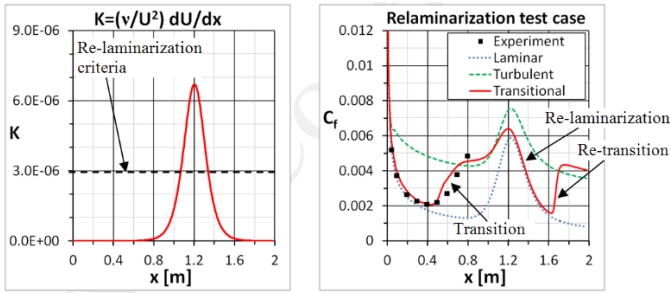


Figure 4: Re-laminarization test case: (left) acceleration parameter K and (right) skin friction coefficient

with zero pressure gradient (T3B, T3A, T3A- and the Schubauer- Klebanoff) are summarized in the upper row of Figure 5. In general, the agreement of the new model with the experimentally measured skin friction and transition locations is good. The model was able to predict transition from a Reynolds number (based on plate length and inlet velocity) of $50\,000$ all the way out to 3×10^6 as the freestream turbulence was lowered. The results of the new model are compared against those of the $\gamma - Re_\theta$ model. The new model gives a steeper transition, which is especially noticeable for the T3A- case.

Results for the cases with streamwise pressure gradient are summarized in the lower row of Figure 5. For the test case with favorable pressure gradient (T3C5), the new model results in good predictions. The $\gamma - Re_\theta$ model gives too late transition, which is apparently due to the fact that the model was tuned on higher inlet turbulence intensity for this test case. Namely, $Tu = 4\%$ was used for the T3C5 cases, while the experimental value was 3% as for all other T3C cases. Naturally, the model gives later transition when Tu is reduced back to 3% . In the present work, this decay was matched with the original Tu value from the experiment equal to 3% . For the case with transition near the suction peak (T3C2) the new model delays the transitional process and in the adverse pressure gradient zone (T3C3) it results in laminar separation, which is not the case in the experiment. The reason for this behavior was investigated by comparing the exact momentum thickness Reynolds number from the laminar boundary layer code with the critical Reynolds number from the AGS correlation (note that the γ transition model reproduces the AGS correlation fairly closely in the Falkner-Skan simulations). Figure 6 shows the AGS correlation for the T3C2 and the T3C3 test cases against the actual momentum thickness of the boundary layer. For the T3C2 case, transition starts in the experiment at around $x = 0.8 - 0.9$. At that location, the AGS correlation is much higher ($Re_{\theta_c} \approx 600$) than the actual Re_θ of the boundary layer ($Re_\theta \approx 390$). It is not clear, why the experiment starts to transition at such a low Re_θ for this case. The intersection between the AGS correlation and the boundary layer Re_θ occurs at around $x = 1.05$. The γ -model does actually start to produce intermittency at that location, but then the remaining running-length to separation is not sufficient to complete the transitional process, so that the model transitions only after separating.

The situation is similar for the T3C3 case, where the AGS correlation and the actual Re_θ do not or only barely intersecting at $x = 1.2$ and then diverge again from each other.

The $\gamma - Re_\theta$ model overcomes this problem by using modified correlations specially tuned for the T3C cases together with additional empirical calibration of the Re_θ

equation aimed at reducing the original freestream Re_θ . This is one of the reasons for the complexity of the $\gamma - Re_\theta$ model formulation and the large number of constants involved. The goal of the current formulation is to avoid this level of complexity in favor of a simpler formulation which can be more easily calibrated by the user. The quality of predictions of the T3C2 and T3C3 cases could be improved simply by adjusting the constant responsible for the sensitivity to adverse pressure gradient (Menter et al, 2015). However, such a change breaks the calibration for Falkner-Skan profiles. Application of the γ -transition model to 2D blade test cases revealed that the calibration based on Falkner-Skan profiles is preferable over the one tuned specially for T3C. Therefore, the Falkner-Skan based calibration is used for all further studies.

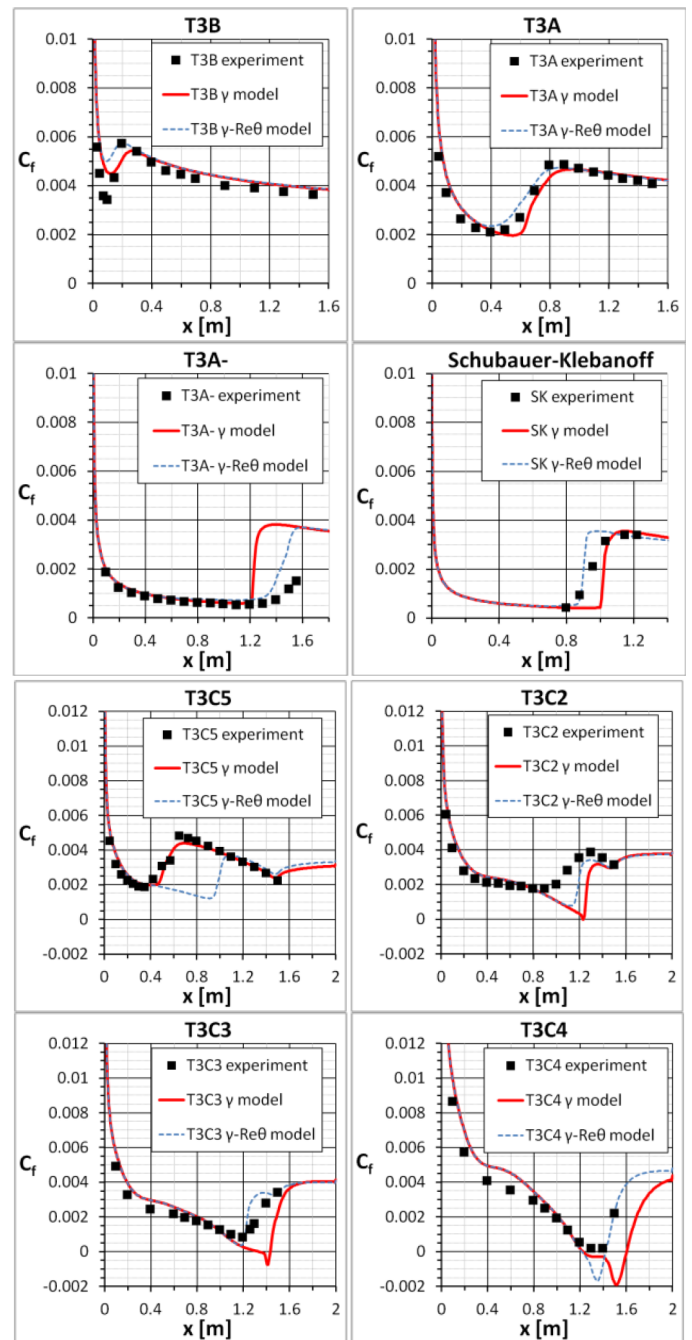


Figure 5: Skin friction coefficient for flat plate test cases: (upper row) zero pressure gradient cases; (lower row) cases with streamwise pressure gradient

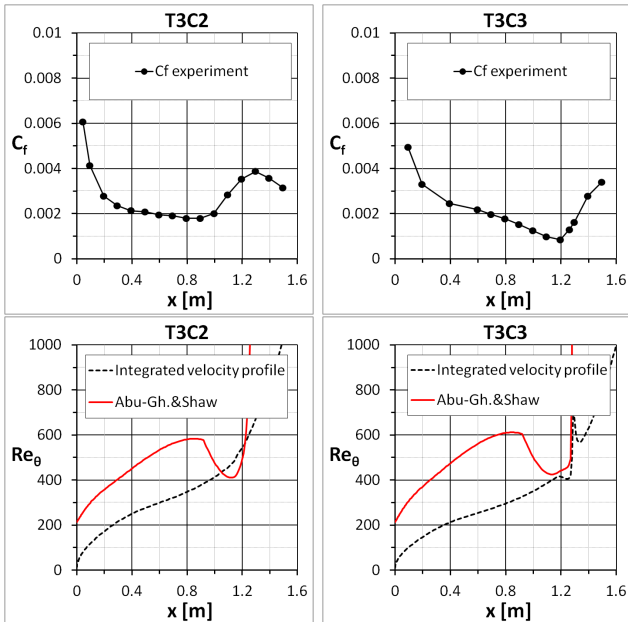


Figure 6: Skin friction coefficient for flat plate test cases: (upper row) zero pressure gradient cases; (lower row) cases with streamwise pressure gradient

It should also be noted for completeness that there are significant differences between the simulations and the experiments in the wall shear stress for the T3C cases already in the laminar region. It was not possible to trace the source of this discrepancy. Even fully laminar simulations without any turbulence maintained a significantly higher laminar wall shear stress than observed in the experiments. It is a discrepancy which puts a question mark on the data. It was attempted to modify the Re number in order to match the laminar wall shear stress. The required Re number increase for the T3C2 and T3C3 cases was about 30%. This led to a significantly improved transition location, but the change is clearly outside any conceivable measurement uncertainty. Similar discrepancies between model predictions and data have been observed by Ge et al. (2014).

4 Application Test Cases

NACA 0021 airfoil

The NACA 0021 airfoil is a 21% thick symmetrical airfoil representative for horizontal-axis wind turbine (HAWT) applications (Salwell, 2005). The experimental results were obtained in the wind tunnel at the Monash University. The airfoil profile can be seen from the computational mesh used for the present calculations (Figure 7). The grid was of a C-type with the total number of hexahedral elements 118 000.

In this study, the experimental results are compared to the numerical results obtained using the γ transition model, the $\gamma - Re_\theta$ model and the SST (fully turbulent) model. All calculations were performed assuming incompressible flow and a Reynolds number of 2.7×10^5 . The inlet turbulence level was selected so that the freestream turbulence level around the airfoil was approximately 0.6% which corresponds to the turbulence level in the experiments. The simulations were carried out for a range of angles of attack from 0° up to 28° with the increasing step of 1° . This range of angles covers the so-called deep stall regime when the flow separates from the leading

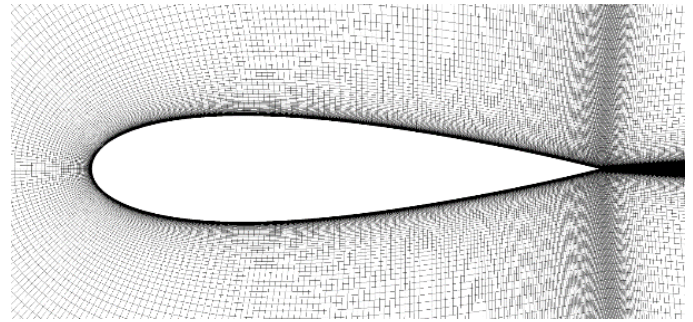


Figure 7: Skin friction coefficient for flat plate test cases: (upper row) zero pressure gradient cases; (lower row) cases with streamwise pressure gradient

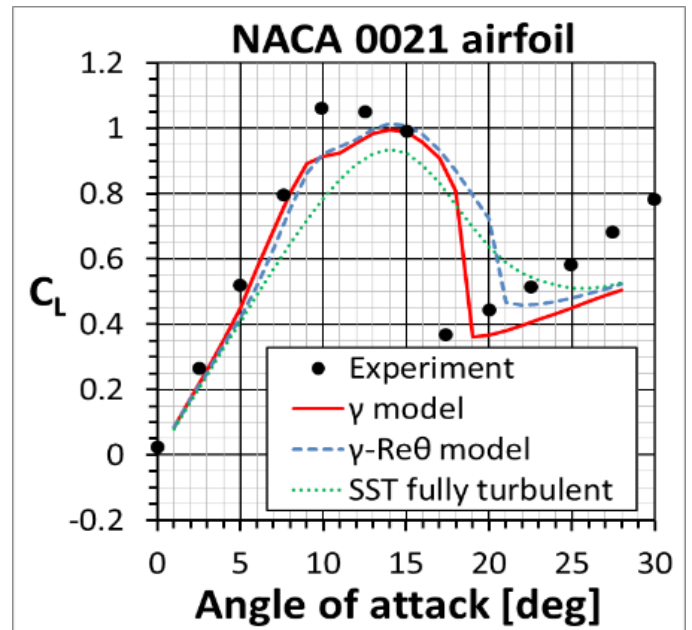


Figure 8: Lift coefficient for NACA 0021 airfoil

edge of the airfoil. The predicted C_L distribution as a function of angle of attack is shown in Figure 8.

For angles lower than the critical one (deep stall angle, 18° in the experiments), transitional simulations predict a separation bubble close to the leading edge which alters the pressure distribution in this region and gives higher C_L values compared to the fully turbulent simulations. The positive result of capturing this effect is especially visible for the medium angles between 5° and 15° . Airfoil stall occurs when the trailing edge turbulent separation meets the back-end of the laminar separation bubble. This critical angle is overestimated by the $\gamma - Re_\theta$ model, while the result of the γ -model is quite close to the experiment, due to a slightly larger laminar bubble predicted by the γ -model.

Pratt and Whitney Pak-B low pressure turbine cascade

Huang et al. (2003) conducted experiments on the Pak-B blade cascade for a range of Reynolds numbers and turbulence intensities. The experiments were performed at the design incidence angle for Reynolds numbers of 50 000, 75 000, and 100 000 based on inlet velocity and axial chord length, with turbulence intensities of 0.08%, 2.35% and 6.0% (which corresponded to values of 0.08%, 1.6%, and 2.85% at the leading edge of the blade). In

the experiments of Lake et al. (1999, 2000) the Pak-B cascade was investigated for Reynolds numbers of 43 000, 86 000, and 172 000 and freestream turbulence intensities of 1.5% and 10% (1.0% and 4.0% at the leading edge). Some of these cases were selected for the simulations in the present work. The computational grid consisted of 143 336 hexahedral elements.

Figure 9 shows the results of the simulations. In this figure, the computed pressure coefficient distributions for various Reynolds numbers and freestream turbulence intensities are compared to experimental data. The most important feature of this test case is the extent of the separation bubble on the suction side, characterized by the plateau in the pressure distribution. The size of the separation bubble is actually a complex function of the Reynolds number and the freestream turbulence value. As the Reynolds number or freestream turbulence decrease, the size of the separation and hence the pressure plateau increases.

The computations with the new transition model compare quite well with the experimental data for all of the cases considered, illustrating the ability of the model to capture the effects of Reynolds number and turbulence intensity variations on the size of a laminar separation bubble and the subsequent turbulent reattachment. It should be stressed, that the fully turbulent simulations completely miss this phenomena since the boundary layer remains attached over the entire length of the suction surface.

Significantly more cases are reported in Menter et al. (2015), including unsteady rotor-stator cases and full 3D compressor simulations.

5 Summary

An overview of the current state of the model development within the LCTM family has been provided. The new γ -transition model is part of the LCTM model family and a further development of the $\gamma - Re_{\theta}$ model. It solves only one transport equation for the turbulence intermittency, γ and avoids the need for the second Re_{θ} equation of the $\gamma - Re_{\theta}$ model. The new model has several advantages over the $\gamma - Re_{\theta}$ transition model. Firstly, it reduced the computational effort by solving only one transport equation instead of two. In addition, it avoids the dependency of $Re_{\theta c}$ equation on the velocity U . This makes the γ -transition model Galilean invariant. It can therefore be applied to surfaces which move relative to the coordinate system for which the velocity field is computed. Finally, the model formulation is simple and can be fine-tuned based on a small number of user parameters. Like the $\gamma - Re_{\theta}$ model, the γ model is based strictly on local variables. The γ model preserves the main characteristics of LCTM formulations of combining conventional transport equations with experimental correlations.

Acknowledgements

The current work has been jointly sponsored by GE Global Research and ANSYS Inc.

References

[1] Abu-Ghannam, B.J., Shaw, R. (1980): Natural Transition of Boundary Layers - The Effects of Turbulence, Pressure Gradient, and Flow History. *J. of Mech. Eng. Science*, 22(5), 213-228.

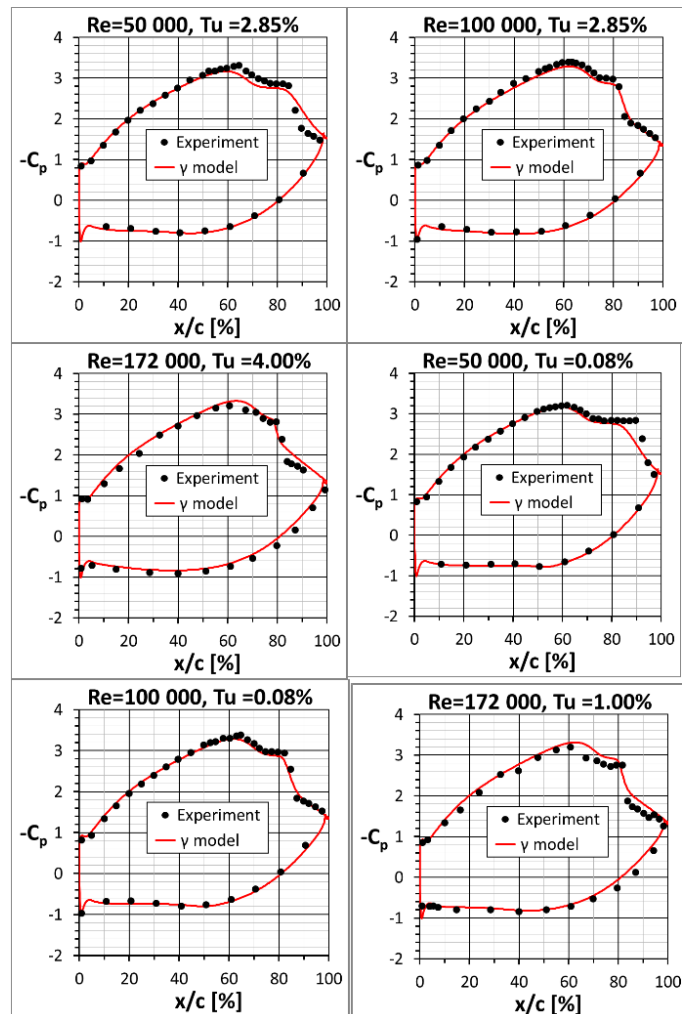


Figure 9: Blade loading for the Pak-B Low-Pressure turbine at various freestream turbulence intensities (Tu) and Reynolds numbers (Re)

- [2] Coder, J. M., Maughmer M. D. (2012): One-Equation Transition Closure for Eddy-Viscosity Turbulence Models in CFD. AIAA Paper 2012-0672.
- [3] Dassler, P., Kozulovic, D., Fiala, A. (2012): Transport Equation for Roughness Effects on Laminar-Turbulent Transition. In: Proc. Conference on Modelling Fluid Flow, CMFF'12, Budapest, Hungary.
- [4] Durbin, P.A.(2012): An intermittency model for bypass transition. *Int. J. Heat Fluid Flow* 36, 1-6.
- [5] Ge, X., Arolla, S., Durbin, P.(2014): A Bypass Transition Model Based on the Intermittency Function. *J. Flow Turbulence and Combustion*, DOI 10.1007/s10494-014-9533-9.
- [6] Grabe, C., Krumbein, A. (2014)-Prediction of Crossflow Transition. AIAA Paper 2014-1269.
- [7] Huang, J., Corke, T. C., Thomas, F. O. (2003): Plasma Actuators for Separation Control of Low Pressure Turbine Blades. AIAA Paper AIAA-2003-1027.
- [8] Lake, J. P., King, P. I., Rivir, R. B. (2000): Low Reynolds Number Loss Reduction on Turbine Blades With Dimples and V-Grooves. AIAA Paper AIAA-00-0738.

- [9] Lake, J. P., King, P. I., Rivir, R. B. (1999): Reduction of Separation Losses on a Turbine Blade With Low Reynolds Number. AIAA Paper AIAA-99-0242.
- [10] Langtry, R.B., Menter, F.R. (2009): Correlation-Based Transition Modeling for Unstructured Parallelized Computational Fluid Dynamics Codes. AIAA J. 47(12), 2984-2906.
- [11] Langtry, R.B., Likki, S.R., Suzen, Y.B., Huang, P.G., and Völker, S., (2006b), "A Correlation based Transition Model using Local Variables Part 1-Model Formulation", ASME Journal of Turbomachinery, Vol. 128, Issue 3, pp. 413 - 422.
- [12] Mayle, R.E. (1991): The Role of Laminar-Turbulent Transition in Gas Turbine Engines. ASME J. of Turbomach. 113(4), 509-537.
- [13] Medida, S., Baeder, J. (2013): A New Crossflow Transition Onset Criterion for RANS Turbulence Models. AIAA Paper 2013-3081
- [14] Menter, F.R. (1994): Two-equation eddy-viscosity turbulence models for engineering applications. AIAA J. 32(8), 269-289
- [15] Menter, F.R., Esch, T. and Kubacki, S., (2002), "Transition Modelling Based on Local Variables", 5th International Symposium on Engineering Turbulence Modelling and Measurements, Mallorca, Spain.
- [16] Menter, F. R., Langtry, R., Völker, S. (2006a), "Transition Modelling for General Purpose CFD Codes". Flow, Turbulence and Combustion, Volume 77, Numbers 1-4, Springer Netherlands
- [17] Menter, F.R., Smirnov, P., Liu, T. and Avancha R. (2015): A One-Equation Local Correlation-Based Transition Model Flow, Turbulence and Combustion, 2015, Volume 95, Issue 4, pp 583-619
- [18] Swalwell, K.E. (2005): The effect of turbulence on stall of horizontal axis wind turbines. PhD thesis, Monash University, Australia.
- [19] Seyfert, C., Krumbein, A. (2012): Correlation-Based Transition Transport Modeling for Three-dimensional Aerodynamic Configurations. AIAA Paper 2012-0448.
- [20] Walters, D.K., Lylek, J.H. (2004): A New Model for Boundary-Layer Transition Using a Single-Point Rans Approach. ASME J. of Turbomach. 126(1), 193-202
- [21] Walters, D.K., Cokljat, D. (2008): A Three-Equation Eddy-Viscosity Model for Reynolds-Averaged Navier-Stokes Simulations of Transitional Flows. J. of Fluids Eng. 130
- [22] Wilcox, D.C. (1993): Turbulence Modeling for CFD. DCW Industries, Inc., La Canada, CA,

ON THE DEVELOPMENT OF A PHENOMENOLOGICAL TRANSITION MODEL FOR TURBOMACHINERY FLOWS

V. Marciniak

German Aerospace Center (DLR) - Institute of Propulsion Technology, Cologne, Germany.

Abstract

The aim of this work is to describe the development of a new transition model for turbomachinery flows based on a phenomenological approach. The main modelling concepts obtained from the combination of experimental observations and theoretical knowledge are presented and used to form the mathematical formulation of the model. Furthermore, an overview of the numerical methods used for the implementation of the model is given. Finally, flows over an industrial high-lift low-pressure turbine cascade are computed and compared to experimental data to illustrate the capability of the new model.

1 Introduction

Boundary layer transition is well-known to have an important impact on the performance of some components of the current generation of jet engines. Unfortunately, transition consists in successive and very complex phenomena which are not yet completely understood. For this reason, it is tempting to derive models relating the occurrence of transition to well-chosen sets of flow variables. This approach relies on experimental data and the models stemming from it are denoted in the literature as correlation-based.

In the past years, numerous correlation-based models have become very popular for research and industry purposes, probably because of their user-friendliness and relative broad range of applicability. However the capability of such models are inherently limited by the scope of experiments used to derive them. This can be observed in the work of Longhitano [1], who modified the γ - Re_{Θ} model of Langtry and Menter [2] to simulate the long and open separation bubbles occurring in the T106C cascade: the investigated setup allows to reproduce the effects of bubble bursting for this cascade, but the results for other cascades are very poor.

An other family of models, based on the laminar kinetic energy concept, is reported in the literature to be able to simulate also transition successfully. Concerning specifically turbomachinery flows, the model of Pacciani et al. [3] has been designed to simulate open, long and short separation bubbles. This ability is confirmed by Marciniak [4] but it is also noted that the range of applicability of this model is restricted to low-Reynolds flows with a relatively small level of turbulence intensity. Additionally, the model does not use a fully local formulation and does not simulate bypass transition, which greatly reduces the possibilities to use it in an industrial environment.

It is then important to derive a new model using only local variables and being able to simulate the different

types of separation bubbles as well as bypass transition. Additionally, transition predictions should be possible for the whole range of flow conditions found in a turbomachine. To do so, it is chosen to derive the model accordingly to a phenomenological approach. This publication summarizes the main findings of such a work. First, the main physical ideas are presented followed by the complete formulation of the model. Then, some details concerning the implementation of the model are given and finally some computations of flows over a low-pressure turbine cascade are discussed to assess the performance of the model.

2 Derivation of the Model

2.1 Laminar Kinetic Energy

With the help of experiments and mathematical analysis, Mayle et al. [5] show that in a laminar boundary layer subjected to free-stream turbulence, low-frequency stream-wise fluctuations are present upstream of the start of bypass transition. The authors denote the energy relative to these fluctuations as laminar kinetic energy.

Moreover, the experimental data relative to the development of separation bubbles presented by Volino [6] proves also that low-frequency stream-wise fluctuations can be found prior transition onset in laminar shear layers. Therefore, the concept of laminar kinetic energy can be extended to the description of separation-induced transition. Numerous experiments demonstrate that the presence of this energy has a very limited impact on the flow. It is then chosen to neglect the direct influence of laminar kinetic energy on the flow.

Similarly to the work of Walters [7], it can be noticed that the Reynolds-averaged equations are valid for any kind of flow, e.g. laminar, transitional or turbulent. It is then possible to describe the evolution of laminar kinetic energy by a transport equation similar to a Reynolds stress equation. Obviously, since the laminar and turbulent kinetic energies are of different nature, it is expected that they obey to different physics and consequently a specific modelling must be developed.

2.2 Transition Representative Length

The use of a phenomenological approach enables to take into account the mechanisms governing the evolution of the laminar kinetic energy in the formulation of the model. A detailed literature review, found in [8], shows that a large number of phenomena can be potentially related to the production of laminar kinetic energy. Especially for shear layers, many studies consider that the Kelvin-Helmholtz instability is the principal mechanism

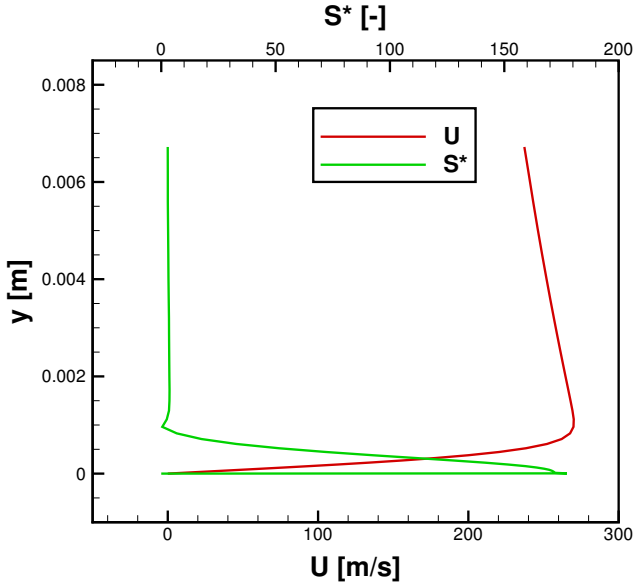


Figure 1: Stream-wise Velocity Profile of a pre-transitional boundary layer

producing laminar kinetic energy. However, the analysis of the results of Volino [9], Makiel et al.[10], Diwan et al.[11] and Winant et al.[12] lead to the conclusion that the appearance of laminar kinetic energy is linked to mechanisms similar to those involved in bypass transition. Therefore only these mechanisms are taken into account in the modelling.

Since it is assumed that only bypass mechanisms generate laminar kinetic energy, it is possible to use the results of Lardeau et al.[13] stating that for bypass transition, the production term is proportional to the square of the strain norm. In order to be dimensionally consistent, the modelled production term $P_{k_l}^*$ must be multiplied by a factor having the dimension of a viscosity. Eq. (1) details the modelling of this factor as the product of the square root of the laminar kinetic energy, k_l , and a length representative of transition l_{tr} - with C_a being a calibration constant.

$$P_{k_l}^* = C_a \sqrt{k_l} l_{tr} S^2 \quad (1)$$

The transition representative length must scale with a characteristic size of the bypass transition mechanisms. For instance, the distance between the solid surface and the height where the non-turbulent fluctuations are produced can be chosen. Using again the result of Lardeau et al. [13], it can be deduced that laminar kinetic energy is produced where relatively high values of the strain norm are present. This fact is used to design the numerical filter H_S , detailed in Eq. (2), aiming to discriminate the regions of high non-dimensionalised strain norms S^* .

$$H_S = \begin{cases} 1 & \text{if } S^* \geq C_H \\ 0 & \text{otherwise} \end{cases} \quad (2)$$

For an arbitrary chosen value of the calibration constant C_H , the action of the numerical filter H_S on the stream-wise velocity profile U of a pre-transitional boundary layer is shown in Figure (1) and Figure (2). The computation of the transition representative length is carried out by multiplying the result of the numerical filter H_S by the wall distance y as seen in Eq. (3).

$$l_{tr} = y * H_S \quad (3)$$

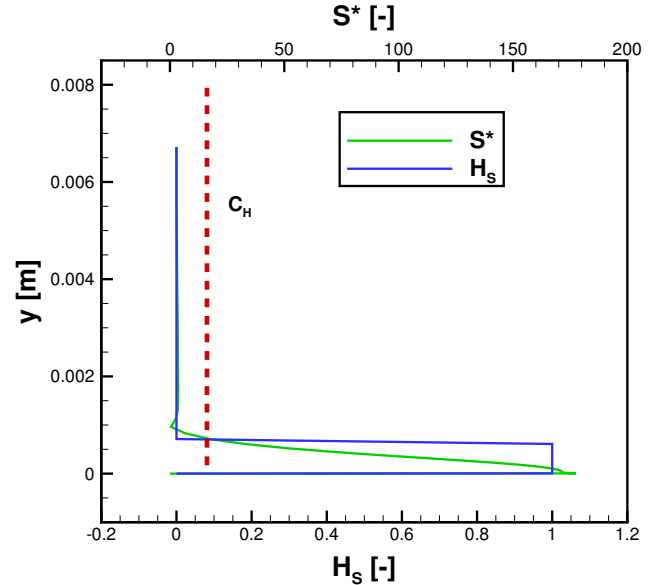


Figure 2: Action of the numerical filter H_S on a pre-transitional boundary layer

This formulation allows to compute the transition representative length in shear and boundary layers according to only one method based on local values. Finally, it must also be noted that the formulation of the production term takes only into account the amplification of the laminar kinetic energy. Indeed, according to Eq. (1) a non-zero value of laminar kinetic energy must be found in order to activate the production term. The next section will clarify how this condition is satisfied by the model.

2.3 Stagnation Point Flows

The definition of the laminar kinetic energy used for the derivation of the model implies that this quantity is only found in significant amount in boundary and shear layers. For this reason, in the free-stream, the presence of laminar kinetic energy should be negligible. The laminar kinetic energy required to start the amplification must be created by an other mechanism involved into bypass transition, namely the penetration of disturbances from the free-stream into the boundary layer. The situation at the vicinity of the leading edge of a turbomachine blade -also denoted as stagnation point flows- is of particular interest.

The work of Gostelow et al. [14] demonstrates that upstream of the leading edge of a compressor blade, significant amount of vorticity can be found. In accordance to the well-known mechanisms of vortex tilting and stretching, the presence of vorticity can be interpreted as an increase of turbulence kinetic energy. The nature of the fluctuations is investigated by Kestin et al. [15] who show that in stagnation point flows, three-dimensional instabilities appear. Since these fluctuations are caused by an instability mechanism, their nature can be assumed to be non-turbulent. The experiments of Bearman [16] reveal that along the stagnation streamline, an amplification or damping of the fluctuations occurs, depending on their length scales. Despite the fact that the nature of the fluctuations changes close to the leading edge of a blade, there are no direct evidences proving that they are non-turbulent. Nevertheless, in this work, it is assumed that turbulent kinetic energy becomes laminar kinetic energy close to the leading edge.

In the model, this mechanism is taken into account via an additional production term, which derivation is based on the work of Kato and Launder [17]. Indeed, near a stagnation point, $S^2 \gg S\Omega$ while $S^2 \approx S\Omega$ otherwise. These observations are used to derive the production term of laminar kinetic energy related to the penetration of fluctuations close to the stagnation point P_{stg} , detailed in Eq. (4).

$$P_{stg} = \max \left(\mu_t \left(S^2 - \frac{2}{3} k_t \frac{\partial U_i}{\partial x_i} - S\Omega \right), 0.0 \right) \quad (4)$$

2.4 Formulation of the Model

In this work, the laminar kinetic energy is considered to have no direct influence on the flow. It follows that in order to be able to modify the flow, the laminar kinetic energy equation must be coupled to a turbulence model. Due to its relative simplicity and robustness, the $k - \omega$ model of Wilcox [18] has been selected.

The complete formulation of the transition model consists in the three transport equations Eq. (5), Eq. (6) and Eq. (7).

$$\frac{D\rho k_l}{Dt} = P_{k_l} + \frac{\partial}{\partial x_j} \left[\mu \frac{\partial k_l}{\partial x_j} \right] - 2 \frac{\mu k_l}{y^2} - T \quad (5)$$

$$\frac{D\rho k_t}{Dt} = f_2(P_{k_t} - \beta^* \rho \omega k_t) + \frac{\partial}{\partial x_j} \left[(\mu + \sigma_k \mu_t) \frac{\partial k_t}{\partial x_j} \right] + T - P_{stg} \quad (6)$$

$$\frac{D\rho \omega}{Dt} = \left(\alpha \frac{\omega}{k} \right) P_{k_t} - \beta \rho \omega^2 + \frac{\partial}{\partial x_j} \left[(\mu + \sigma_\omega \mu_t) \frac{\partial \omega}{\partial x_j} \right] \quad (7)$$

The final formulation of the production term of laminar kinetic energy, given in Eq. (8), takes into account the two mechanisms involved in bypass transition discussed previously and is in accordance with the principle of completion developed by Chassaing [19].

$$P_{k_l} = \begin{cases} P_{stg} & \text{if } P_{stg} > 0.0 \\ P_{k_l}^* & \text{otherwise} \end{cases} \quad (8)$$

In order to be able to predict transition, the boundary layer must be laminar, at least at its beginning, to enable the production of laminar kinetic energy. For this reason, the function f_2 , given in Eq. (9) and Eq. (10), is introduced to modulate the production and dissipation of turbulent kinetic energy.

$$f_2 = 1 - \exp \left(\frac{-\psi_2}{C_{2-1}} \right) \quad (9)$$

$$\psi_2 = \max \left(\frac{\rho k_t}{\mu \omega} - C_{2-2}; 0.0 \right) \quad (10)$$

Transition is triggered by a transfer of laminar to turbulent kinetic energy. This is incorporated in the model via the term T defined in Eq. (11).

$$T = C_T f_1 \omega k_l \quad (11)$$

$$f_1 = 1 - \exp \left(\frac{-\psi_1}{C_{1-1}} \right) \quad (12)$$

$$\psi_1 = \max \left(\frac{\rho(k_t + k_l)}{\mu \omega} - C_{1-2}; 0.0 \right) \quad (13)$$

It is interesting to note that the transfer variable chosen is $\frac{\rho(k_t + k_l)}{\mu \omega}$. This term is designed to avoid any unphysical halt of transition which would be caused by the activation of T .

The eddy viscosity μ_t is computed using the so-called Durbin limitation [20], defined in Eq. (14) and Eq. (15). This correction of the turbulence model ensures the realizability of the predicted Reynolds stress.

$$\mu_t = C_\mu \rho k_t T_D \quad (14)$$

$$T_D = \min \left(\frac{1}{C_\mu \omega}, \frac{1}{\sqrt{6} C_\mu S} \right) \quad (15)$$

The boundary conditions for Eq. (6) and Eq. (7) are the same as those used by Wilcox [18]. Concerning Eq. (5), at the inlet as well as on solid surfaces, the laminar kinetic energy is equal to zero. At the outlet of the computational domain, the flux of laminar kinetic energy is set to zero.

The model obtained is named LKE-TRL in order to avoid any confusion with the different three-equations models based on the laminar kinetic energy concept found in the literature. More details about the derivation can be found in [8], Chapter 3.

3 Numerical Methods

The model has been implemented in DLR's in-house flow solver dedicated to the simulation of turbomachine components TRACE. The viscous fluxes are discretized using a central difference scheme while for the convective fluxes the TVD upwind scheme of Roe is used. The numerical methods used for the implementation of the model can be found in [8], Chapter 4.

4 Application: T107 Cascade

4.1 Flows Investigated

The low-pressure turbine cascade T107 stems from a blade design of MTU Aero Engines and it can be denoted as a high-lift profile. This qualification is usually given to a turbine cascade when its Zweifel number $-Z_w$ defined in Eq. (16)- is greater than 1.0.

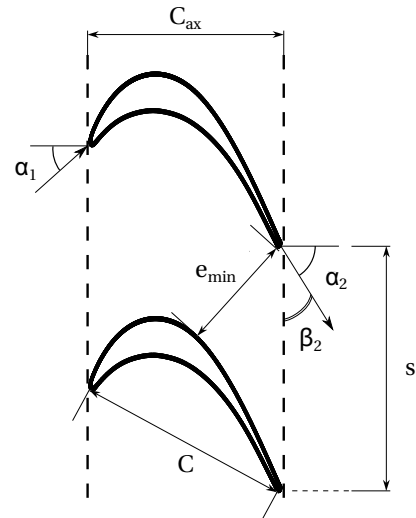


Figure 3: Geometry of a low-pressure turbine cascade

$$Z_w = 2 \frac{s}{C_{ax}} \cos^2 \alpha_2 | \tan \alpha_2 - \tan \alpha_1 | \quad (16)$$

With the help of the angle defined in Figure (3), the Zweifel number for the T107 is found to be equal to 1.12. Additionally, the cascade is designed so that on the suction side, the suction peak is located at approximately 60% relative chord, meaning that the blade's design is aft-loaded. Consequently, a strong adverse pressure gradient can be expected downstream of the suction peak which could favor the separation of the boundary layer. In the following, in order to preserve the proprietary nature of the design, the cascade geometry is not further detailed and all the results presented are scaled with arbitrary chosen values.

The experimental investigations have been carried out at DLR and the measurements have been reported by Hoeger [21]. The wind tunnel used for the measurements enabled to vary independently the Mach and Reynolds numbers. It was chosen to vary the theoretical Reynolds number Re_{2th} between 100,000 and 900,000 while the Mach number remained unchanged to the design value. In particular, for a low-pressure turbine, it is of prime interest to investigate the flows at the lowest Reynolds numbers since they are representative of the cruise conditions. Moreover, in order to be closer to the conditions found in a jet engine, turbulence has been generated in the wind tunnel with the help of a passive grid. The turbulence grid was located in front of a contraction and far enough from the cascade to consider that the turbulence generated was isotropic and homogenous. During the experiments, the free-stream turbulence intensity was equal to approximately 4.0%.

4.2 Performance of the Cascade

The performance of a low-pressure turbine is evaluated by its ability to deviate the flow with an acceptable level of losses. Obviously, the evolution of these two parameters depends on the occurrence of transition on the cascade. Therefore, two parameters are chosen to evaluate the capability of the transition model to simulate transition, namely the total pressure losses, defined in Eq. (17) and the exit angle β_2 , defined on Figure (3).

$$\zeta = \frac{P_{01} - P_{02}}{P_{01} - P_2} \quad (17)$$

As written previously, the losses are scaled by a reference value chosen arbitrarily ζ_{Ref} while an exit flow angle resulting from the inviscid theory $\beta_{2(inviscid)}$, defined in Eq. (18), is subtracted from the true value of exit flow angle β_2 .

$$\sin \beta_{2(inviscid)} = \frac{e_{min}}{s} \quad (18)$$

The scaled losses and exit flow angles are shown in Figure (4) and Figure (5) respectively. The losses computed by the model match very well the experimental values. As expected, the losses increase as the Reynolds number decreases. Especially close to $Re_{2th} = 200,000$, the model is able to reproduce the rapid increase of the losses related to the bubble bursting phenomenon reported by Hoeger [21].

The exit flow angles computed by the model are able to reproduce the trend of the experimental data, despite an offset of less than one degree. A striking feature of the experimental data is that the flow exit angle starts only to increase notably when the Reynolds number falls below 200,000. This augmentation is also a consequence of the bubble bursting.

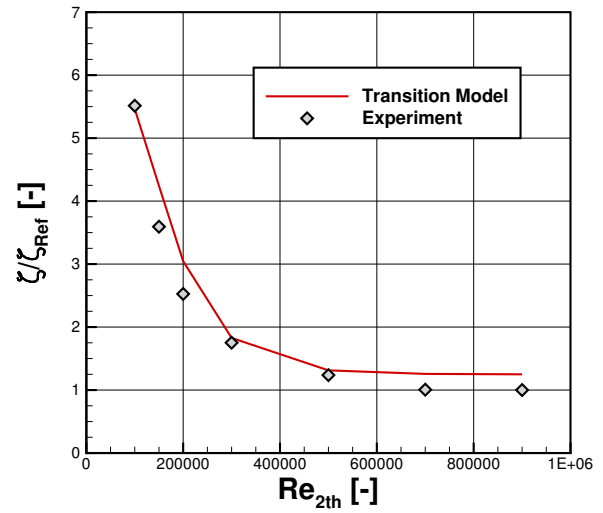


Figure 4: T107 cascade performance: evolution of the total pressure losses

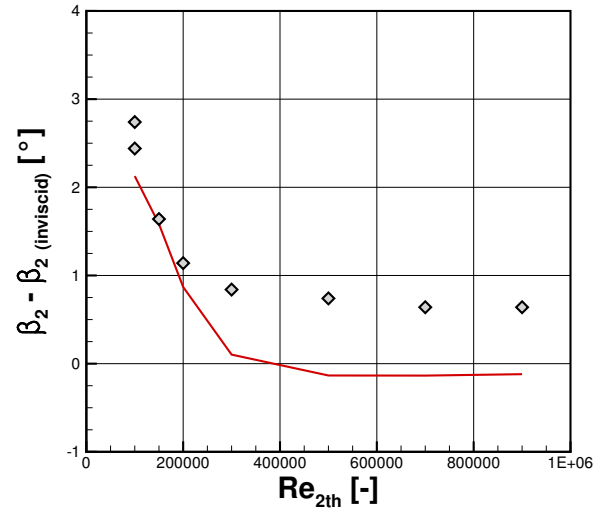


Figure 5: T107 cascade performance: evolution of the exit flow angles

From this analysis, the model is able to simulate quite accurately the global performance of the low-pressure turbine cascade. However a more complete analysis, enabling to evaluate in more details the ability of the model to predict the flow physics can be found in [8], Chapter 5.

5 Conclusion

This paper shows that a new transition model derived according to a phenomenological approach can successfully simulate flows of engineering relevance for turbomachines. Furthermore, the capability of the model to predict transition on different industrial turbine and compressor cascades has been investigated and analyzed in [8], Chapter 6.

From the comparisons between the computations and the experiments, it seems that the modelling of transition by the mechanisms involved in bypass transition when high levels of turbulence free-stream intensity are present is adequate for a lot of flow conditions. Indeed, in addition to bypass transition and the different types of transition bubbles, the model demonstrates its ability to predict also shock-induced transition as well as tran-

sition in wakes. Obviously, the simulations of flows at low free-stream turbulence intensity and low Reynolds number are not satisfactory since the mechanisms related to bypass transition are not involved in these cases. However with the phenomenological approach presented here, it can be hoped that additional mechanisms, such as the Kelvin-Helmholtz instabilities or the Tollmien-Schlichting waves, can be in the future incorporated into the model to improve its performance. To this aim, the analysis of DNS computations of flows over low-pressure turbine and compressor cascades published recently can be carried out to confirm -or invalidate- the current views on the transition process.

For the author of this paper, this is currently the best direction to follow for the derivation of the transition models required for the design of greatly improved jet engines.

Acknowledgment

The permission from MTU Aero Engines to publish the results concerning the T107 low-pressure turbine cascade is greatly acknowledged.

References

- [1] M. Longhitano, "Investigation of a correlation-based transition model for turbomachinery simulations," Master's thesis, Politecnico di Torino - Technische Universität München, 2012.
- [2] R. B. Langtry, *A Correlation-Based Transition Model using Local Variables for Unstructured Parallelized CFD Codes*. PhD thesis, Universität Stuttgart, 2006.
- [3] R. Pacciani, M. Marconcini, A. Fadai-Ghotbi, S. Lardeau, and M. A. Leschziner, "Calculation of high-lift cascades low pressure turbine conditions using a three-equation model," in *Proceedings of ASME Turbo Expo 2009: Power for Land, Sea and Air*, 2009.
- [4] V. Marciniak, "Modeling flows in low-pressure turbine cascades at very low reynolds numbers," *CEAS Aeronautical Journal*, vol. 6, pp. 257–270, 2015.
- [5] R. E. Mayle and A. Schulz, "The path to predicting bypass transition," *Journal of Turbomachinery*, vol. 119, pp. 405–411, 1997.
- [6] R. J. Volino, "Separated flow transition under simulated low-pressure turbine airfoil conditions - part 2: Turbulence spectra," *Journal of Turbomachinery*, vol. 124, pp. 656–664, 2002.
- [7] D. K. Walters, "Physical interpretation of transition-sensitive RANS models employing the laminar kinetic energy," *Ercoftac Bulletin*, vol. 80, pp. 67–71, 2009.
- [8] V. Marciniak, *Phenomenological Transition Modelling For Turbomachinery Flows*. PhD thesis, Ruhr-Universität Bochum, 2016.
- [9] R. J. Volino, "Separated flow transition under simulated low-pressure turbine airfoil conditions - part 1: Mean flow and turbulence statistics," *Journal of Turbomachinery*, vol. 124, pp. 645–655, 2002.
- [10] E. Makiel and R. E. Mayle, "Transition in a separation bubble," *Journal of Turbomachinery*, vol. 118, pp. 752–759, 1996.
- [11] S. S. Diwan and O. N. Ramesh, "On the origin of the inflectional instability of a laminar separation bubble," *Journal of Fluid Mechanics*, vol. 629, pp. 263–298, 2009.
- [12] C. D. Winant and F. K. Browand, "Vortex pairing: the mechanism of turbulent mixing layer growth at moderate reynolds number," *Journal of Fluid Mechanics*, vol. 63, pp. 237–255, 1974.
- [13] S. Lardeau, L. Ning, and M. A. Leschziner, "Large eddy simulation of transitional boundary layers at high free-stream turbulence intensity and implications for RANS modeling," *Journal of Turbomachinery*, vol. 129, pp. 311–317, 2007.
- [14] J. P. Gostelow, W. A. McMullan, G. J. Walker, and A. Mahallati, "The role of streamwise vorticity in flows over turbomachine blade suction surfaces," in *Proceedings of ASME Turbo Expo 2011*, 2011.
- [15] J. Kestin and R. T. Wood, "On the stability of two-dimensional stagnation flow," *Journal of Fluid Mechanics*, vol. 44, pp. 461–479, 1970.
- [16] P. W. Bearman, "Some measurements of the distortion of turbulence approaching a two-dimensional bluff body," *Journal of Fluid Mechanics*, vol. 53, pp. 451–467, 1972.
- [17] M. Kato and B. E. Launder, "The modeling of turbulent flow around stationary and vibrating square cylinders," in *9th Symposium on Turbulent Shear Flows*, pp. 10.4.1–10.4.6, 1993.
- [18] D. C. Wilcox, "Reassessment of the scale-determining equations for advanced turbulence models," *AIAA Journal*, vol. 26 (11), pp. 1299–1310, 1988.
- [19] P. Chassaing, *Turbulence en mécanique des fluides: Analyse du phénomène en vue de sa modélisation à l'usage de l'ingénieur*. Collection Polytech, 2000.
- [20] G. Medic and P. A. Durbin, "Toward improved prediction of heat transfer on turbine blades," *Journal of Turbomachinery*, vol. 124, pp. 187–192, 2002.
- [21] M. Hoeger, *Theoretische und experimentelle Untersuchungen an Schaufelprofilen mit Grenzschichtumschlag über eine laminare Ablöseblase*. PhD thesis, Technische Universität Braunschweig, 1992. ISBN 3-928628-00-3.

AN INTERMITTENCY TRANSPORT MODEL FOR TRANSITIONAL FLOWS ON SMOOTH AND ROUGH WALLS

L. Wei¹, X. Ge², J. George¹ and P. Durbin³

¹*MetroLaser Inc., Laguna Hills, CA 92653, USA*

²*University of Memphis, Memphis, TN 38152, USA*

³*Iowa State University, Ames, Iowa 50011, USA*

Abstract

Laminar to turbulent transition occurs in a broad range of industrial applications, and in nature. There are many mechanisms (natural or bypass) that lead to transition. Accurately predicting both the onset location and length of transition has been persistently difficult. A new, local, intermittency function-based transitional model for both low (<1%) and high freestream turbulence intensity flows, over smooth and rough surfaces, is introduced and formulated. It is coupled with the $k-\omega$ RANS model. Only a single transport equation for intermittency function is used and non-local operations were avoided in order to satisfy the requirements of general-purpose CFD. Equivalent sandgrain roughness and the displacement of origin approaches were employed to model surface roughness.

The intermittency model was validated on the ERCOFTAC experimental zero-pressure-gradient smooth flat plate boundary layer cases T3A-, T3A, T3B with leading-edge freestream turbulence intensity 0.9%, 3.5%, 6%, respectively. Skin friction profiles agree well with the experimental data. The model was then tested on flow over Stripf's low pressure turbine blade, with a broad range of roughnesses, from hydraulically smooth to fully rough. The Nusselt number along the blade surface predicted by the current model is compared with Stripf's experimental data and the agreement for both the transition onset location and transition length is decent.

1 Introduction

Rotor blades, such as in turbines or rotorcraft, often are subjected to laminar-turbulent transition with either high or low perturbations, and often operate in harsh conditions, which lead to variable surface roughness. It is important to be able to estimate the influence of transition and roughness on their aerodynamic and/or heat transfer performance, through CFD modelling.

1.1 Transition Modeling on Smooth Surfaces

Accurate prediction of laminar to turbulent transition remains a difficulty for general-purpose CFD engineering modelling. One reason is that transition occurs via different mechanisms in different situations. For aerodynamic flows with very low freestream turbulence intensities ($\lesssim 0.2\%$), laminar to turbulent transition starts with linear instabilities, such as Tollmien-Schlichting waves, which develop downstream as nonlinear modes, and final

break down to turbulence. This is called natural transition [1, 2]. However, for freestream turbulence intensities $\gtrsim 1\%$, the transition occurs via diffusion of turbulence into the laminar boundary layer. This is called bypass transition [3]. There also are other transition mechanisms; for instance, separation-induced transition, which occurs in the detached shear layer. It is quite difficult for one model to accommodate all such mechanisms.

There has been a renewed effort on transition modelling recently. One focus has been to combine Reynolds Averaged Navier-Stokes (RANS) based turbulence models with a transition criterion. For instance, an empirical critical Reynolds number is compared to the flow Reynolds number. This approach invokes an *integral* boundary layer thickness [4, 3, 5]. To avoid the integral thickness, [2] proposed a method that links only local boundary layer quantities to a correlation for the critical *vorticity* Reynolds number [6]. More specifically, it couples two additional transport equations (for the intermittency function γ and the transition momentum thickness Reynolds number $Re_{\theta t}$) with the SST $k-\omega$ based RANS turbulence model. It is often called a 'correlation-based' $\gamma - Re_{\theta t}$ transition model.

A simpler approach is to use only one transport equation, for the intermittency function γ , and only local variables. Such a model was first proposed in [7], using the intermittency approach of [8]. This model was further developed in [9, 10] and some further improvements are described herein.

1.2 Roughness Studies

Section 1.1 cited studies of transition modelling on smooth surfaces; there are very few studies of transition modelling on rough surfaces. Roughness effects on wall-bounded flows has been referred to as an "Achilles Heel of CFD" [11, 12]. Although there have been many experimental studies of turbulent flows over rough walls (see [13] for a review), there are very few benchmark data sets for transition on rough surfaces. Here we use the turbine data of [14].

Roughness is commonly characterized by an equivalent sandgrain height (r), as first proposed by Schlichting [15]. He defined r as the size of sandgrain in a certain pipe flow experiment producing the observed skin friction. Some researchers proposed correlations to compute r ([16, 17, 18]). The correlation proposed by Koch and Smith [18] only uses statistical parameters of the surface roughness to calculate r .

A displacement of origin concept [19] provides a way to incorporate the equivalent sandgrain roughness into the RANS turbulence model, through modified boundary conditions. A hydrodynamic roughness is obtained

from the sandgrain roughness via a calibration procedure which fits the log-law displacement predicted by the model to an empirical formula. Then the rough surface is represented by modified boundary conditions for model field variables [20]. This method is applied to $k-\omega$ based RANS turbulence in [21, 22]. Another objective of the current study is to apply the displacement of origin and equivalent sandgrain roughness concepts to bypass transition modelling.

2 Intermittency Transport Model

2.1 Model for smooth walls

As an improvement on the model of [9], the present formulation for smooth walls can accommodate transition at low turbulence intensity. This improvement was made mainly by modifying the source and sink terms of the intermittency transport equation. In addition, the new model replaced ramp functions with smooth functions, so that it can be applied to optimization, *etc.*

The formulation of the new model for smooth walls starts from the intermittency transport equation [8]:

$$\frac{D\gamma}{Dt} = D_\gamma + P_\gamma - E_\gamma. \quad (1)$$

D_γ is the diffusion term, defined as

$$D_\gamma = \partial_j \left[\left(\frac{\nu}{\sigma_l} + \frac{\nu_T}{\sigma_\gamma} \right) \partial_j \gamma \right], \quad (2)$$

where $\sigma_l = 5.0$ and $\sigma_\gamma = 0.2$ are empirical coefficients.

P_γ is the source term, defined as

$$P_\gamma = F_\gamma |\Omega| (\gamma_{max} - \gamma) \sqrt{\gamma}, \quad (3)$$

where $\gamma_{max} = 1.1$, $|\Omega| = \sqrt{2\Omega_{ij}\Omega_{ij}}$,

$$F_\gamma = 2 [1 + \tanh(4(90 - R_\nu))] \times [1 + \tanh(4(R_\nu - 1.08R_{c1}))]. \quad (4)$$

The ramp functions in [9] are replaced by tanh's. The parameters are

$$\left. \begin{aligned} R_t &\equiv \frac{\nu_T}{\nu}, \\ T_\omega &\equiv R_t^2 \frac{|\Omega|}{\omega}, \\ R_\nu &\equiv \frac{d^2 |\Omega|}{2.188\nu}, \\ R_{c1} &= \frac{272}{T_\omega^2} + 55. \end{aligned} \right\} \quad (5)$$

Compared with [9], T_ω , R_{c1} , F_γ were modified to strengthen the influence of R_t , as R_t is closely related to the turbulence level. The critical Reynolds number for transition is approximately inverse to the free stream turbulence intensity, and it increases quickly when the free stream turbulence intensity decreases below 1% [3].

E_γ is the sink term, driving γ to zero in order to have a laminar region before transition, and vanishing after transition. It is defined as

$$E_\gamma = G_\gamma F_{turb} |\Omega| \gamma^{1.5}, \quad (6)$$

with

$$F_{turb} = e^{-(R_\nu R_t)^{1.2}}. \quad (7)$$

The ramp was replaced by a smooth function, and G_γ was modified as follows:

$$G_\gamma = 1.875 [1 + \tanh(4(100 - R_\nu))] \times [1 + \tanh(4(R_\nu - 16))]. \quad (8)$$

The intermittency function γ enters the $k-\omega$ model through the term γ_{eff} , which multiplies the production term of the k equation:

$$\frac{Dk}{Dt} = \min \left(2\nu_T |S|^2, k|S|/\sqrt{3} \right) \gamma_{eff} - C_\mu k\omega + \partial_j \left[\left(\nu + \frac{\nu_T}{\sigma_k} \right) \partial_j k \right], \quad (9)$$

$$\frac{D\omega}{Dt} = 2C_{\omega 1} |S|^2 - C_{\omega 2} \omega^2 + \partial_j \left[\left(\nu + \frac{\nu_T}{\sigma_\omega} \right) \partial_j \omega \right]. \quad (10)$$

Otherwise, this is the standard model, with $\nu_T = k/\omega$, $C_\mu = 0.09$, $C_{\omega 1} = 5/9$, $C_{\omega 2} = 3/40$, $\sigma_\omega = \sigma_k = 2$. The transition term is

$$\gamma_{eff} = \max [\min(1, \gamma), \min(2, F_{R_t} F_{R_\nu} F_{R_s})], \quad (11)$$

where

$$F_{R_t} = e^{-(R_t/10)^3}, \quad (12)$$

$$F_{R_\nu} = \max(R_\nu - 200, 0), \quad (13)$$

$$F_{R_s} = \min [1.0, \max(10 + 5R_s, 0)] \times \min [1.0, \max(10 - 5R_s, 0)]. \quad (14)$$

The intermittency transport equation allows γ to be greater than 1, but a limiter, $\min(1, \gamma)$, clips off these values. This is done to ensure that γ is driven exactly to unity.

R_s is the adverse pressure gradient detector, which is used to account for the influence of both adverse pressure gradient and separation. It is defined as

$$R_s \equiv d \cdot \frac{\mathbf{n}_w \cdot \nabla |S| \omega}{\sqrt{2} |S|^2}, \quad (15)$$

where $|S| = \sqrt{S_{ij}S_{ji}}$ and \mathbf{n}_w the unit wall normal vector.

2.2 Roughness Modification

Roughness affects the onset of transition, and it could also influence transition length. Experimental studies [23, 24, 25] have shown increased transition length for a turbine blade with certain roughness, in the 'transitionally rough' turbulent regime.

In the current model, σ_γ in the diffusion term D_γ , which affects transition length, is modified as follows:

$$\sigma_\gamma = 0.2 + 0.5 [1 + \tanh(0.4(36 - R_r))] \times [1 + \tanh(0.1(R_r - 30))], \quad (16)$$

where,

$$R_r \equiv \frac{r \sqrt{(\nu + \nu_T) |\Omega|}}{\nu}, \quad (17)$$

and r is the equivalent sandgrain roughness. R_r is similar to r^+ , but R_r uses only local variables.

To accommodate the effect of roughness on transition onset location, the model for smooth walls, presented in the last section, is extended through the concept of the effective origin [10]. Specifically, R_ν and R_s become

$$R_\nu \equiv \frac{(d + 0.26r)^2 |\Omega|}{2.188\nu}, \quad (18)$$

$$R_s \equiv (d + 0.26r) \cdot \frac{\mathbf{n}_w \cdot \nabla |S| \omega}{\sqrt{2}|S|^2}, \quad (19)$$

where d is the wall distance.

The modified sink terms G_γ and F_{turb} are,

$$G_\gamma = 1.875 [1 + \tanh(4(100 + R_{c3} - R_\nu))] [1 + \tanh(4(R_\nu - 16 - R_{c2}))], \quad (20)$$

and

$$F_{turb} = e^{-(R_{\nu_{new}} R_t)^{1.2}}, \quad (21)$$

where

$$R_{c2} = 3.0 \left[\frac{(0.26r)^2 |\Omega|}{2.188\nu} \right]^{0.8}. \quad (22)$$

The following modifications were introduced to avoid a spurious roughness effect at leading edges:

$$R_q = 0.3 \frac{(d + 0.26r)^2 \sqrt{|Q|} \text{sign}(Q)}{\nu}, \quad (23)$$

$$R_{c3} = \max[\min(R_q, 100), -100], \quad (24)$$

$$R_{\nu_{new}} = R_\nu e^{-F_Q^{1.5}/350}. \quad (25)$$

$$F_Q = \max\left[0, \frac{r^2 \sqrt{|Q|} \text{sign}(Q)}{\nu}\right], \quad (26)$$

$$Q = \Omega_{ij} \Omega_{ij} - S_{ij} S_{ij}. \quad (27)$$

The functional dependence on F_Q , R_{c3} and $R_{\nu_{new}}$ is to account for the influence of strong favorable pressure gradient [10]: $|\Omega|$ becomes very large in the near-wall region with strong favorable pressure gradient, which would make R_ν so large as to cause the sink term to vanish. The above modification is to reduce R_ν in F_{turb} (via $R_{\nu_{new}}$) and increase the upper bound of R_ν in G_γ (e.g. R_{c3}) of the sink term.

3 Validation Tests

3.1 Smooth Flat Plate Boundary Layer

The new model was first tested on transitional flows over a smooth, flat plate, zero-pressure gradient boundary layer, with different freestream turbulence intensities (Tu_{in}) and freestream velocities (U_∞). The plate length of 1.5 m and a kinematic viscosity of $\nu = 1.5 \times 10^{-5} m^2 s^{-1}$ were selected in order to compare with the ERCOFTAC T3A-, T3A, and T3B cases. T3A-, T3A, and T3B have $U_\infty = 25 m/s, 5.2 m/s, 9.4 m/s$, and $Tu_{in} = 0.9\%, 3.5\%, 6\%$, respectively.

The inlet turbulent kinetic energy $k_{in} = 1.5(Tu_{in} U_\infty)^2$ and specific dissipation rate $\omega_{in} = k_{in}/(R_t \nu)$ were specified. R_t is determined by matching the computed $Tu(x)$ to data. The freestream turbulence intensity profile is plotted in Figure (1). It agrees excellently with the experimental data. We found $R_t = \nu_t/\nu = 8.7, 14, 100$ for T3A-, T3A, and T3B, respectively.

The predicted skin friction coefficient C_f for the current model is compared with the original model [9, 10] and the experiment data for T3A-, T3A and T3B in Figure (2), Figure (4), and Figure (5), respectively. It can be seen from Figure (2) that for the low Tu case T3A-, the current model significantly improves the prediction:

transition moves from 0.5×10^6 to 1.7×10^6 , in good agreement with the experimental value. (Note that the transition location is defined as the location where C_f starts to rise significantly toward the turbulent level).

It is also noted that the predicted C_f right before transition for T3A- seems a little higher than the experimental values, which may be explained by the contours of intermittency function γ , displayed in Figure (3). Through molecular and turbulent diffusion, freestream turbulence is diffused into the laminar boundary layer right after the leading-edge of the plate, which promotes generation of the turbulence kinetic energy. The sink term (E_γ) counters this, and causes γ to drop to zero, except in a layer very near the wall. That thin layer is in the model to prevent the sink from switching on next to the wall in fully turbulent flow.

The current model improves the prediction for flows with very low freestream Tu , but at the same time, it maintains the good prediction for higher Tu . Figure (4), Figure (5) show that the current model gives similar predictions as the original model for cases T3A and T3B.

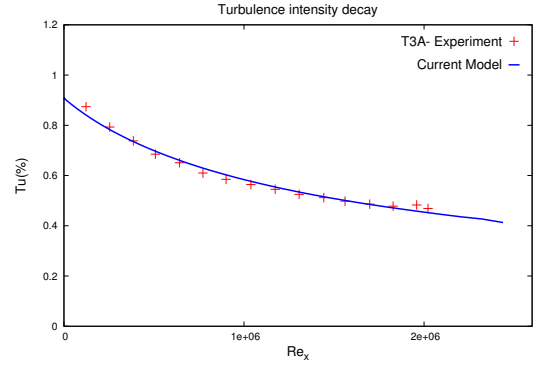


Figure 1: Turbulence intensity decay for T3A-

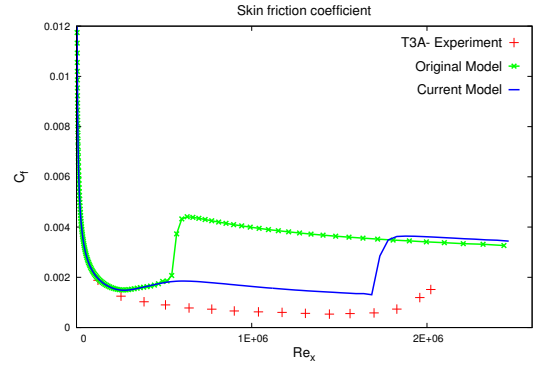
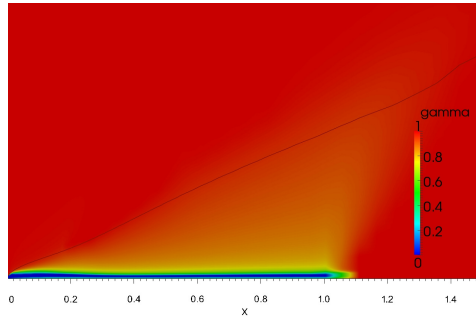


Figure 2: Skin friction coefficient for T3A-

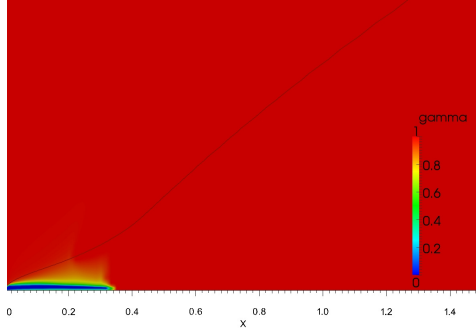
3.2 Rough Low Pressure Turbine Blade

The Stripf's [23, 25] low pressure turbine (LPT) was selected for validation tests. The computational domain is shown in Figure (6). The true chord $c = 113.34 mm$; $U_{in} = 33.086 m/s$; $Tu_{in} = 3\%$ and $Re_{in} = 250,000$. The roughness height ranges from 0 to $395 \mu m$ (fully rough). The blade temperature is set as $300^\circ K$ and the fluid $400^\circ K$. $\rho = 1.2 kg/m^3$, $C_p = 1,000 m^2/s^2 K$. The laminar and turbulent Prandtl numbers are set as 0.72 and 0.86, respectively.

The inlet turbulent kinetic energy k_{in} is mainly based on the inlet turbulence intensity (Tu_{in}), and the inlet



(a) Current Model



(b) Original Model

Figure 3: The intermittency γ contour for T3A-. The black solid line represents the edge of the 99% boundary layer.

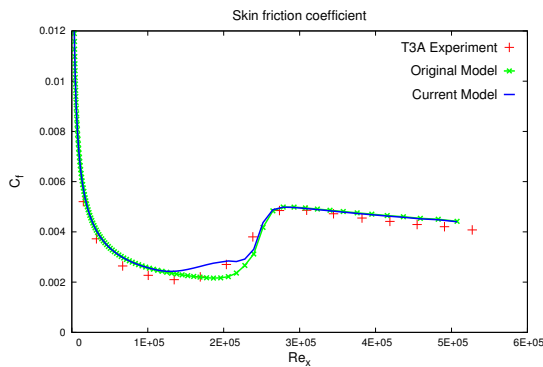


Figure 4: Skin friction coefficient for T3A

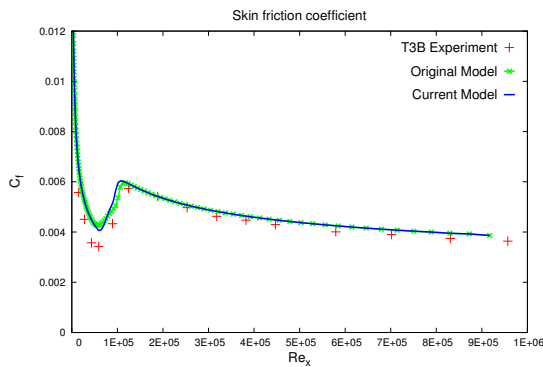


Figure 5: Skin friction coefficient for T3B

specific dissipation rate ω_{in} is adjusted based on the Tu decay profile. As indicated in [10], however, there is some uncertainty regarding the freestream turbulence around the turbine blade. The k_{in} and ω_{in} in the current study

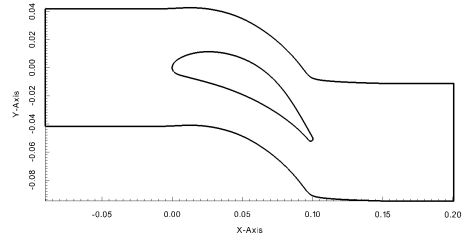


Figure 6: LPT Computational Domain

were adjusted based on the Nu profile for the smooth surface. Then the influence of the roughness is modelled by changing the equivalent sandgrain roughness (r). The current Tu_{in} is 1.5%, which is similar to [10].

The Nusselt number is defined as $Nu = hc/\kappa$, where h is the heat transfer coefficient and κ is the thermal conductivity. Nu distributions along the suction side of the blade are plotted in Figure (7), compared with the experimental data. The x coordinate is the surface distance normalized by the true chord (s/c). It can be seen that the profiles are in good agreement to data on both transition onset location and transition length, for the various roughnesses. Compared with the smooth surface, heat transfer on the rough surfaces rises earlier, and is significantly enhanced.

4 Conclusion

A new local intermittency-function-based transition model, for both low and high freestream turbulence intensity, over smooth/rough surfaces, was introduced. The roughness model was based on a modified displacement of origin version of the $k-\omega$ RANS model and in addition. Only a single transport equation for the intermittency function was needed. In order to satisfy general-purpose CFD requirements, non-local operations, such as computing boundary layer integral thickness, were avoided in the current model.

The model validation tests were performed for various types of flows over smooth/rough surfaces, such as the ERCOFTAC experimental flat plate zero-pressure-gradient boundary layer cases T3A-, T3A, T3B. The predicted skin friction agreed well with the experimental data.

The roughness model was validated on flows over Stripf's low pressure turbine blade with a range of roughnesses. The Nusselt number along the blade surface, predicted by the current model, are in agreement with Stripf's experimental data; the agreement for both the transition onset location and transition length is decent. After transition, the suction side heat transfer is over predicted. This implies that the $k-\omega$ model is not accurate there; the post transition prediction of the RANS model must be improved as part of improving the overall prediction method.

Acknowledgements

This work is supported by SBIR Phase II research program under the contract No. W911W6-14-C-0003, with program monitor Dr. Mark Calvert, and by NSF under award CBET 1228195.

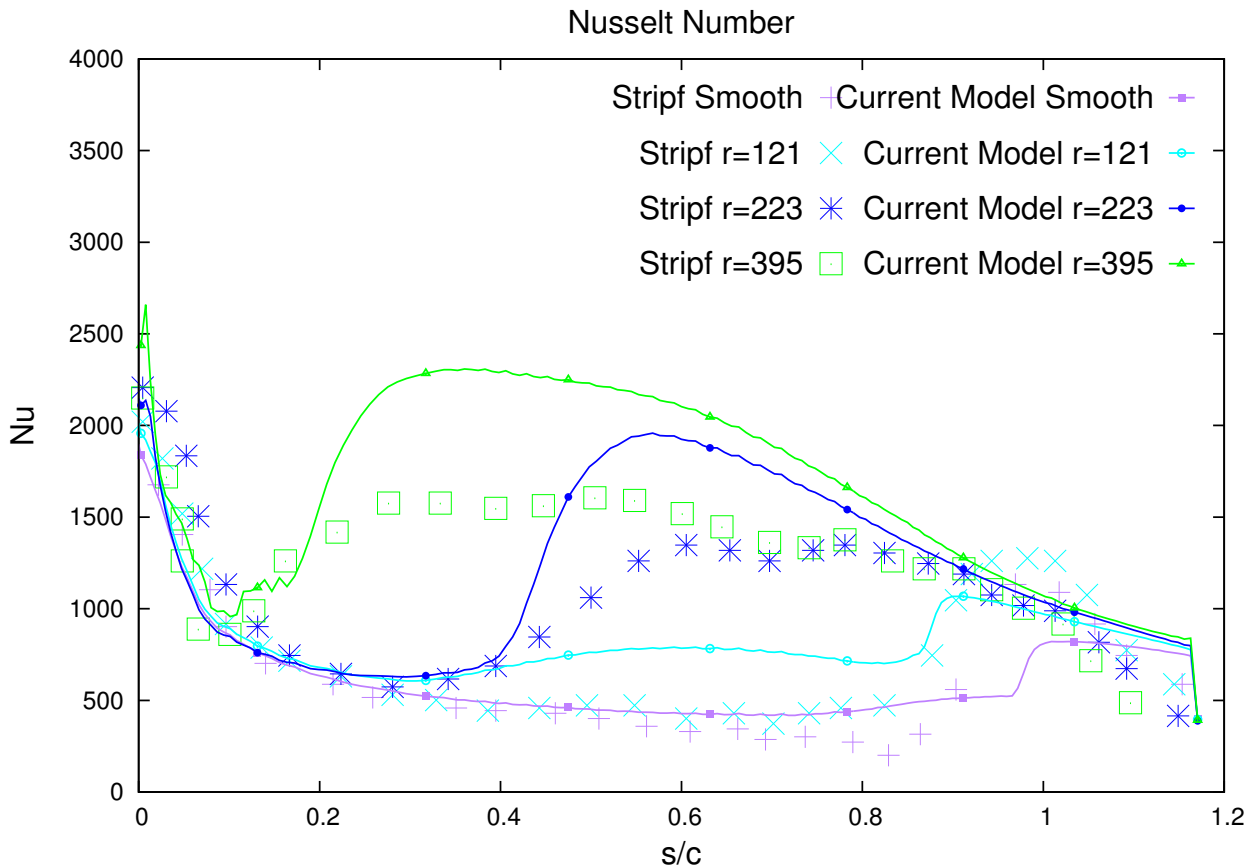


Figure 7: Nu for the Stripf's LPT blade with different roughness ($r, \mu m$)

References

- [1] H. Schlichting, *Boundary layer theory, 7th Ed.* New York: McGraw-Hill, 1979.
- [2] R. Langtry and F. Menter, "Correlation-based transition modelling for unstructured parallelized computational fluid dynamics codes," *AIAA Journal*, vol. 47, no. 12, pp. 2894–2906, 2009.
- [3] R. E. Mayle, "The 1991 IGTI scholar lecture: The role of laminar-turbulent transition in gas turbine engines," *Journal of Turbomachinery*, vol. 113, no. 4, pp. 509–536, 1991.
- [4] J. Steelant and E. Dick, "Modelling of bypass transition with conditioned Navier-Stokes equations coupled to an intermittency transport equation," *International Journal for Numerical Methods in Fluids*, vol. 23, no. 3, pp. 193–220, 1996.
- [5] Y. Suzen, P. Huang, and L. Hultgren, "Predictions of separated and transitional boundary layers under low-pressure turbine airfoil conditions using an intermittency transport equation," *Journal of Turbomachinery*, vol. 125, pp. 455–464, 2003.
- [6] E. R. Van Driest and C. B. Blumer, "Boundary Layer Transition- Freestream Turbulence And Pressure Gradient Effects," *AIAA Journal*, vol. 6, pp. 1303–1306, 1963.
- [7] P. A. Durbin, "An intermittency model for bypass transition," *International Journal of Heat and Fluid Flow*, vol. 36, no. 0, pp. 1–6, 2012.
- [8] K. Lodefier, B. Merci, C. DeLanghe, and E. Dick, "Transition modelling with the $k - \omega$ turbulence model and an intermittency transport equation," *J. of Thermal Science*, pp. 220–225, 2003.
- [9] X. Ge, S. Arolla, and P. A. Durbin, "A bypass transition model based on the intermittency function," *Flow, Turbulence and Combustion*, vol. 93, no. 1, pp. 37–61, 2014.
- [10] X. Ge and P. A. Durbin, "An intermittency model for predicting roughness induced transition," *International Journal of Heat and Fluid Flow*, vol. 54, pp. 55–64, 2015.
- [11] V. Patel, "flow at high Reynolds number and over rough surfaces -Achilles heel of CFD," *J. Fluids Eng.*, vol. 120, pp. 434–444, 1998.
- [12] J. George, A. D. Simone, G. Iaccarino, and J. Jiménez, "Modeling roughness effects in turbulent boundary layers by elliptic relaxation," in *Center for Turbulence Research, Proceedings of the Summer Program*, 2010.
- [13] J. Jiménez, "Turbulent Flows Over Rough Walls," *Annual Review of Fluid Mechanics*, vol. 36, pp. 173–196, 2004.
- [14] M. Stripf, A. Schulz, and S. Wittig, "Surface roughness effects on external heat transfer of a hp turbine vane," *Journal of Turbomachinery*, vol. 127, pp. 200–208, 02 2005.
- [15] H. Schlichting, "Eperimental investigation of the problem of surface roughness," Tech. Rep. NACA-TM-823, National Advisory Committee for Aeronautics, 1937.

- [16] R. L. Simpson, "A generalized correlation of roughness density effects on the turbulent boundary layer.," *AIAA Journal*, pp. 242–244, Feb. 1973.
- [17] A. Sigal and J. E. Danberg, "New correlation of roughness density effect on the turbulent boundary layer," *AIAA Journal*, vol. 28, pp. 554–556, Mar. 1990.
- [18] C. Koch and L. Smith, "Loss sources and magnitudes in axial-flow compressors," *ASME J. Eng. Power*, vol. 98, pp. 411–424, 1976.
- [19] P. A. Durbin, G. Medic, J.-M. Seo, J. Eaton, and S. Song, "Rough wall modification of two-layer $k - \epsilon$," *Journal of Fluids Engineering*, vol. 123, pp. 16–21, 03 2001.
- [20] P. A. Durbin, "Limiters and wall treatments in applied turbulence modeling," *Fluid Dynamics Research*, vol. 41, no. 1, p. 012203 (18pp), 2009.
- [21] J.-M. Seo, *Closure Modeling and Numerical Simulation for Turbulent Flows: Wall Roughness Model, Realizability, and Turbine Blade Heat Transfer*. PhD thesis, Flow Physics and Computation Division, Dept. of Mechanical Engineering, Stanford University, 2004.
- [22] T. Knopp, B. Eisfeld, and J. B. Calvo, "A new extension for $k - \omega$ turbulence models to account for wall roughness," *International Journal of Heat and Fluid Flow*, vol. 30, no. 1, pp. 54 – 65, 2009.
- [23] M. Stripf, "Einfluss der oberflächenrauigkeit auf die transitionale grenzschicht an gasturbinenschaufeln," *Forschungsberichte aus dem Institut für Thermische Strömungsmaschinen*, vol. 38, 2007.
- [24] R. Boyle and M. Stripf, "Simplified approach to predicting rough surface transition," *Journal of Turbomachinery*, vol. 131, p. 041020, 07 2009.
- [25] M. Stripf, A. Schulz, H.-J. Bauer, and S. Wittig, "Extended models for transitional rough wall boundary layers with heat transfer part I: Model formulations," *Journal of Turbomachinery*, vol. 131, p. 031016, 04 2009.

AN ALGEBRAIC TRANSITION MODEL COMBINED WITH THE $k - \omega$ RANS MODEL FOR TURBOMACHINERY USE

S. Kubacki¹ and E. Dick²

¹ *Institute of Aeronautics and Applied Mechanics, Warsaw University of Technology, Nowowiejska 24, 00-665, Warsaw, Poland; slawomir.kubacki@meil.pw.edu.pl*

² *Department of Flow, Heat and Combustion Mechanics, Ghent University, St.-Pietersnieuwstraat 41, 9000 Ghent, Belgium; erik.dick@ugent.be*

Abstract

The functioning of a recently developed algebraic model for laminar to turbulent boundary layer transition under high free-stream turbulence is illustrated [1]. The model uses only local variables and is tuned for turbomachinery flows. The transition model is combined with the newest $k - \omega$ RANS turbulence model by Wilcox [2]. It takes into account two effects in an attached pre-transitional boundary layer: damping of short-wavelength disturbances induced by the free stream and breakdown of the near-wall perturbed flow with generation of fine-scale turbulence.

1 Physics of Transition

Transition from laminar to turbulent state in turbomachinery boundary layer flows is influenced by Reynolds number, free-stream turbulence and pressure gradient. With a turbulence level above 0.5-1 %, the free-stream turbulence induces streamwise elongated disturbances in the near-wall region of an attached laminar boundary layer, termed streaks or Klebanoff modes. These are zones of forward and backward jet-like perturbations alternating in spanwise direction. The Klebanoff modes grow downstream both in length and amplitude and finally some streaks cause turbulent spots. Transition is then called of bypass type, which means that the instability by Tollmien-Schlichting waves is bypassed. Bypass mechanisms are discussed by Hack and Zaki [3]. Klebanoff modes are initiated by deep penetration into the boundary layer of low-frequency perturbations from the free stream. The strong damping of high-frequency components in a laminar boundary layer is called shear sheltering. It is the stronger the higher is the shear rate. There are two mechanisms by which the boundary layer perturbed by streaks may become unstable. One is instability by inflection of the velocity profile in wall-normal direction between the boundary layer edge and a low-speed streak. The other is instability of the velocity profile in wall normal direction in the overlap zone of the leading edge of a high-speed streak and the trailing edge of a low-speed streak. Both instabilities are triggered by high-frequency components in the free-stream turbulence, although these are sheltered by the boundary layer. The breakdown is earlier and much faster than with transition initiated by Tollmien-Schlichting waves.

In a boundary layer with laminar separation and low free-stream turbulence, transition is initiated by inviscid Kelvin-Helmholtz instability of the laminar free shear layer, with formation of spanwise vortices. They group at selective streamwise wavelengths, analogous

to Tollmien-Schlichting waves in an attached boundary layer [4]. The roll-up vortices break down as they travel downstream. The breakdown process is rather slow with low free-stream turbulence, but, under high free-stream turbulence, the process of bypass transition with formation of streaks in the pre-transitional attached boundary layer prior to separation can co-exist with the Kelvin-Helmholtz generated spanwise vortices in the separated layer. The breakdown of the vortex rolls is then strongly accelerated by perturbations due to the Klebanoff modes. For sufficiently strong free-stream turbulence, the Kelvin-Helmholtz instability may even be bypassed by the breakdown of the streaks. So, a bypass mechanism is possible in a separated shear layer, similar as in an attached boundary layer.

2 Model for Bypass Transition

The transport equations for turbulent kinetic energy and specific dissipation rate are

$$\frac{Dk}{Dt} = \gamma \nu_s S^2 - \beta^* k \omega + Diff(k) \quad (1)$$

$$\frac{D\omega}{Dt} = \alpha \frac{\omega}{k} \nu_s S^2 - \beta \omega^2 + Diff(\omega) \quad (2)$$

The factor γ (see later Eq. 7) is a multiplier of the production term in the k -equation. It is a starting function for the production of turbulent kinetic energy. The production term is $\nu_s S^2$ where ν_s is the small-scale eddy viscosity (see later Eq. 5), which is part of the full eddy viscosity ν_t . S is the magnitude of the shear rate tensor $S = (2S_{ij}S_{ij})^{1/2}$, with components $S_{ij} = 1/2(\partial U_i/\partial x_j + \partial U_j/\partial x_i) - 1/3(\partial U_k/\partial x_k)\delta_{ij}$. The introduction of γ and ν_s are the only changes for transition modelling in the $k - \omega$ model. In the laminar part of a boundary layer, γ is set to zero. There is then no production of k , but turbulent kinetic energy enters by diffusion out of the free-stream flow. In the laminar part of a boundary layer, the ω -equation stays active. This is allowed since the ω -equation has a nonzero laminar-flow solution for vanishing k and vanishing eddy-viscosity.

The turbulent kinetic energy k is split, based on the model for shear sheltering by Walters and Leylek [5] and Walters and Cokljat [6], into a small-scale part k_s and a large-scale part k_l by

$$k_s = f_{ss} k, \quad k_l = k - k_s \quad (3)$$

The splitting expresses that high-frequency disturbances are damped in the outer part of a laminar boundary layer. According to the findings of Jacobs and Durbin [7], shear sheltering is determined by the relative importance

of two time scales: the time scale of convection relative to an observer inside the shear layer and the time scale of wall-normal diffusion into the boundary layer. The convective time scale is obviously the time scale of the main strain $\tau_c = 1/\Omega$, where Ω is the magnitude of the vorticity tensor, i.e. $\Omega = (2\Omega_{ij}\Omega_{ij})^{1/2}$, with components $\Omega_{ij} = 1/2(\partial U_i/\partial x_j - \partial U_j/\partial x_i)$. The diffusive time scale is fundamentally l_d^2/ν , with l_d the diffusive length scale and ν the kinematic fluid viscosity. For fluctuations in a laminar boundary layer, this length scale was estimated by Walters [8], assuming proportionality between \sqrt{k}/l_d , where \sqrt{k} is the velocity scale of the fluctuations, and the mean velocity gradient, which is Ω . This results in $l_d \sim \sqrt{k}/\Omega$ and $\tau_d \sim k/\nu\Omega^2$. The ratio of the diffusive and convective time scales forms the Reynolds number $k/\nu\Omega$. With this Reynolds number, Walters and Cokljat [6] define a shear-sheltering factor, which we employ, by

$$f_{ss} = \exp[-(C_{ss}\nu\Omega/k)^2] \quad (4)$$

With the shear-sheltering factor, the turbulent kinetic energy of the turbulence that penetrates the pretransitional boundary layer is split into a large-scale part and a small-scale part (Eq. 3). The large-scale or long-wavelength part is the part that reaches wall vicinity and causes the streaks. Fluctuations in the streaks are dominantly unidirectional and can thus be characterized as laminar. In the modelling approach of Walters and Leylek [5] and Walters and Cokljat [6], this effect is expressed by two ingredients. One is that production of turbulence in the pre-transitional boundary layer is only due to the small-scale eddy viscosity (Eq. 1). We follow this description. The second is by writing an equation for laminar-fluctuation kinetic energy with a similar form as an equation for turbulent kinetic energy, but with a production term written with a large-scale eddy viscosity. We use the expressions of small-scale and large-scale eddy viscosities from their modelling approach, but we do not use an equation for laminarfluctuation kinetic energy.

The eddy viscosity associated to small and large scales is calculated in the same way as the eddy viscosity of the original turbulence model, but by replacing k by k_s and k by k_l :

$$\nu_s = k_s/\tilde{\omega}_s, \quad \text{with} \quad \tilde{\omega}_s = \max(\omega, C_{lim}\sqrt{2S_{ij}S_{ij}}/a_s) \quad (5)$$

$$\nu_l = k_l/\tilde{\omega}_l, \quad \text{with} \quad \tilde{\omega}_l = \max(\omega, C_{lim}\sqrt{2S_{ij}S_{ij}}/a_l) \quad (6)$$

$C_{lim} = 7/8$. The constant a_s is 0.3, as in the original model. The constant a_l is set to 0.45, which is larger than the standard value 0.3. The reason for this augmentation is discussed later. The resulting eddy viscosity, used in the Navier-Stokes equations, is $\nu_t = \nu_s + \nu_l$.

For the expression of the starting function γ , we rely on the work of Walters and Leylek [5]. Since breakdown is induced by free-stream turbulence, it is natural to let start up transition by a non-dimensional factor characterising the kinetic energy of the turbulence penetrating the pre-transitional boundary layer. Physically, breakdown starts when the production rate of turbulent perturbations inside the boundary layer exceeds their diffusion. The onset parameter in the laminarfluctuation kinetic energy model by Walters and Leylek [5] is $Re_y = \sqrt{k}y/\nu$, where y is the distance to the nearest wall. It may be interpreted as the ratio of the velocity scale of the turbulence, to the velocity scale of molecular diffusion for a diffusion length equal to the distance to

Table 1: Transition model constants. 2D and 3D means two- and three-dimensional flow

C_{SS}	C_T	A_T	a_l
2.0	14.5(2D), 15.5(3D)	10.0	0.45

the wall, thus ν/y . The starting function γ is

$$\gamma = \min(\zeta_T/A_T, 1); \quad \zeta_T = \max(\sqrt{k}y/\nu - C_T, 0) \quad (7)$$

where C_T is a threshold value and A_T a growth rate.

The starting function γ is zero in the inner part of a laminar boundary layer (approximately for $y/\delta < 0.5$). The damping factor f_{SS} (Eq. 4) is also small there. It means that small-scale turbulence is suppressed by both γ and f_{SS} in a laminar boundary layer. The starting function controls the small-scale turbulence production in the near-wall region. In the fully turbulent region both $\gamma = 1$ and $f_{SS} = 1$ over most of the boundary layer thickness. In a turbulent boundary layer, the shearshestering term f_{SS} is still active very close to a wall (near to the viscous sublayer), but this does not change the behaviour of the turbulence model.

In the model of Wilcox [2] the β coefficient (Eq. 2) is $\beta = \beta_0 f_\beta$ with $\beta_0 = 0.0708$. The f_β function is introduced to resolve the round-jet/plane-jet anomaly. The limit values of f_β are 1.0 (2D flow) and 0.85 (axisymmetric jet flow). Our observation is that f_β may be spuriously activated in 3D boundary layers (resulting in $f_\beta = 0.85$), so that turbulence is then suppressed with respect to 2D boundary layer flow. Transition onset is then delayed in 3D flows with respect to 2D flows. In the current work the model function f_β is changed to $f_{\beta S} = f_{d\gamma} f_\beta + (1 - f_{d\gamma})$, $f_{d\gamma} = \min(f_d, \gamma)$. The f_d term is the DES model shielding function by Spalart et al. [9], and γ is the starting function (Eq. 7). We use the shielding function f_d as a detector of the near-wall region. This change ensures that $f_\beta = 1$ over most of a 3D boundary layer, so that transition onset is not altered with respect to a 2D flow. The modification is only active near to walls (for f_d and γ close to zero, $f_{\beta S} = 1$) and it is inactive further away from walls ($f_d = \gamma = 1$, $f_{\beta S} = f_\beta$). So the underlying turbulence model is not modified in free-shear flows.

The algebraic transition model contains 4 constants: C_{SS} , C_T , A_T , and a_l (see Table 1). These parameters have been tuned on three ERCOFTAC flat plate test cases of the T3C series, T3C2, T3C3 and T3C5, relevant for bypass transition.

Steady 2D (2D RANS) and unsteady 3D (3D URANS) flow simulations of the T3C flat plates with sharp leading edges were performed with uniform profiles of velocity, k and ω at the inlet to the computational domain, located 0.05 m upstream of the leading edge. The parameters C_T , A_T and C_{SS} were tuned for the cases T3C5, with transition in accelerating flow, and T3C2, with transition just after the change of accelerating flow to decelerating flow. A somewhat higher value of the C_T constant is used in 3D simulations than in 2D simulations. With 3D URANS, there is some contribution to the modelled turbulence production term by the resolved part of the turbulence, as a result of a more fluctuating velocity field. This has as consequence that transition onset shifts upstream in 3D unsteady flows, with respect to 2D steady flows. The parameter a_l in the stress limiter of the large-scale eddy viscosity (Eq. 6) has a role for transition in adverse pressure gradient flow. We remind that the role of the stress limiter in the basic turbulence

model, used here for the small-scale eddy viscosity (Eq. 5), is the adjustment of the reattachment length of a turbulent separated boundary layer. The production of turbulence in a turbulent free shear layer is reduced by the limiter, as ω is spontaneously small in such a layer. The limiting allows increasing the reattachment length in an adverse pressure gradient flow [2]. Similarly, the stress limiter for the large-scale eddy viscosity (Eq. 6) reduces the production of turbulence in the outer part of a pre-transitional boundary layer in an adverse pressure gradient flow and delays the transition onset. The large scale eddy-viscosity is not used directly in the production term of the turbulent kinetic energy (Eq. 1), but it is part of the full eddy viscosity in the Navier-Stokes equations. Limiting of the large-scale eddy viscosity results in lower shear stress and, thus, reduced production of turbulent kinetic energy. We set $C_{lim} = 7/8$ and adjust a_l . The calibration was performed for the T3C3 case, which is characterized by a very late transition in adverse pressure gradient flow.

3 Computational Organisation

The computational grids consist of a structured boundary layer part with quadrilateral (2D) or hexahedral (3D) cells near to walls and an unstructured part away from walls. The grids are refined near to the walls. The y^+ parameter varies between 0.1 and 0.8 along walls. Typically about 40 cells are used across the boundary layer grid part. For 2D steady flow simulations in the cascades (N3-60, T106A) grids with $1.1 - 1.3 \times 10^5$ cells were employed. The grid density requirements are lower for flows over the flat plates, used for tuning, where grids with 0.8×10^5 cells were used. The 3D grids are generated by projection of the 2D meshes in the spanwise z -direction. The width of the computational domain was set to $L_z = 0.12C$ in z -direction (C means the chord length or length of the plate). This width was chosen based on the work of Lardeau et al. [10], who performed LES of the flow over part of a compressor blade at a comparable Reynolds number by setting $L_z = 0.12C$. They showed that such a spanwise width is sufficient for resolving the three-dimensional instability and breakdown to turbulence of a separated laminar boundary layer. 30 grid cells were used uniformly distributed in spanwise direction in all 3D cases. The 3D grids consist of $3.3 - 3.9 \times 10^6$ cells for cascades and 2.4×10^6 cells for flat plates. We take into account that 3D URANS can resolve instability of a separated boundary layer, provided that the eddy viscosity by the turbulence model is at a very low value. Actually, this then means functioning of 3D URANS as LES, which, of course, requires sufficient resolution in space and time and sufficient accuracy of the discretisation.

4 N3-60 Cascade

We first illustrate the performance of the model for transition in attached boundary layer state (2D RANS and 3D URANS) and in laminar boundary layer separation state (3D URANS) with the N3-60 cascade, measured by Zarzycki and Elsner [11]. The N3-60 profile is the enlarged profile of a stator vane in the high pressure part of a steam turbine. Geometric data are: blade chord 300 mm, axial blade chord 203.65 mm, blade pitch 240 mm. The exit velocity is $U_e = 30m/s$, which gives an exit Reynolds number of 6×10^5 . Measurements are available for inflow turbulence $T_u = 3\%$ and $T_u = 0.4\%$ in

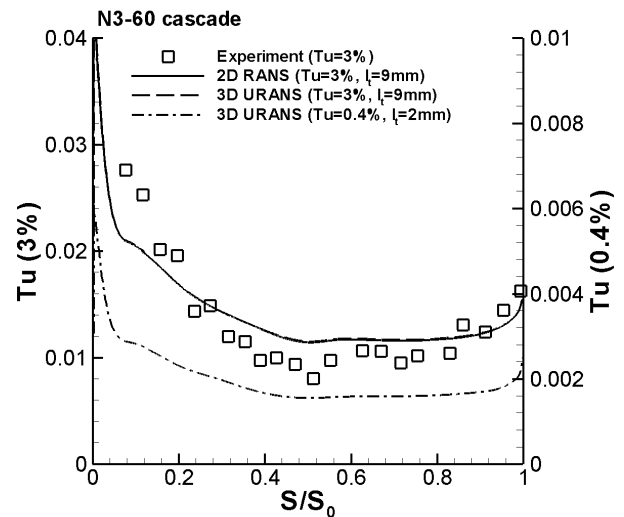


Figure 1: N3-60 cascade. Turbulence intensity along the suction side of the blade at distance 10 mm from the blade surface for $T_u = 3\%$ and $T_u = 0.4\%$

the leading edge plane. Laminar separation occurs at the suction side for $T_u = 0.4\%$.

At the inlet to the computational domain, placed at 0.34 times the axial chord length upstream of the leading edge, a uniform flow velocity in the axial direction was imposed. The inlet turbulence intensity in the leading edge plane was set, according to the two sets of experimental data. The inlet turbulent length scale was not reported in the measurements. For $T_u = 3\%$, the inlet turbulent length scale was adjusted by matching the measured turbulence intensity at a distance of 10mm from the blade surface (this is above the boundary layer edge). The obtained turbulent length scale is 9mm for $T_u = 3\%$. Fig. 1 shows the comparison between computed and measured turbulence intensity. The agreement is reasonably good which means that the inlet conditions for the modelled scalars have been set correctly.

For low turbulence level at inlet ($T_u = 0.4\%$), the evolution of the free-stream turbulence along the blade surface is not available in the database. We assume a smaller length scale at the entrance to the cascade than for high inlet turbulence level since no turbulence grid was installed in the laboratory measurements. We select $l_t = 2mm$, but we show later (for the T106A cascade) that results for transition in separated state are not very sensitive to the turbulent length scale. Fig. 1 shows the turbulent intensity at 10 mm above the blade surface for $T_u = 0.4\%$ obtained in the 3D URANS simulation. At the leading edge of the blade ($S/S_0 = 0$) the turbulence intensity decays sharply from 0.5-0.4% to 0.2%.

Fig. 2 shows time-averaged modelled turbulent kinetic energy for $T_u = 3\%$ (resolved turbulent kinetic energy is very small in this case; not shown) and the comparison between computed and measured shape factor H along the suction side of the blade. The transition onset ($S/S_0 = 0.75$) and the growth rate in the transition region are reproduced correctly with the current model.

Fig. 3 (top) shows time-averaged resolved turbulent kinetic energy for $T_u = 0.4\%$. The level of modelled k , is very low everywhere (not shown). Transition is obtained by resolved instability and onset of breakdown of the vortex structures originating from roll-up of the separated boundary layer. So nothing specific is done to trigger transition. The starting function γ is very low in the boundary layer along the full length of the suction

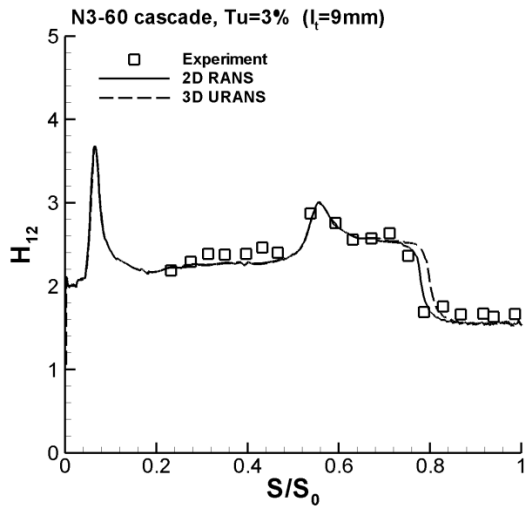
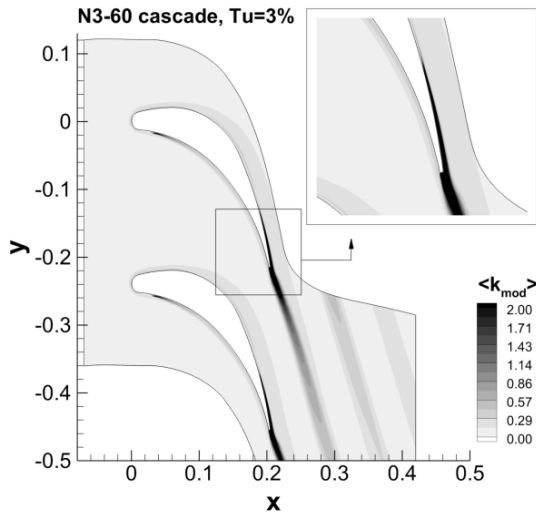


Figure 2: N3-60 cascade, $T_u = 3\%$. 3D URANS. Time-averaged modelled turbulent kinetic energy (top) and shape factor along the suction side of the blade (bottom)

side (not shown). It means that the role of the transition model is shielding the laminar and separated parts of the boundary layer from free-stream disturbances and that the transition process is resolved. So, the role of the transition model becomes very secondary. The shape factor distribution is shown in Fig. 3 (bottom). The agreement between measurement and simulation is good.

5 T106A Cascade

Computations were performed on the T106A cascade, measured by Opoka et al. [12]. The T106A profile is the enlarged profile of an LP gas turbine blade. Geometric data are: blade chord 198 mm, axial blade chord 170 mm, blade pitch 158.2 mm. The measured inflow angle is 37.7° . The exit Reynolds number is 1.6×10^5 . Measurements are available for inflow turbulence $T_u = 4\%$ and $T_u = 0.5\%$ in the leading edge plane. Laminar separation occurs at the suction side for $T_u = 0.5\%$. Due to the rather low Reynolds number, the flow is prone to separation for $T_u = 4\%$.

Both cases were simulated by time-accurate 3D URANS. A steady 2D RANS simulation was also done for $T_u = 4\%$. The inlet to the computational domain was set at 0.62 times the axial chord upstream of the leading edge. The inflow angle was set to 39.7° , which is 2° more

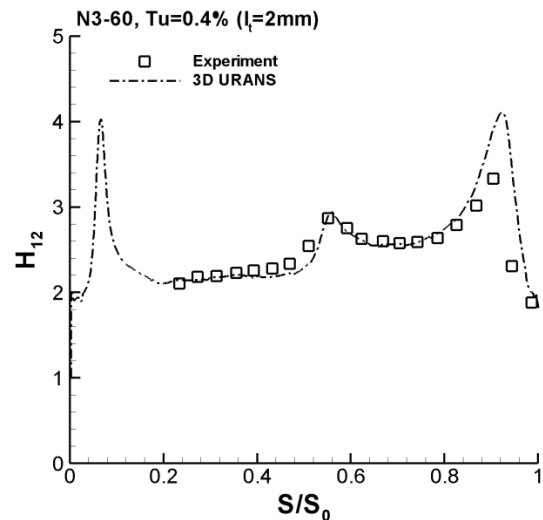
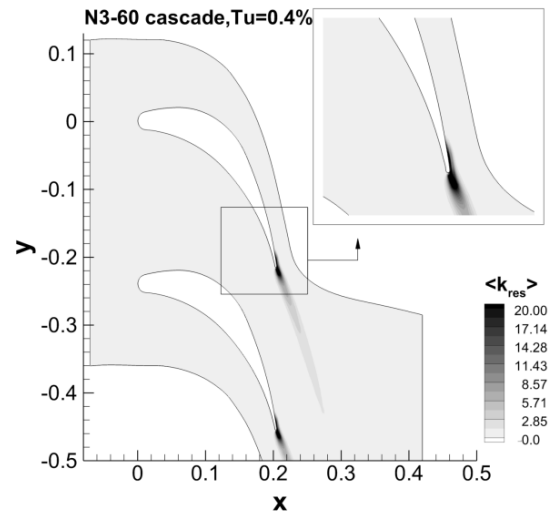


Figure 3: N3-60 cascade, $T_u = 0.4\%$. 3D URANS. Time-averaged resolved turbulent kinetic energy (top) and shape factor along the suction side of the blade (bottom)

than in the experiments, in order to match the pressure distribution on the profile (not shown). The need for a corrected inlet angle comes from flow leakage through the slots of a bar-passing mechanism at the entrance to the cascade in the experiments.

There is no information in the experiments on the turbulent length scale. In the computations, the inlet values of the turbulent kinetic energy were adjusted such that the turbulence intensity at distance 10 mm from the suction-side blade surface in the leading edge plane was equal to 4.0% and 0.5%. The inlet turbulent length scale was estimated based on a series of 2D RANS simulations with $T_u = 4.0\%$. Tests allowed to identify a range of turbulent length scales for which the transition model shows strong sensitivity ($l_t = 5 - 10\text{mm}$). From this dataset we selected $l_t = 7\text{mm}$. We cannot reproduce the inlet conditions with full confidence due to insufficient information about the experiments. A smaller turbulent length scale is needed with $T_u = 0.5\%$, since in the experiments the turbulence grid was removed. We selected $l_t = 2\text{mm}$. But for $T_u = 0.5\%$, results are not sensitive to turbulent length scale, as we show with the later Fig. 5 (bottom).

Fig. 4 (top) shows time-averaged modelled turbulent kinetic energy for $T_u = 4\%$ (resolved turbulent kinetic energy is very small; not shown). There is turbulence

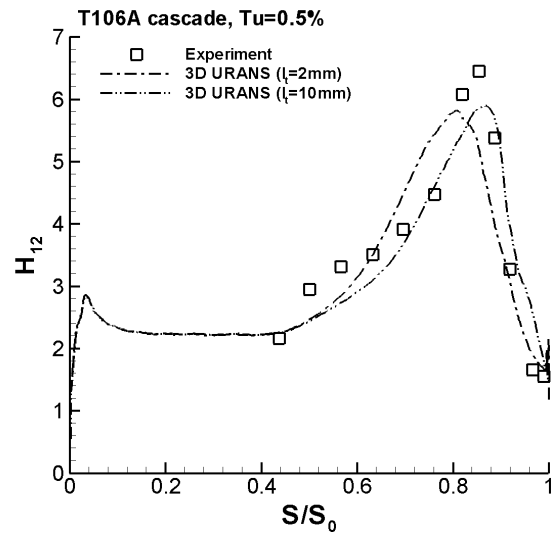
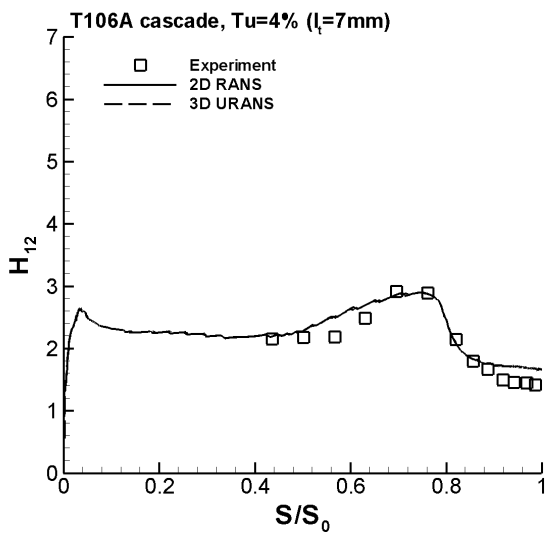
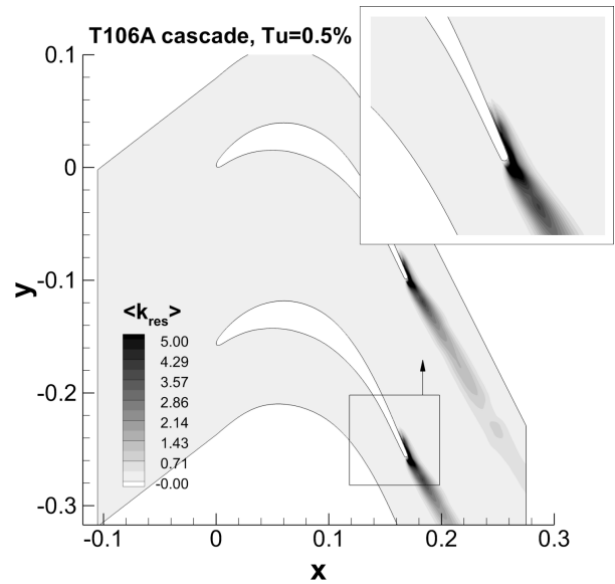
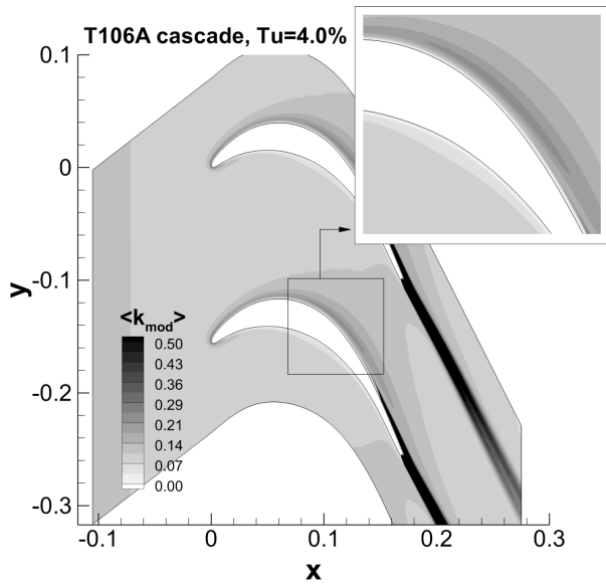


Figure 4: T106A cascade, $T_u = 4.0\%$. 3D URANS. Time-averaged modelled turbulent kinetic energy (top) and shape factor along the suction side of the blade (bottom)

Figure 5: T106A cascade, $T_u = 0.5\%$. 3D URANS. Time-averaged resolved turbulent kinetic energy (top) and shape factor along the suction side of the blade (bottom)

production due to shear at the suction side of a blade, already starting at the leading edge. It means that the turbulence level at the position of the transition is determined by both the oncoming turbulence and the turbulence produced in vicinity of the suction side. Fig. 4 (bottom) shows the shape factor on the suction side obtained with 2D RANS and 3D URANS for $T_u = 4\%$. The transition is of bypass type but the flow is prone to separation. Both results are in good agreement with the experiments and are also very close to each other. The growth rate of the turbulent production in the transitional flow region ($S/S_0 = 0.8$) is properly reproduced by the present model.

Fig. 5 (top) shows time-averaged resolved turbulent kinetic energy for $T_u = 0.5\%$. The level of modelled k , is very low everywhere (not shown). Similarly as for the low Tu -case with the N3-60 profile, transition is obtained by resolved instability and onset of breakdown of the vortex structures originating from roll-up of the separated boundary layer. Fig. 5 (bottom) shows the comparison of the shape factor from measurements and computations with 3D URANS for $T_u = 0.5\%$. In this case, the transition occurs in the separated laminar boundary

layer. Changing the turbulent length scale from 2 mm to 10 mm causes only a small change in the shape factor distribution. The separation is somewhat later, but the transition in the separated boundary layer is somewhat faster with $l_t = 10mm$ than with $2mm$. In this case, the role of the underlying turbulence/transition model is much less than in the high turbulence case. It also means that in flows with strong laminar boundary layer separation at low free-stream turbulence a change of the inlet turbulent length scale has much less influence on the transition onset location than in attached boundary layer flows at high free-stream turbulence. The above results indicate that 2D RANS and 2D URANS cannot be successful for transition in separated state at low free-stream turbulence, since 2D simulations cannot detect three-dimensional instability and breakdown.

6 Conclusions

An algebraic model has been illustrated for simulation of bypass transition. The model requires only local variables and is coupled with the newest version of the $k-\omega$ RANS turbulence model by Wilcox.

The model gives good results for transition in boundary layers in attached state (N3-60 cascade, $T_u = 3\%$), state prone to separation (T106A cascade, $T_u = 4\%$) and separated state (N3-60 cascade, $T_u = 0.4\%$; T106A cascade, $T_u = 0.5\%$). The 3D URANS technique is successful for transition simulation in a separated laminar boundary layer at low free-stream turbulence level owing to its ability to resolve the instability of the vortex structures in the separated shear layer.

Acknowledgement

The first author acknowledges support from a research project funded by the Polish National Science Centre (contract number UMO-2011/01/B/ST8/07267).

References

- [1] Kubacki S., Dick E., An algebraic model for bypass transition in turbomachinery boundary layer flows. *Int. J. Heat and Fluid Flow*, 58, 68-83, 2016.
- [2] Wilcox D.C., Formulation of the $k - \omega$ turbulence model revisited. *AIAA J.*, 46, 2823-2837, 2008.
- [3] Hack M.J.P., Zaki T.A., Streak instabilities in boundary layers beneath free-stream turbulence, *J. Fluid Mech.* 741, 280-315, 2014.
- [4] McAuliffe B.R., Yaras M.I., Transition mechanisms in separation bubbles under low- and elevated freestream turbulence, *J. Turbomachinery* 132, 011004/1-10, 2010.
- [5] Walters D.K., Leylek J.H., A new model for boundary layer transition using a single-point RANS approach, *J. Turbomachinery* 126, 193-202, 2004.
- [6] Walters D.K., Cokljat D., A three-equation eddy-viscosity model for Reynolds-averaged Navier-Stokes simulations of transitional flow, *J. Fluids Engineering* 130, 2401/1-14, 2008.
- [7] Jacobs. R.G., Durbin P.A., Simulations of bypass transition, *J. Fluid Mech.* 428, 185-212, 2001.
- [8] Walters. K., Physical interpretation of transition-sensitive RANS models employing the laminar kinetic energy concept, *Ercoftac Bulletin* 80, 67-76, 2009.
- [9] Spalart P.R., Deck S., Shur M.L., Squires K.D., Strelets M.Kh., Travin A., A new version of detached-eddy simulation, resistant to ambiguous grids, *Theor. Comput. Fluid Dyn.*, 20, 181-195, 2006.
- [10] Lardeau S., Leschziner M., Zaki T., Large eddy simulation of transitional separated flow over a flat plate and a compressor blade. *Flow Turbulence Combust.*, 88, 19-44, 2012.
- [11] Zarzycki R., Elsner W., The effect of wake parameters on the transitional boundary layer on a turbine blade, *IMEchE Part A, J. Power and Energy*, 219, 471-480, 2005.
- [12] Opoka M.M, Thomas R.L., Hodson H.P., Boundary layer transition on the high lift T106A low-pressure turbine blade with an oscillating downstream pressure field, *J. Turbomachinery*, 130, 021009/1-10, 2008.

TRANSITION MODELLING IN INTERNAL AND EXTERNAL AERODYNAMICS USING VARIOUS TRANSITION MODELS

J. Příhoda¹, J. Fürst², P. Straka³, P. Louda² and M. Kožíšek¹

¹*Institute of Thermomechanics AS CR, Prague, Czech Republic*

²*Faculty of Mechanical Engineering, Czech Technical University in Prague, Czech Republic*

³*Aerospace Test and Research Establishment, Plc, Prague, Czech Republic*

prihoda@it.cas.cz

Introduction

The advanced modelling of the laminar/turbulent transition is of a great importance for numerical simulations of flows in internal and external aerodynamics, especially for flows around turbine and compressor blades and airfoils where the transition substantially influences the prediction of energy losses and heat transfer.

Besides the natural transition under very low free-stream turbulence, the bypass transition caused by the diffusion of turbulent fluctuations from turbulent free stream to the boundary layer usually occurs in technical applications especially in turbomachinery. The transition can arise in attached and/or separated flows as well. Moreover, the transition can be evoked by the passing wakes of upstream blades in turbomachinery.

Most of transition models are based on the transport and/or algebraic equation for the intermittency coefficient, as e.g. Lodefier and Dick [1], Langtry and Menter [2], and Thermann and Niehuis [3], Straka and Příhoda [4]. Nevertheless, all these models need empirical correlations for the onset and length of the transition region and their application is limited for low free-stream turbulence. Further, the three-equation $k-k_L-\epsilon$ model of Walters and Leylek [5] is based on the laminar kinetic concept proposed by Mayle and Schulz [6].

The paper deals with the transition modelling in flows with different free-stream turbulence levels. Several different approaches were applied especially the algebraic transition model according to Straka and Příhoda [7], the model with transport equations for the free-stream and near-wall intermittency components by Lodefier and Dick [1], and the three-equation $k-k_L-\omega$ model of Walters and Cokljat [8].

Mathematical Model

The Favre-averaged Navier-Stokes equations are closed partly by the explicit algebraic Reynolds stress turbulence model (EARSM) according to Hellsten [9] connected with the algebraic transition model of Straka and Příhoda [7] and partly by the three-equation $k-k_L-\omega$ model of Walters and Cokljat [8]. Further, the $\gamma-\zeta$ transition model of Lodefier and Dick [1] was used together with the SST and/or the EARSM turbulence models.

Mathematical models based on the finite-volume method were implemented into in-house numerical codes and/or into the OpenFOAM code for incompressible and compressible flows.

Algebraic Transition Model

The modified algebraic transition model is based on the concept of different values of the intermittency coefficient in the boundary layer γ_i and in the free stream γ_e . The intermittency coefficient in the boundary layer is given by the relation

$$\gamma_i = 1 - \exp[-\hat{n}\sigma(Re_x - Re_{xt})^2] \quad (1)$$

proposed by Narasimha [10]. The transition onset is given by the momentum Reynolds number $Re_{\theta t}$ as a function of the free-stream turbulence Tu and the pressure gradient parameter λ_t . The empirical correlation for the transition onset proposed by Straka and Příhoda [4] was later modified for the low free-stream turbulence by Příhoda et al. [11].

The length of the transition region is expressed by the parameter $N = \hat{n}\sigma Re_{\theta t}^3$ introduced by Narasimha [12] where \hat{n} and σ are spot generation and spot propagation parameters. The empirical correlation proposed by Solomon et al. [13] was used for the attached flow. The onset and length of transition region in separated flow is determined according to Mayle [14] using correlations allowing the same approach as in the attached flows.

According to Langtry and Menter [2], the maximum of the vorticity Reynolds number

$$Re_{v,max} = \max(y^2|\Omega|/\nu) \quad (2)$$

is used to avoid the calculation of the momentum Reynolds number Re_θ in cases with complex flow geometry. This link is given by the relation

$$Re_\theta = Re_{v,max}/C \quad (3)$$

where $C = 2.185$ for the Blasius laminar boundary layer. Using similar solutions of Falkner and Skan [15], this relation was generalized in the form $C = f(L)$ where the pressure gradient parameter L is defined by the relation

$$L = Re_{v,max}^2 \frac{\nu}{U_e^2} \frac{dU_e}{dx} \quad (4)$$

The smooth link-up between both zones is considered by the relation

$$\gamma = \frac{\gamma_i + \gamma_e}{2} + \frac{\gamma_e - \gamma_i}{2} \operatorname{tgh} \left[C_\gamma \left(\frac{y}{\delta_{995}} - 1 \right) \right] \quad (5)$$

with the constant $C_\gamma \approx 12 \div 18$. The boundary layer thickness δ_{995} is given by the relation $\delta_{995}/y_{max} = g(L)$ where y_{max} is the position of the maximum vorticity

Reynolds number. Free-stream parameters relevant for the estimation of the transition are determined at the edge of the boundary layer.

The algebraic transition model was used together with the EARSM model proposed by Hellsten [9]. The Reynolds stress in the EARSM model is expressed by the anisotropy tensor $a_{ij} = \tau_{ij}/k - 2\delta_{ij}/3$ given by the fourth order polynomial with coefficients depending on invariants of strain-rate and vorticity tensors. Turbulent scales are expressed by the turbulent energy k and the specific dissipation rate ω . The turbulent time scale $\tau \sim 1/\omega$ is modified near the wall by the Kolmogorov time scale. The transport equations for k and ω are used in the two-layer form with two sets of model coefficients and with the blending function similarly as the SST model proposed by Menter [16]. For the reduction of the undesirable overproduction of the turbulent energy in the stagnation region, the production term in the turbulent energy equation was modified by Straka and Pířhoda [7]. For the prediction of the transitional flows, the production and destruction terms in the k -equation are multiplied by the intermittency coefficient γ . Similarly, the effective viscosity is given by $\mu_{ef} = \mu + \gamma\mu_t$ in the transition region.

The algebraic model was implemented into the inhouse numerical code. The code is based on the finite volume method of the cell-centered type with the Osher's-Solomon's approximation of the Riemann solver and a two-dimensional linear reconstruction with the Van Albada's limiter. The governing equations are discretized using a multi-block quadrilateral structured grid with a block overlapping implementation.

$k - k_L - \omega$ model

The three-equation model proposed by Walters and Leylek [5] and later modified by Walters and Cokljat [8] is based on the assumption that velocity fluctuations before the transition can be divided into small vortices contributing to the production of turbulence and large mainly longitudinal vortices near the wall contributing to the production of non-turbulent fluctuations. The transition process is expressed by the transfer from the energy of non-turbulent velocity fluctuations k_L to the turbulent energy k_T of three-dimensional turbulent velocity fluctuations. The transition model is based on transport equations for the turbulent energy k_T , laminar energy k_L and the specific dissipation rate ω . The $k - k_L - \omega$ model is based on local variables only and can be used for complex geometries using unstructured grids.

The free accessible program OpenFOAM with the own implementation of the revised $k - k_L - \omega$ model was used for the simulation of the transitional flows. The system of governing equations was solved by the SIMPLE and SIMPLEC algorithms respectively for incompressible and compressible flows (see Fürst et al. [17], Kořížek et al. [18]). The convective terms were discretized by the upwind method with the reconstruction of the second degree and the viscous terms by means of the central scheme.

Further, the model was modified for very low freestream turbulence by the introduction of the pressure gradient sensitive parameter in the threshold function for the natural transition onset (see Fürst et al. [19]).

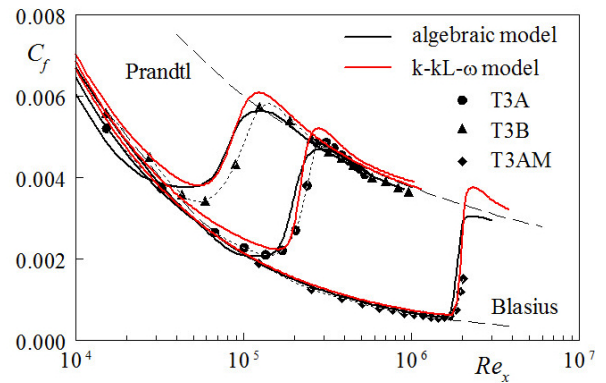


Figure 1: Skin friction distribution for test cases T3A, T3B and T3AM

The $\gamma - \zeta$ Transition Model

The $\gamma - \zeta$ transition model of Lodefier and Dick [1] is based on transport equations for near-wall and freestream intermittency components. This model with the SST turbulence model of Menter [16] and/or the EARSM turbulence model of Hellsten [9] was implemented into the in-house numerical code based on the implicit finite volume method for the simulation of 2D and 3D compressible flow assuming structured multi-block grids (see Louda et al. [20, 21]).

The Reynolds stress in the Navier-Stokes equations was multiplied by the turbulence weighting factor $\tau_t = \max[\min(\zeta + \gamma, 1); 0]$. Similarly, the production and destruction terms in the k -equation were modified in the transitional flow. The ω -equation is unchanged for transition modelling, but the time scale restriction by Medic and Durbin [22] was introduced in the destruction term to improve the behaviour in impact zones. The empirical criteria of Abu-Ghannam and Shaw [23] and Mayle [14] were used for the estimation of the transition onset. The length of the transition was determined by means of parameters $\hat{n}\sigma$ according to Steelant and Dick [24].

The $\gamma - \zeta$ transition model is not up to now modified for local variables and so needs the integration across the boundary layer. Relevant values of free-stream turbulence level and the pressure gradient parameter are determined at the boundary layer edge, where the free-stream velocity gradient determined in the streamwise direction.

Results

The algebraic transition model and the $k - k_L - \omega$ model were tested by several test cases covering flows with the transition in attached and separated flows with various free-stream turbulence and pressure gradient, namely boundary-layer flows, flows around airfoils including the effect of the foregoing wake, and flow through the VKI turbine blade cascade (see Straka et al. [25, 26], Fürst et al. [17, 27]). Some models then were used for simulations of 2D and 3D compressible flows through linear turbine blade cascades. The transition models were tested by means of test cases from the ERCOFTAC database concerning to flatplate flow with various free-stream turbulence both with the constant free-stream velocity (T3A, T3AM, T3B), and with the velocity distribution corresponding to the suction side of the aft-loaded turbine blade (T3C).

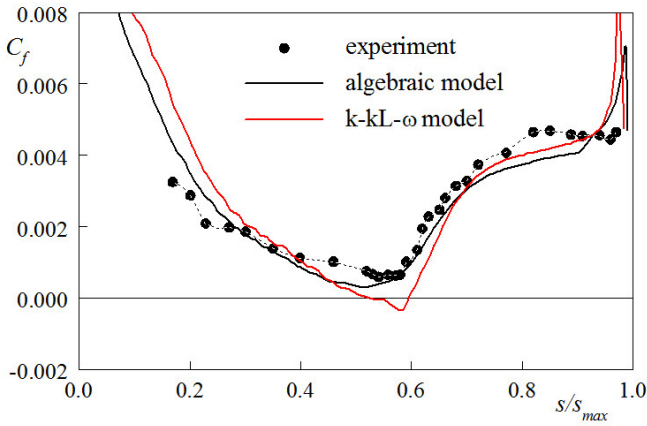


Figure 2: Skin friction distribution on the suction side of the VKI turbine blade

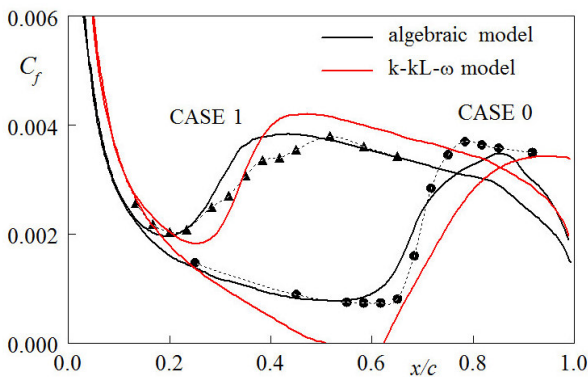


Figure 3: Skin friction distribution on the airfoil NACA 0012

The predicted distribution of the skin friction coefficient for the flat-plate cases is compared with experimental data in Fig. 1. Numerical results predicted very well the onset and the length of the transition region for the all cases covering flow both with low free-stream turbulence ($Tu < 1\%$), and with high free-stream turbulence ($Tu \approx 6\%$), corresponding to turbomachinery flows.

The proposed transition model was further applied for the subsonic flow in the plane turbine blade cascade VKI according to Canepa et al. [28]. Simulations were carried out for the outlet Reynolds number related to the chord $Re_c = 5.9 \times 10^5$ and the inlet angle $\alpha_1 = 0^\circ$. The inlet turbulence intensity was chosen $Tu = 1.5\%$. The distribution of the skin friction coefficient $C_f = 2\tau_w/\rho_e U_e^2$ on the blade suction side is shown in Fig. 2.

The agreement of numerical results obtained by both models is quite good even though the three-equation model predicts a short separation region.

The effect of an incoming wake on the transition on airfoils was tested by means of measurements of Lee and Kang [29]. The flow around the NACA 0012 airfoil located in the wake behind another upstream airfoil was simulated for the Reynolds number $Re_c = 6 \times 10^5$, zero angle of attack and free-stream turbulence $Tu = 0.3\%$.

The distribution of the friction coefficient C_f on the NACA 0012 airfoil is shown in Fig.3 for the single airfoil (CASE 0) and for two airfoils in tandem (CASE 1). The agreement of both predicted parameters with experimental data is again quite good especially for the algebraic transition model. Due to the incoming wake, the transition onset is moved upstream from $x/c = 0.62$ to

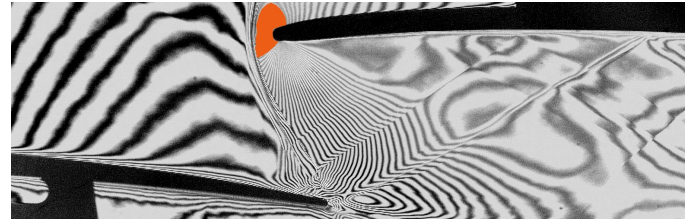


Figure 4: Interferogram of flow field in the blade cascade

$x/c = 0.20$. The effect of the foregoing airfoil on the pressure coefficient is small.

The algebraic transition model was applied for simulations of compressible flows through turbine blade cascades. Among others, numerical simulation of 2D compressible flow through the linear turbine blade cascade TR-U-4 corresponding to the tip-section of the LP part of a steam turbine was carried out, see Luxa et al. [30]. The numerical simulation was carried out for the stagger angle $\gamma = 78.37^\circ$, the relative spacing $t/b = 0.951$ and the design inlet flow angle $\alpha_1 = 81.25^\circ$. Simulations completed for the Reynolds number $Re_{2is} = 1.8 \times 10^6$ and Mach number $M_{2is} = 1.998$ were focused particularly on the effect of shock waves on the shear layer development including the laminar/turbulent transition. Interactions of shock waves with shear layers on both sides of the blade result usually in the transition in attached and/or separated flow and so to the considerable impact to the flow structure and energy losses in the blade cascade.

Due to supersonic inlet conditions, the flow through the blade cascade is influenced by parasitic shock waves arising by the reflection from the computational domain boundaries. The application of the quadrilateral block-structured computational grids with their overlapping leads moreover to the reflection of shock waves on the block boundaries. Therefore the computational domain was adequately prolonged before and behind the blade cascade to weaken these reflections.

The constant values of the total pressure p_{01} , total temperature T_{01} and incidence angle α_1 were prescribed as inlet conditions. The static pressure was extrapolated from the computational domain. The static pressure given by the outlet isentropic Mach number was prescribed as the outlet condition. Inlet free-stream turbulence was chosen $Tu = 5\%$. The ratio of viscosities μ_t/μ was chosen according to the length of inlet part. The free-stream turbulence in the distance of one spacing before the cascade was $Tu = 1.2\%$.

The interferogram of the flow through the blade cascade is shown in Fig. 4. The flow field in the interblade channel is supersonic, with a small subsonic region around the leading edge. In the relatively small area of the interblade channel, very intense supersonic simple expansion takes place on the suction side near the leading edge. The interaction is more complex and included a local separation.

The distribution of the pressure coefficient along the blade obtained is shown in Fig. 5. The coordinate s is measured along the blade surface from the leading edge. The pressure distribution does not correspond quite well to experiment, but it is clear that location of the exit shock/suction side boundary layer interaction is at $s/s_{max} \approx 0.5$.

The field of Mach number isolines obtained by the numerical simulation is shown in Fig. 6. Because of the stagger angle and inlet flow conditions, the concave side of the blade is the suction type while the convex side is of the pressure type.

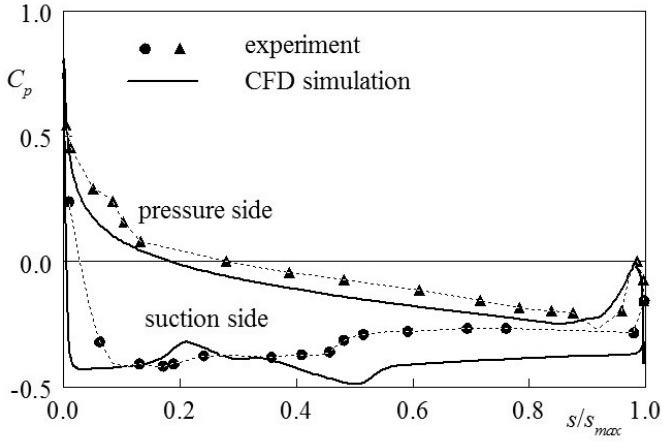


Figure 5: Distribution of the pressure coefficient

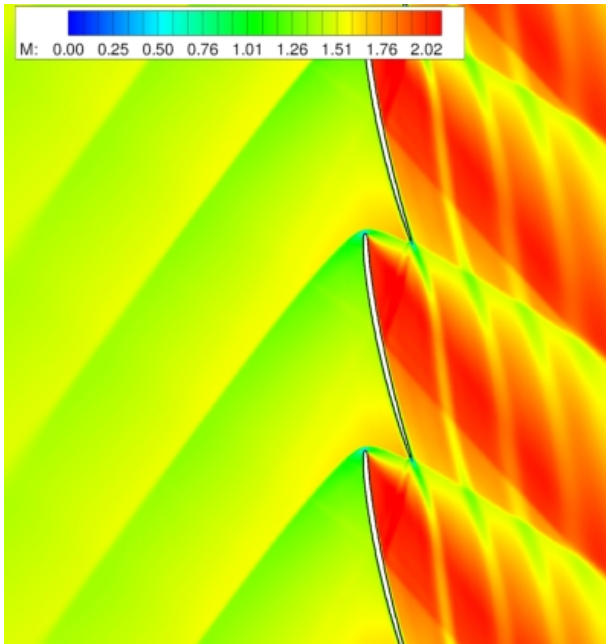


Figure 6: Mach number isolines in the detail of the computational domain

The bypass transition on the suction side is evident from the distribution of the skin friction coefficient shown in Fig. 7. The interaction of the boundary layer with the inner branch of the exit shock wave can be seen at distance $s/s_{max} \approx 0.5$ from the leading edge. Following the smooth development of the laminar boundary layer, the separated-flow transition with a short separation region and following reattachment occurs on the pressure side before the trailing edge due to the interaction with the front shock wave from the adjacent blade.

Comparison of the flow field in the interaction region obtained by simulation and schlieren technique is shown in Fig. 8. It follows from preceding figures that the reflected oblique shock wave impinges on the suction side where the interaction with the boundary layer causes the bypass transition in attached flow at the distance $s/s_{max} \approx 0.5$ from the leading edge. On the contrary, the impact of the front shock wave from the adjacent blade leads on the pressure side to the transition in separated flow at the distance $s/s_{max} \approx 0.88$ from the leading edge.

Both experimental and numerical results show flow structure typical for the shock/boundary layer interaction with the local separation region. Impinging front

shock causes boundary layer to separate with separation point upstream of the interaction. Effective change of the flow surface at the separation point and reattachment point results in origin of two left running shock-waves. In case of experiment, the separation region is noticeably longer and the point of front shock impingement is closer to the trailing edge. The interaction of shock waves with shear layers on the both blade sides leads to the transition in attached and separated flow respectively and therefore to a noticeable impact on the flow structure and energy losses. Simulations show the important effect of the transition modelling on the relevant description of flow through the blade cascade.

Finally, the transition $\gamma - \zeta$ model of Lodefier and Dick [1] with the EARSM turbulence model of Hellsten [8] was applied for the simulation of the 3D compressible flow with side walls through the turbine blade cascades, see Louda et al. [20, 21]. Numerical results are shown for the transonic flow through the prismatic turbine blade cascade VS33 with the relative spacing $t/b = 0.7$ and the aspect ratio $AR = 1$. Simulations were carried out for the inlet angle $\alpha_1 = 0^\circ$, the outlet isentropic Mach number $M_{2is} = 0.9$ and the Reynolds number $Re_{2is} = 8.5 \times 10^5$ based on the chord length. The inlet turbulence was described by $Tu = 5\%$ and $\mu_t/\mu = 100$. The effect of boundary layers on side walls was not considered.

The mathematical model is solved by the implicit AUSM finite volume method on multi-block structured grids. The implementation of transition model does not rely on explicit prescription of boundary layer edge and is adaptive as long as the whole thickness of boundary layer is contained in one block, which is typically O grid around the blade consisting of several blocks in tangential direction. The grid is refined near walls giving wall distance $y^+ < 1$ for first cell centres. Also the treatment of corners is automatic.

The 3D view of the Mach number isolines very near the suction side and one of side walls is shown in Fig. 9. There is an abrupt increase of the Mach number where the transition starts on the suction side.

The location of transition on the suction side can be observed by means of the near-wall intermittency γ plotted in Fig. 12. The figure shows γ on the wall, where the blue colour corresponds to laminar state and the red colour to turbulent state. The transition onset moves upstream in the proximity of the side wall. The boundary layer is fully laminar on the pressure side.

The skin friction distribution on the blade at different span-wise positions is shown in Fig. 11. The value of

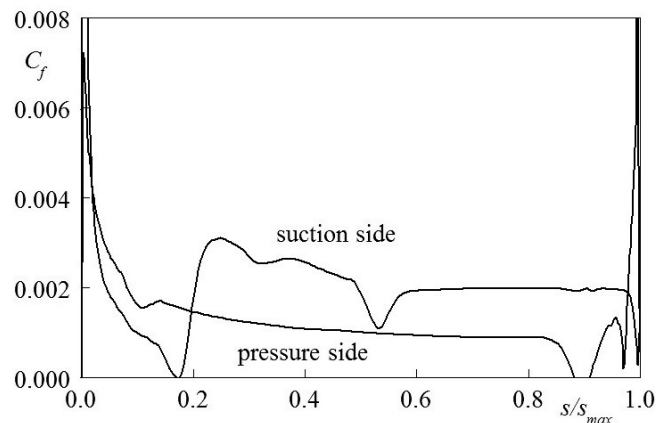


Figure 7: Distribution of the skin friction

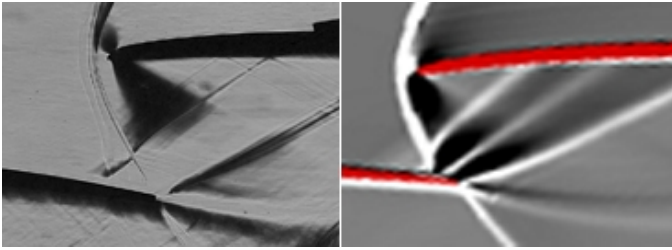


Figure 8: Comparison of flow in the region of interaction of the front shock and pressure side boundary layer (a) experiment; b) CFD simulation)

$z/b = 0$ denotes mid-span plane and the negative values merely correspond to the suction side, where is no separation of the flow (no zero crossing except at the leading and trailing edge). The transition occurs latest in central part of the blade in 2D flow. Approaching side wall, the transition onset moves forward from $z/b \approx 0.3$ but very near the side wall ($z/b = 0.49$) is again shifted slightly downstream.

Conclusions

Several transition models were tested by the standard test cases and applied for the simulation of transitional flows in various boundary conditions mostly for turbomachinery flows. The simple algebraic model is suitable for testing and verification of necessary empirical correlations. Presently the modification of the algebraic transition model for the wall roughness effect is in progress. The $k-k_L-\omega$ model can be applied for the simulation of complex shear flows on unstructured grids without any restriction. On the other hand, the algebraic transition model was adapted for local variables only but structured grids are preferred near walls.

The transition models with the algebraic and/or transport equation for the intermittency coefficient should be modified for local variables only for the application in complex boundary conditions using unstructured grids. The three-equation model seems to be more general as it can be used without any restrictions but the generalization of used empirical inputs is rather complicated unlike transition models with the intermittency coefficient.

Acknowledgement

The work was supported by the Czech Science Foundation under the grant P101/12/1271 and by the Technology Agency of the Czech Republic under the grant TA03020277. The institutional support RVO 61388998 is also gratefully acknowledged.

References

- [1] Lodefier K., Dick E., "Modelling of unsteady transition in low-pressure turbine blade flows with two dynamic intermittency equations", *Flow, Turbulence and Combustion*, Vol. 76, pp. 103-132, 2006
- [2] Langtry R. B., Menter F. R., "Correlation-based transition modeling for unstructured parallelized computational fluid dynamics codes", *AIAA Jour.*, Vol. 47, pp. 2894-2906, 2009
- [3] Thermann H., Niehuis R., "Unsteady Navier-Stokes simulation of a transonic flutter cascade near-stall

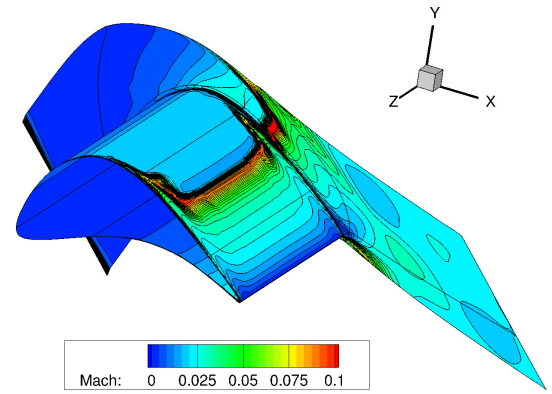


Figure 9: Isolines of Mach number near walls

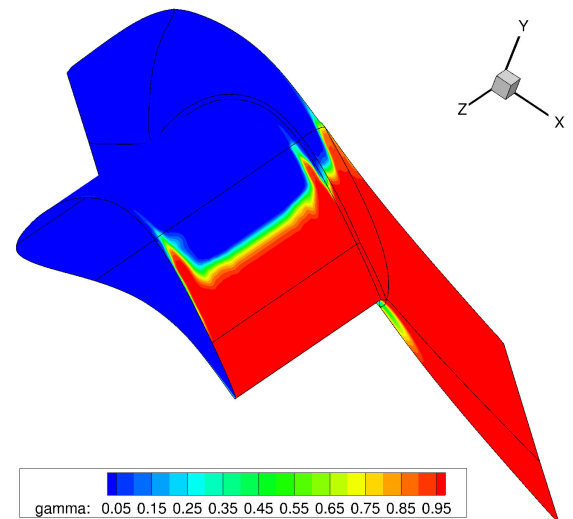


Figure 10: Isolines of intermittency γ near the walls

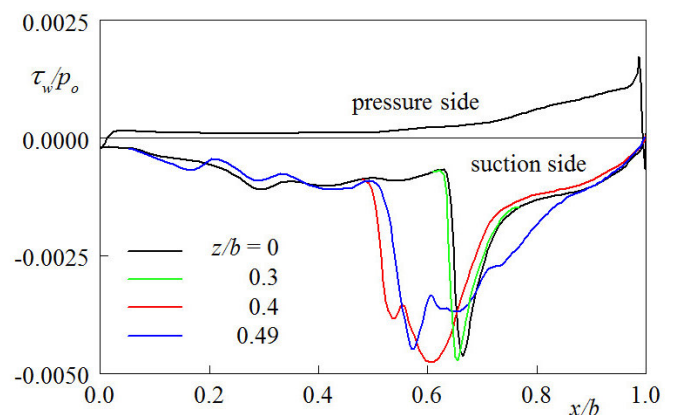


Figure 11: Skin friction on blade surface along the span

- conditions applying algebraic transition models", *Jour. Turbomachinery*, Vol. 128, pp. 474-483, 2006
- [4] Straka P., Příhoda J., "Application of the algebraic bypass-transition model for internal and external flows", *Proc. Conf. Experimental Fluid Mechanics 2010*, Liberec, 636-641, 2010
- [5] Walters D. K., Leylek J. H., "A new model for boundary-layer transition using a single-point RANS approach", *Jour. Turbomachinery*, Vol. 126, pp. 193-202, 2004
- [6] Mayle R. E., Schulz A., "The path to predicting bypass transition", *Jour. Turbomachinery*, Vol. 119, pp. 405-411, 1997
- [7] Straka P., Příhoda J., "Numerical simulation of compressible transitional flow through high-loaded turbine blade cascade", *Proc. Conf. Topical Problems of Fluid Mechanics 2014*, Praha, pp. 131-134, 2014
- [8] Walters D. K., Cokljat D., "A three-equation eddy-viscosity model for Reynolds-averaged Navier-Stokes simulations of transitional flow", *Jour. Fluids Engineering*, Vol. 130, pp. 121401, 2008
- [9] Hellsten A., "New two-equation turbulence model for aerodynamics applications", PhD Thesis, Helsinki University of Technology, 2004
- [10] Narasimha R., "On the distribution of intermittency in the transition region of a boundary layer", *Jour. Aerospace Science*, Vol. 24, pp. 711-712, 1957
- [11] Příhoda J., Straka P., Fürst J., Popelka L., "Comparison of various laminar/turbulent transition models", *AIP Conference Proceedings*, Vol. 1608, American Institute of Physics, pp. 202-205, 2014
- [12] Narasimha R., "The laminar-turbulent transition zone in the boundary layer", *Progress in Aerospace Science*, Vol. 22, pp. 29-80, 1985
- [13] Solomon W. J., Walker G. J., Gostelow J. P., "The laminar-turbulent transition zone in the boundary layer", *Jour. Turbomachinery*, Vol. 118, pp. 744-751, 1996
- [14] Mayle R. E., "The role of laminar-turbulent transition in gas turbine engines," *Jour. Turbomachinery*, Vol. 113, pp. 509-537, 1991
- [15] Falkner V. M., Skan S. W., "Some approximate solutions of the boundary layer equations", *Phil. Mag.*, Vol. 12, pp. 865-896, 1930
- [16] Menter F. R., "Two-equation eddy-viscosity turbulence models for engineering applications", *AIAA Jour.*, Vol. 32, pp. 1598-1605, 1994
- [17] Fürst J., Příhoda J., Straka P., "Numerical simulation of transitional flows", *Computing*, Vol. 95, pp. 163-182, 2013
- [18] Kožíšek M., Martinez J., Fürst J., Příhoda J., Dofferer P., "Implementation of $k - k_L - \omega$ turbulence model for compressible transitional flow into OpenFOAM", *Conf. Topical Problems of Fluid Mechanics 2015*, Praha, pp. 93-98, 2015
- [19] Fürst J., Islam M., Příhoda J., Wood D., "Towards pressure gradient sensitive transitional $k - k_L - \omega$ model: The natural transition for low Re airfoils", *Proc. Conf. Topical Problems of Fluid Mechanics 2015*, Praha, pp. 65-70, 2015
- [20] Louda P., Kozel K., Příhoda J., "On numerical simulation of transition to turbulence in turbine cascade", *Lecture Notes in Computational Science and Engineering*, Vol. 108, 10 p., Springer, 2015
- [21] Louda P., Příhoda J., Kozel K., "Numerical modelling of bypass transition in turbine cascades", *Proc. Conference on Modelling Fluid Flow (CMFF'15)*, Budapest, 7 p., 2015
- [22] Medic G., Durbin P., "Toward improved prediction of heat transfer on turbine blades", *Jour. Turbomachinery*, Vol. 124, pp. 187-192, 2002
- [23] Abu-Ghannam B. J., Shaw R.: "Natural transition of boundary layers - The effects of turbulence, pressure gradient and flow history", *Jour. Mech. Eng. Sci.*, Vol. 22, pp. 213-228, 1980
- [24] Steelant J., Dick E., "Modelling of bypass transition with conditioned Navier-Stokes equations coupled to an intermittency transport equation", *Int. Jour. Num. Methods in Fluids*, Vol. 23, pp. 193-220, 1996
- [25] Straka P., Příhoda J., "Modification of an algebraic bypass-transition model in region near the stagnation point", *Proc. Conf. Topical Problems of Fluid Mechanics 2011*, Praha, pp.105-108, 2011
- [26] Straka P., Příhoda J., Šimurda D., "Modelling of the effect of the foregoing wake on the bypass transition on the airfoil", *EPJ Web of Conferences*, Vol. 45, 01091, 8 p., 2012
- [27] Fürst J., Straka P., Příhoda J., Šimurda D., "Comparison of several models of the laminar/turbulent transition", *EPJ Web of Conferences*, Vol. 45, 103032, 6 p., 2013
- [28] Canepa E., Cattanei A., Pittaluga F., Ubaldi M., Zunino P., "Transitional boundary layer on the suction side of a turbine blade at different Reynolds numbers", *Proc. 5th European Conf. on Turbomachinery*, Praha, pp. 911-923, 2003
- [29] Lee H., Kang S.-H., "Flow characteristics of transitional boundary layers on an airfoil in wakes", *Jour. Fluids Engineering*, Vol. 122, pp. 522-532, 2000
- [30] Luxa M., Příhoda J., Šimurda D., Straka P., Synáč J., "Investigation of the compressible flow through the tip-section turbine blade cascade with super-sonic inlet", *Proc. of the 12th International Symposium on Experimental Computational Aerothermodynamics of Internal Flows*, Paper No. ISAIF12-027, 8 p., Lercici, Italy, 2015

ADAPTING THE γ - \widetilde{R}_{θ_t} TRANSITION MODEL TO A k - l TURBULENCE MODELING FRAMEWORK

A. Minot¹, J. Marty², J. Perraud² and G. Casalis²

¹SAFRAN Snecma

²ONERA - the French Aerospace Lab

Abstract

A common way to model transition is through the use of the γ - \widetilde{R}_{θ_t} model of Langtry and Menter [1] along side a k - ω turbulence model. In this paper, we test the γ - \widetilde{R}_{θ_t} transition model along side the k - l of Smith [2] turbulence model. We show that light modifications of the transition model are necessary in order to obtain a correct behavior of the new k - l - γ - \widetilde{R}_{θ_t} model. Furthermore, we found that these modifications yielded accurate prediction of transition location on attached high-pressure turbine flows, but that for detached flows, recalibration of the transition model was necessary.

1 Introduction

In turbomachine applications, laminar-turbulent transition influences strongly on the aerodynamic performances. This is especially true in the turbines because of the small Reynolds number and/or the high adverse pressure gradient which may lead to boundary layer separation and development of separation bubbles. In RANS computations, transition can be modeled through the use of transition criteria and intermittency functions [3, 4], a single transport equation [5, 6] or two transport equations [1]. The present investigation focuses on the last method. The γ - \widetilde{R}_{θ_t} model of Langtry and Menter is usually coupled to the k - ω turbulence models as in [7, 8, 9, 10]. This is the original version of the transition model. Some authors worked on the adaptation of this transition model to other turbulence model such as the Spalart-Allmaras model [11] as in [12], with a special treatment for the turbulence intensity as there is no transport equation for the turbulent kinetic energy, and the Reynolds Stress Model as in [10]. As the k - l turbulence model of Smith [2] is a good candidate for the fully turbulent or transition simulation of compressor flows [4] and is also used in turbine applications, the aim of this investigation is to adapt the γ - \widetilde{R}_{θ_t} model of Langtry and Menter to this turbulence model. After a short description of the original turbulence and transition models and of the test cases, modifications to the transition model are detailed. These modifications are then validated with high- and low-pressure turbines. As discrepancies still exist, the correlation functions used in the transition model are recalibrated.

2 Transition and Turbulence Modeling

The k - l of Smith In the turbulence model of Smith [2], the second turbulent scale is directly a turbulent length scale. Smith [2] developed a k - l turbulence model from the work of Rotta [13] and Ng and Spalding [14] who developed a k - kl turbulence model in which kl behaves as y^3 close to the wall and leads to numerical issues. In the Smith model, the second turbulent scale l is proportional to y near the wall, leading to a better robustness of the model. This turbulence model is well adapted to the prediction of separation, compressibility effects and viscous sub-layer of the boundary layer. The two transport equations of this turbulence model are:

$$\begin{aligned} \frac{\partial \rho q^2}{\partial t} + \frac{\partial \rho U_j q^2}{\partial x_j} &= P_k - D_k \\ &+ \frac{\partial}{\partial x_j} \left[(\mu + \sigma_q \mu_t) \frac{\partial q^2}{\partial x_j} \right] \quad (1) \\ \frac{\partial \rho l}{\partial t} + \frac{\partial \rho U_j l}{\partial x_j} &= (2 - E_2) \frac{\rho q}{B_1} \left[1 - \left(\frac{l}{\varkappa L} \right)^2 \right] \\ &- \frac{\mu_t}{l} \sigma_q \left(\frac{\partial l}{\partial x_j} \right)^2 \left(\frac{l}{\varkappa L} \right)^2 \\ &+ \rho l \frac{\partial U_j}{\partial x_j} + 2 \sigma_q \frac{\mu_t}{q^2} \frac{\partial l}{\partial x_j} \frac{\partial q^2}{\partial x_j} \\ &+ \frac{\partial}{\partial x_j} \left[(\mu + \sigma_q \mu_t) \frac{\partial l}{\partial x_j} \right] \quad (2) \end{aligned}$$

with L the wall distance, $q^2 = k$ and

$$P_k = \mu_t S_{ij} S_{ij}, \quad D_k = \frac{2 \rho q^3}{B_1 l} + 2 \mu \frac{\partial q}{\partial x_j} \frac{\partial q}{\partial x_j} \quad (3)$$

The turbulent viscosity is then expressed as a function of the two turbulent scales [2].

The γ - \widetilde{R}_{θ_t} transition model The laminar-turbulent transition is modeled with the γ - \widetilde{R}_{θ_t} model based on two additional transport equations to the RANS system [1]. The first one is for a numerical intermittency quantity γ which is set to 0 in the laminar boundary layer, increases gradually from 0 to 1 in the transitional flow, and is set to 1 anywhere else (except possibly in detached boundary layers). It should be noticed that all turbulent terms are relative to k - ω SST model as in the original formulation. The equation for γ is the following:

$$\begin{aligned} \frac{\partial(\rho \gamma)}{\partial t} + \frac{\partial(\rho U_j \gamma)}{\partial x_j} &= P_\gamma - E_\gamma \\ &+ \frac{\partial}{\partial x_j} \left[\left(\mu + \frac{\mu_t}{\sigma_f} \right) \frac{\partial \gamma}{\partial x_j} \right] \quad (4) \end{aligned}$$

where the intermittency production term is defined as follows:

$$P_\gamma = F_{\text{length}} c_{a1} \rho S (\gamma F_{\text{onset}})^{0.5} (1 - c_{e1} \gamma) \quad (5)$$

This term is responsible for the boundary layer transition, with the F_{length} and F_{onset} functions controlling the transition length and location respectively. F_{onset} contains the transition criterion originally introduced by Menter *et al.* and is based on the R_{θ_c} correlation function which depends on the transition Reynolds number R_{θ_t} . Only the functions investigated in the present study are detailed (e.g. F_{onset}). The other ones are described in depth in [15] (e.g. F_{length}).

$$R_\nu = \frac{\rho y^2 S}{\mu}, R_T = \frac{\rho k}{\mu \omega}, F_{\text{onset}1} = \frac{R_\nu}{2.193 R_{\theta_c}} \quad (6)$$

$$F_{\text{onset}2} = \min(\max(F_{\text{onset}1}, F_{\text{onset}1}^4), 2.0) \quad (7)$$

$$F_{\text{onset}3} = \max\left(1 - \left(\frac{R_T}{2.5}\right)^3, 0\right) \quad (8)$$

$$F_{\text{onset}} = \max(F_{\text{onset}2} - F_{\text{onset}3}, 0) \quad (9)$$

The dissipation term, responsible for setting γ to its cut-off value in the laminar boundary layer as well as for relaminarization, is defined as follows:

$$E_\gamma = c_{a2} \rho \Omega \gamma F_{\text{turb}} (c_{e2} \gamma - 1), F_{\text{turb}} = e^{-\left(\frac{R_T}{4}\right)^4} \quad (10)$$

The constants for the γ transport equation are:

$$\begin{aligned} c_{a1} &= 2.0, & c_{a2} &= 0.06, \\ c_{e1} &= 1.0, & c_{e2} &= 50, & \sigma_f &= 1.0 \end{aligned} \quad (11)$$

The second transport equation of the transition model is for the Reynolds number $\widetilde{R_{\theta_t}}$:

$$\begin{aligned} \frac{\partial(\rho \widetilde{R_{\theta_t}})}{\partial t} + \frac{\partial(\rho U_j \widetilde{R_{\theta_t}})}{\partial x_j} &= P_{\theta_t} \\ &+ \frac{\partial}{\partial x_j} \left[\sigma_{\theta_t} (\mu + \mu_t) \frac{\partial \widetilde{R_{\theta_t}}}{\partial x_j} \right] \end{aligned} \quad (12)$$

with:

$$P_{\theta_t} = c_{\theta_t} \frac{\rho}{t_P} (R_{\theta_t} - \widetilde{R_{\theta_t}}) (1.0 - F_{\theta_t}) \quad (13)$$

$$t_P = \frac{500 \mu}{\rho U^2}, c_{\theta_t} = 0.03 \quad (14)$$

The F_{θ_t} function is defined so to be equal to 1 in the boundary layer and to 0 outside of it. Different values of the σ_{θ_t} constant can be used depending on the choice of correlation functions. In the present investigation, the value $\sigma_{\theta_t} = 10$ is used. This means that the F_{length} and R_{θ_c} correlations are those of Content and Houdeville [16]. It should be noticed that the correlation for R_{θ_t} is the one of Langtry *et al.* [1].

In case of a large laminar separation, transition is accelerated through the use of a separation bubble model:

$$\gamma_{\text{sep}} = \min\left(s_1 \max\left[0, \left(\frac{R_\nu}{3,235 R_{\theta_c}}\right) - 1\right] F_{\text{reattach}}, 2\right) F_{\theta_t} \quad (15)$$

with $s_1 = 2$ and:

$$F_{\text{reattach}} = e^{-\left(\frac{R_T}{20}\right)^4}; \quad \gamma_{\text{eff}} = \max(\gamma, \gamma_{\text{sep}}) \quad (16)$$

Table 1: T106C Main Characteristics

Chord c [mm]	93.01
Pitch to chord ratio g/c	0.95
Aspect ratio h/c	2.40
Inlet flow angle β_1 [deg]	32.7
Blade stagger [deg]	30.7
Isentropic exit Mach number M_{2is}	0.65
Diffusion factor	0.42

Table 2: Geometrical Parameters of LS89 Turbine Airfoil

Chord [mm]	67.65
Pitch [mm]	57.50
Blade stagger [°]	55.0
Inlet flow angle [°]	0

3 Test Case

The present investigation is based on two experimental facilities which are respectively relative to low-pressure turbine and to high-pressure turbine.

3.1 High-lift Low-pressure Turbine T106C

The T106C as a very high-lift mid-loaded low pressure turbine airfoil, characterized by a suction side velocity peak at mid curvilinear abscissa followed by a strong flow deceleration towards the trailing edge [17]. This blade section has a stronger adverse pressure gradient than currently designed LPT and has been widely studied through both experimental and numerical investigations. This LPT blade was experimentally investigated in the framework of the European project TATMo. The characteristics of the T106C cascade are summarized in Table (1). During the experimental investigations, different freestream turbulence intensities have been considered. The natural inlet turbulence intensity of the facility is 0.9%. A passive turbulence grid was employed upstream of the cascade in order to generate distinct levels of free-stream turbulence intensity, from 1.8 to 3.2% in the vicinity of the leading edge. The Reynolds number Re_{2is} based on the isentropic exit Mach number M_{2is} and the blade chord c ranges from 80 000 to 250 000.

3.2 High-pressure Turbine LS89

The LS89 is a linear cascade of turbine airfoils representative of high-pressure turbine stator and experimentally tested in VKI wind tunnels [18]. The geometrical parameters are summarized in Table (2). Several operating points are simulated using *elsA* software [19]. The inflow conditions are measured 55 mm upstream of blade leading edge, which is the inlet plane of the computational domain, and are detailed in Table (3). As the second turbulent scale (e.g. turbulence length scale) is unknown, the values of $\frac{\mu_t}{\mu}|_{\text{in}}$ in the present computations are similar to those used in [20].

Table 3: Inflow Conditions for LS89

	MUR129	MUR235	MUR 241
$P_i _{in}$ (bars)	1.849	1.828	3.269
$T_i _{in}$ (K)	409.2	413.3	418.9
$Tu _{in}$ (%)	1.0	6.0	6.0
$\frac{\mu_t}{\mu} _{in}$	10	100	100
$M_{2,is}$	0.840	0.927	1.09
$R_{2,is}$	$1,09 \cdot 10^6$	$1,08 \cdot 10^6$	$2,11 \cdot 10^6$

4 Adapting the $\gamma\text{-}\widetilde{R}_{\theta_t}$ to the $k\text{-}l$ of Smith

To the best of the authors' knowledge the use of the $\gamma\text{-}\widetilde{R}_{\theta_t}$ model in a $k\text{-}l$ framework has never been done. We therefore use the same coupling between the transition and turbulence models as for the $k\text{-}\omega$: the terms (P_k) and (D_k) of the turbulent kinetic energy transport equation (Eq. (1)) are replaced by \tilde{P}_k and \tilde{D}_k :

$$\begin{aligned}\tilde{P}_k &= \gamma_{eff} \cdot P_k \\ \tilde{D}_k &= \min[\max(\gamma_{eff}; 0, 1); 1, 0] \cdot D_k\end{aligned}\quad (17)$$

where γ_{eff} is the effective intermittency given by equation (Eq. (16)).

In a $k\text{-}l$ framework, two terms in the transition model containing ω need to be reformulated:

$$R_T = \frac{\rho k}{\mu \omega} \quad (18)$$

$$R_\omega = \frac{\rho \omega y^2}{\mu} \quad (19)$$

The term Eq. (18) is simply re-written:

$$R_T = \frac{\mu_t}{\mu} \quad (20)$$

In order to reformulate Eq. (19), we use the fact that the dissipation terms of the turbulent kinetic energy transport equation for both the $k\text{-}\omega$ model of Wilcox and the $k\text{-}l$ model of Smith, were designed to reproduce the same phenomena in the free-stream. As Eq. (19) is only used outside of the boundary layer, we can obtain it through identification of the two dissipation terms:

$$\frac{2\rho(2k)^{\frac{3}{2}}}{B_1 l} \sim \beta^* \rho \omega k \Leftrightarrow \omega \sim \frac{\sqrt{2k}}{B_1 \beta^* l} \quad (21)$$

$$R_\omega = \frac{\rho \sqrt{2k} y^2}{B_1 \beta^* l \mu} \quad (22)$$

In themselves, these modifications are sufficient to render computations possible. However, as we can see in Figure (1), this quasi-direct implementation of the $k\text{-}l\text{-}\gamma\text{-}\widetilde{R}_{\theta_t}$ model leads to a very early transition of the boundary layer. A study of the flow-field reveals that the turbulence model activates even though the transition model still detects that the boundary layer should be laminar. This means that, in its current form, the transition model does not correctly cut-off the $k\text{-}l$ turbulence model.

To explain this, we need to look in depth at individual terms inside the $\gamma\text{-}\widetilde{R}_{\theta_t}$ model. To do so, we will perform

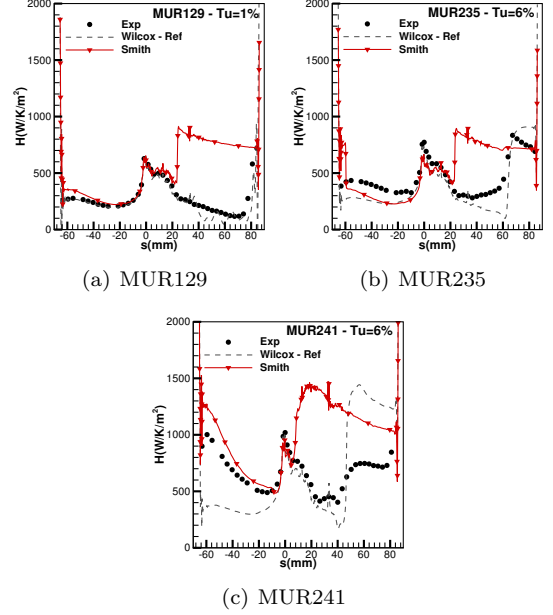


Figure 1: LS89 - heat transfer coefficient - Evaluation of the basic $k\text{-}l\text{-}\gamma\text{-}\widetilde{R}_{\theta_t}$ model - positive curvilinear abscissa correspond to the suction side

streamwise extractions along the maximum of R_ν in the normal direction, which is the line along which the transition model activates. Such extractions are shown on Figure (2), which were performed on LS89 MUR235 computations, along the suction side. The $k\text{-}\omega\text{-}\gamma\text{-}\widetilde{R}_{\theta_t}$ Wilcox computation is shown as a reference.

On Figure (2)-(b), we can see that, in the direct formulation of the $k\text{-}l\text{-}\gamma\text{-}\widetilde{R}_{\theta_t}$ model, the F_{onset3} function, in blue, drops to 0 before mid-cord. This function is actually a cut-off term designed to keep F_{onset} at 0 in the laminar boundary layer. Because F_{onset3} does not function correctly in a $k\text{-}l$ framework, it needs to be modified. We propose the following formulation:

$$F_{onset3} = \max\left(1 - \left(\frac{R_T}{2.5}\right)^3, 1 - F_{onset2}^7, 0\right) \quad (23)$$

We can see on Figure (2)-(c) that this modification of F_{onset3} allows it to have, in the $k\text{-}l\text{-}\gamma\text{-}\widetilde{R}_{\theta_t}$ model, a similar shape to the one in the $k\text{-}\omega\text{-}\gamma\text{-}\widetilde{R}_{\theta_t}$ model.

Though this does give us the correct shape of the F_{onset} function, we can see that we still have a small, but non-negligible build-up of turbulent viscosity in the laminar boundary layer (orange curve, to be read using the right axis). This problem comes from the residual levels of intermittency in the laminar boundary layer.

Indeed, in the $\gamma\text{-}\widetilde{R}_{\theta_t}$ model, the intermittency is not strictly null in the laminar boundary layer but rather kept at a small value. This means that production of turbulence is not completely inhibited. In a $k\text{-}\omega$ framework, this does not lead to any turbulent viscosity build-up due to the very high values taken by the second turbulent variable ω in the laminar boundary layer. It seems however that the $k\text{-}l$ model of Smith is very sensitive to small values of intermittency. We had already noticed this behavior with other transition models.

We therefore propose to lower the residual level of γ in the case of the $k\text{-}l$ Smith. This is done through the

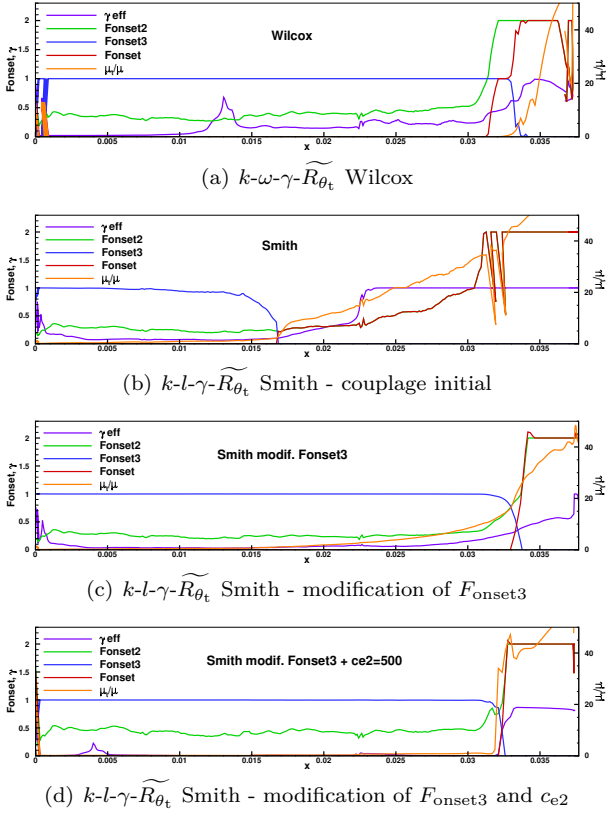


Figure 2: LS89 MUR235 - Boundary layer extractions along the maximum of R_ν

c_{e2} constant of the $\gamma-\widetilde{R}_{\theta_t}$ model, which we raise from $c_{e2} = 50$ to $\boxed{c_{e2} = 500}$. We can see on Figure (2)-(d) that this allows all the inner variables of the $\gamma-\widetilde{R}_{\theta_t}$ to behave correctly, which should lead to correct estimation of the transition location.

For clarity, all modifications to the $\gamma-\widetilde{R}_{\theta_t}$ model to fit a $k-l$ framework have been boxed out. Let us now evaluate this new model.

5 Evaluation of the $k-l-\gamma-\widetilde{R}_{\theta_t}$ Model

The proposed $k-l-\gamma-\widetilde{R}_{\theta_t}$ model was evaluated on three LS89 cases. Results are shown in Figure (3). We can see that the $k-\omega-\gamma-\widetilde{R}_{\theta_t}$ and $k-l-\gamma-\widetilde{R}_{\theta_t}$ models behave rather similarly. In particular, results are identical in the laminar boundary layers, and both model display an abrupt transition at the end of the physical transition zone. Also, both model predict a laminar boundary layer on the pressure-side of the MUR241 case when the experiment displays a turbulent one.

The main difference between the $k-\omega-\gamma-\widetilde{R}_{\theta_t}$ and $k-l-\gamma-\widetilde{R}_{\theta_t}$ models lies in the capture of the heat transfer in the turbulent boundary layers, with the advantage going to the $k-l-\gamma-\widetilde{R}_{\theta_t}$ model. Indeed, it captures exceptionally well the drop in H after transition on the MUR235 case, where the $k-\omega-\gamma-\widetilde{R}_{\theta_t}$ model predicts a plateau. On the suction-side of the MUR241 case, both model miss the experimental turbulent heat transfer but the $k-l-\gamma-\widetilde{R}_{\theta_t}$ is still closer to the experiments.

Our new $k-l-\gamma-\widetilde{R}_{\theta_t}$ model was then evaluated on the

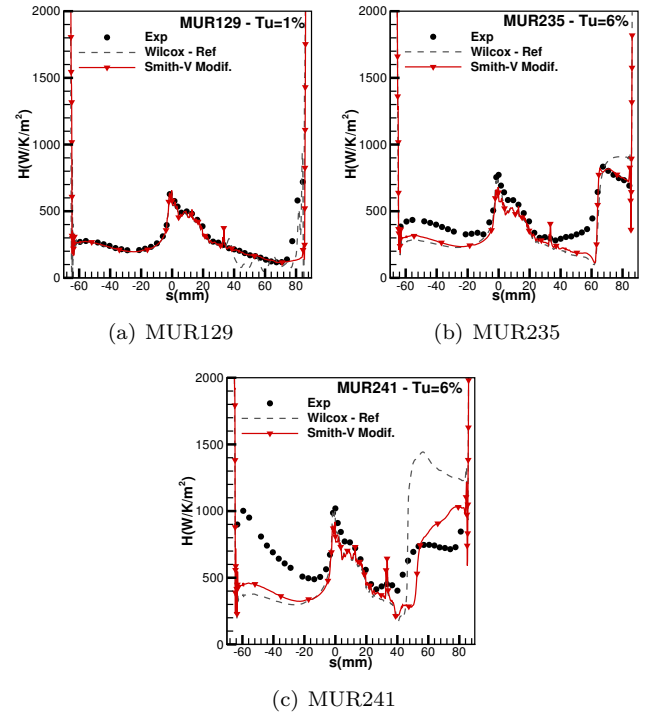


Figure 3: LS89 - heat transfer coefficient - Comparison of the $k-\omega-\gamma-\widetilde{R}_{\theta_t}$ and the proposed $k-l-\gamma-\widetilde{R}_{\theta_t}$ model - positive curvilinear abscissa correspond to the suction side

T106C cases which feature separation-induced transition. On these cases, as can be seen on Figure (4), the $k-l-\gamma-\widetilde{R}_{\theta_t}$ model fails to correctly represent the pressure distribution around the blade. This is due to an error on the transition location which induces an incorrect shape of the separation bubble.

Let us remember that to this point, the $k-l-\gamma-\widetilde{R}_{\theta_t}$ model is still using the correlation functions that were developed for the $k-\omega-\gamma-\widetilde{R}_{\theta_t}$ model by Content and Houdeville [16] on flat plate cases. It seems that for HL-LPT flows, the $k-l-\gamma-\widetilde{R}_{\theta_t}$ model needs to be recalibrated.

6 Recalibration of the $\gamma-\widetilde{R}_{\theta_t}$ Model for HL-LPT Flows

We have developed a method that allows to obtain new F_{length} and R_{θ_c} functions dedicated to LPT flows. This method cannot be described in length here, so we will only point out that it relies on an optimization process that uses the T106C cases at different Reynolds number and inlet turbulence levels as test cases. This process is described in [21], and its capacities have been demonstrated on the $k-\omega-\gamma-\widetilde{R}_{\theta_t}$ model. We are now applying it to the $k-l-\gamma-\widetilde{R}_{\theta_t}$ model.

Results given by the recalibrated model are shown in Figure (5). We can see that the recalibration greatly improves results, but that the $k-l-\gamma-\widetilde{R}_{\theta_t}$ model still has more trouble capturing these HL-LPT flows than the $k-\omega-\gamma-\widetilde{R}_{\theta_t}$ model. At $Tu = 3.2\%$ the two models give similar results. However, for the larger bubble cases at $Tu = 1.8\%$ and $Tu = 0.9\%$, the $k-l-\gamma-\widetilde{R}_{\theta_t}$ model has trouble predicting the correct shape of the bubble.

Note that we are here comparing the LPT-calibrated

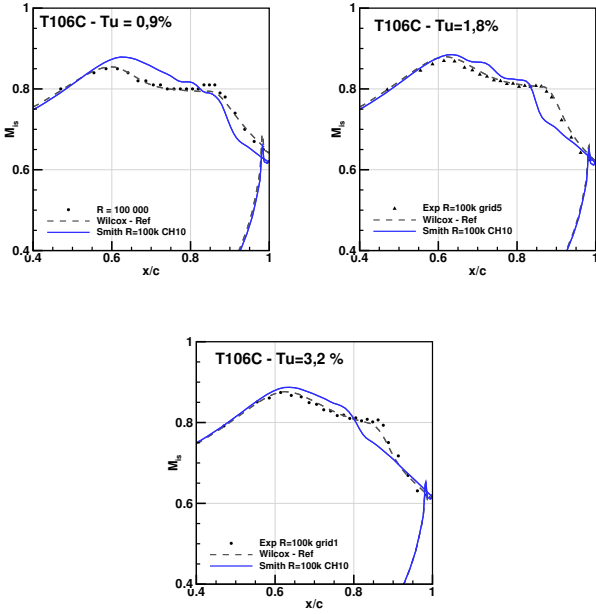


Figure 4: T106C, $R_{2, is} = 100\,000$ - Comparison of the $k-\omega-\gamma-\widetilde{R}_{\theta_t}$ and the proposed $k-l-\gamma-\widetilde{R}_{\theta_t}$ model

$k-l-\gamma-\widetilde{R}_{\theta_t}$ model to the flat plate-calibrated CH10 $k-\omega-\gamma-\widetilde{R}_{\theta_t}$ and not our recent LPT-calibrated $k-l-\gamma-\widetilde{R}_{\theta_t}$ model [21], so the performance of the $k-l-\gamma-\widetilde{R}_{\theta_t}$ model on this case is disappointing.

7 Conclusions

The $\gamma-\widetilde{R}_{\theta_t}$ transition model has been coupled to the $k-l$ turbulence model of Smith. To do so, three different terms in the $\gamma-\widetilde{R}_{\theta_t}$ model need to be reformulated and the c_{e2} constant reajusted. We found that this $k-l-\gamma-\widetilde{R}_{\theta_t}$ model gives satisfactory results on bypass transition cases but needs to be recalibrated for more difficult to model configurations such as separation induced transition.

This recalibration improves results but the $k-l-\gamma-\widetilde{R}_{\theta_t}$ model still has difficulties capturing the correct bubble shape. In particular, our current version of the $k-l-\gamma-\widetilde{R}_{\theta_t}$ model is out-performed by the standard CH10 version of the $k-\omega-\gamma-\widetilde{R}_{\theta_t}$ model.

A major conclusion is the evidence that switching the second turbulent variable from ω to l is a major modification for the $\gamma-\widetilde{R}_{\theta_t}$ model even though it interacts with the RANS system through the k equation only. It is possible that the transition model requires further modifications to be fully adapted to a $k-l$ framework. Additional work will therefore be done in order to better characterize the applicability of this $k-l-\gamma-\widetilde{R}_{\theta_t}$ model.

Acknowledgment

The present research was funded by SAFRAN-Snecma and the French Ministry of Research under grant number ANRT/Cifre-2012/1332. The authors warmly thanks Itham Salah El Din and Didier Bailly for there participation in the model recalibration and Hugues Deniau as

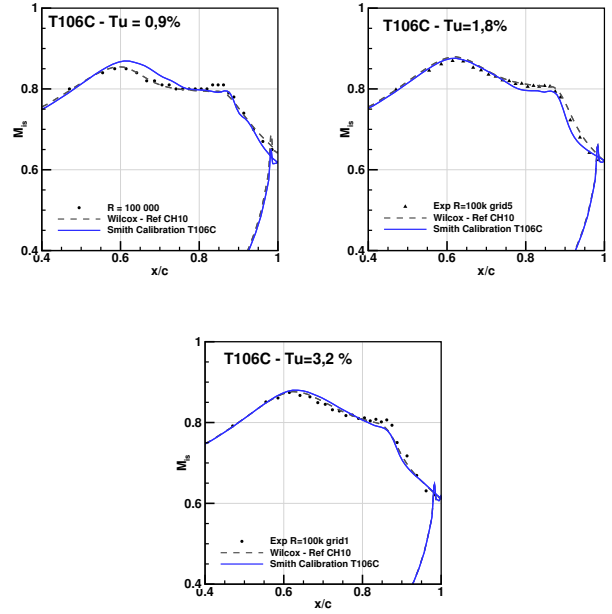


Figure 5: T106C, $R_{2, is} = 100\,000$ - Comparison of the $k-\omega-\gamma-\widetilde{R}_{\theta_t}$ and the LPT-calibrated $k-l-\gamma-\widetilde{R}_{\theta_t}$ model

well as Michel Gazaix for their help in the code development aspects of this work.

References

- [1] R. B. Langtry and F. R. Menter, "Correlation-Based Transition Modeling for Unstructured Parallelized Computational Fluid Dynamics Codes," *AIAA Journal*, vol. 47, pp. 2894–2906, Dec. 2009.
- [2] B. Smith, "Prediction of hypersonic shock wave turbulent boundary layer interactions with the k-l two equation turbulence model," *AIAA*, vol. 1995-232, Jan. 1995.
- [3] J. Cliquet, R. Houdeville, and D. Arnal, "Application of Laminar-Turbulent Transition Criteria in Navier-Stokes Computations," *AIAA Journal*, vol. 46, pp. 1182–1190, May 2008.
- [4] J. Marty, G. Cottin, and B. Auipoix, "Steady Numerical Investigations of the Transition Process on an Axial Multistage High Pressure Compressor," *ERCOFTAC Bulletin*, vol. 80, pp. 41–44, September 2009.
- [5] J. Steelant and E. Dick, "Modelling of laminar-turbulent transition for high free-stream turbulence," *Journal of Fluids Engineering*, vol. 123, pp. 22–30, 2001.
- [6] R. Pacciani, M. Marconcini, A. Arnone, and F. Bertini, "Predicting high-lift lp turbine cascades flows using transition-sensitive turbulence closures," *Journal of Turbomachinery*, vol. 136, no. 5, p. 051007, 2013.
- [7] Y. Watanabe, T. Misaka, S. Obayashi, T. Arima, and Y. Yamaguchi, "Application of crossflow transition criteria to local correlation-based transition model," in *47th AIAA Aerospace Sciences Meeting Including The New Horizons Forum and Aerospace*

- Exposition*, AIAA 2009-1145, (Orlando, Florida), 6-8 January 2009.
- [8] P. Smirnov and F. Menter, “Sensitization of the SST Turbulence Model to Rotation and Curvature by Applying the Spalart-Shur Correction Term,” *Journal of Turbomachinery*, vol. 131, pp. 041010–1–8, October 2009.
- [9] R. Corral and F. Gisbert, “Prediction of separation-induced transition using a correlation-based transition model,” in *ASME Turbo Expo 2010: June 14–18, Glasgow, UK*, no. GT2010-23239, 2010.
- [10] S. Frauholz, B. U. Reinartz, S. Müller, and M. Behr, “Transition prediction for scramjets using $\gamma\text{-}\widetilde{R}_{\theta_t}$ model coupled to two turbulence models,” *Journal of Propulsion and Power*, vol. 31, no. 5, pp. 1404–1422, 2015.
- [11] P. Spalart and S. Allmaras, “A One-Equation Turbulence Model for Aerodynamic Flows,” *La Recherche Aéronautique*, vol. 1, pp. 5–21, 1994.
- [12] S. Medida and J. D. Baeder, “Role of improved turbulence and transition modeling methods in rotorcraft simulations,” in *AHS 69th Annual Forum, Phoenix, Arizona, May 21–23*, 000340, 2013.
- [13] J. Rotta, “Über eine Methode zur Berechnung turbulenter Scherströmungen,” technical report, Aerodynamische Versuchsanstalt Göttingen, 1968.
- [14] K. Ng and D. Spalding, “Some applications of a model of turbulence to boundary layers near walls,” *Physics of Fluids*, vol. 15, no. 1, pp. 20–30, 1972.
- [15] A. Minot, X. De Saint Victor, J. Marty, and J. Perraud, “Advanced numerical setup for separation-induced transition on high-lift low-pressure turbine flows using the $\gamma\text{-}\widetilde{R}_{\theta_t}$ model,” in *ASME Turbo Expo 2015*, no. GT2015-42160, American Society of Mechanical Engineers, 2015.
- [16] C. Content and R. Houdeville, “Application of the $\gamma\text{-}\widetilde{R}_{\theta_t}$ laminar-turbulent transition model in navier-stokes computations,” *AIAA Journal*, vol. 2010-4445, June 2010.
- [17] J. Michálek, M. Monaldi, and T. Arts, “Aerodynamic Performance of a Very High Lift Low Pressure Turbine Airfoil (T106C) at Low Reynolds and High Mach Number With Effect of Free Stream Turbulence Intensity,” *Journal of Turbomachinery*, vol. 134, p. 061009, November 2012.
- [18] T. Arts and M. Lambert de Rouvroit, “Aero-Thermal Performance of a Two-Dimensional Highly Loaded Transonic Turbine Nozzle Guide Vane: A Test Case for Inviscid and Viscous Flow Computations,” *Journal of Turbomachinery*, vol. 114, no. 1, p. 147, 1992.
- [19] L. Cambier, S. Heib, and S. Plot, “The Onera elsA CFD software: input from research and feedback from industry,” *Mechanics & Industry*, vol. 14, no. 03, pp. 159–174, 2013.
- [20] A. Benyahia, *Mise en œuvre et évaluation d’un modèle de transition à équations de transport pour la simulation d’écoulements en turbomachines*. PhD thesis, Institut Supérieur de l’Aéronautique et de l’Espace, 2012.
- [21] A. Minot, I. S. El-Din, R. Barrier, J.-C. Boniface, and J. Marty, “Improvement of laminar-turbulent transition modeling within a low-pressure turbine,” in *ASME Turbo Expo 2016*, no. GT2016-57637, American Society of Mechanical Engineers, 2016.

NUMERICAL INVESTIGATION OF SURFACE ROUGHNESS EFFECT WITH INTERMITTENCY TRANSPORT MODEL

W.Elsner and P.Warzecha

*Institute of Thermal Machinery, Czestochowa University of Technology,
Al. Armii Krajowej 21, 42-200 Czestochowa, Poland
welsner@imc.pcz.czyst.pl*

1 Introduction

The surface roughness has a strong influence on the efficiency, heat transfer and the machine maintenance cost. It results from the fact, that the roughness increases the skin friction of the turbulent boundary layer and shifts the laminar-turbulent transition upstream the flow. Surface roughness generally adversely affects turbomachines aerodynamic efficiency due to thickened boundary layer and increase of blockage. This is true for attached boundary layers developing at sufficiently high Reynolds number as was demonstrated by Boyle and Senyitko [1], who showed that at Reynolds numbers $Re = 8 \times 10^5 \div 1.8 \times 10^6$ surface roughness doubled the vane loss. Similar observations were done by Waigh and Kind [2] and Hummel et al. [3]. The losses can also be decreased, what is the case for airfoils with large laminar separation bubble present in modern low pressure turbines (LPT) operating at low Reynolds number. The roughness accelerates l-t transition in separated shear layer and reduces or even eliminates separation bubble. Therefore, it is not surprising that recent studies on high-lift LPT blades suggest that a blade with as-cast surface roughness could have a lower loss than a polished one [4].

The accurate and reliable prediction of the effect of surface roughness on fluid flow and heat transfer is of great interest for designers. It is known however, that proper prediction of l-t transition is one of the challenges even for a smooth surface. The increased need for more accurate flow simulations has resulted in an intense development of transition modeling approaches in the last decade. They provide an answer regarding the position of transition onset and the length of transitional region. Numerical modeling of roughness in a transitional boundary layer is not as popular as for smooth surface, but there are exist several models, which account for wall roughness. The most common approach is to incorporate an appropriate correlations to common near wall treatment models. Modeling of the flow on a rough surface should cover the entire blade surface, so correct computations of the laminar, turbulent and transitional boundary layers are required. However, because the roughness influence exerted upon the laminar boundary layer, at least for relative low roughness heights is negligible, therefore the modeling of turbulent and transitional boundary layer are the two main tasks in handling the surface roughness.

The critical review of correction available for the shear stress transport (SST) model was presented by Aupoix and Spalart [5]. Some transition models have been also proposed recently, of which the most interesting are a model relying on roughness-sensitive correlations (Stripf

et al. [6]) and the extension of $\gamma - Re_{\theta t}$ model by the other transport equation for the variable called “roughness amplification” introduced by Dassler et al. [7]. Another valuable model recently proposed by Ge and Durbin [8] is based on single intermittency transport equation and formulated in local variables only. Elsner and Warzecha [9] based on $\gamma - Re_{\theta t}$ model formulated their own proposal, which incorporate the roughness transition correlation of Stripf et al. [6].

The paper discusses the results of verification of the last approach based on a flat plate data with zero and non-zero pressure gradients test cases as well as on the high pressure turbine blade case. For the last case experimental data produced by Stripf et al. [6] are used. Finally, the data of LH [17] were used to show the ability of the model to predict the impact of the roughness on separated boundary layer.

2 Model Formulation

The model of Elsner and Warzecha (ITM_R hereinafter) [9] is based on the SST turbulence model and $\gamma - Re_{\theta}$ transition model by Menter et al. [10]. Somewhat earlier, in 2010 Piotrowski et al. [11] proposed an extension to this model by development of two in-house correlations for onset location and transition length. The model has been calibrated using zero and non-zero pressure gradient flat plate test cases as well as HP turbine blade profile.

Elsner and Warzecha [9] proposed further modifications to the ITM model in order to take into account the effect of surface roughness. For technical geometries the blade surface is not uniform and becomes rough due to industrial process or alternation of the surface due to erosion, deposition, pitting or corrosion. In addition, the surface quality is changing with time. For simplicity in most studies the roughness is characterized by an equivalent sandgrain height k_s . Similar assumption was applied in this work. To take into account roughness effect it was necessary to describe the impact of roughness on a turbulent boundary layer and on the transition location. To predict the behavior of turbulent boundary layer two modifications of SST have been introduced [12]. The first one concerns the wall boundary condition of a specific dissipation rate ω . Modification of the specific dissipation rate for rough surface leads to its finite value:

$$\omega_w = \frac{\mu_\tau^2}{\nu} S_R \quad (1)$$

where S_R is a nondimensional coefficient defined as:

$$\begin{aligned} S_R &= (50/K_S^+)^2 \quad \text{for } K_S^+ \leq 25 \\ S_R &= (100/K_S^+)^2 \quad \text{for } K_S^+ > 25 \end{aligned} \quad (2)$$

K_S^+ is a sand grain height given by:

$$K_S^+ = \frac{\mu_\tau k_s}{\nu} \quad (3)$$

where k_s is the equivalent sand roughness.

For ideally smooth solid surface $\omega \rightarrow \infty$. It was also necessary to redefine eddy viscosity μ_τ .

$$\mu_\tau = \frac{a_1 \rho k}{\max(a_1 \omega; |\Omega| F_2 F_3)} \quad (4)$$

This modification prevents the modeled shear-stress from being activated in the near wall region such as sublayer or rough layer. The additional function F_3 is equal to zero in the near-wall region and unity elsewhere. a_1 is a constant equal 0.31 and Ω is the absolute value of vorticity.

To model the l-t transition the correlations based on Stripf et al. [6] data have been applied. It is known [10] that the source term in the intermittency transport equation, through F_{length} and onset F_{onset} parameters, is a function of critical transition Reynolds number Re_{θ_c} and vorticity Reynolds number Re_v i.e. $F_{onset} = f(Re_v, Re_{\theta_c})$. Both F_{onset} and F_{length} parameters are located in the production term of intermittency transport equation. F_{onset} function plays a key role in the induction of l-t transition, because it triggers the intermittency production, while F_{length} is a function, which controls the length of the transition zone. Vorticity Reynolds number is calculated locally in classic way and defined as:

$$Re_v = \frac{\rho y^2}{\mu} \frac{\partial u}{\partial y} = \frac{\rho y^2}{\mu} S \quad (5)$$

Re_{θ_c} determines location where the intermittency starts to increase in the boundary layer, which occurs upstream of the location determined by transition Reynolds number Re_{θ_t} . To determine Re_{θ_c} Piotrowski et al. [11] proposed to tie its value with $\widetilde{Re}_{\theta_c}$, which results from the transport equation of the momentum thickness Reynolds number Re_{θ_t} according to the relation: $Re_{\theta_c} = F_P \widetilde{Re}_{\theta_t}$, where F_P is an unknown function and $\widetilde{Re}_{\theta_t}$ is determined at the wall. Based on Stripf et al. [6] correlations a modification to the transition location has been introduced. For this purpose a new momentum thickness Reynolds number has been defined that depends also on the ratio of roughness height k_r and displacement thickness δ^* as follows:

$$\widetilde{Re}_{\theta_t_R} = \widetilde{Re}_{\theta_t} \quad \text{for } k_r/\delta^* \leq 0.01 \quad (6)$$

$$\widetilde{Re}_{\theta_t_R} = \left(\frac{1}{\widetilde{Re}_{\theta_t}} + 0.0061 F_\Lambda \left(\frac{k_r}{\delta^*} - 0.01 \right)^{f_{Tu}} \right)^{-1} \quad (7)$$

for $k_r/\delta^* > 0.01$

Two auxiliary functions are f_Λ which takes into account roughness topographies and f_{Tu} which is a function of the local free stream turbulent intensity Tu_{l-t} expressed as percentage:

$$F_{Tu} = \max(0.9; 1.61 - \exp(-Tu_{l-t})) \quad (8)$$

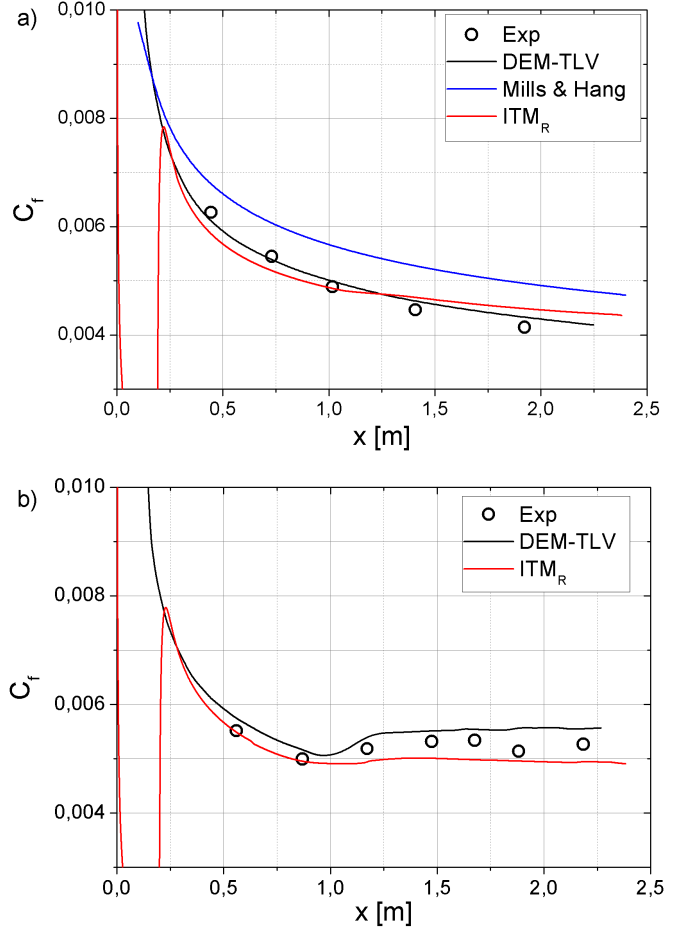


Figure 1: Skin friction coefficient C_f for zero-pressure gradient test case: $U_\infty = 27m/s$ (a) and for non zero-pressure gradient test case: $U_\infty = 26m/s$ (b)

The transport equations for intermittency and momentum thickness Reynolds number as well as SST turbulence model with all modifications were implemented in the commercial package ANSYS Fluent with the use of User Defined Functions (UDFs).

3 Model Validation

Initially, the model was tested on smooth surfaces. A comprehensive overview of the tests was presented in a paper by Piotrowski et al. [11]. They consider several test cases with various inlet and boundary conditions including among other ERCOFTAC flat plate zero pressure gradient Test Cases (T3A and T3B) and one with varying pressure distribution (T3C4). Further on authors consider N3-60-0.4 turbine blade Test Case with inlet turbulence intensity $Tu = 0.4\%$. The tests proved that the model appears to be sufficiently precise and enables accurate predictions of boundary layer development for various flow configurations and inflow conditions. The quality of the prediction was compared with other intermittency based models.

Flat plate test case

For smooth walls, there are many test cases, but it is difficult to find in the literature well documented experimental studies for rough surfaces. In the absence of contemporary data, one can refer to studies from the seven-

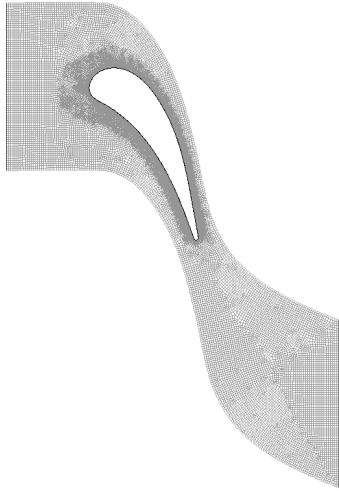


Figure 2: Geometry and the mesh of HPTV blade vane

ties performed at Stanford University and Sandia Laboratories [13,14]. Thus the ITM_R model was initially verified on simple test cases i.e. a flat plate turbulent boundary layer with zero pressure gradient published by Healzer [13] and a flat plate turbulent boundary layer with non-zero pressure gradient published by Coleman et al. [14]. In both experiments the same test section of dimensions $2.4m$ in length, $0.508m$ in wide and $0.102m$ in height has been used. The roughness was obtained by means of copper balls with a diameter of $d_0 = 1.27mm$ brazed together in a most dense configuration. Based on available data the equivalent sand roughness was calculated and equal to $k_s = 0.62 \times d_0 = 0.79mm$. Among the available data two cases were selected i.e. with $U_\infty = 27m/s$ for the zero pressure gradient and $U_\infty = 26m/s$ for the non-zero pressure gradient test case. The inlet turbulence intensity was in both cases equal $Tu = 0.4\%$.

Fig. 1a shows experimental and numerical results for skin friction coefficient distribution for zero pressure gradient test cases. The results for ITM_R model are compared with experimental results (circles) and results obtained by Stripf with DEM-TLV model [15]. Additionally, the curve presenting the semi-empirical formula proposed by Mills and Hang [16] is shown. This formula:

$$C_f = (3.476 + 0.707 \ln(x/K_s))^{-2.46} \quad (9)$$

defines skin friction coefficient on sand-roughened flat plate, which is valid in the full-rough regime. One may observe that ITM_R model predicts the skin friction coefficient along the plate with quite good accuracy compared to experiment. For this case the results are almost identical with DEM-TLV data. It is seen also that Mills and Hang correlation overpredict the experimental data especially in the second part of the plate.

The next test concerns the non-zero pressure gradient case, which was experimentally investigated for several variable free stream velocity distributions along flat plate [14]. The case with inlet velocity $U_\infty = 26m/s$ was chosen. Fig. 1b shows the comparison of skin friction coefficient predicted by numerical models with experiment. A slight discrepancy can be seen for both ITM_R and DEM-TLV models where the first one takes slightly lower and the second one slightly higher values. Nevertheless it is clear that the performance of the ITM_R model is sufficient to calculate rough wall turbulent boundary layer and it may be applied for more demanding test cases.

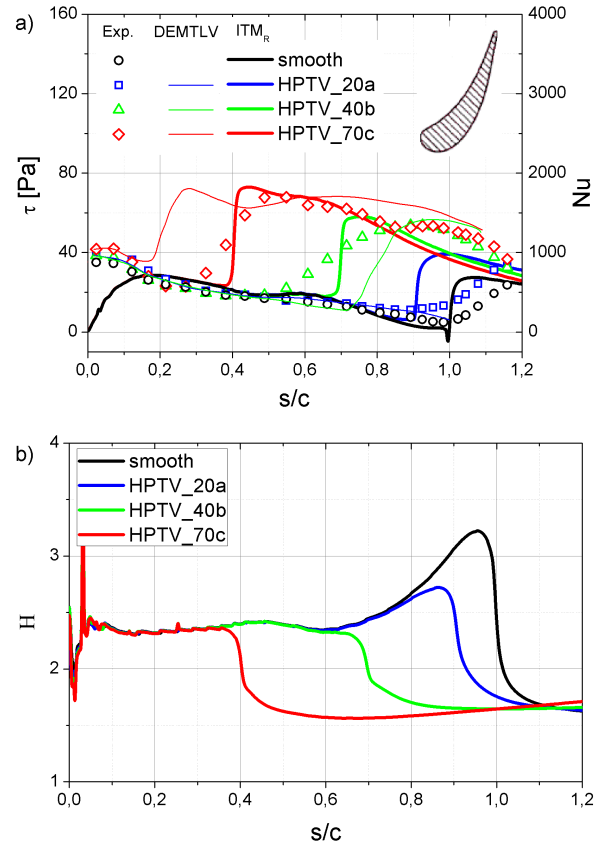


Figure 3: Shear stress (own numerical results) and Nusselt number (Stripf experimental and DEM-TLV results) (a) and shape factor (own numerical results) (b) for the HPTV blade

High pressure turbine blade test case

For confirmation that the proposed approach can be used for more complex industrial cases it was validated against data of the high pressure turbine vane (HPTV), of a chord $c = 93.95mm$, experimentally and numerically investigated at Karlsruhe University [15]. The geometry and the grid is presented in Fig. 2.

The validation of the roughness model was performed for Reynolds number $Re = 1.4 \times 10^5$ and turbulence intensity $Tu = 3.5\%$. The applied deterministic roughness consisted of evenly spaced truncated cones uniformly distributed on the blade surface. Roughness height varied from $20\mu m$, through $37\mu m$, and finally $70\mu m$. The equivalent sand roughness k_s needed to model the flow was calculated by Stripf et al. [15] according to Waigh and Kind correlation. Additionally, a smooth surface was used as a reference case. Table 1 contains the basic roughness parameters as well as boundary layer data needed for flow calculations. The displacement thickness and turbulence intensity given in Table 1 were determined at the l-t transition point detected during calculations.

Fig. 3a presents the shear stress distribution obtained numerically by ITM_R model (solid lines) juxtaposed with Nusselt number distributions (points) calculated from the experiment and obtained with DEM-TLV model by Stripf et al. [16]. Both shear stress and Nusselt number are good indicators of transition onset location. Shear stress is proportional to velocity gradient, while Nusselt number is proportional to the temperature gradient near the wall and both quantities rise dramatically on the border of laminar and turbulent flow.

Table 1: Roughness parameters and basic boundary layer parameters

Test Case	Roughness parameters			Boundary layer parameters			
	k_r [mm]	K_S^+ [-]	k_r/δ^* [-]	δ^* [mm]	Tu_{l-t} [%]	τ [Pa]	u_τ [m/s]
HPTV_20a	0.072	22.0 5	0.46	0.157	0.98	39	6.21
HPTV_40b	0.129	48.1 3	1.26	0.102	1.0	57.9	7.57
HPTV_70c	0.238	99.0 3	3.26	0.073	1.19	72	8.44

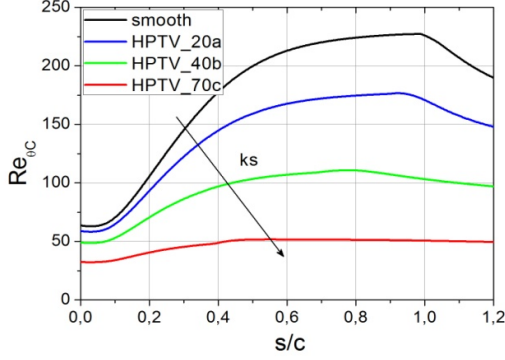


Figure 4: Distributions of critical Reynolds number Re_{θ_c} along the wall

One can observe that ITM_R model gives qualitatively good prediction of the boundary layer development, although the increase of shear stress is more abrupt than raise of experimental Nusselt number. Comparing both numerical results one may conclude that ITM_R model detects l-t transition more accurately. For the smooth case at the rear part of the blade a small separation reported by Stripf et al. [16] has been confirmed. It is the most important region as the state of boundary layer here decides about the magnitude of losses. With the increase of roughness height the transition location is shifted upstream. Even for the smallest value of k_r ($20\mu m$) the boundary layer looks to be sensitive to the surface roughness. The impact of roughness could be also clearly evaluated by the analysis of shape factor (see Fig. 3b), which is among the most precise indicators of the boundary layer state. For a smooth case the shape factor reaches the value $H = 3.4$ in the rear part of the suction side indicating laminar separation, and with the increase of k_r this peak is damped and for the remaining cases the drop of H value to turbulent state (≈ 1.6) is located more upstream.

The functioning of the model can be explained by the analysis of the critical transition Reynolds number Re_{θ_c} (Fig. 4) which determines the location where the intermittency starts to increase in the boundary layer. It can be seen that the surface roughness makes the critical Reynolds number smaller and thus triggers the intermittency production term at an earlier phase accelerating the transition.

Flat plate test case with separation

As it was already mentioned, high-lift turbine blades used in modern turbine aeroengines are subjected to strong adverse pressure gradient and surface roughness could be considered as one of the passive methods of

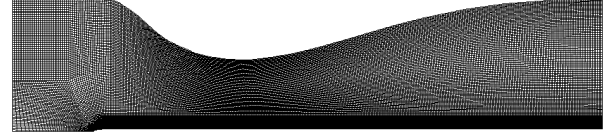


Figure 5: The mesh for LH Test Case

boundary layer control. For confirmation that the proposed approach can be used for such an industrial flow, in the absence of appropriate test cases, it was decided to select Lou and Hourmouziadis flat plate test case (LH hereinafter) [17]. The advantage of that test case is the fact that the induced pressure profile is typical for suction side of highly-loaded turbine airfoil. The drawback is that the only available data are for a smooth wall. That is why it cannot be treated as a proper validation test case for roughness, however we are able to show the expected behavior of the model for strong adverse pressure gradient and separated boundary layer. Experimental setup and database is available in [17]. For the analysed case the inlet turbulence intensity was $Tu = 0.6\%$ and the inflow velocity was set to $U_\infty = 9m/s$. The geometry and the mesh is presented in Fig. 5.

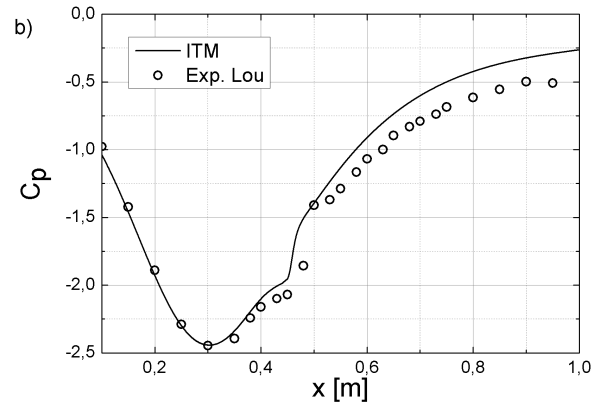


Figure 6: Pressure coefficient C_p distribution for the smooth case

The roughness parameters used for the analyzed test cases were collected in Table 2. It is seen that k_r varies from 320 to $570\mu m$.

Fig. 6 shows the calculated and measured pressure coefficient C_p for a smooth case. The main flow over the flat plate is accelerated up to $x = 0.3m$ and then diffused by the adverse pressure gradient. The separation bubble is clearly seen between 0.39 and $0.47m$, where plateau of C_p can be noticed.

The position and the dimension of the separation bubble is marked by the white line in Fig. 7 and 8. The

Table 2: Roughness parameters and basic boundary layer parameters

Test Case	Roughness parameters			Boundary layer parameters			
	k_r [mm]	K_S^+ [-]	k_r/δ^* [-]	δ^* [mm]	Tu_{l-t} [%]	τ [Pa]	u_τ [m/s]
ITMR26	0.32	26	0.19	1.66	0.426	0.49	0.64
ITMR41	0.46	41	0.30	1.52	0.423	0.56	0.68
ITMR56	0.57	56	0.46	1.23	0.420	0.69	0.76

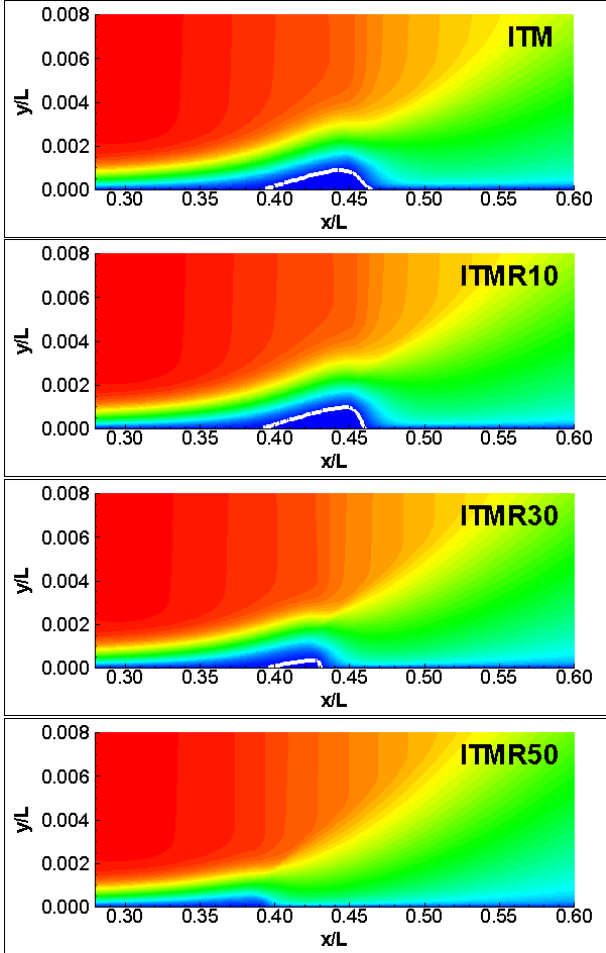


Figure 7: Contour plots of normalized velocity U/U_∞ for different roughness height

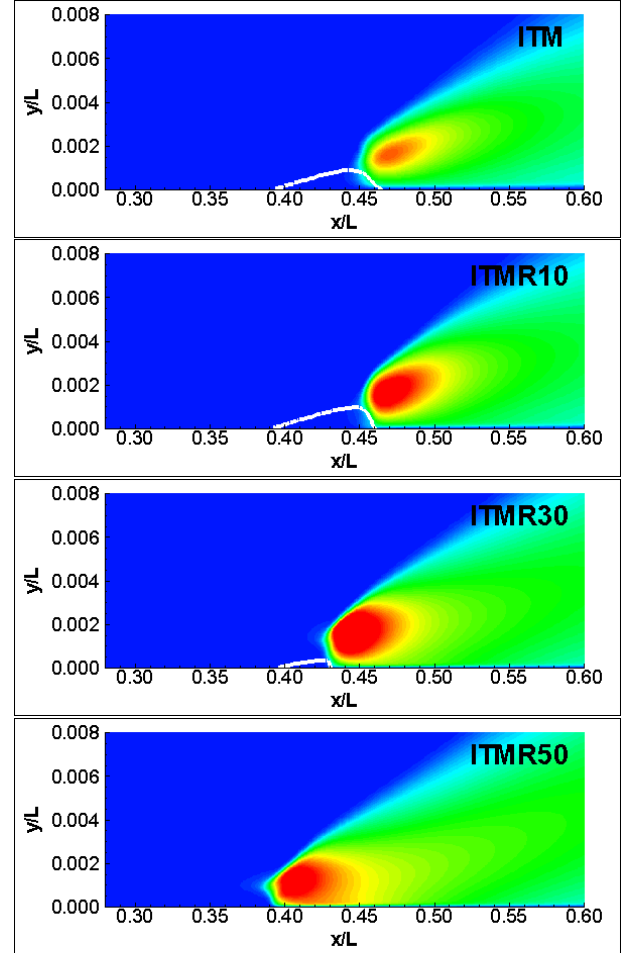


Figure 8: Contour plots of normalized u'/U_∞ for different roughness height

graphs, where ITM corresponds to smooth wall and ITM_R to the rough wall, present the impact of surface roughness on near wall region, especially visible in the area of separation. The higher roughness promotes an earlier transition of the separated boundary layer and leads to the reduction of the size of separation bubble (test cases ITMR26 and ITMR41) and even to its disappearance for the highest roughness level (test case ITMR56). It should be noted however, that the point of detachment does not vary, but there is a shift of reattachment upstream the flow accompanied by the reduction of the bubble height. Fig. 8 shows that it is due to the rise of turbulent kinetic energy in the separated laminar boundary layer and the increase of the momentum transfer towards the wall.

Fig. 9 presents the shear stress and shape factor for smooth and rough walls. It is seen that the shape factor for the smooth wall follows closely the experimental data up to $x = 0.45m$, where separated shear layer undergoes transition and reattaches. At this point the computed

distribution of H is somewhat underpredicted, while in the recovery region after the reattachment ($x = 0.47m$) it takes slightly higher values in comparison with experiment. The above observations are confirmed looking in shear stress distributions. It can be further noted that increase in the roughness level leads to rise in the value of shear stress not only in transition region, but also downstream detachment point.

4 Conclusions

The paper draws the attention to the problem of accurate and reliable predictions of surface roughness impact on fluid flow, which is of great interest for designers. The modeling approach (ITM_R model) based on $\gamma - Re_{\theta t}$ model accounting for effect of surface roughness has been presented. The studies proved that the ITM_R model appears to be sufficiently precise and enables a qualitatively correct prediction of boundary layer development for tested flow configurations. The model gives good re-

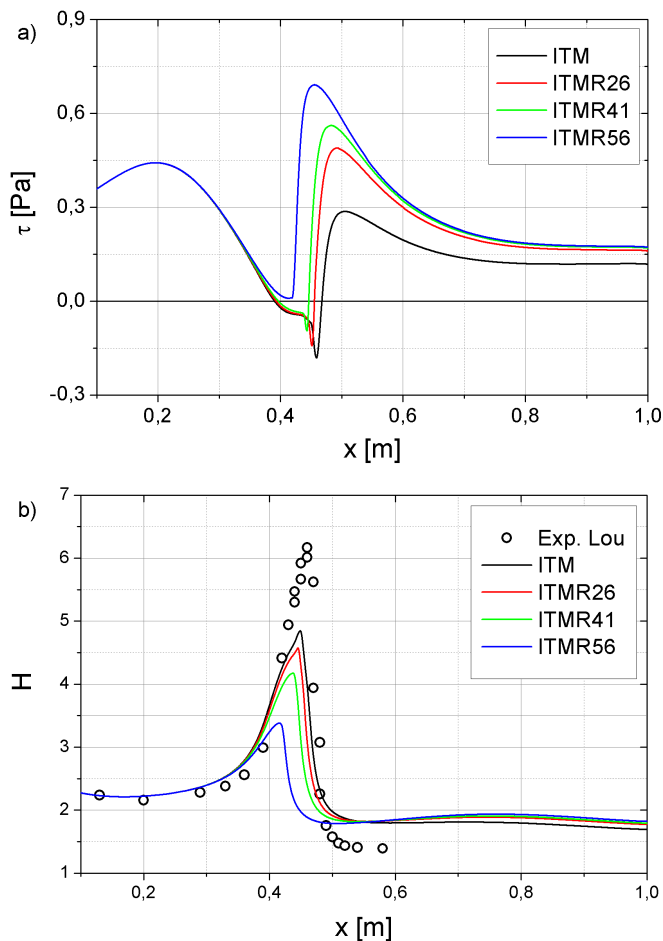


Figure 9: Shear stress (a) and shape factor (b) for LH Test Case

sults for transition in attached boundary layers, but it should work also well for separated boundary layers. One should be however aware of the complexity of the task, as the modeling of l-t transition and especially modeling of l-t transition on rough surfaces are far from being mature.

Acknowledgement

The research was supported by the Ministry of Science and Higher Education's under the statutory funds BS-03-301/98).

References

[1] Boyle R.J., Senyitko R.G., 2003, "Measurements and predictions of surface roughness effects on turbine vane aerodynamics", ASME paper GT- 2003-38580.

[2] Waigh D.R., Kind R.J., 1998, "Improved Aerodynamic Characterization of Regular Three- Dimensional Roughness", AIAA Journal, Vol. 36, No. 6, pp. 1117-1119.

[3] Hummel F., Lötzerich M., Cardamone P., Fottner L., 2005, "Surface roughness effects on turbine blade aerodynamics", J. of Turbomachinery, vol. 127, pp. 453-461.

[4] Montomoli F., Hodson H., Haselbach F., 2010, "Effect of roughness and unsteadiness on the performance of a new LPT blade at low Reynolds numbers", ASME J. of Turbomachinery, vol. 132, pp. 031018_1-031018_9.

[5] B. Aupoix B., Spalart P. R., 2003, Extensions of the Spalart-Allmaras Turbulence Model to Account for Wall Roughness, Int. J. Heat Fluid Flow, 24: 454-462.

[6] Stripf M., Schulz A., Bauer H.-J., Witting S., 2009, "Extended models for transitional rough wall boundary layers with heat transfer - part I: model formulation", ASME J. of Turbomachinery, vol. 131, pp. 031016_1-031016_10.

[7] Dassler P., Kozulovic D., Fiala A., 2010, "Modelling of roughness-induced transition using local variables", V European Conference on CFD, EC-COMAS CFD 2010

[8] Ge X., Durbin P.A. 2015, An intermittency model for predicting roughness induced transition, International Journal of Heat and Fluid Flow, vol. 54, pp. 55-64

[9] Elsner, W., Warzecha, P., 2014, Numerical study of transitional rough wall boundary layer. J. Turbomach. 136, 011010.

[10] Menter F.R., Langtry R.B., Likki S.R., Suzen Y.B., Huang P.G., Völker S., 2006, "A correlation - based transition model using local variables P.I - Model formation", ASME, J. of Turbomachinery, vol. 128, pp. 413-422.

[11] Piotrowski W., Elsner W., Drobnik S., 2010, "Transition prediction on turbine blade profile with Intermittency Transport Equation", ASME J. of Turbomachinery, vol. 132, pp. 011020_1-011020_10.

[12] Hellsten A., Laine S., 1997, "Extension of the $k - \omega$ SST turbulence model for flows over rough walls", AIAA Journal, pp. 97-3577.

[13] Healzer J.M., 1974, "The turbulent boundary layer on a rough, porous plate: experimental heat transfer with uniform blowing", Dep. of Mech. Eng. Stanford University, report HMT-18.

[14] Coleman H.W., Moffat R.J., Kays W.M., 1977, "The accelerated fully rough turbulent boundary layer", J. Fluid Mech., vol. 82, part 3, pp. 507-528

[15] Stripf M., Schulz A., Bauer H.-J., Witting S., 2009, "Extended models for transitional rough wall boundary layers with heat transfer - part II: model validation and benchmarking", ASME J. of Turbomachinery, vol. 131, pp. 031017_1- 031017_11

[16] Mills A., Hang X., 1983, "On the skin friction coefficient for a fully rough flat plate", ASME J. of Fluids Engineering, pp. 364-365.

[17] Lou W., Hourmouziadis, J., 2000, "Separation bubbles under steady and periodic-unsteady main flow conditions", Trans. ASME J. of Turbomachinery, Vol. 122, pp. 634-643.

COMPARISON OF RANS AND EMBEDDED LES CALCULATIONS WITH MEASUREMENTS OF TRANSITIONAL FLOW ALONG A FLAT PLATE

P. Bader¹, W. Sanz¹, C. Steinmayr² and P. Leitl²

¹*Institute of Thermal Turbomachinery and Machine Dynamics
Graz University of Technology
8010 Graz, Inffeldgasse 25/A, Austria*

²*bionic surface technologies GmbH
8010 Graz, Brockmannngasse 49, Austria*

Abstract

Flow in turbomachines is generally highly turbulent. The boundary layers, however, often exhibit laminar-to-turbulent transition. Relaminarization from turbulent to laminar flow may also occur. The state of the boundary layer is important since it strongly influences transport processes like skin friction and heat transfer.

It is therefore vitally important for the designer to understand the process of laminar-to-turbulent transition and to be able to determine the position of transition onset and the length of the transitional region. Several approaches exist to numerically predict transition along a solid body, but the uncertainty of these simulations are quite unknown. In order to get more insight into the process of transition and relaminarization it is often helpful to study simplified test cases first. Therefore, in this paper the transitional flow along a flat plate is experimentally and numerically studied and the capability of numerical approaches to predict the transition process accurately will be highlighted.

Constant temperature anemometry (CTA) as well as laser Doppler anemometry (LDA) measurements are performed to study the transitional flow. The measurement results are then compared with the results of different numerical simulations using the Reynolds-averaged Navier-Stokes (RANS) approach with different transition models as well as an embedded large eddy simulation (eLES). Time averaged and instantaneous velocity profiles are compared with the measurement data. Additionally time signals of the CTA probe are compared with the LES data.

In this way the capability of modern RANS models and of an embedded large eddy simulation in predicting transition are studied. The features of an eLES regarding the simulation of transition are presented.

1 Introduction

In flows along solid body surfaces the boundary layer represents the narrow zone between the wall and the free stream where viscous effects are important. Its state of flow (laminar or turbulent) may have strong impact on transport processes like wall friction and heat transfer. These processes influence the efficiency as well as the thermal stress for example of a turbine blade. In turbomachinery the laminar or turbulent state of the boundary

layer may therefore affect the efficiency of the stages and has an effect on other flow characteristics in the machine as well [1].

At the first contact of a flow with a stationary structure, the boundary layer is laminar and then develops from laminar to turbulent (under the appropriate flow conditions) via a transitional region. There are mainly three different types of transition: Natural, bypass and separated-flow transition. Schlichting and Gersten [2] extensively discussed the different stages a boundary layer passes through within the natural transition zone before becoming fully turbulent. In turbomachinery, where generally high free-stream turbulence exists whose fluctuations act on the boundary layer flow, bypass transition is the dominant feature where the earlier stages of natural transition are bypassed.

Many parameters, like free-stream velocity, acceleration, free-stream turbulence etc., may influence the state of a boundary layer. It is therefore important to understand the effect of these parameters on the onset position and length of the transitional zone in order to predict and potentially control the state of the boundary layer. In turbomachinery, the efficiency of blades and stages can be improved considering transition, thus improving the overall machine performance. In 1991, Mayle published a comprehensive review of the importance of transition in gas turbines [3]. He analyzed experiments performed by several research groups in order to find the influence of different flow parameters on the transition process.

Additional experiments have been performed in the last years by many research groups. Yip et al. performed in-flight measurements, detected transition with the help of Preston tubes and analyzed the influence of the flight conditions on the boundary layer along an airfoil [4]. In this way they performed full-scale Reynolds number flow measurements including relaminarization and attachment-line transition. Oyewola et al. used hot-wire anemometry and laser Doppler anemometry (LDA) to investigate the effect of wall suction on a turbulent boundary layer [5, 6]. Widmann et al. performed near-wall measurements with particle image velocimetry (PIV) in order to measure Tollmien-Schlichting waves [7]. Hot-film measurements were performed, e.g., by Mukund et al. [8] who investigated relaminarization along a convex surface. Preston-tube and thermographic measurements by Bader and Sanz [9] and Bader et al. [10] showed an interesting comparison between different measurement

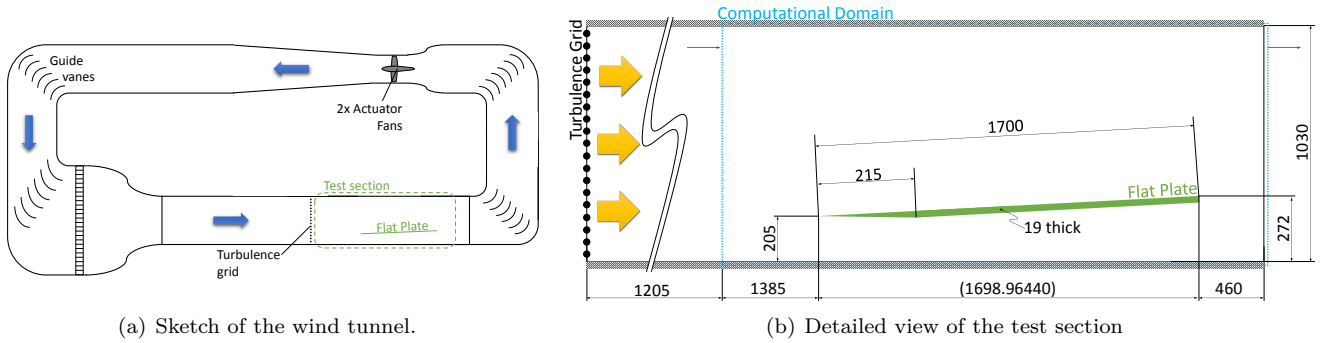


Figure 1: Göttinger-type wind tunnel with closed test section used for experiments

techniques regarding their capability to detect transition.

In addition to measurements, numerical models were developed to predict the laminar-to-turbulent transition process. Common models are, for example, the $k-k_L-\omega$ model by Walters and Cokljat [11], the intermittency γ model by Menter et al. [12] and the $\gamma-Re_\theta$ model by Menter et al. [13] and Langtry [14]. For the latter, various correlations for important model parameters were developed [15, 16, 17, 18, 19].

So far, mainly the transition from laminar to turbulent flow was investigated. Under certain flow conditions (like high acceleration), however, a reverse transition or relaminarization from turbulent to laminar can occur. Up to now, only few measurements on relaminarization were reported [20, 21, 22]. Therefore, at the Institute of Thermal Turbomachinery and Machine Dynamics (ITTM) of Graz University of Technology a project was launched in order to understand the process of relaminarization.

The aim of this project is to understand the process of transition and relaminarization even further. Experimental and numerical means have been extensively applied to tackle this task. So several measurement techniques have been used to predict transition and have been validated against each other [9, 10]. In the present paper the results of constant-temperature anemometry (CTA) as well as laser Doppler anemometry (LDA) will be presented. The measurement results are compared to computational fluid dynamics (CFD) calculations.

For the CFD simulations Reynolds-averaged Navier-Stokes (RANS) simulations with different transition models as well as large eddy simulation (LES) have been performed. As transition models for the RANS simulations two intermittency models, namely the γ and the $\gamma-Re_\theta$ model and the $k-k_L-\omega$ model have been used. The LES solution was obtained applying a RANS-LES hybrid approach to reduce the computational effort, called embedded large eddy simulation (eLES). The CFD simulations have been done by Bionic Surface Technologies GmbH (BST). Their special expertises are riblet simulations and their application. These numerical simulations also function as prestudies for investigations in the influence of riblets on transition.

2 Experimental Setup

In this section, the experimental setup used for the CTA and LDA measurements is presented. The detailed results of the hot wire measurements have already been presented by Bader et al. [10] and are only shortly discussed here. The measurement data is used for the evaluation of the simulations in the next section.

2.1 Test Facility

The tests were performed in a Göttinger-type wind tunnel with closed test section at the Institute of Fluid Mechanics and Heat Transfer. A sketch of the tunnel is given in Fig. 1(a). The wind tunnel is powered by two fans with a total power input of 75 kW. The air is conveyed to the nozzle and the test section via two corners with guide vanes. The maximum achievable flow-rate equivalent velocity is about 30 m/s. The nozzle exit cross section is 2 m wide and 1 m high. Downstream from the nozzle, a 6 m long channel for developing flow velocity profiles is installed. The test section itself is about 2.6 m long. The top panel of the tunnel is adjustable for controlling the pressure gradient along the test section.

Since the turbulence of the wind tunnel flow is well below 1 %, a turbulence grid is installed upstream from the test section in order to raise the turbulence level to about 3 % to 4 %. The turbulence grid consists of equally spaced cylindrical rods. As suggested by Roach, the grid has a solidity below 50 %, and its position upstream from the first measuring point satisfies the $x/d > 10$ criterion, where x represents the streamwise coordinate and d the diameter of the rods [23].

Downstream from the turbulence grid, but upstream from the flat plate, the first measurement section is located (inlet of the computational domain in Fig. 1(b)). At this plane the turbulence level and the free-stream velocity were measured in order to get the inlet boundary conditions for the numerical simulations.

Figure 1(b) also shows the position of the flat plate. The plate is inclined by two degrees against the bottom wall of the channel in order to ensure that the flow is attached at the upper surface. The plate distance from the side walls is larger than the boundary layer thickness there in order to avoid influences from the sidewall boundary layers on the flow along the plate.

2.2 Hot Wire Anemometry

In the present work hot wire anemometry was also applied for measuring flow velocities. A multi-channel constant-temperature anemometer (CTA) 54N82 with a 54N95 transmitter from *Dantec Dynamics A/S* was used with miniature X-wire probes type 55P63 with 90° tilted heads for the velocity measurements along the plate. Straight probes type 55P61 were used for measuring the free-stream turbulence upstream from the plate. For the temperature compensation, a 90P10 reference temperature probe was used. The measurements were performed with a sampling frequency of 10 kHz, collecting a total number of 80,000 samples for each measuring position.

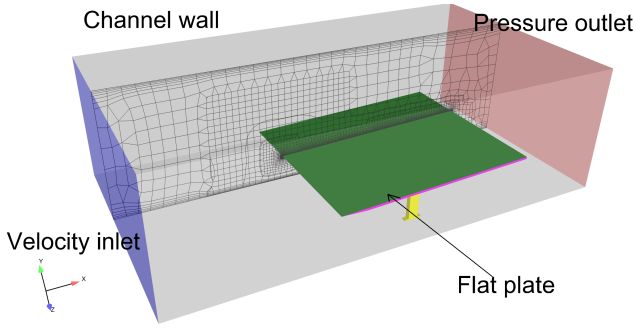


Figure 2: Numerical domain of the 3D RANS simulation

2.3 Laser Doppler Anemometry

Additionally LDA measurements were performed in order to get the velocity and its fluctuations within the boundary layer. The two-dimensional LDA system by *Dantec Dynamics A/S* consists of a 6 Watt Argon-Ion Laser, two Burst Spectrum Analyzer (BSA) processors, 57N35 model S and 57N20, and a 60x41 FiberFlow transmitter ($\lambda_1 = 514.5 \text{ nm}$, $\lambda_2 = 488 \text{ nm}$).

As optic a 60 mm probe head (60x67 2D probe) with a beam distance of 75.24 mm, a focal distance of 1000 mm and a beam diameter of 2.2 mm (in front of the lens) is used.

For seeding a fog generator from *EHLE-HD* was applied with *Slow Fog* glycol-water-based seeding medium. The density is approximately $\rho = 1260 \text{ kg/m}^3$, thus the seeding particles act as a low pass filter up to about $f(-3\text{dB}) = 41 \text{ kHz}$ [24].

3 CFD Simulation

The simulations were performed for a free-stream velocity of 10 m/s where transitional flow was detected along the plate in the measurements. The measured turbulence intensity was $Tu = 3.15 \%$ in the free stream at the plate leading edge. The turbulent boundary conditions at the inlet of the computational domain were found by the requirement of matching the measured free-stream turbulence intensity along the plate.

3.1 3D RANS Simulations

In this section the CFD results of a Reynolds-averaged Navier-Stokes (RANS) simulation are presented. The calculations have been performed with the commercial solver ANSYS® Fluent® v15.0. In order to predict transition three different transition models have been used and are compared to each other. Two models, the γ [12] and the $\gamma-Re_\theta$ model [13], are based on the intermittency approach. The intermittency which is defined as the ratio of time when the flow is turbulent to the total time is an indicator of the transitional state of the boundary layer. It is modelled with a transport equation and is used to modify the turbulence production in the SST turbulence model equations [13]. The γ model has been recently derived from the more complex $\gamma-Re_\theta$ model and needs only one transport equation. The third model, the $k-k_L-\omega$ model [11], additionally considers the transport of the so-called laminar kinetic energy which precedes the transition process. It triggers the formation of turbulence kinetic energy in the transition process.

For the calculation a three dimensional mesh was used covering the whole flow domain with all details like the plate mounting. The domain starts 1385 mm upstream

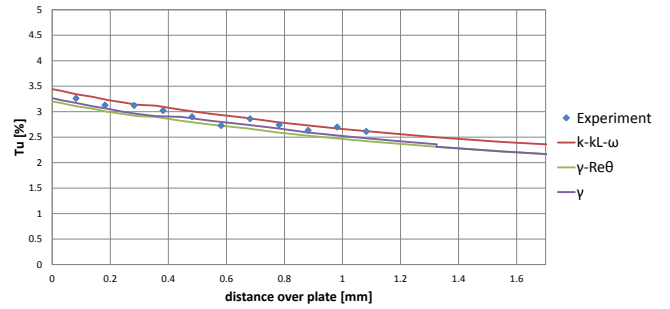


Figure 3: Comparison of measured and simulated free-stream turbulence intensity

of the leading edge of the flat plate (see Figure 1(b)) with a velocity inlet boundary condition. The numerical mesh was generated with the program HEXPRESS™ of NUMECA. It is an unstructured mesh with a cell number of around 8 million cells. The geometry together with the applied numerical boundary conditions and a mesh sketch can be seen in Figure (2). The near wall condition on grid fineness of $y^+ \leq 1$ for transition modeling was fulfilled along the plate's upper side.

3.1.1 Development of Turbulence Intensity

At first the turbulence inlet boundary conditions were adjusted in order to capture the measured free-stream turbulence intensity along the flat plate (see Figure (3)). All three simulated cases exhibit a very good agreement with the measurement values, so that the flow conditions along the plate can be considered as similar. It is interesting that the $k-k_L-\omega$ model shows a slightly higher turbulence for the same inlet boundary conditions.

3.1.2 Skin Friction Coefficient

At the trailing edge in the center of the plate a foothold is mounted at the bottom side to hold the plate in its position. This support has a slight influence on the flow at the rear part of the plate at the centerline. To avoid this influence on the result the following evaluation of the skin friction coefficient was made at a z-position of 750 mm ($\approx 33\%$ plate width) where it is negligible.

The calculated skin friction coefficient c_f is plotted over the plate length in Figure (4). c_f is defined as

$$c_f = \frac{\tau_w}{1/2 \cdot \rho \cdot U_{\infty,0}^2} \quad (1)$$

where $U_{\infty,0}$ represents the inlet velocity of 10 m/s, τ_w the wall shear stress and ρ the fluid density.

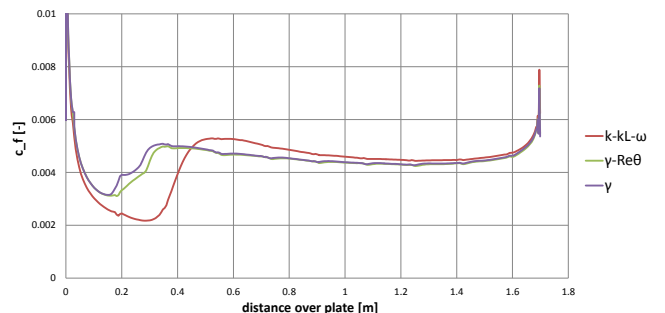


Figure 4: Calculated skin friction coefficient along the plate

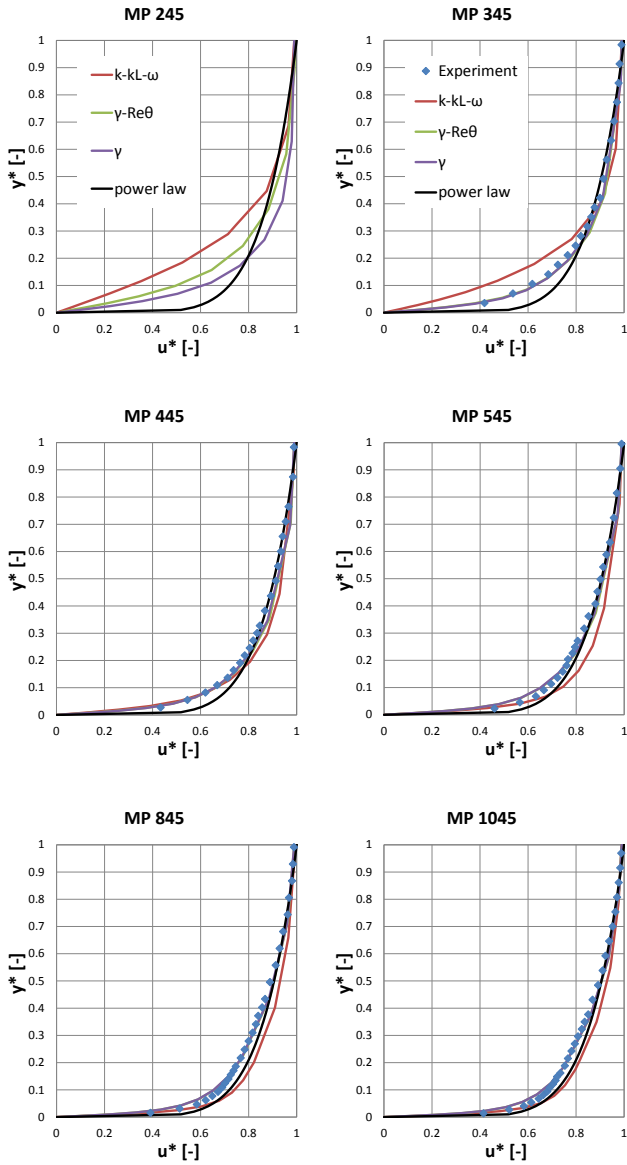


Figure 5: Dimensionless velocity profiles along the plate; comparison of RANS solutions with the measurements

All three models show a decrease of the skin friction coefficient in the leading edge region as expected in a laminar boundary layer flow upstream of the start of the transitional zone. The intermittency models both show a rise in skin friction and thus beginning transition significantly more upstream than the $k-k_L-\omega$ model. On the other hand this model predicts a slightly more rapid transition process. Due to the later transition the skin friction of the $k-k_L-\omega$ model is slightly higher after transition compared to the other models. The sudden rise of the skin friction coefficient at the trailing edge is caused by the enlargement of the flow area there which leads to an overspeed.

3.1.3 Velocity Profiles

A detailed insight into the boundary layer flow is given by the dimensionless velocity profiles at different positions along the plate. In Figure (5) the the non-dimensional velocity u^* is plotted for a dimensionless wall distance

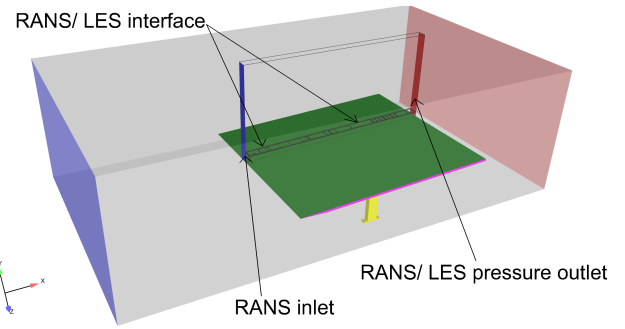


Figure 6: Position of eLES domain

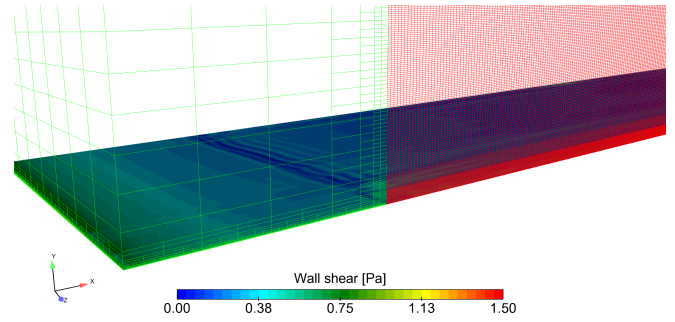


Figure 7: Sketch of the mesh in the RANS inlet section and in the LES region; instantaneous wall shear is shown along the plate

y^* . These values are defined as

$$y^* = \frac{y}{\delta(x)} \quad (2)$$

$$u^* = \frac{u(y)}{U_\infty(x)} \quad (3)$$

where $\delta(x)$ represents the local boundary layer thickness and $U_\infty(x)$ the local free-stream velocity at each position. The edge of the boundary layer is defined as the distance normal to the wall with

$$u(y = \delta(x)) = 0.99 U_\infty(x) \quad (4)$$

Besides the measurement and simulation data the 1/7th-power law profile is plotted in Figure (5), which is a good approximation of a fully turbulent boundary layer and which is defined as

$$u^* = (y^*)^{\frac{1}{7}} \quad (5)$$

At the first location MP 245, which is located 245 mm downstream of the plate leading edge, the three calculated velocity profiles differ remarkably from the 1/7th-power law indicating that all simulations predict laminar or transitional flow which agrees with the results shown in Figure (4). The $k-k_L-\omega$ velocity profile deviates most; the boundary layer is still laminar. The transition predicted by the γ model is a little bit more advanced compared to the one of the $\gamma-Re_\Theta$ model.

Once transition is completed the two intermittency models predict identical results. So in measurement point MP 345, which is located 345 mm downstream of the plate leading edge, the intermittency results agree well with the measured velocity profile. The profile is not fully turbulent compared to the 1/7th-power law indicating that transition is not yet completed. The $k-k_L-\omega$ velocity profile rises linearly to approximately $y^* \sim 0.3$

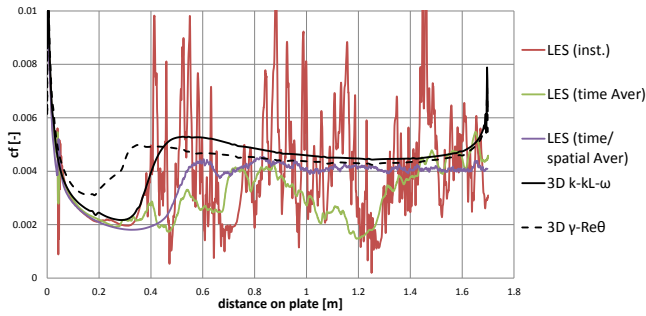


Figure 8: Comparison of skin friction coefficient along the plate for eLES and RANS simulations

revealing its still laminar character which agrees with the observations of the skin friction distribution of Figure (4).

At the next position MP 445 all calculated velocity profiles agree well with each other and with the measured profile especially close to the wall. This is approximately the location where all models predict the same skin friction coefficient value in Figure (4).

With rising distance from the leading edge measured and calculated profiles become more turbulent, converging towards the 1/7th-power law. But whereas the intermittency models nearly perfectly match the measured velocity profiles, the $k-k_L-\omega$ model exhibits a fuller profile. This observation agrees with the higher skin friction value in Figure (4). It also fits better to the 1/7th-power law at the last two positions which indicates a "more turbulent" flow at the back of the plate compared to the measured and intermittency model velocity profiles.

4 Embedded Large Eddy Simulation (eLES)

Large eddy simulation is said to be able to predict transition without additional modelling. In order to see its capability an embedded LES (eLES) is performed on the same test case. Embedded LES is a method that combines LES and RANS in such a way that an LES region is embedded in a surrounding RANS zone. Special interfaces are necessary for the information transport between the different regions.

For the simulation with eLES not the whole three dimensional test area of the wind tunnel was simulated, but a small section of 80 mm width as displayed in Figure (6). This is acceptable as the RANS simulations above show only small variations in transverse direction. Although the computational domain is reduced the mesh size increases due to the higher mesh density necessary for LES. The mesh was generated according to the guideline for transition modelling with eLES by Menter [25]. The dimensionless cell size within the boundary layer is $\Delta x^+ < 40$ (streamwise), $\Delta y^+ < 1$ (normal to wall) and $\Delta z^+ < 20$ (transversal).

The mesh used in this study has two different calculation domains. The near-wall part of the reduced flow domain is covered by an LES domain (see Figure (6)). A RANS domain is arranged in front and on top of the LES domain. Figure (7) shows the two flow domains at the inlet and gives a sketch of the RANS and LES meshes. The cell size in the LES mesh is about 1/20th of the one in the RANS zone. The requirements on grid fineness for the LES computation lead to about 45 million cells for the LES domain, the total cell number including the

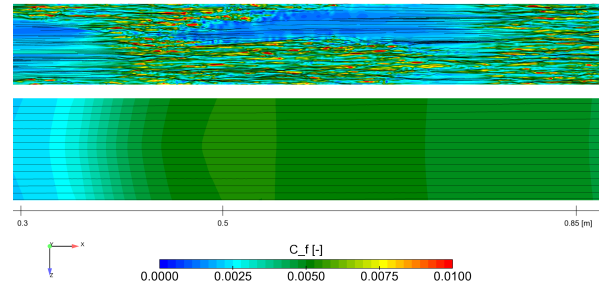


Figure 9: Detailed view of instantaneous eLES (top) and RANS (bottom) skin friction coefficient in the transitional region (245 mm-645 mm from leading edge).

RANS zones is about 62 million.

Classical LES requires unsteady boundary conditions at turbulent inlets/interfaces. For the RANS-LES interface ANSYS® Fluent® v15.0 offers the vortex method and the spectral synthesizer. Both methods create stochastically discrete vortices at the inlet. Their distribution, strength, and size are modeled in order to provide the desirable characteristics of real turbulence. The input parameters are the turbulent scales (k and ω or k and ϵ) from an upstream RANS computation (for further details see [26] and [25]).

In order to use the stochastic turbulence generator at the interface, in this simulation a short RANS zone is placed in the leading edge region. The $k-k_L-\omega$ model is used there, the inlet boundary conditions were taken from the 3D RANS solution, with the variables velocity \vec{v} , turbulence kinetic energy k_T , laminar kinetic energy k_L and specific dissipation rate ω . At the streamwise plate position $x = 0.004$ m the LES domain starts, so that the interface between the RANS and LES domain is situated in the laminar region. The spectral synthesizer was chosen at the RANS-LES interface in front and on the top of the LES zone. With this configuration it was possible to generate a laminar flow in the first section of the flat plate which gets turbulent at downstream positions. Figure (7) shows the wall shear in the interface region. Small disturbances starting at the interface move into the LES region. In the side walls of the computational domain periodic flow conditions are assumed.

For the simulation a timestep of $t_s = 2.5 \cdot 10^{-5}$ has been used. Convergence of the solution is checked by plotting the total drag of the flat plate over time. 8000 time iterations were performed which took about 4 weeks on a 10-core computer; the solution was stored for every 100th step leading to 80 instantaneous distributions for the data evaluation.

Figure (8) shows a comparison of the skin friction coefficient c_f along the plate between the RANS results and the eLES. The diagram includes an instantaneous eLES result, a time-averaged result at mid line and a time- and transversely averaged result.

The instantaneous distribution shows large fluctuations starting approximately at the location of the transition onset as predicted by the $k-k_L-\omega$ model. The time-averaged result also indicates an increase of the c_f value at a similar location. But the fluctuations indicate that additional time snapshots should be used for averaging to obtain a "steady" result. The additional spatial averaging in transversal direction increases the number of instantaneous solutions used for averaging so that a smoother c_f distribution is obtained with values in the fully turbulent region close to the RANS results. But the averaged eLES solution predicts the most downstream transition

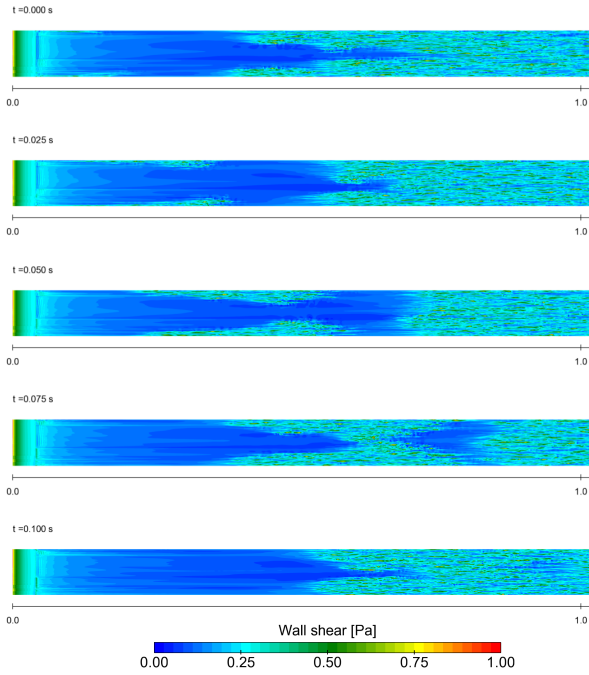


Figure 10: Instationary wall shear stress distributions from LES

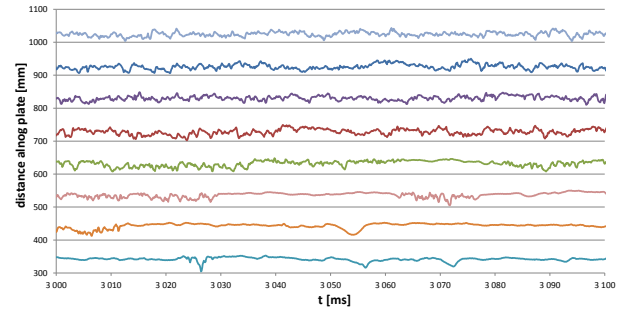
onset compared to all three RANS results.

The interface between RANS and LES domain can be observed in a slight spike shortly after the leading edge of the plate, but the nature of the laminar boundary layer is not influenced by the interface.

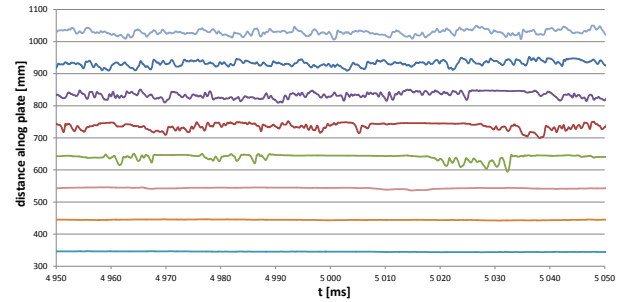
Figure (9) gives a comparison of an instantaneous c_f distribution (top view) with the RANS $k-k_L-\omega$ solution (bottom view) along the plate surface in the transitional region ($245 \text{ mm} \leq x \leq 645 \text{ mm}$). The peak values seen in Figure (8) are visible as red spots in the eLES domain and can be considered as turbulent bursts which are transported downstream. They also cause relatively strong lateral fluctuations which are shown by the streamlines close to the wall in the eLES solution. The large regions of low skin friction (blue zones) are of laminar character which is also shown by the nearly straight streamlines. It is interesting that the local c_f values show maxima about five times higher than the averaged c_f -values.

In order to better show the unsteady nature of the flow Figure (10) gives five snapshots of the wall shear stress distribution covering a time period of 0.1 s. In the first snapshot we see two spots of high wall shear evolving at both side walls of the computational domain. They grow and cover a more and more broad zone of the flow section until they eventually merge at $t = 0.75 \text{ s}$. The zone of low wall shear is pushed forward by the evolving turbulence and is finally trapped between regions of high turbulence ($t = 0.75 \text{ s}$). Finally it also transitions under the influence of the neighboring turbulent fluctuations.

Time signals of velocity fluctuations are also an appropriate indicator of the state of the boundary layer. Figure (11) compares the time signals of the CTA measurement with the eLES results. The signals are taken at several streamwise positions, 3 mm above the plate. It can be observed that measured and simulated signals have similar characteristics, although the measurement signal possesses additional higher-frequency oscillations. In the measurements the first two signals ($x = 345 \text{ mm}$ and $x = 445 \text{ mm}$) offer long laminar periods; further downstream, fluctuations start to increase but still lam-



(a) Measurement



(b) eLES solution

Figure 11: Time signal of velocity at different streamwise positions

inar zones can be found between turbulent packages ($x = 545 \text{ mm}$ and $x = 645 \text{ mm}$). At $x = 745 \text{ mm}$ the boundary layer appears to be fully turbulent. In the eLES first turbulent packages turn up more downstream at $x = 645 \text{ mm}$; laminar periods can be still detected at $x = 745 \text{ mm}$ and $x = 845 \text{ mm}$. At $x = 945 \text{ mm}$ the time signal seems fully turbulent. This again indicates a later and shorter transition process as also observed in the c_f distribution of Figure (8).

In Figure (12) the non-dimensional velocity profiles $u^*(y^*)$ of the eLES solution are plotted in two ways: time-averaged at the mid line and time- and transversally-averaged. The measurement data and again the power law according to Equation (Eq. (5)) are also included. Additionally in Figure (13) several instantaneous velocity profiles are compared with each other. The small differences between time-averaged and time-space-averaged profiles show that more snapshots than 80 are necessary to obtain a "steady" result.

At the first position (MP 345) the eLES curves show similar behavior close to the wall and their slope indicates the laminar character there. This is confirmed by the instantaneous profiles of Figure (13) which all show the same slope close to the wall and only small deviations to each other. At larger wall distance the time-space-averaged profile approaches the 1/7th-power law. The difference to the measurement results again reveals that the measurement shows a transitional boundary layer there. At the next position (MP 445) there are small differences between both eLES results; and the simulation still shows a laminar profile whereas the measured profile approaches the power law indicating its turbulent character. At MP 645 the slope of both eLES profiles is steeper but has not yet reached the fully turbulent distribution. The instantaneous profiles also show partly laminar, partly turbulent character which agrees with the observations of Figure (10). At MP 845 measured and calculated profiles agree well with the 1/7th-power law; the flow is turbulent. The instantaneous profiles fluctu-

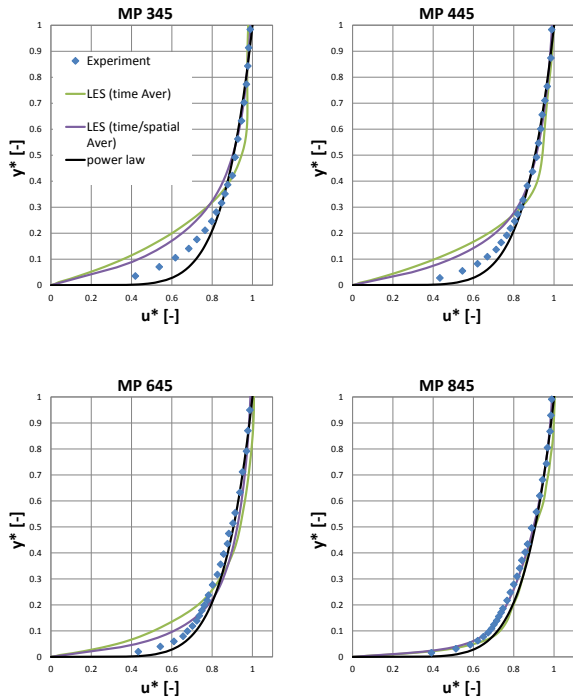


Figure 12: Dimensionless velocity profiles along the plate; comparison of LES results with the measurements

ate and differ remarkably as expected from a turbulent boundary layer.

5 Summary and Conclusions

Accurate transition prediction is still a topic of research. Therefore in this work this problem is tackled by experimental and numerical investigations of the transitional flow along a flat plate. Three different RANS simulations with transition modeling and an eLES were evaluated based on CTA and LDA data of the velocity profiles. The best results are obtained with the intermittency based transition models which could capture the transition zone best based on a comparison between measured and calculated boundary layer velocity profiles. The γ model which was derived from the more complex $\gamma-Re_{\theta}$ model gives nearly identical results at a reduced computational effort. The third RANS model, the $k - k_L - \omega$ model, gives also reasonable results but predicts a too late transition process compared to the experiments.

The eLES method which combines RANS and LES domains gives an insight into the unsteady development of transition. Very long computational times are necessary to obtain a converged time-averaged "steady" flow. The eLES could clearly capture the transition process. The evolution and development of turbulent bursts are visible in the wall shear stress contours. The associated velocity profiles in the boundary layer show laminar and turbulent profiles in the transition zone. But the predicted transition process takes place too far downstream similar to the $k - k_L - \omega$ model predictions.

Summarizing, for the test case presented all numerical approaches give reasonable results and are able to predict transition. But the simplest approach, the intermittency based RANS simulations, exhibits the best agreement with the measurement data especially regarding the transition process. Further evaluations will be performed on non-zero-gradient flows in order to improve the knowledge on the accuracy of transition modelling.

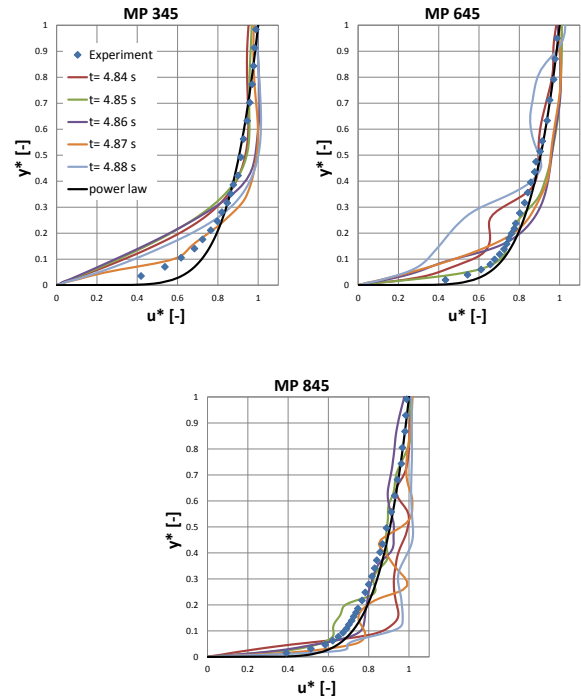


Figure 13: Instantaneous dimensionless velocity profiles from LES at three streamwise positions

Acknowledgment

The authors would like to thank the Institute of Fluid Mechanics and Heat Transfer, especially Günter Brenn and Walter Meile, for providing their wind tunnel and parts of the measuring equipment and also for their continuous support during the test campaign.

The authors gratefully acknowledge the support from the Austrian Federal Ministry of Transport, Innovation and Technology by funding the project RELAM in the frame of the Austrian Aeronautics Program TAKE OFF.

References

- [1] P. Bader and W. Sanz, "Steady and unsteady CFD calculation of the laminar-to-turbulent transition in a turning mid turbine frame with embedded design," *ASME Turbo EXPO 2015, Montreal, Canada*, 2015. GT2014-42617.
- [2] H. Schlichting and K. Gersten, *Grenzschicht-Theorie (Boundary-Layer Theory)*. Springer-Verlag Berlin Heidelberg, 2006.
- [3] R. E. Mayle, "The role of laminar-turbulent transition in gas turbine engines," *ASME Journal of Turbomachinery*, vol. 113, pp. 509–537, October 1991.
- [4] L. P. Yip, P. Vijgen, J. D. Hardin, and C. P. van Dam, "In-flight pressure distributions and skin-friction measurements on a subsonic transport high-lift wing section," *AGARD CP-515*, 1993.
- [5] O. Oyewola, L. Djenidi, and R. A. Antonia, "Combined influence of the reynolds number and localised wall suction on a turbulent boundary layer," *Experiments in Fluids*, vol. 35, pp. 199–206, July 2003.
- [6] O. Oyewola, "LDV measurements in a perturbed turbulent boundary layer," *Journal of Applied Science*, vol. 6, no. 14, pp. 2952–2955, 2006.

- [7] A. Widmann, A. Duchmann, A. Kurz, S. Grundmann, and C. Tropea, “Measuring Tollmien-Schlichting waves using phase-averaged particle image velocimetry,” *Experiments in Fluids*, vol. 53, pp. 707–715, 2012.
- [8] R. Mukund, R. Narasimha, P. R. Viswanath, and J. D. Crouch, “Multiple laminar-turbulent transition cycles around a swept leading edge,” *Experiments in Fluids*, vol. 53, pp. 1915–1927, 2012.
- [9] P. Bader and W. Sanz, “On the setup of a test bench for predicting laminar-to-turbulent transition on a flat plate,” *Proceedings of the 12th International Symposium on Experimental Computational Aerothermodynamics of Internal Flows, Genova, Italy*, 2015. ISAI12-074.
- [10] P. Bader, W. Sanz, J. Peterleithner, J. Woisetschlager, F. Heitmeir, W. Meile, and G. Brenn, “Measuring flat plate transition with laser interferometric vibrometry (LIV),” *ASME Turbo Expo 2016, Seoul, South Korea*, 2016. GT2016-56043.
- [11] K. Walters and D. Cokljat, “A three-equation eddy-viscosity model for Reynolds-averaged Navier-Stokes simulations of transitional flows,” *Journal of Fluids Engineering*, vol. 130, pp. 1214011–12140114, 2008.
- [12] F. Menter, P. Smirnov, T. Liu, and R. Avancha, “A one-equation local correlation-based transition model,” *Flow, Turbulence and Combustion*, vol. 95, no. 4, pp. 583–619, 2015.
- [13] F. R. Menter, R. B. Langtry, S. R. Likki, Y. B. Suzen, P. G. Huang, and S. Volker, “A correlation based transition model using local variables part 1: Model formulation,” *ASME Journal of Turbomachinery*, vol. 128, no. 3, pp. 413–422, 2006.
- [14] R. B. Langtry, *A correlation-based transition model using local variables for unstructured parallelized CFD codes*. PhD Thesis, Institute of Thermal Turbomachinery and Machinery Laboratory, University Stuttgart, 2006.
- [15] W. Elsner, W. Piotrowski, and S. Drobniak, “Transition prediction on turbine blade profile with intermittency transport equations,” *ASME Turbo Expo 2008, Berlin, Germany*, 2008. GT2008–50796.
- [16] R. B. Langtry and F. R. Menter, “Correlation-based transition modeling for unstructured parallelized computational fluid dynamics codes,” *AIAA Journal*, vol. 47, no. 12, pp. 2894–2906, 2009.
- [17] N. N. Sorensen, “CFD modeling of laminar-turbulent transition for airfoil and rotors using the $\gamma - Re_{\Theta}$ model,” *Wind Energy*, vol. 12, no. 8, pp. 715–733, 2009.
- [18] P. Malan, K. Suluksna, and E. Juntasaro, “Calibrating the $\gamma - Re_{\Theta}$ transition model for commercial CFD.” Submitted to the 47th AIAA Aerospace Sciences Meeting, Orlando, Florida, 2009. AIAA 2009–1142.
- [19] M. Kelterer, R. Pecnik, and W. Sanz, “Computation of laminar-turbulent transition in turbomachinery using the correlation based $\gamma - Re_{\Theta}$ transition model.” *ASME Turbo Expo 2010, Glasgow, Scotland*, 2010. GT2010-22207.
- [20] M. Ichimiya, I. Nakamura, and S. Yamashita, “Properties of a relaminarizing turbulent boundary layer under a favorable pressure gradient,” *Experimental Thermal and Fluid Science*, vol. 17, pp. 37–48, 1998.
- [21] R. Mukund, P. R. Viswanath, R. Narasimha, and J. D. Praband Crouch, “Relaminarization in highly favourable pressure gradients on a convex surface,” *Journal of Fluid Mechanics*, vol. 566, pp. 97–115, 2006.
- [22] S. Dorfer, *Auslegung und experimentelle Untersuchung eines Relaminarisierungstestfalls*. Diploma Thesis, Institute of Thermal Turbomachinery and Maschine Dynamics, Graz University of Technology, Austria, 2011.
- [23] P. R. Roach, “The generation of nearly isotropic turbulence by means of grids,” *International Journal of Heat and Fluid Flow*, vol. 8, pp. 82–92, 1987.
- [24] J. Boree, L. Ben, and R. Bazile, “Optical methods for the measurement of constant and variable density flows,” *International summer school on variable density turbulent flows, Barcelona, Spain*, 2003.
- [25] F. R. Menter, “ANSYS FLUENT best practice: Scale-resolving simulations in Ansys CFD,” *ANSYS Inc. Germany*, 2012.
- [26] ANSYS Inc., Canonsburg, *ANSYS FLUENT Theory Guide*, 15 ed., 2013.

APPLICATION CHALLENGES FOR TRANSITION PREDICTION TECHNIQUES IN AN UNSTRUCTURED CFD CODE

A. Krumbein, N. Krimmelbein, C. Grabe and N. Shengyang

*German Aerospace Center (DLR), Institute of Aerodynamics and Flow Technology
C²A²S²E Center for Computer Applications in AeroSpace Science and Engineering*

1 Introduction

At present, computational fluid dynamics (CFD) is evolving from a single discipline to become one of the components of multi-disciplinary simulation environments. These multi-disciplinary simulation environments comprise CFD codes, computational structure mechanics codes and flight mechanics methods and are meant to be used for approaching the vision of the digital aircraft [1]. The wording 'flying the equations' expresses the idea of executing highly coupled simulations involving many different software components and carrying out high-fidelity CFD for realistic aircraft configurations in a time-accurate manner within the complete flight range, that is, for the design point as well as for situations near the flight envelope which limits the flight range.

For achieving the necessary reliability of the simulation results on the CFD side, especially near the flight envelope, significant improvements of the turbulence and transition models must be developed and incorporated into the codes. For the simulation of turbulence effects within Reynolds-averaged Navier-Stokes (RANS) solvers Reynolds stress models (RSM) is an approach that more and more CFD users have started to use and to request experiencing that for specific flow phenomena the results can match experimental findings significantly better than eddy-viscosity models (EVM) [2-4]. For the consideration of effects of boundary-layer transition in external flows about aircraft laminar-turbulent transition prediction techniques providing the points of transition onset and the transitional flow regime must be applicable in a fully automatic and autonomous manner so that transition prediction can be carried out during the ongoing run of a CFD simulation.

In the DLR TAU code [5], the unstructured CFD simulation system for external compressible aerodynamics at DLR, we focus on two different basic concepts [6], at present, streamline-based approaches and local correlation-based approaches with transport equations. In the following, we outline briefly some of the major challenges for the application of transition prediction techniques that we see for the future realization of 'flying the equations'.

2 Streamline-based Approaches

The streamline-based approaches are based on a coupled iteration between the RANS solver and a transition prediction module that provides transition locations which have to converge to fixed positions as well as the solution process of the RANS equations has to converge, Fig. 1. For arbitrary three-dimensional configurations the detection of the transition locations is done along the direction of the inviscid flow at the boundary-layer edge, the edge streamlines, which are then used as integration paths for

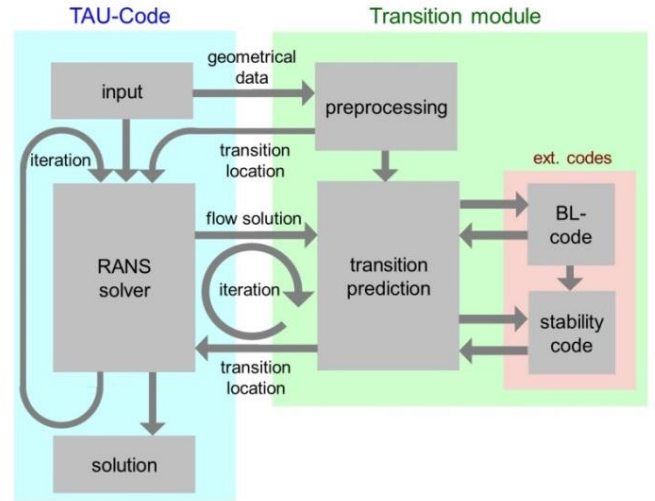


Figure 1: Coupled iteration between RANS solver and transition module

the application of transition criteria [7]. For the estimation of the transition onset locations the ϵ^N method [8, 9] and the two-N-factor strategy [10, 11] are applied. Thus, the approach directly accounts for natural transition due to Tollmien-Schlichting (T-S) instabilities and standing crossflow (CF) waves and for separation-induced transition [12] while for by-pass and attachment-line transition empirical criteria are used. The stability analysis and the application of the ϵ^N method are carried out using a fully automated local, linear stability code [13]. A fundamental task for the application of transition prediction methods in a CFD code is the provision of the necessary laminar boundary-layer data based on quantities available in the CFD solution. The boundary-layer data for stability codes are usually the complete laminar boundary-layer profiles in wall-normal direction for all flow variables of the base flow, that is, all three velocity components and temperature [12] as well as their 1st and 2nd derivatives. For empirical criteria classical integral boundary-layer parameters may be necessary, in addition. All boundary-layer data must be provided with sufficiently high accuracy, so that errors which may be introduced by numerical uncertainties via the representation of the base flow in the CFD solution are reduced to a minimum. This requirement is of highest importance especially for an acceptable estimation of crossflow transition onset points which, in general, are very sensitive to the accuracy of their determining inputs. For the application of stability codes this aspect highly depends on the accuracy of the 2nd derivative of the crossflow velocity profile. Whereas for an accurate representation of the streamwise velocity profile including its 1st and

2^{nd} derivatives about 50 cells in the prismatic grid layer around the surface are sufficient for a proper stability analysis with respect to T-S waves, about 130 cells are often needed for the same accuracy of the crossflow velocity profile and its corresponding derivatives. These numbers are based on the current practice to resolve laminar and turbulent boundary layers using the same grid design, that is, a clustering of grid lines at solid walls. This clustering is necessary for a proper resolution of the high gradient changes of turbulent boundary-layer profiles near the walls. For laminar boundary layers, however, the highest gradient changes are located further away from the wall, near the edge of the laminar boundary layer, and the adequate grid design for their resolution would be a more or less equidistant distribution of about 70 cells between the solid wall and the boundary-layer edge [14]. For the sake of a lower grid generation effort adapted boundary-layer grids in laminar and turbulent flow regions are not yet used in practice. Another difficulty is the need for a number of automated consecutive grid adaptation steps during the ongoing RANS computation in order to change the boundary-layer resolution according to the current transition onset locations until all of them have reached a converged state.

For a practical high-fidelity CFD simulation of a full realistic aircraft configuration within a multi-disciplinary simulation system a lower grid generation effort or the omission of grid adaptation are not an issue anymore because all tools for the realization of a proper grid design for the laminar and transitional boundary layers are part of an automated simulation system. Thus, it seems beneficial to accept and resolve the following application challenges:

- Significant reduction of grid points in fully-laminar regions
- Incorporation of automatic grid adaptation techniques/tools into the simulation environment
- Automatic adaptation of the computational grid designed for fully-turbulent flow in the laminar and transitional flow regimes after every transition prediction iteration step
- Adaptation based on available inherent knowledge of laminar and transitional boundary-layer thicknesses

In [14] the issue of a specific grid adaptation for flows with laminar-turbulent transition has been discussed to some extent.

The use of fully resolved laminar boundary layers in streamline-based transition prediction approaches using very fine RANS computational grids is crucial for high-lift systems of aircraft in off-design conditions. The widely used method to apply a laminar boundary-layer code instead can lead to significant errors in the estimated transition location of the main wing element if the angle of attack does not correspond to the slat position of the design point [6]. If one is interested in reliable information about the transition process based on an analysis of the boundary-layer instability for complex aircraft configurations in terms of the amplification or damping of specific instability modes and if one wants to investigate how this process might be influenced, for example, by the surface shape or the flow conditions such an approach seems to be the only one possible, at present. If the transition process itself is not of interest the local correlation-based approaches with transport equations can be an alternative.

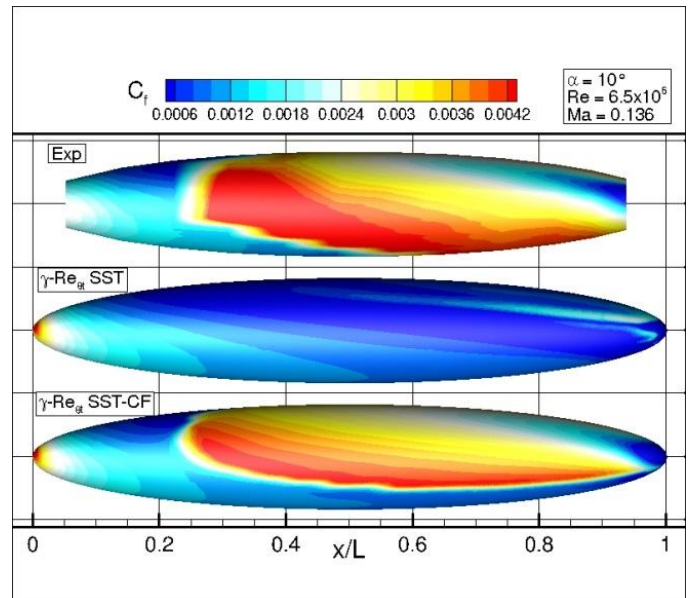


Figure 2: Coupled iteration between RANS solver and transition module

3 Transport Equation Approaches

If a CFD-based aerodynamic analysis is focused on performance prediction and if the major interest is the impact of the laminar-turbulent transition on quantities used to assess the performance of an aircraft, such as pressure and skin friction distributions or integral coefficients, the knowledge of the physics of the transition process itself is of minor relevance and the correct representation of the influence of transition on the boundary-layer development, the interaction with the turbulence model and the sufficiently accurate reproduction of, for example, separated flow regions is crucial and the evaluation of data along explicitly known integration paths is not necessary.

3.1 $\gamma - Re_\theta - CF$ Model

In this case the $\gamma - Re_\theta - CF$ local correlation-based transition transport model [15-17] is available in the TAU code. The $\gamma - Re_\theta - CF$ is the extension of the $\gamma - Re_\theta$ model by Langtry/Menter [18] and based on the C1 criterion and a helicity Reynolds number for the estimation of the transition onset location due to crossflow transition. For a number of simple test cases the CF-extension has yielded extremely promising results, for example, for the prolate spheroid in Fig. 2 [7, 16, 17] and extensive still ongoing validation activities based on wing and aircraft configurations have confirmed the positive assessment of the model so far [17]. However, for a final reliable and conclusive validation of the CF-extension more relevant test cases have to be computed and evaluated.

3.2 Coupling to Reynolds Stress Models

Whereas these CF-related validation activities are based on the original formulation of the $\gamma - Re_\theta$ model which is tightly coupled to the Menter SST $k - \omega$ EVM the $\gamma - Re_\theta - CF$ model must also be made available together with RSM [19]. An effort in this respect is the need for a re-calibration of the model functions which were tuned to match a number of calibration test cases when

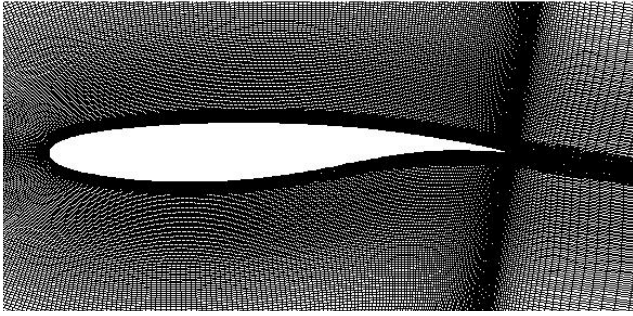


Figure 3: Computational grid for the Messerschmidt-Bölkow-Blohm (MBB) VA-2 airfoil

the $\gamma - Re_\theta$ model is used with the SST model. For the TAU code the coupling of the $\gamma - Re_\theta - CF$ model to the SSG/LRR RSM [2] is currently underway. This differential RSM is available either with a ω -equation [3] or with a g -equation [4], g being $g = 1/(\omega^{1/2})$, the latter leading to a significant higher numerical stability, on the one hand, and to a reduced grid dependence in the near wall region, on the other hand.

The reason for the coupling of the $\gamma - Re_\theta - CF$ model to an RSM was not primarily the expectation that the predictive performance of the transition model would be increased. The major reason was that a turbulence model that can yield significantly better results for specific flow phenomena, such as, transonic shock locations, the representation of separations in corner flows, or the separation onset behavior in strongly three-dimensional flows, should be combined with a transition modeling approach that has a high potential for configurations of highest geometrical complexity. The first validation tests of the model coupled to the SSG/LRR- ω RSM showed that still a beneficial effect on the transition behavior appears.

An example for this finding is given in the following. In Fig. 3 the very fine computational grid of the Messerschmidt-Bölkow-Blohm (MBB) VA-2 airfoil [20] is depicted. The hexahedral grid with 75,000 points has 380 surface points and about 90 points in wall-normal direction inside the boundary-layer. $y^+(1)$ is less than 0.5.

Computations were carried out for $M = 0.2$, $Re = 2.0 \times 10^6$, and $\alpha = 3.5^\circ$ with comparable values for the free-stream turbulence intensity (FSTI) of the oncoming flow directly upstream of the airfoil which were within the given range of FSTI values for the wind tunnel, 0.5 - 0.7%. In Fig. 4 a comparison for the measured skin friction distributions with the computed distributions is depicted. Fully-turbulent computations using the SSG/LRR- ω turbulence model were done as well as computations using the $\gamma - Re_\theta$ transition model together with the SST and the SSG/LRR- ω turbulence models. Computations of more angles of attack for this airfoil yielded similar results. The differences in the results can be attributed to the different development characteristics of the FSTI from the far-field boundaries of the computational grid towards the airfoil for the two couplings of the $\gamma - Re_\theta$ model. In the $k - \omega$ case the far-field distance has an influence. At present, it seems that the coupling to the RSM yields more consistent results in a situation when the FSTI is high and, as necessary for airfoil flows, the far-field distance of the computational grid is as large as, at least, 20 chord lengths or more. Although this case is characterized by a rather large FSTI and, thus, seems

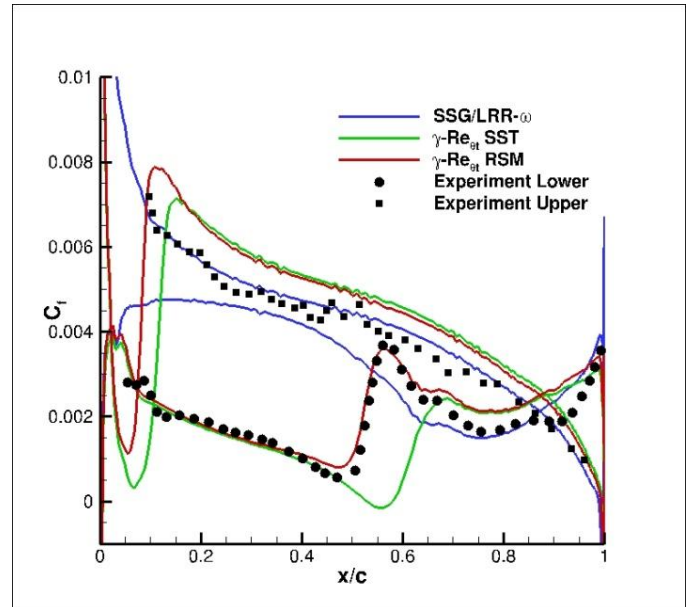


Figure 4: Skin friction distributions for the VA-2 airfoil at $\alpha = 3.5^\circ$

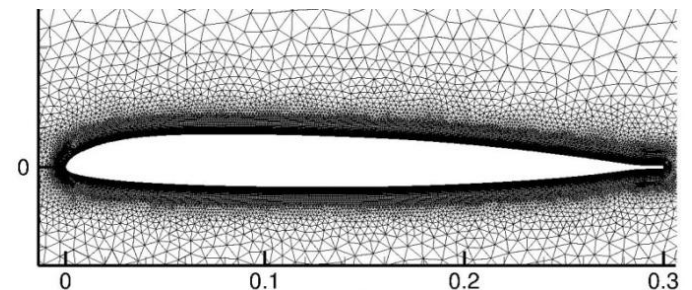


Figure 5: Computational grid for DSA-9A helicopter blade airfoil

to be of low relevance for applied aerodynamics that is exactly what can constitute a possible off-design situation which must be caught with some confidence. More results of these ongoing activities are going to be shown elsewhere.

3.3 Application in Unsteady Flows

Another area where transport equation approaches may have an advantage over streamline-based approaches is unsteady flows with temporal variations above a certain threshold, for example, rotating propellers. For fast estimates they may be an attractive alternative. The predictive performance and reliability of the $\gamma - Re_\theta$ and $\gamma - Re_\theta - CF$ models in unsteady flows, especially, in rotating systems, their capabilities and limitations depending on case-specific parameters and the corresponding sensitivities as well as their correct usage for different unsteady situations (for example, local unsteady flow phenomenon at fixed geometry or moving geometry inducing global unsteady flow field) are still to be investigated in most profound details based on sufficiently many validation cases with reliable experimental data. With the TAU code first steps have been done for a number of airfoil flow cases undergoing pitching oscillations. The DSA-9A helicopter blade airfoil which was designed, built and tested at DLR in an internal project [21] was computed using the hybrid computational grid in Fig. 5 with 67,000 overall grid points, 850 points on the surface contour and 60 prism layers for the resolution of

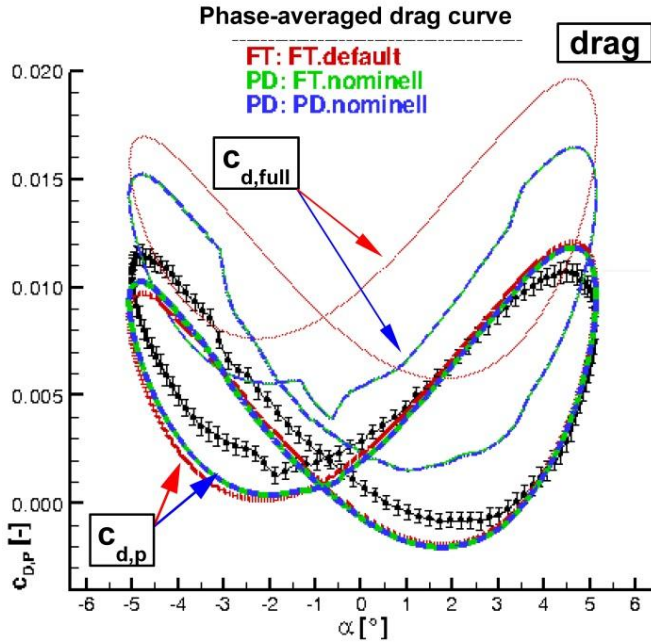


Figure 6: $c_{d,full}$ and $c_{d,p}$ for DSA-9A pitching oscillation at $M = 0.3$, $Re = 1.8 \times 10^6$ with $\alpha(t) = 0^\circ + 5^\circ \sin(\omega t)$, $\omega^* = 0.12$

the boundary layers. The flow conditions were $M = 0.3$, $Re = 1.8 \times 10^6$ and $\alpha(t) = 0^\circ + 5^\circ \sin(\omega t)$ with the reduced frequency $\omega^* = 2\pi f c/U_\infty = \omega c/U_\infty = 0.12$, the frequency $f = 6\text{ Hz}$ and the FSTI = 0.037%. The oscillation period was resolved using 9600 equidistant physical time steps applying a dual-time stepping scheme with 2nd order accuracy in time. The inner (pseudo-time) iterations were considered sufficiently converged either if the density residual had decreased by three orders of magnitude for each single time step or if a Cauchy-convergence control mechanism had detected that all three integral coefficients (lift: c_l , drag: c_d , pitching moment: c_m) satisfied the following conditions:

$$\frac{|c_q^{\tau=m} - c_q^{\tau=m-k}|}{|c_q^{\tau=m}|} \leq 10^{-5} \quad \text{for } k = (1, 2, \dots, 50)$$

τ denoting the inner iteration counter, m the current inner iteration step, k a previous inner iteration step and $q = l, d, m$ the corresponding integral coefficient, that is, that the relative changes of all three integral coefficients have been lower than 10^{-5} for 50 inner iterations when the physical time step was considered converged. The computations have been carried out for five oscillation periods and were found to yield virtually identical results after the 2nd period.

While almost no difference between fully-turbulent results using the Menter SST $k-\omega$ model and results using the original $\gamma-Re_\theta$ model were found for the lift a visible difference can be seen in the different curves for the drag over the angle of attack in Fig. 6. Here, the fully-turbulent results in red are compared to $\gamma-Re_\theta$ results obtained using two different initializations of the flow field at the beginning of the unsteady computation. For the one computation the oscillation which was started at $\alpha_{init} = 0^\circ$ was initialized with a fully-turbulent flow field for α_{init} (green), the other one was initialized with the flow field obtained from a computation using the $\gamma-Re_\theta$ model (blue), both leading to identical results eventually. The difference in the curves for the complete value of c_d ($c_{d,full}$) including pressure ($c_{d,p}$) and viscous

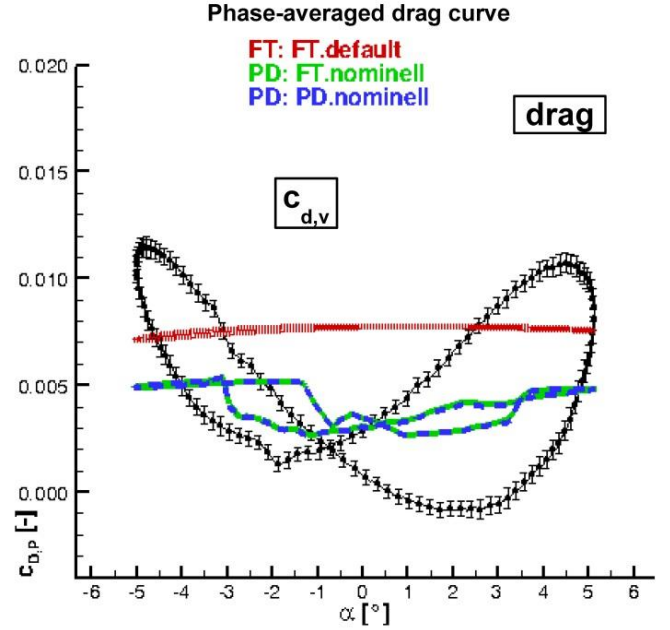


Figure 7: $c_{d,v}$ for DSA-9A pitching oscillation at $M = 0.3$, $Re = 1.8 \times 10^6$ with $\alpha(t) = 0^\circ + 5^\circ \sin(\omega t)$, $\omega^* = 0.12$

($c_{d,v}$) drag contributions is very large and cannot taken directly for comparison with the measured curve (black symbols; bars denote variation over all measured periods) because it reflects the pressure part only. If one compares the pressure drag only the differences between the fully-turbulent curve and the curve with transition have decreased significantly. In Fig. 7 the comparison of the viscous drag contribution is depicted showing that the local characteristics of the transition process over one period is contained in the viscous drag whereas the global character of the oscillation is contained in the pressure drag, as was expected.

A meaningful comparison can be made if the drag curves from the computation are deduced in the same way as was done for the curve from the experiment. Here, the drag value for each angle of attack was determined by integration of the surface pressure distribution from the experiment. For the integration only the measured values at the pressure sensor locations shown in Fig. 8 were used. If the same integration procedure is applied to the computed pressure distributions the solid curves in Fig. 9 (denoted by $c_{d,p} @ PS$) are the outcome. As one can see the differences between the fully-turbulent curve and the curve with transition are larger than before and the local characteristics of the transition process over one period are now clearly visible in the curve with transition. In some regions the results with transition seem to be somewhat nearer to the experimental values. Globally, the deviations between the experimental and computed curves are now larger than in the cases of the pure pressure drag curves. A clear improvement of the computed results with transition can be seen in the comparison of the curves for the pitching moment c_m . Again for the determination of a single moment value the integration of the surface pressure distribution was restricted to the pressure sensor locations. Also for the pitching moment the local characteristics of the transition process over one period are reflected in the curve with transition in strong contrast to the fully-turbulent curve and over a significant portion of the downstroke of the oscillation the moment curve is now within the range of the error bars from the experiment. Why the

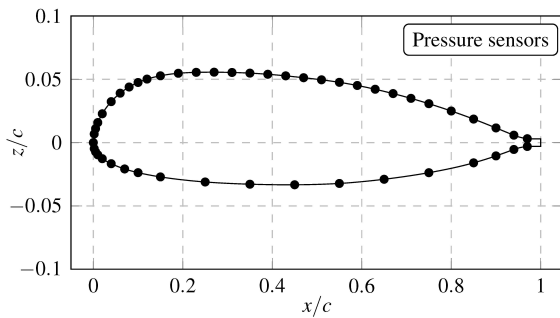


Figure 8: Distribution of pressure sensors in the DSA-9A measurement campaign, taken from [21]

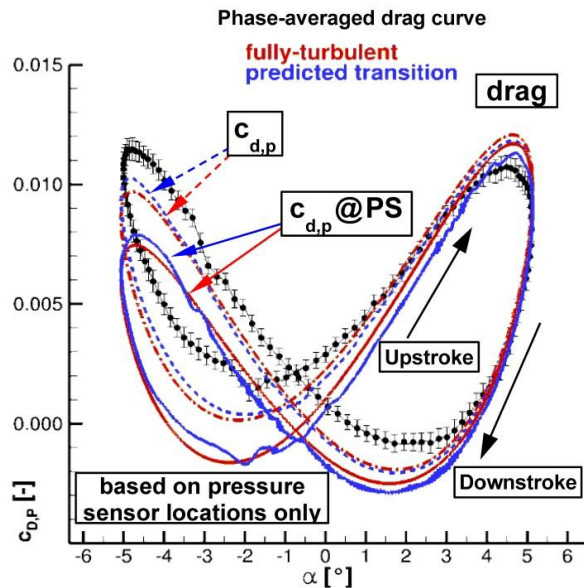


Figure 9: $c_{d,p}$ at pressure sensor locations ($c_{d,p}$ @ PS) for DSA-9A pitching oscillation at $M = 0.3$, $Re = 1.8 \times 10^6$ with $\alpha(t) = 0^\circ + 5^\circ \sin(\omega t)$, $\omega^* = 0.12$

curve deviates from the measurements around the upper dead point where the fully-turbulent curve exhibits an excellent agreement with the experiment is still an open question.

A final assessment of these findings can only be made if more cases of pitching oscillations have been computed and analyzed. In addition to the comparison of integral coefficients it is necessary to compare measured and computed transition locations and transition regions. Currently, more pitching oscillation cases based on the DSA-9A airfoil are under investigation and a profound analysis of the results and comparisons with existing experimental data are underway. In this respect, the results shown here are of preliminary character.

A strong application challenge for any transition prediction method in CFD will be airfoil oscillations with dynamic stall. Especially the correct separation behavior for the upper dead point where very high angles of attack are reached during the oscillation is a crucial issue and may pose problems to current transition prediction techniques. Another critical point in this respect is the correct interaction of the transition model and the turbulence model in order to correctly reflect the highly unsteady vortex system evolving during the oscillation and moving from upstream to downstream on the upper airfoil surface.

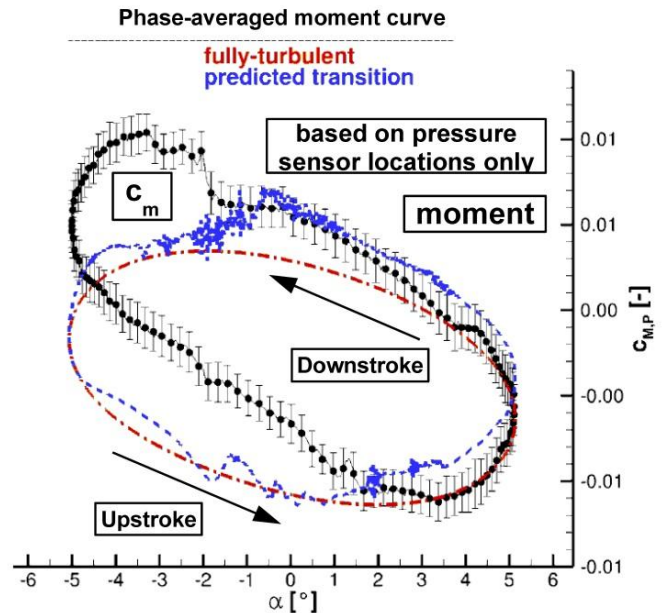


Figure 10: c_m at pressure sensor locations for DSA-9A pitching oscillation at $M = 0.3$, $Re = 1.8 \times 10^6$ with $\alpha(t) = 0^\circ + 5^\circ \sin(\omega t)$, $\omega^* = 0.12$

Another area of application which is of highest importance in this respect are helicopter rotor flows, first in hover and then in forward flight. Especially for the latter case dynamic stall is one of the major flow phenomena which are to be described correctly by a coupled model or modeling approach in order to successfully simulate the overall flow problem.

4 Conclusions

In this article we have addressed a number of application challenges for transition prediction techniques which are effective today or have come up very recently. For the nearest future, however, there are more challenges conceivable which constitute work on the infra-structure in RANS solvers as well as model enhancements and modifications. Two challenges of major priority are:

- Hybrid laminar flow control (HLFC): Both, streamline-based as well as transport equation approaches, must be made capable of being applied to HLFC problems so that they can be used in fully automatic manner for very complex aircraft configurations.
- Combination of a suitable transport equation approach that transports the N-factors for T-S and CF waves according to the two-N-factor strategy with the e^N method for the estimation of the transition onset locations. Only then, the advantages of two fundamental approaches for transition prediction may be exploited to a possible maximum.

For the time being, however, within the framework of a multi-disciplinary simulation environment and for the application of CFD solvers at the borders of the flight envelope we are convinced that the final goal of achieving fully reliable high-fidelity simulation data can be obtained only, with regard to laminar-turbulent transition, if more than one transition prediction technique is available in the system.

References

- [1] N. Kroll et. al., DLR Project Digital-X: towards virtual aircraft design and flight testing based on high-fidelity methods, CEAS Aeronautical Journal (), 1-25, DOI: 10.1007/s13272-015-0179-7
- [2] V. Togiti, B. Eisfeld, O. Brodersen, O., Turbulence Model Study for the Flow Around the NASA Common Research Model, Journal of Aircraft, Vol. 51, No. 4, pp. 1331-1343, 2014
- [3] B. Eisfeld, C. Rumsey, V. Togiti, Second-Moment RANS Model Verification and Validation using the Turbulence Modeling Resource Website, AIAA 2015-2924
- [4] V. Togiti, B. Eisfeld, Assessment of g-Equation Formulation for a Second-Moment Reynolds Stress Turbulence Model, AIAA 2015-2925
- [5] TAU-Code User Guide, Release 2015.2.0, Institute of Aerodynamics and Flow Technology, German Aero-space Center (DLR), October 13, 2015, pp. 0-545
- [6] A. Krumbein, N. Krimmelbein, C. Grabe, Nie S., Development and Application of Transition Prediction Techniques in an Unstructured CFD Code, AIAA 2015-2476
- [7] N. Krimmelbein, R. Radespiel, Transition prediction for three-dimensional flows using parallel computation, Computers&Fluids, Vol. 38, 2009, pp. 121-136
- [8] A.M.O. Smith, N. Gamberoni, Transition, Pressure Gradient and Stability Theory, Douglas Aircraft Company, Long Beach, Calif. Rep. ES 26388, 1956
- [9] J.L. van Ingen, A suggested Semi-Empirical Method for the Calculation of the Boundary Layer Transition Region, University of Delft, Dept. of Aerospace Engineering, Delft, The Netherlands, Rep. VTH-74, 1956
- [10] G. Schrauf, Transition Prediction Using Different Linear Stability Analysis Strategies, AIAA-94-1848-CP
- [11] C. J. Atkin, G. H. Schrauf, Progress in Linear Stability Methods for Design Applications, ECCOMAS 2000
- [12] R. Radespiel, J. Windte, U. Scholz, Numerical and Experimental Analysis of Moving Airfoils with Laminar Separation Bubbles, AIAA Journal, Vol. 45, No. 6, 2007, pp. 1346-1356
- [13] G. Schrauf, LILO 2.1 User's Guide and Tutorial, Bremen, Germany, GSSC Technical Report 6, originally issued Sep. 2004, modified for Version 2.1 July 2006
- [14] H. W. Stock, W. Haase, Some Aspects of Linear Stability Calculations in Industrial Applications, Transitional Boundary Layers in Aeronautics, Proceedings of the colloquium 'Transitional Boundary Layers in Aeronautics', Amsterdam, 6-8 December 1995, ISBN: 0-444-85812-1, 1996, pp. 225-238
- [15] C. Grabe, A. Krumbein, Correlation-based Transition Transport Modeling for Three-dimensional Aerodynamic Configurations, Journal of Aircraft, Vol. 50, No. 5, 2013, pp. 1533-1539
- [16] C. Grabe, A. Krumbein, Extension of the $\gamma - Re_\theta$ Model for Prediction of Crossflow Transition, AIAA 2014-1269
- [17] C. Grabe, Nie S., A. Krumbein, Transition Transport Modeling for the Prediction of Crossflow Transition, submitted for presentation at AIAA Aviation 2016, 13-17 June 2016, Washington, D.C., USA
- [18] F. R. Menter, R. B. Langtry, Correlation-Based Transition Modeling for Unstructured Parallelized Computational Fluid Dynamics Codes, AIAA Journal, Vol. 47, No. 12, 2009, pp. 2894-2906
- [19] Nie, S., Implementation and investigation of coupling Reynolds Stress Model with $\gamma - Re_\theta$ model into DLR TAU code, Internal Report, Deutsches Zentrum für Luft- und Raumfahrt (DLR), Institute of Aerodynamics and Flow Technology, Braunschweig, Germany, 2014
- [20] G. G. Mateer, D. J. Monson, F. R. Menter, Skin-Friction Measurements and Calculations on a Lifting Airfoil, AIAA Journal, Vol. 34, No. 2, 1996, pp. 231-23
- [21] K. Richter et. al, Unsteady Boundary Layer Transition on the DSA-9A Rotor Blade Airfoil, 41st European Rotorcraft Forum 2015, Munich, Germany, September 2015

INTEGRATION OF A DBD PLASMA ACTUATOR MODEL IN TRANSITIONAL TURBULENCE MODELING

P. Kaparos, Z. Vlahostergios and K. Yakinthos

*Laboratory of Fluid Mechanics & Turbomachinery,
Department of Mechanical Engineering, Aristotle University of Thessaloniki, Greece*

Abstract

The prediction and control of the boundary layer laminar to turbulent transition is a process of major interest for mechanical engineering applications. For example, an effective boundary layer transition control during the flight of an aircraft can be of significant importance for improving its flight endurance and maneuverability. In turbomachinery also, the accurate transition control over compressor and turbine blades has the potential to provide major increase in the overall engine performance.

For the boundary layer transition prediction, numerous studies are available, focusing on the accurate numerical modeling with the use of advanced and sophisticated turbulence models. For instance, Chen et al. [1], modeled the by-pass transition in boundary layers formed on turbomachinery blades with cubic non-linear eddy-viscosity models. Walters and Leyleck [2] derived three-equation turbulence models based on the laminar kinetic energy concept and predicted with a remarkable precision the by-pass transition on simplified turbine stator and compressor blade flows. Vlahostergios et al. [3] used a cubic non-linear turbulence model coupled with the laminar kinetic energy concept for the prediction of the boundary layer separation induced transition.

In the literature, there are numerous techniques that investigate accurate and sophisticated ways of transition control, (Balakumar and Hall [4] among others). A new and promising technique is the use of plasma actuators for boundary layer and flow control. The function of plasma actuators is based on the induced ionic wind that acts as a jet within the boundary layer, adding momentum and thus modifying its characteristics.

In the current work, the control of by-pass transition over a flat plate with sharp leading edge, under zero free-stream pressure gradient, with a single Dielectric Barrier Discharge (DBD) plasma actuator is numerically investigated. Previous works have shown that the use of DBD plasma actuators is able to control efficiently the laminar to turbulent transition. For example Ustinov et.al [5] showed experimentally the boundary layer transition delay and the drag reduction due to this delay that can be achieved by the use of a DBD plasma actuator.

The DBD actuator is modeled with the approach of Suzen et al. [6]. This model uses two additional transport equations that describe the electric field and the net charge density. These equations are coupled with the Reynolds Averaged Navier-Stokes (RANS) equations in the ANSYS FLUENT commercial computational fluid dynamics (CFD) software (ANSYS® Scientific Research, Release 15) with the use of user defined functions (UDF). The three-equation eddy-viscosity model of Walters and Cokljat [7] is adopted. This model uses an additional

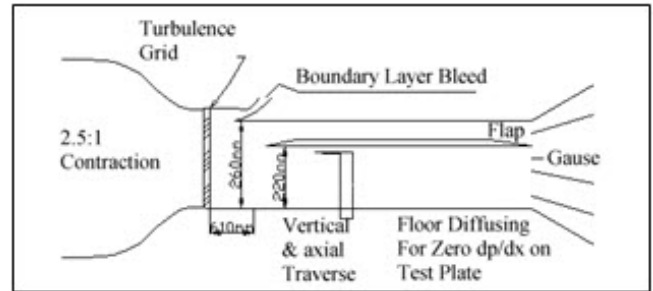


Figure 1: The sharp leading edge ZPG flat plate experimental setup (from ERCOFTAC site)

transport equation to model the laminar kinetic energy transport.

For the assessment of the modeling approach, the skin friction coefficient and the shape factor of the ERCOFTAC T3A case is used. Additionally, the laminar kinetic energy distribution and the distribution of one of the production terms affecting the laminar and turbulent kinetic energies interaction are provided. The numerical results show that the DBD plasma actuator is capable to control and delay the boundary layer transition from the laminar to turbulent regime.

1 The Experimental Test Case

The experimental database of ERCOFTAC is one of the most detailed databases for cases related to the interaction between turbulence generation and transitional characteristics of the boundary layers. In the current contribution, the effect of a DBD plasma actuator on the boundary layer development over a flat plate with a sharp leading edge and zero pressure gradient (ZPG) along the streamwise direction is investigated. The case is coded as T3A in the ERCOFTAC experimental database and has the lowest free-stream velocity among the ZPG ERCOFTAC test cases. This case was selected for its inlet flow conditions: as reported by Moreau [8], the impact of the DBD plasma actuator on the flow control diminishes as the free-stream velocity increases. Thus, the low free-stream velocity of the T3A case, combined with the DBD actuator flow control technique, can provide the highest impact on the boundary layer flow development. The T3A test case has a free-stream velocity of 5.4m/s and an inlet turbulent intensity of 3%. The experimental setup of the ZPG cases of ERCOFTAC is shown in Figure 1.

2 Overview of the Modeling

2.1 The $k - k_L - \omega$ Transition Turbulent Model

The turbulence model for the modeling of the transitional boundary layer is the three-equation turbulence model of Walters and Cokljat [7] which uses the laminar kinetic energy concept [9]. The choice of this model was based on its excellent results for the modeling of the ERCOFTAC ZPG cases T3A, T3B and T3A-, as shown in [7]. The model transport equations referring to the turbulent kinetic energy k_T , the laminar kinetic energy k_L and the specific dissipation rate ω , are shown in eqs.1-3 respectively.

$$\frac{Dk_T}{Dt} = P_{K_T} + R_{BP} + R_{NAT} - \omega k_T - 2\nu \left(\frac{\partial \sqrt{k_T}}{\partial x_j} \right)^2 + \frac{\partial}{\partial x_j} \left[\left(\nu + \frac{a_T}{a_k} \right) \frac{\partial k_T}{\partial x_j} \right] \quad (1)$$

$$\frac{Dk_L}{Dt} = P_{K_L} - R_{BP} - R_{NAT} - 2\nu \left(\frac{\partial \sqrt{k_L}}{\partial x_j} \right)^2 \quad (2)$$

$$\frac{\partial \omega}{\partial t} = C_{\omega 1} \frac{\omega}{k_T} P_{k_T} + \left(\frac{C_{\omega R}}{f_W} - 1 \right) \frac{\omega}{k_T} (R_{BP} + R_{NAT}) - C_{\omega 2} \omega^2 + C_{\omega 3} f_{\omega} \alpha_T f_W^2 \frac{\sqrt{k_T}}{d^3} + \frac{\partial}{\partial x_j} \left[\left(\nu + \frac{a_T}{a_{\omega}} \right) \frac{\partial \omega}{\partial x_j} \right] \quad (3)$$

The superiority of this model in predicting by-pass transition and in comparison to the other linear eddy-viscosity models is mainly focused on the use of one additional transport equation for the laminar kinetic energy k_L . As referred by Mayle and Schultz [9], k_L is linked to the pre-transition perturbations that lead to by-pass transition and is added in the total turbulent kinetic energy budget. As a result, a more accurate representation of the Reynolds-stresses distribution inside the boundary layer transitional region is achieved. The total Reynolds-stress tensor is given by eq.4.

$$\overline{u'_i u'_j}_{TOT} = \frac{2}{3} (k_T + k_L) \delta_{ij} - \nu_{TOT} \left(\frac{\partial U_i}{\partial x_j} + \frac{\partial U_j}{\partial x_i} \right) \quad (4)$$

In eq.4, $\nu_{TOT} = \nu_{T,s} + \nu_{T,l}$, is the total eddy-viscosity which is a result of the contribution of a small scale eddy-viscosity $\nu_{T,s}$ and a large scale eddy-viscosity $\nu_{T,l}$. These eddy-viscosities are related to the small and the large turbulent scales respectively. Further details regarding this three-equation turbulence model, the laminar kinetic energy concept and the source terms that are present in eqs.1, 2 and 3 can be found in [7] and [9].

2.2 The DBD Plasma Actuator Model

The DBD plasma actuator consists of two electrodes, which are separated by a dielectric material. The main operational principle of the DBD plasma actuator is based on the air ionization and it is shown in fig.2. One electrode is exposed to the flow and the other electrode (ground electrode) is under the dielectric material and it is in no-contact with the incoming flow. High voltage is applied to the two electrodes and the air near the wall

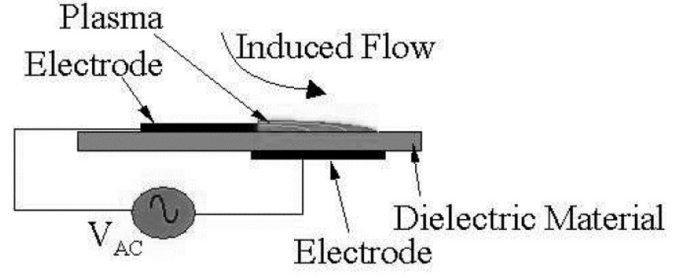


Figure 2: DBD plasma actuator configuration (figure from [4])

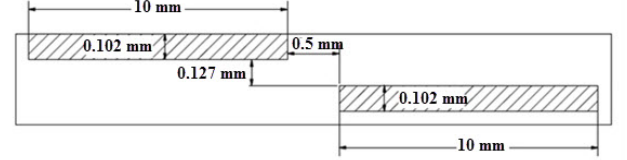


Figure 3: The DBD plasma actuator geometry

region and above the ground electrode is ionized. The generated ionic wind is affected by the intensity of the voltage and produces a jet-like body force that acts on the flow.

The geometrical characteristics of the DBD actuator configuration that has been modeled in the current study, in order to create the DBD computational actuator model, are shown in Figure 3.

Regarding the modeling of the ionic wind that the DBD actuator produces, the mathematical model of Suzen and Huang [6] is adopted. This model introduces two additional transport equations solved in combination with the RANS equations and the turbulence model equations, in order to compute the resulting jet-like body force that acts on the fluid. Based on [10] and [11], the first transport equation describes the external electric field (φ) transport, given by eq.5, and the second one the net charge density (ρ_c) transport, which is given by eq.6.

$$\frac{\partial}{\partial x_j} \left(\varepsilon_r \frac{\partial \varphi}{\partial x_j} \right) = 0 \quad (5)$$

$$\frac{\partial}{\partial x_j} \left(\varepsilon_r \frac{\partial \rho_c}{\partial x_j} \right) = \frac{\rho_c}{\lambda_d^2} \quad (6)$$

The diffusion coefficient ε_r is the relative permittivity and its value depends on the working medium. For air is unity and for the kapton dielectric material, used in the current work, is 2.7. In eq.5, λ_d is the Debye length, which is a characteristic length giving the distance over which significant charge separation occurs. As reported by Ibrahim and Skote [12], the Debye length determines whether the charged body forces can be taken into consideration. The final RANS momentum equations are given by eq.7. The plasma jet-like body force is treated as an additional source term in the momentum equations.

$$\frac{\partial \rho \overline{U}_i}{\partial t} + \overline{U}_j \frac{\partial \rho \overline{U}_i}{\partial x_j} = - \frac{\partial \overline{P}}{\partial x_i} - \frac{\partial}{\partial x_j} \left[\mu \left(\frac{\partial \overline{U}_i}{\partial x_j} + \frac{\partial \overline{U}_j}{\partial x_i} \right) \right] - \frac{\partial}{\partial x_j} (\rho \overline{u'_i u'_j}) - \rho_c \frac{\partial \varphi}{\partial x_i} \quad (7)$$

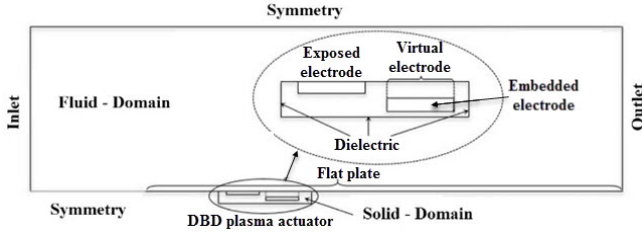


Figure 4: Computational solid and fluid domains

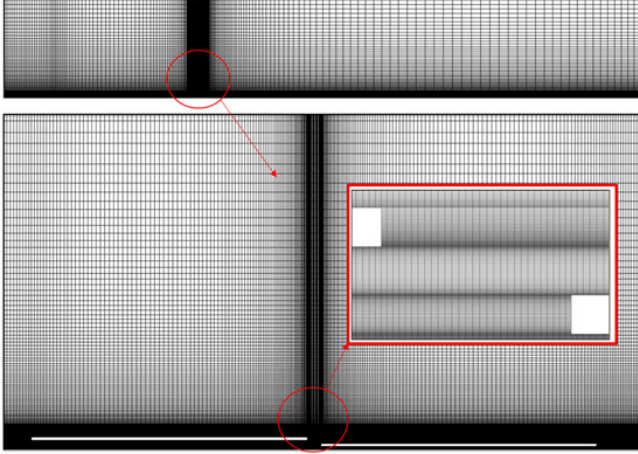


Figure 5: Computational grid of fluid and solid domains

2.3 Computational Details

The numerical computations were performed with the FLUENT commercial CFD solver (ANSYS@Scientific Research, Release 15). The FLUENT $k - k_L - \omega$ turbulence model of Walters and Cokljat [7] was coupled with the transport equation for the electric field and the net charge density, (eqs.5 and 6 respectively), which were integrated in the computational procedure with the use of user defined functions (UDF).

The computational domain was divided in two domains: the fluid domain and the solid domain. The RANS equations together with the turbulence model equations and the net charge density equations were solved in the fluid domain, while the electric field transport equation was solved in both domains. The solid-domain consists of the exposed electrode, the embedded electrode and the kapton dielectric material. The fluid and the solid computational domains are shown in fig.4.

Grid independency studies, (regarding only the fluid flow without the DBD actuator solid domain), were performed by adopting two structured 2D computational grids, having 5×10^4 and 1×10^5 cells, which provided grid independent results. For the integration of the DBD actuator and the solid domain, a finer unstructured 2D computational grid of 2×10^5 tetrahedral elements was generated. The finer grid, shown in fig.5, was generated based on the limit of the maximum allowed grid spacing around the DBD actuator electrodes, in order to properly simulate the electric field and net charge density distribution. As proposed by Abdollahzadeh et al. [10], the grid spacing around the DBD electrodes should not exceed the Debye length. The imposed boundary conditions for the fluid domain are shown in fig.6. Figure 7 shows the boundary conditions that were applied to the electrodes and to the fluid-solid domain interface.

The boundary condition for the net charge density above the embedded electrode is given by eq.8. The function $G(x)$ (eq.9), is a half Gaussian distribution and it

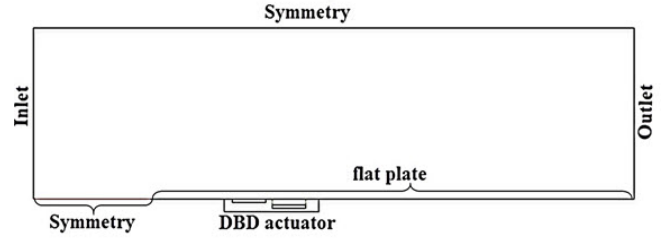


Figure 6: Boundary conditions of the fluid domain

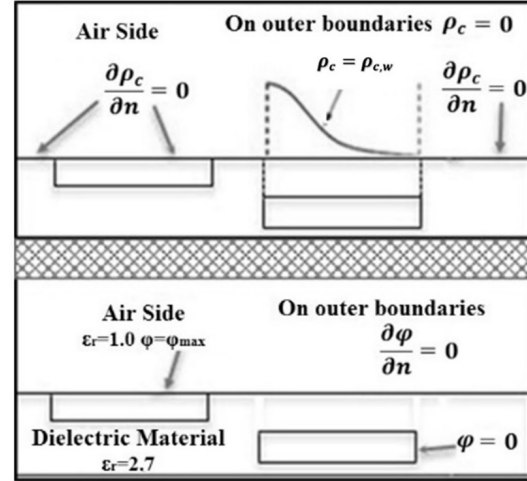


Figure 7: Boundary conditions of the net charge density (up) and electric field (down)

is used to produce the net charge density distribution as proposed by Enloe et al. [13].

$$\rho_{c,w}(x) = \rho_c^{max} G(x) \quad (8)$$

$$G(x) = e^{-\frac{(x-\mu)^2}{(2\sigma)^2}}, x \geq 0 \quad (9)$$

Table 1 shows all the used constant values, which are based on the work of Suzen et al. [6]. The quantity μ indicates the position of the maximum net charge density along the flat plate. This location is usually fixed (also in the current paper) upon the start of the embedded ground electrode. This electrode is also referred as the virtual electrode. Finally, the parameter σ controls the gradual decay of the net charge density from the peak position up to the end of the virtual electrode.

Figure 8 shows the numerical solution of eqs.5 and 6, the exposed and the embedded (ground) electrodes, the distribution of the non-dimensional electric field, φ/φ_{max} on the fluid-solid domain and of the non-dimensional net charge density ρ_c/ρ_{cmax} on the fluid domain.

In order to investigate the effect of the applied voltage magnitude on the transitional characteristics of the boundary layer, various voltage values were applied to the electrodes i.e. 10, 20 and 30 kV. The range of the

Table 1: Values of the DBD plasma actuator numerical model

λ_d	Debye length	0.001 m
ρ_{cmax}	Maximum charge	0.0008 C/m ³
σ	Scale parameter	0.3

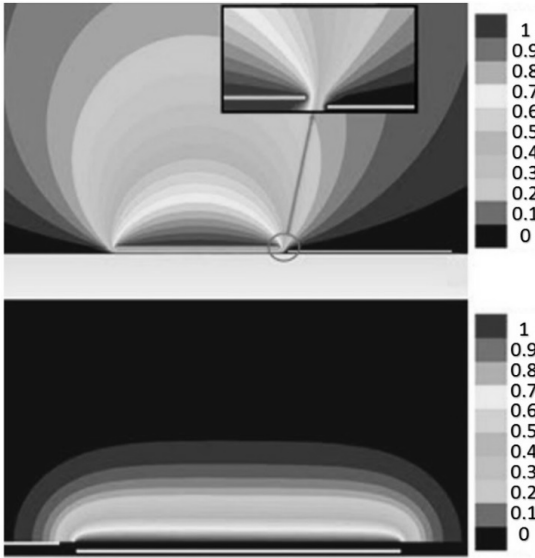


Figure 8: Contour plots, up: φ/φ_{max} , down: ρ_c/ρ_{cmax}

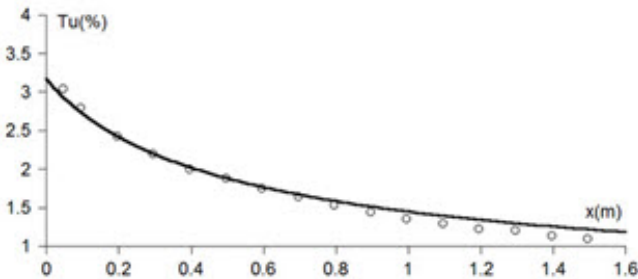


Figure 9: Experimental and computational turbulence decay. Circles: experimental data, plain line: computational results

applied voltage values was based in similar applications found in the literature.

For the determination of accurate (close to the experiment) boundary conditions for the turbulence model quantities, the computed free-stream turbulent intensity decay was matched with the experimental one. The best values for the turbulent intensity T_u and the turbulent length scale l_s were $T_u = 4.5\%$ and $l_s = 15mm$. The comparison of the experimental with the calculated turbulence decay is shown in fig.9.

In order to have the maximum impact on the boundary layer development and transition control, the selection of the optimal position of the DBD plasma actuator was chosen based on the study of Ustinov et al. [5], which is the transition onset location. For the T3A case and based on the computational results of the $k - k_l - \omega$ model, the transition onset position is located at $x \sim 400mm$, as it can be seen from the distribution of the skin friction coefficient C_f in fig.10 (dashed line).

3 Results and Discussion

As a general observation the $k - k_l - \omega$ model is able to capture with a very good accuracy the transition of the boundary layer from laminar to turbulent state for the T3A case, (dashed lines in figs 10 and 11).

For the investigation of the effect of the DBD actuator on the by-pass transition, the C_f development was examined with the DBD-off, the DBD-on at its maximum value (30kV) versus the experimental data, which

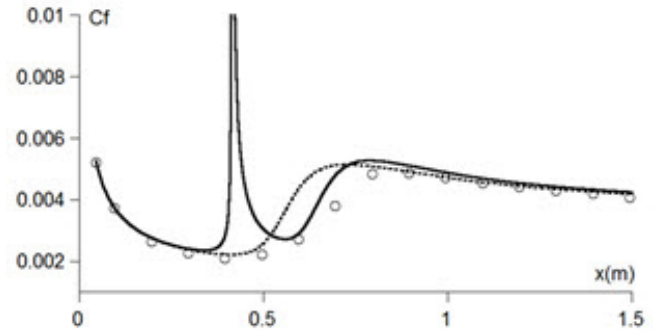


Figure 10: C_f distribution, Circles: experiment, plain line: DBD-on (30kV), dashed line: DBD-off

refer to the flow development without a DBD actuator. These data are used only as a reference base to validate the $k - k_l - \omega$ model and to numerically quantify the effect of the plasma DBD actuator on the transition process. Figure 10 presents the C_f distribution with the DBD actuator off and with the DBD on, at 30kV in comparison with the T3A experimental data of the C_f distribution.

The peak value of C_f , which is shown in fig.10 (plain line), is located at the position of the DBD actuator and it is an indication that the actuator is activated and the flow is accelerated. This peak value is a result of the additional body force term added in the momentum equations. For the case of 30kV it is clearly seen that the transition onset shifts downstream, from $x \sim 0.4m$ to $x \sim 0.56 - 0.6m$. For $x \sim 0.6m$ transition is initiated, as shown from the local C_f increase, which has values smaller than the case with the DBD-off.

For the further assessment of the impact of the plasma DBD actuator on the boundary layer development, the non-dimensional shape factor distribution H for the maximum applied voltage of 30kV is presented in fig.11. The shape factor takes values from 2.59, (indicating a laminar boundary layer), to 1.4 (referring to a fully turbulent boundary layer). The effect of the actuator on the boundary layer development is shown from $x \sim 0.6$ until the end of the flat plate, where the shape factor takes smaller values closer to the laminar flow regime. This observation comes in agreement with the C_f distribution shown in fig.10. Additionally, the DBD actuator added momentum at $x = 0.4m$, is depicted with a decrease of H together with the peak of the C_f value close on this location as shown in fig.10. The flow near this region is accelerated due to the DBD actuator momentum force by giving larger C_f and smaller H values. In order to examine the effect of the different voltage values applied on the electrodes, computations were performed for 10, 20 and 30kVs. Figure 12 presents the C_f distributions with the DBD-off compared with the DBD-on for the various voltages. From fig.12 it is concluded that the transition onset location is shifted downstream as the applied voltage increases. The maximum shift is achieved with the highest voltage value of 30kV while the transition delay is proportional to the applied voltage. Additionally, the transition length increases as the applied voltage increases. Table 2 presents the effect of the different voltages on transition onset and transition end locations.

During bypass transition, energy is transferred from the laminar (k_L) to the turbulent kinetic energy (k_T). The generation term R_{BP} appears with opposite sign in eqs.1 and 2 and represents this energy transfer mechanism. For a more comprehensive understanding of how

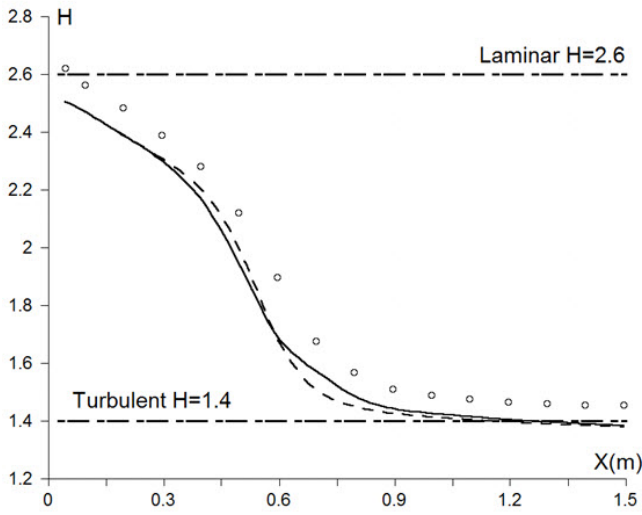


Figure 11: Shape factor distributions, Circles: experiment, plain line: DBD-on (30kV), dashed line: DBD-off

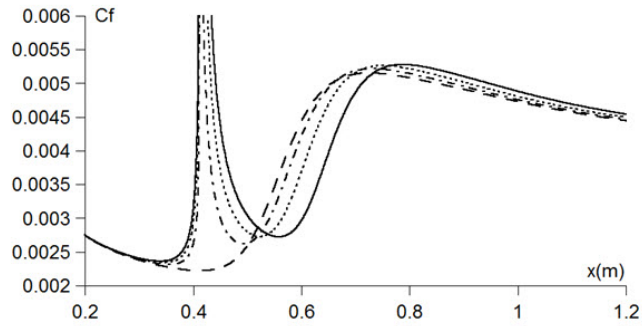


Figure 12: C_f distributions, dash-dot line: DBD-on (10kV), dotted line: DBD-on (20kV), plain line: DBD-on (30 kV), dashed line: DBD-off

the integrated plasma actuator force is coupled with and affects the laminar kinetic energy and the term R_{BP} , the distributions of k_L and R_{BP} inside the transition region for various applied voltages are presented.

Figure 13 shows the k_L development along the sharp leading edge flat plate for three stations inside the transition region and one after transition, with reference to the DBD-off case. As transition is developing, the k_L energy gradually diminishes and the only contribution to the turbulent nature of the flow is provided by the turbulent kinetic energy k_T , [7]. This behavior can be concluded from fig.13. As the voltage is increased, the laminar kinetic energy is amplified at the region where transition begins. This can be seen by observing the stations $x = 0.595m$ and $x = 0.695m$ for the case of 30kV.

The transition onset location downstream shift, can be also concluded. For each case, as the voltage increases, the location where k_L takes the maximum value, (and as a result the transition onset location), moves downstream indicating that a transition delay is achieved.

Table 2: Transition onset and end for different applied voltages

Voltage (kV)	10	20	30
Transition onset (m)	0.5	0.53	0.56
Transition end (m)	0.72	0.74	0.8

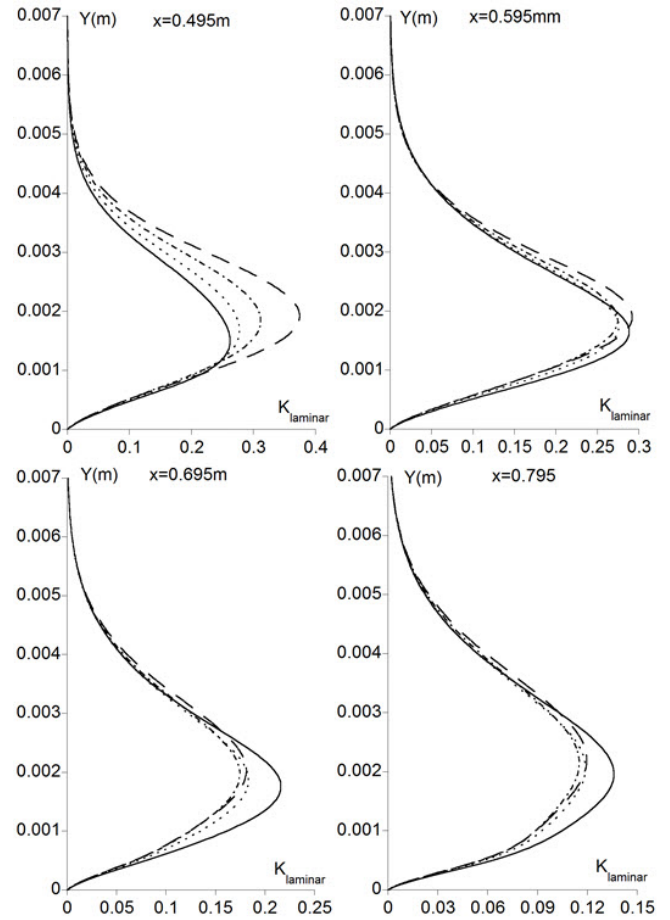


Figure 13: k_L distributions, dash-dot line: DBD-on (10kV), dotted line: DBD-on (20kV), plain line: DBD-on (30 kV), dashed line: DBD-off

Regarding the R_{BP} term, the distributions inside the transition region and for the various applied voltages, are shown in fig.14. The energy transfer between k_L and k_T takes place as transition is developing. The generation term R_{BP} acts as a sink term in the k_L energy balance. As the applied voltage increases, R_{BP} decreases. This is related to the fact that the laminar kinetic energy is dominant in the pre-transitional region. During transition the energy is transferred to k_T . Since the applied voltage delays transition, it is expected that the R_{BP} maximum value will also shift downstream, as the voltage is increased.

Finally, it must be noticed that during the current study, other turbulent quantities were examined also, e.g. the Reynolds-stresses, turbulent kinetic energy dissipation and velocity distributions for various stations along the flat plate. As a general observation, one can conclude that the by-pass transition is suppressed and its onset location moves downstream. The velocity profiles are more laminar in the region where transition is suppressed. For all the stations outside the transition region, the distributions for all the quantities are the same, as it was expected, since the voltage influence is limited near the area where the DBD actuator is installed.

4 Conclusions

In the present work, the effect of a DBD plasma actuator on the control of the boundary layer by-pass transition mechanism has been numerically investigated. The examined transitional case is the boundary layer flow

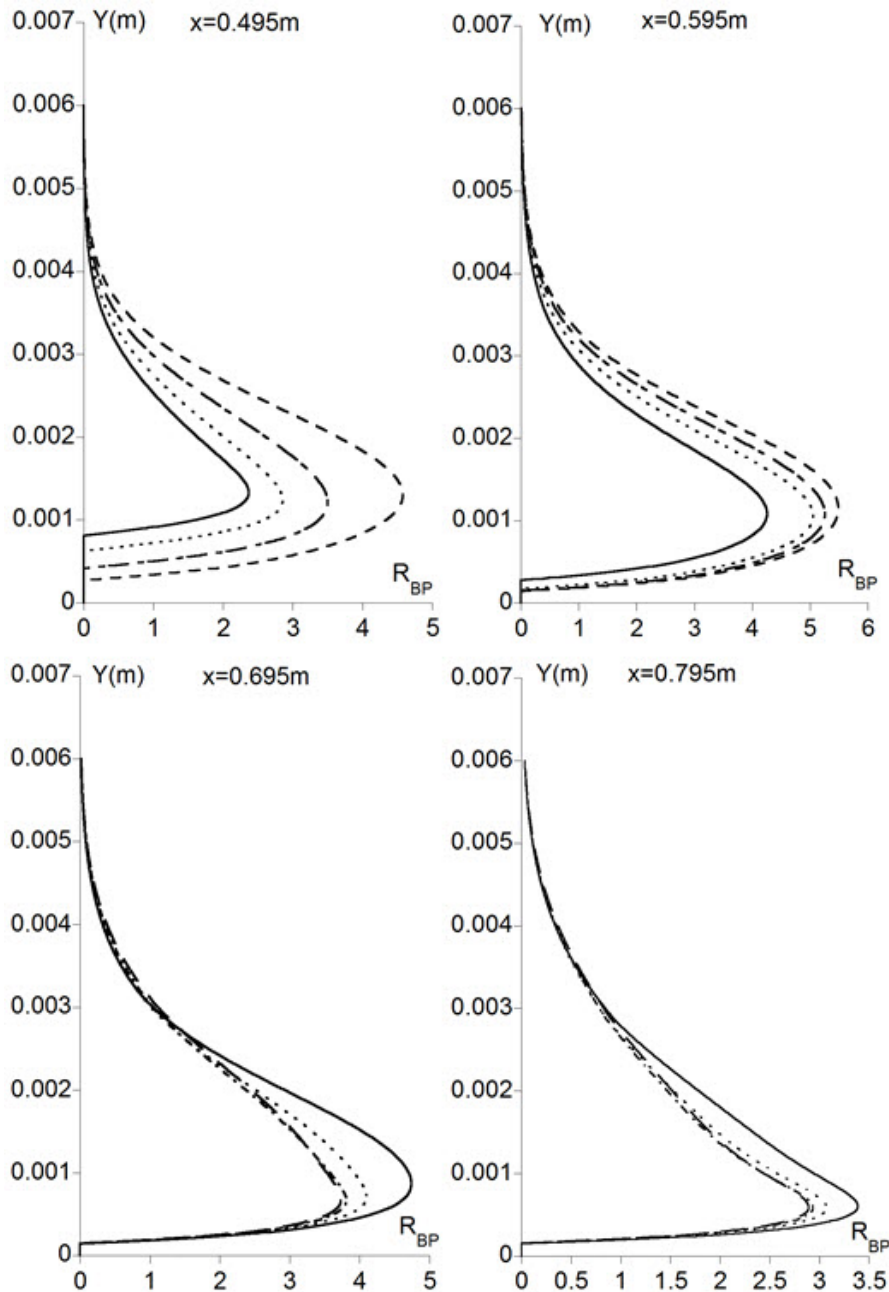


Figure 14: R_{BP} distributions, dash-dot line: DBD-on (10kv), dotted line: DBD-on (20kv), plain line: DBD-on (30 kv), dashed line: DBD-off

development on a flat plate with a sharp leading edge, under zero free-stream pressure gradient, coded as T3A by ERCOFTAC. The DBD actuator was modeled with the simplified model of Suzen et al. [6]. For the turbulence modeling, the three-equation linear eddy-viscosity model of Walters and Cokljat [7] was adopted, which incorporates the laminar kinetic energy concept. Several voltages were applied in the DBD electrodes in order to investigate the effect of the ionized plasma in controlling the bypass transition process. The results showed that momentum added to the flow, through the DBD, results in a transition delay. These observations were strengthened by examining the behavior of the laminar kinetic energy distributions in relation to the DBD applied voltage. From the study it is concluded that the use of DBD actuators as boundary layer control devices, alters the turbulent characteristics of the flow inside the transition region and more specifically can delay the by-pass transition.

References

- [1] W.L. Chen, F.S. Lien, M.A. Leschziner, "Non-linear eddy-viscosity modelling of transitional boundary layers pertinent to turbomachine aerodynamics," in *International Journal of Heat and Fluid Flow*, 19, 1998.
- [2] K.D. Walters, J.H. Leylek, "Computational fluid dynamics study of wake induced transition on a compressor-like flat plate," in *ASME Journal of Turbomachinery*, 127, 2005.
- [3] Z. Vlachostergios, K. Yakinthos, A. Goulas, "Separation-induced boundary layer transition: Modeling with a non-linear eddy-viscosity model coupled with the laminar kinetic energy equation," in *International Journal of Heat and Fluid Flow*, 30, 2009.

- [4] P. Balakumar, P. Hall, "Optimum Suction Distribution for Transition Control," in *Theoretical and Computational Fluid Dynamics*, 13, 1996.
- [5] M. Ustinov, M. Kogan, V. Litvinov, and A. Uspensky, "Natural laminar-turbulent transition delay by dielectric barrier discharge," in *J. Phys. Conf. Ser.*, 318, 2011.
- [6] Y. B. Suzen, P. G. Huang, J. D. Jacob, and D. E. Ashpis, in "Numerical Simulations of Plasma Based Flow Control Application," AIAA-2005-4633, 2005.
- [7] D. K. Walters and D. Cokljat, "A Three-Equation Eddy-Viscosity Model for Reynolds-Averaged Navier-Stokes Simulations of Transitional Flow," in *J. Fluids Eng.*, 130, 2008.
- [8] E. Moreau, "Airflow control by non-thermal plasma actuators," in *J. Phys. D. Appl. Phys.*, 40, 2007.
- [9] R. E. Mayle and A. Schulz, "The Path to Predicting Bypass Transition," in *ASME Journal of Turbomachinery*, 119(3), 1996.
- [10] M. Abdollahzadeh, J. Páscoa, and P. Oliveira, "Numerical modelling of boundary layer control using dielectric barrier discharge," in *MEFTE IV Conf.*, 2012.
- [11] H. M. Saeed Kavousfar, Esmail Esmailzadeh, "Modeling of Plasma Actuator and its Effect on Flow Field Around Rectangular Cylinder," in *Indian J.Sci.*, 1(2), 2014.
- [12] I. H. Ibrahim and M. Skote, "Effects of the scalar parameters in the Suzen-Huang model on plasma actuator characteristics," in *International Journal of Numerical Methods for Heat and Fluid Flow*, 23(6), 2009.
- [13] C. L. Enloe, T. E. McLaughlin, R. D. Van Dyken, K. D. Kachner, E. J. Jumper, T. C. Corke, M. Post, and O. Haddad, "Mechanisms and Responses of a Dielectric Barrier Plasma Actuator: Geometric Effects," *AIAA J.*, 42(3), 2004.

ERCOFTAC Programme of Events in 2016

Organiser: Dr. Richard E. Seoud
richard.seoud-ieo@ercoftac.org

http://www.ercoftac.org/events/programmeof_events_v1/

1. Oil & Gas - Best Practices and Technology Trends (II), 20-21 April 2016, Kongsberg, Oslo, Norway.
2. CFD for Dispersed Multi-phase-Flows (VI), Kongsberg, Oslo, Norway, 13-14 June 2016.
3. Lattice Boltzmann Methods for Industrial Apps: Overview, Guidance and Examples (I), 13-14 June 2015, ONERA, Paris.
4. Best Practices in Combustion CFD: I.C. Engines, 2-3 Nov 2016, TU Darmstadt, Germany.
5. Advanced Computing for Fluid Solver, Amazon, London, 15-16 September 2016.
6. Uncertainty Management and Quantification in Industrial Design and Analysis, U. Ghent, Belgium, November 2016.
7. FSI , Acoustics and Big Data: Impact to Industrial Applications (II), EDF, Paris, France December 7, 2016.
8. High Order Methods for Industrial CFD, Summer/Autumn 2016.

Enquiries and registration of interest: richard.seoud-ieo@ercoftac.org

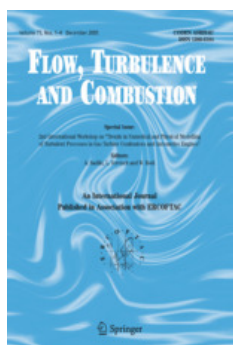
ERCOFTAC Workshops and Summer Schools

ERCOFTAC Workshops, Conferences – 2016

Title	Location	Date	Coordinators	Organiser
New Challenges in Turbulence Research IV	Les Houches, France	20-25/03/2016	Cambon, C. Godeferd, F.	SIG 35
New challenges in shear-driven and buoyancy-driven turbulent flows	Paris, France	5-6/05/2016	Cambon, C.	SIG 35
Gas Engine Combustion Fundamentals	Zurich, Switzerland	?/06/2016	Wright, Y.M. Boulouchos, K.	SIG 28
Uncertainty Quantification in CFD and Fluid Structure Interaction	Crete, Greece	5-10/06/2016	Sarkar, S.	SIG 45
13th International Workshop on Measurement and Computation of Turbulent Flames	Seoul, Korea	28-30/07/2016	Janicka, J. Barlow, R. S.	SIG 28
11th International ERCOFTAC Symposium on Engineering Turbulence Modelling and Measurements	Palermo, Italy	21-23/09/2016	Guerts, B. et al.	

ERCOFTAC Summer Schools, Courses – 2016

Title	Location	Date	Coordinators	Organiser
Summer School on Near-Wall Reactive Flow	Bensheim, Germany	6-10/06/2016	Dreizler, Aa Poinsot, T. Sadiki, A.	SIG 28



RECENT TABLE OF CONTENTS OF FLOW TURBULENCE AND COMBUSTION

AN INTERNATIONAL JOURNAL PUBLISHED BY SPRINGER
IN ASSOCIATION WITH ERCOFTAC

EDITOR-IN-CHIEF: M. A. LESCHZINER

EDITORS: A. DREIZLER, K. FUKAGATA, E. GUTMARK, K. HANJALIC, A. M. KEMPF, S.
MENON, M. REEKS, W. RODI

FOUNDING EDITOR: F. NIEUWSTADT

VOLUME 96, NUMBER 2, MARCH 2016

Special Issue dedicated to the 2nd International Conference:
Towards Sustainable Combustion - SPEIC2014

Editors: Mário Costa, Edgar Fernandes, Norberto Fueyo, Javier Ballester and Pedro L. Garcia-Ybarra

Preface

M. Costa, E. Fernandes, N. Fueyo, J. Ballester, P.L. Garcia-Ybarra

Upward Propagation of Very Lean Methane-Air Flames in Vertical Tubes

V. Muntean, F.J. Higuera

Effects of Lewis Number on Head on Quenching of Turbulent Premixed Flames: A Direct Numerical Simulation Analysis

J. Lai, N. Chakraborty

Effect of Air-excess on Blends of RON70 Partially Premixed Combustion

S. Wang, P.C. Bakker, L.M.T. Somers, L.P.H. de Goey

Multi-Technique Analysis of Soot Reactivity from Conventional and Paraffinic Diesel Fuels

M. Lapuerta, J. Rodríguez-Fernández, J. Sánchez-Valdepenas, M.S. Salgado

2-methylfuran Oxidation in the Absence and Presence of NO

K. Alexandrino, Á. Millera, R. Bilbao, M.U. Alzueta

Pulsed Flame for Syngas Production via Partial Methane Oxidation

A. Fomin, T. Zavlev, V. Tsionsky, I. Rahinov, S. Cheskis

Spray-Flame Dynamics in a Rich Droplet Array

C. Nicoli, P. Haldenwang, B. Denet

Experimental and Numerical Simulations of Spray Impingement and Combustion Characteristics in Gasoline Direct Injection Engines under Variable Driving Conditions

J. Seo, H.Y. Kim, S. Park, S.C. James, S.S. Yoon

Experimental Investigation and Comparison of Pulverized Coal Combustion in CO₂/O₂ and N₂/O₂ Atmospheres

J. Hees, D. Zabrodiec, A. Massmeyer, M. Habermehl, R. Kneer

H₂O and CO₂ Dilution in MILD Combustion of Simple Hydrocarbons

P. Sabia, M. Lubrano Lavadera, G. Sorrentino, P. Giudicianni, R. Ragucci, M. de Joannon

The Effect of Diluent on the Sustainability of MILD Combustion in a Cyclonic Burner

G. Sorrentino, P. Sabia, M. de Joannon, A. Cavaliere, R. Ragucci

Transported PDF Modeling of Ethanol Spray in Hot-Diluted Coflow Flame

L. Ma, B. Naud, D. Roekaerts

Consistent Behavior of Eulerian Monte Carlo fields at Low Reynolds Numbers

L. Valino, R. Mustata, K.B. Letaief

Large Eddy Simulation of Spray Auto-ignition Under EGR Conditions

S. Gallot-Lavallée, W.P. Jones

Effects of the Local Flow Topologies Upon the Structure of a Premixed Methane-air Turbulent Jet Flame

L. Cifuentes, C. Dopazo, J. Martin, P. Domingo, L. Vervisch

Micro-scale Mixing in Turbulent Constant Density Reacting Flows and Premixed Combustion

C. Dopazo, L. Cifuentes, J. Hierro, J. Martin

Statistical Analysis of Turbulent Flame-Droplet Interaction: A Direct Numerical Simulation Study

D.H. Wacks, N. Chakraborty, E. Mastorakos

ERCOFTAC Special Interest Groups

1. Large Eddy Simulation

Salvetti, M.V.
University of Pisa, Italy.
Tel: +39 050 221 7262
Fax: +39 050 221 7244
mv.salvetti@ing.unipi.it

4. Turbulence in Compressible Flows

Dussauge, Jean-Paul
IUSTI, Marseille
jean-paul.dussauge
@polytech.univmrs.fr

5. Environmental Fluid Mechanics

Armenio, V.
Universit di Trieste, Italy.
Tel: +39 040 558 3472
Fax: +39 040 572 082
armenio@dica.units.it

10. Transition Modelling

Dick, E.,
University of Ghent, Belgium.
Tel: +32 926 433 01
Fax: +32 926 435 86
erik.dick@ugent.be

12. Dispersed Turbulent Two Phase Flows

Sommerfeld, M.
Martin-Luther University, Germany.
Tel: +49 346 146 2879
Fax: +49 346 146 2878
martin.sommerfeld@iw.uni-halle.de

14. Stably Stratified and Rotating Flows

Redondo, J.M.
UPC, Spain.
Tel: +34 934 017 984
Fax: +34 934 016 090
redondo@fa.upc.edu

15. Turbulence Modelling

Jakirlic, S.
Darmstadt University of Technology,
Germany.
Tel: +49 615 116 3554
Fax: +49 615 116 4754
s.jakirlic@sla.tu-darmstadt.de

20. Drag Reduction and Flow Control

Choi, K-S.
University of Nottingham, England.
Tel: +44 115 951 3792
Fax: +44 115 951 3800
kwing-so.choi@nottingham.ac.uk

24. Variable Density Turbulent Flows

Anselmet, F.
IMST, France.
Tel: +33 491 505 439
Fax: +33 491 081 637
anselmet@irphe.univ-mrs.fr

28. Reactive Flows

Roekaerts, D.
Delft University of Technology,
The Netherlands.
Tel: +31 152 782 470
D.J.E.M.Roekaerts@tudelft.nl

32. Particle Image Velocimetry

Stanislas, M.
Ecole Centrale de Lille, France.
Tel: +33 320 337 170
Fax: +33 320 337 169
Michel.Stanislas@ec-lille.fr

33. Transition Mechanisms, Prediction and Control

Hanifi, A.
FOI, Sweden.
Tel: +46 855 503 197
Fax: +46 855 503 397
ardeshir.hanifi@foi.se

34. Design Optimisation

Giannakoglou, K.
NTUA, Greece.
Tel: +30 210 772 1636
Fax: +30 210 772 3789
kgianna@central.ntua.gr

35. Multipoint Turbulence Structure and Modelling

Cambon, C.
ECL Ecully, France.
Tel: +33 472 186 161
Fax: +33 478 647 145
claude.cambon@ec-lyon.fr

36. Swirling Flows

Braza, M.
IMFT, France.
Tel: +33 534 322 839
Fax: +33 534 322 992
braza@imft.fr

37. Bio-Fluid Mechanics

Poelma, C.
Delft University of Technology, Holland.
Tel: +31 152 782 620
Fax: +31 152 782 947
c.poelma@tudelft.nl

38. Micro-thermofluidics

Borhani, N.
EPFL, Switzerland.
Tel: +41 216 933 503
Fax: +41 216 935 960
navid.borhani@epfl.ch

39. Aeroacoustics

Bailly, C.
Ecole Centrale de Lyon, France.
Tel: +33 472 186 014
Fax: +33 472 189 143
christophe.bailly@ec-lyon.fr

40. Smoothed Particle Hydrodynamics

Le Touze, D.
Ecole Centrale de Nantes, France
Tel: +33 240 371 512
Fax: +33 240 372 523
David.LeTouze@ec-nantes.fr

41. Fluid Structure Interaction

Longatte, E.
EDF, France.
Tel: +33 130 878 087
Fax: +33 130 877 727
elisabeth.longatte@edf.fr

42. Synthetic Models in Turbulence

Nicolleau, F.
University of Sheffield, England.
Tel: +44 114 222 7867
Fax: +44 114 222 7890
f.nicolleau@sheffield.ac.uk

43. Fibre Suspension Flows

Lundell, F.
The Royal Institute of Technology,
Sweden.
Tel: +46 87 906 875
fredrik@mech.kth.se

44. Fundamentals and Applications of Fractal Turbulence

Fortune, V.
Université Pierre et Marie Curie, France.
Tel: +33 549 454 044
Fax: +33 549 453 663
veronique.fortune@lea.univ-poitiers.fr

45. Uncertainty Quantification in Industrial Analysis and Design

Lucor, D.
d'Alembert Institute, France.
Tel: +33 (0) 144 275 472
didier.lucor@upmc.fr

ERCOFTAC Pilot Centres

Alpe - Danube - Adria

Steiner, H.
Inst. Strömungslehre and
Wärmeübertragung
TU Graz, Austria
kristof@ara.bme.hu

Belgium

Geuzaine, P.
Cenaero,
CFD Multi-physics Group,
Rue des Frères Wright 29,
B-6041 Gosselies,
Belgium.
Tel: +32 71 919 334
philippe.geuzaine@cenaero.be

Brasil

Rodriguez, O.
Department of Mechanical Engineering,
Sao Carlos School of Mechanical
Engineering,
Universidade de Sao Paulo,
Brasil.
oscarmhr@sc.usp.br

Czech Republic

Bodnar, T.
Institute of Thermomechanics AS CR,
5 Dolejskova,
CZ-18200 Praha 8,
Czech Republic.
Tel: +420 224 357 548
Fax: +420 224 920 677
bodnar@marian.fsik.cvut.cz

Spain

Onate, E.
Universitat Politècnica de Catalunya,
Theofilis, V.
Universidad Politécnica de Madrid, Spain
Spain.
onate@cimne.upc.edu
vassilis@aero.upm.es

France South

Braza, M.
IMF Toulouse,
CNRS UMR - 5502,
Allée du Prof. Camille Soula 1,
F-31400 Toulouse Cedex, France.
Tel: +33 534 322 839
Fax: +33 534 322 992
Braza@imft.fr

France West

Danaila, L.
CORIA, University of Rouen,
Avenue de l'Université BP12,
76801 Saint Etienne du Rouvray
France.
Tel: +33 232 953 702
luminita.danaila@coria.fr

Germany North

Gauger, N.R.
Chair for Scientific Computing
TU Kaiserslautern
Paul-Ehrlich-Strasse 34
67663 Kaiserslautern, Germany
Tel: +49 631 205 5635
Fax: +49 631 205 3056
nicolas.gauger@sci.comp.uni-kl.de

Germany South

Becker, S.
Universität Erlangen, IPAT
Cauerstr. 4
91058 Erlangen
Germany
Tel: +49 9131 85 29451
Fax: +49 9131 85 29449
sb@ipat.uni-erlangen.de

Greece

M. Founti.
National Tech. University Of Athens,
School of Mechanical Engineering,
Lab. of Steam Boilers and
Thermal Plants,
Heron Polytechniou 9,
15780 Zografou, Athens, Greece
Tel: +30 210 772 3605
Fax: +30 210 772 3663
mfou@central.ntua.gr

Switzerland

Jenny, P.
ETH Zürich,
Institute of Fluid Dynamics,
Sonneggstrasse 3,
8092 Zürich, Switzerland.
Tel: +41 44 632 6987
jenny@ifd.mavt.ethz.ch

Italy

Rispoli, F.
Tel: +39 064 458 5233
franco.rispoli@uniroma1.it
Borello, D.
Tel: +39 064 458 5263
domenico.borello@uniroma1.it
Sapienza University of Rome,
Via Eudossiana, 18
00184 Roma, Italy

Netherlands

Van Heijst, G.J.
J.M. Burgerscentrum,
National Research School for Fluid
Mechanics, Mekelweg 2,
NL-2628 CD Delft, Netherlands.
Tel: +31 15 278 1176
Fax: +31 15 278 2979
g.j.f.vanheijst@tudelft.nl

Nordic

Wallin, S.
Swedish Defence Research Agency FOI,
Information and Aeronautical Systems,
S-16490 Stockholm,
Sweden.
Tel: +46 8 5550 3184
Fax: +46 8 5550 3062
stefan.wallin@foi.se

Poland

Rokicki, J.
Warsaw University of Technology,
Inst. of Aero. & App. Mechanics,
ul. Nowowiejska 24,
PL-00665 Warsaw, Poland.
Tel: +48 22 234 7444
Fax: +48 22 622 0901
jack@meil.pw.edu.pl

France - Henri Bénard

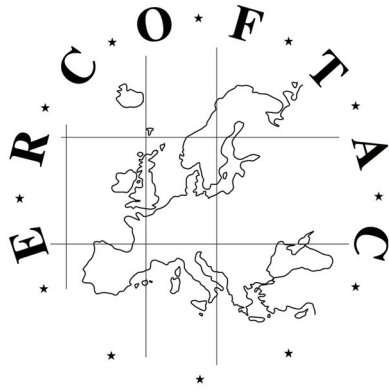
Godefert, F.S.
Ecole Centrale de Lyon.
Fluid Mechanics and Acoustics Lab.,
F-69134 Ecully Cedex,
France.
Tel: +33 4 72 18 6155
Fax: +33 4 78 64 7145
fabien.godefert@ec-lyon.fr

Portugal

da Silva, C. B.
Instituto Superior Técnico,
University of Lisbon
Av. Rovisco Pais, 1049-001 Lisboa
Portugal
carlos.silva@ist.utl.pt

United Kingdom

Standingford, D.
Zenotech Ltd.
University Gate East, Park Row,
Bristol, BS1 5UB
England.
Tel: +44 117 302 8251
Fax: +44 117 302 8007
david.standingford@zenotech.com



Best Practice Guidelines for Computational Fluid Dynamics of Dispersed Multi-Phase Flows

Editors

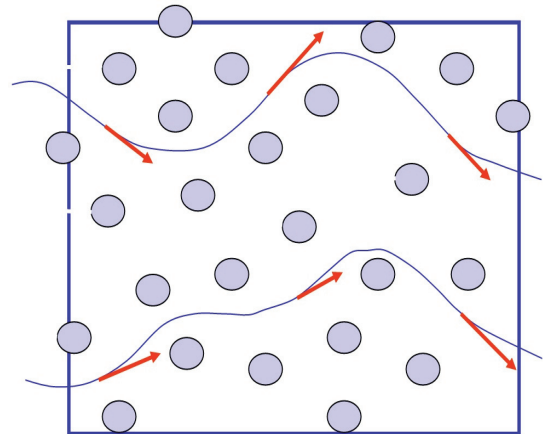
Martin Sommerfeld, Berend van Wachem
&
René Oliemans

The simultaneous presence of several different phases in external or internal flows such as gas, liquid and solid is found in daily life, environment and numerous industrial processes. These types of flows are termed multiphase flows, which may exist in different forms depending on the phase distribution. Examples are gas-liquid transportation, crude oil recovery, circulating fluidized beds, sediment transport in rivers, pollutant transport in the atmosphere, cloud formation, fuel injection in engines, bubble column reactors and spray driers for food processing, to name only a few. As a result of the interaction between the different phases such flows are rather complicated and very difficult to describe theoretically. For the design and optimisation of such multiphase systems a detailed understanding of the interfacial transport phenomena is essential. For single-phase flows Computational Fluid Dynamics (CFD) has already a long history and it is nowadays standard in the development of air-planes and cars using different commercially available CFD-tools.

Due to the complex physics involved in multiphase flow the application of CFD in this area is rather young. These guidelines give a survey of the different methods being used for the numerical calculation of turbulent dispersed multiphase flows. The Best Practice Guideline (BPG) on Computational Dispersed Multiphase Flows is a follow-up of the previous ERCOFTAC BPG for Industrial CFD and should be used in combination with it. The potential users are researchers and engineers involved in projects requiring CFD of (wall-bounded) turbulent dispersed multiphase flows with bubbles, drops or particles.

Table of Contents

1. Introduction
2. Fundamentals
3. Forces acting on particles, droplets and bubbles
4. Computational multiphase fluid dynamics of dispersed flows
5. Specific phenomena and modelling approaches
6. Sources of errors
7. Industrial examples for multiphase flows
8. Checklist of 'Best Practice Advice'
9. Suggestions for future developments



Copies of the Best Practice Guidelines can be acquired electronically from the ERCOFTAC website:

www.ercoftac.org

Or from:

ERCOFTAC (CADO)
PO Box 53877
London, SE27 7BR
United Kingdom

Tel: +44 203 602 8984

Email: magdalena.jakubczak@ercoftac.org

The price per copy (not including postage) is:

ERCOFTAC members

First copy	Free
Subsequent copies	75 Euros
Students	75 Euros

Non-ERCOFTAC academics	140 Euros
Non-ERCOFTAC industrial	230 Euros
EU/Non EU postage fee	10/17 Euros